GRAVITATIONAL LENSING
BY RICH CLUSTERS OF GALAXIES

Ian Robert Smail

January 1993

An account of research undertaken at the Department of Physics, submitted to the University of Durham in accordance with the regulations for admission to the degree of Doctor of Philosophy.

1 2 MAY 1993

ABSTRACT

We present observations and analysis of gravitationally lensed systems designed to test the usefulness of gravitational lensing as a probe into the nature of faint galaxies ($B_j \leq 27$). The analysis techniques used also provide unique observational constraints on the masses and morphologies of the lensing clusters.

Using a catalogue of giant arc candidates constructed with a well determined selection function we initially examine the possible uses of such a catalogue to provide information on the redshift distribution of galaxies to $B_j \sim 26$. We conclude that the extreme sensitivity of the lensing signal to slight differences in the lensing clusters prevents the successful application of this technique. Nevertheless, we show that the tests could be successfully applied to very deep observations of a single rich cluster.

We then illustrate the uniquely detailed view of high redshift galaxies which is provided by giant gravitational arcs by presenting near-infrared imaging of a complete sample of spectroscopically-confirmed giant arcs. Spectral modelling of the multi-band colours of these arcs confirms that the most distant arcs ($z \sim 1$) are remarkably blue at all wavelengths. This observation is incompatible with models for the arc's colours which contain recent star bursts superimposed upon even moderate fractions of underlying evolved stellar populations. We conclude that a constant star formation rate in marginally sub-L^* systems is most consistent with the observations of the $z \sim 1$ arcs.

Using very deep optical images of three moderate and distant redshift clusters selected on either X-ray luminosity or optical richness (Cl1455+22; $z = 0.26$, Cl0016+16; $z = 0.55$ and Cl1603+43; $z = 0.89$) we create robust samples of faint galaxies ($B_j \leq 27$) suitable for lensing studies. These samples are used in two separate analytic methods to study both the redshift distribution of the faint field galaxy population and the mass in the

lensing clusters. Relatively simple tests rule out redshift distributions for the faint field galaxies which depart significantly, at either low or high redshift, from the no evolution prediction. The mass analysis uses newly-developed techniques to reconstruct for the first time the two dimensional mass distribution in the lens from the gravitationally distorted images of galaxies seen through the clusters. We conclude that the morphology of the mass distribution is accurately traced by the cluster galaxies.

Finally, we present the discovery of a very wide separation multiply-imaged system recently found in deep Hubble Space Telescope images of the rich cluster AC114 ($z = 0.31$). Spectroscopic observations of the multiply imaged system confirm its lensed nature and provide a probable redshift of $z = 1.87$ for the source. Preliminary modelling of the cluster mass using all the gravitationally lensed galaxies in the field support the conclusions reached above – the cluster galaxies appear to be fair tracers of the mass.

PREFACE

The work presented in this thesis was carried out between 1989 and 1992 while the author was a research student under the supervision of Prof. R.S. Ellis, in the Department of Physics at the University of Durham.

Some of the work presented here was undertaken in collaboration with the following research staff at Durham: Prof. R.S. Ellis (Chapters 2, 3 & 4), Dr. M.J. Fitchett (Chapter 3 & 5) and Dr. A. Aragón-Salamanca (Chapter 4). However, the major part of the research described here is the author's own work. This work has not been submitted for any degree, diploma or other qualification at any other university.

A number of the results described here have appeared in the following papers:

Ellis, R.S., Allington-Smith, J.R. & Smail, I. 1991, *Mon. Not. R. astr. Soc.*, **249**, 184–190.

Smail, I., Ellis, R.S., Fitchett, M.J., Nørgaard-Nielsen, H.U., Hansen, L. & Jørgensen, H.E. 1991, *Mon. Not. R. astr. Soc.*, **252**, 19–29.

Smail, I., Ellis, R.S., Fitchett, M.J. & Carter, D., in *Clusters & Superclusters of Galaxies – Contributed Talks and Poster Papers*, ed Colless, M.M. *et al.*. (1991).

Sharples, R.M., Smail, I., Ellis, R.S., Couch, W.J., Fitchett, M.J. & Jørgensen, H.E., in *Science with HST*, ST-ECF Workshop (1992).

Smail, I., Ellis, R.S., Aragòn-Salamanca, A., Soucail, G., Mellier, Y. & Giraud, E. 1993, *Mon. Not. R. astr. Soc.*, in press.

CHAPTER 4: GIANT GRAVITATIONAL ARCS:

STAR FORMATION IN HIGH REDSHIFT GALAXIES

CHAPTER 5: STATISTICAL GRAVITATIONAL LENSING OF

THE FAINT GALAXY POPULATION

CHAPTER 7:   CONCLUSIONS

CHAPTER 8:   APPENDIX

1 INTRODUCTION

1.1 Gravitational Lensing

Two main areas of research are investigated in this thesis these are the nature and evolution of the faint field galaxy population and the growth of clusters. The faint blue galaxies uniformly cover the sky in very deep images. Where are they and what are they? To decipher the observations of these objects to give us information on their intrinsic luminosities and star formation rates as a function of time we first need to know their distances – a simple problem to pose but technically demanding to answer. The technique used here to investigate faint galaxies is an original one: gravitational lensing. The observational study of gravitationally lensed galaxies is a young field and has proceeded so far in a rather unfocused manner. We present observational work, the primary aim of which is to create well-defined and robust samples in order to study the faint galaxy population, while minimising the possible effects of biases in the analysis. Galaxies are most obviously distorted by gravitational lensing due to cluster-sized potentials and hence our study of the sources also provides information on the lensing clusters. We can thus place constraints on the evolution in the cluster mass distributions as a function of redshift. These constraints are directly applicable to the theoretical models which describe the growth of structure in

the universe and are unaffected by most of the criticisms aimed at previous observational techniques.

The gravitational lensing of galaxies by cluster potentials results in two general classes of object: arcs and arclets. The dividing line is merely a semantic one based on the observed ellipticity, with an axial ratio: $A \equiv a/b = 2$ being a reasonable choice. The most extreme examples of arcs have $A \gtrsim 10$, are usually curved and are therefore termed giant arcs. These were the first objects identified as gravitationally lensed galaxies (Soucail *et al.* 1987, see Soucail 1992 for an recent review).

The giant arcs are highly elongated images of distant galaxies, the strong distortion arises from the gravitational fields produced by the compact cores of massive rich clusters. The conservation of surface brightness combined with the amplification of the lensing process leads to the arcs having much brighter apparent magnitudes than the original sources. For a typical giant arc the source may be 2-3 magnitudes fainter than the resulting arc. Of course the source is also required to be beyond the lensing cluster, thus the study of the giant arcs is primarily the study of faint high-z field galaxies. This is precisely the class of objects which holds the key to the nature of the faint field galaxy population. The study and the analysis of the number and nature of the giant arcs provides a direct probe of this population. The advantage of the giant arcs, which offsets their relative rarity compared to the arclets, is that being brighter they are open to a wider range of study, including spectroscopic redshifts. The cores of rich clusters thus provide us with a 'natural telescope' to view individual high-z galaxies in great detail. We can then determine the star formation histories and masses of a sample of very distant and intrinsically very faint galactic systems.

The giant arcs are the most extreme events with the highest magnifications/distortions and they are therefore over represented in the current zoo of gravitationally lensed objects.

This bias is in the nature of the lensing process (see Appendix A) and makes selection of a 'representative' sample difficult. Being a young subject the observational samples have so far been rather inhomogenous collections and compilations. This fact, combined with the possible strong roles for many different biases, has weakened the conclusions which could be drawn from gravitational lensing studies.

The more populous arclets are less distorted and thus less amplified than the giant arcs. Unfortunately they are thus too faint for spectroscopic study with current 4m class telescopes. However, the distortions induced by the lensing cluster form a coherent pattern superimposed upon the intrinsic ellipticities and orientations of the faint background population. The coherent nature of the signal can be used to overcome the low signal to noise in individual arclets. The most basic approach is to measure the number of objects which are aligned tangentially to the centre of the lens. Given a sample of identical clusters at different redshifts the variation in the fraction of aligned images with cluster redshift gives the shape of the faint galaxy redshift distribution. However, the fraction of galaxies aligned tangentially arises from a combination of the geometry ($N(z)$ of the sources and lens redshift; z_{cl}) and the amount and distribution of mass in the lens ($M(r)$). To decouple these two factors and so remove the effect of possible changes in the lensing properties of clusters as a function of redshift, more elegant tests are required. For example, as the Einstein radius for a source is an increasing function of its redshift we might hope to see changes in the bulk properties of the background population by looking at their variation as a function of radius in the plane of the lens.

The first study of the weak gravitational lensing effect was performed by Tyson and collaborators (Tyson *et al.* 1990). Using deep B and R or I images of two clusters they claimed to find an excess of tangentially aligned objects – a clear signal of gravitational lensing. They also stated that the excess was dominated by the bluest objects in the field and concluded that 70% of the faint galaxy population to $B_j \leq 26$ were probably very

distant star forming galaxies at $z \gg 1$. There has seemingly been little activity in this field since that letter. The three main groups working on observations of gravitationally lensed galaxies are headed by Tony Tyson in the US, Bernard Fort in Toulouse and Richard Ellis at Durham. The US team is still collecting data connected with statistical arclet studies while the French group has been undertaking a systematic search for giant arcs. This thesis details the work that has been undertaken at Durham covering both of these areas – the study has been orientated towards the main thrusts of the research at Durham: the nature of the faint field galaxy population and the study of large scale structure.

1.2 The Lensed: Faint Field Galaxies

Our intention here is two-fold: to compare current models for the evolution of the faint field galaxies with both individual high signal to noise observations of arcs and statistical tests using large numbers of faint arclets in order to understand the nature and evolution of the faint galaxy population. We start by discussing the current models for the evolution of the faint field population. There are three crucial observational results which have to be complied with by any model for the origin and distribution of faint field galaxies. These are:

• The steep rise in the number of galaxies seen to faint limits in blue optical passbands (Tyson 1988, Metcalfe *et al.* 1990, Lilly *et al.* 1991). The total number of objects detected is far in excess of that predicted by the no evolution model at faint limits, irrespective of the value of q_o. The rise is steepest in bluer passbands showing that the population becomes bluer as the samples reach fainter. No strong feature has been observed in the counts to a limit of $B_j \sim 28$ (Metcalfe, priv. comm.). However, there does appear to be a reduction in the slope of the counts at $B_j \sim 26$.

• However, to the depth reachable by current spectrographs on 4m class telescopes ($B_j \sim$ 24) there appears to be no significant departure from the no evolution prediction of the shape of the redshift distribution for the blue-selected samples (Broadhurst *et al.* 1988, Colless *et al.* 1990, 1992, Cowie *et al.* 1991, Glazebrook *et al.* 1993). Even though by this limit there is already an excess of a factor of at least 4 in the number of galaxies observed above the no evolution prediction. The galaxies that constitute the excess must therefore be coeval with the 'normal' population. The lack of a high redshift tail as predicted by simple luminosity evolution models of galaxy formation is a strong indication that the blueing trend seen in the faint counts is due to evolution at low redshift. Recent observations of red and near-infrared selected samples give results which could be best described as marginal deviations from the no evolution distributions (Lilly 1992, Tresse *et al.* 1992).

• A final observational constraint comes from the number counts of objects in the near-infrared (K band). In contrast to the optical counts, the K counts are very close to the no evolution prediction for a low q_o geometry (Cowie 1991, Gardner *et al.* 1993).

There are a variety of other observations that have some bearing on certain models for the evolution of the faint field population. Of these possibly the most widely applicable is the U band survey of Guhathakurta *et al.* (1990) which requires that the fraction of galaxies with moderate Lyman-breaks beyond $z \sim 3$ is below 7% at $B_j \sim 26.5$. This constrains any high redshift tail of gas-rich systems. The two-point correlation function has also recently been used to study the clustering of faint field galaxies (Efstathiou *et al.* 1991, Couch *et al.* 1992). Although attempts to use this approach to constrain the redshift distribution of the faint galaxy population have been confused by the lack of information about the possible evolution of their clustering strength.

1.2.1 No Evolution Model

All the observations quoted above have been compared with no evolution models. Such a model, while being physically unrealistic, has the advantage of being an easily calculable yard-stick against which the observations can be compared. The no evolution model has the following features. For a galaxy of a given absolute magnitude; M, seen at a redshift; z, the observed magnitude; m, is given by:

$$m = M + 5 \log D_l(z) + 25 + K(z) + E(z)$$

$D_l(z)$ is the luminosity distance (in Mpc), which depends upon the geometry of the universe. $K(z)$ is the k-correction which arises from the difference in the regions of the spectral energy distribution of a galaxy sampled by a filter as the source is shifted to higher red-shift. $E(z)$ is the evolutionary correction which is perhaps the least well determined of all the factors. This term corrects for all changes in the stellar population and state of the galaxy as a function of redshift. When $E(z)$ is calculated only for the normal changes in the mix of star types in a galaxy, as a result of the changes in the stellar population with age, this is termed passive evolution. Taking $E(z) = 0$ we get the no evolution model in which the stellar populations are unchanging with cosmic time.

The no evolution model (N.E.) which is used in the following chapters as a null hypothesis is defined as follows (King & Ellis 1985). The mix and space density of galaxies are taken from local redshift surveys and these are replicated out to high redshift using a fixed luminosity function in a universe with a flat geometry ($q_o = 0.5$, $\Lambda = 0$) under the assumption of conservation of the comoving number density of galaxies. Type-dependent k-corrections determined from the observed low redshift galaxy spectral energy distributions are applied, but as stated no evolutionary correction is used. When isophotal magnitudes are calculated

a type-dependent surface brightness profile is used, which again is assumed to be fixed with redshift. While there are many reasons why such a model may be physically implausible it at least has the advantage of being reasonably well determined. Current doubts about the validity of the comparison dwell on the mix of galaxies selected locally to determine the universal space densities of various galaxy types and on the possible shortcomings of extreme UV observations of local galaxies (Koo & Kron 1992). The latter observations are extremely important in determining the k-corrections applied to each morphological type.

1.2.2 Contending Models

The three basic adjustable parameters which are available to any galaxy evolution model are: the geometry of space, the luminosity function and galaxy number density. Currently popular models which attempt to reconcile the three observational results listed above vary all of these parameters and can thus be divided into three main catagories: Changing the geometry of the universe (q_o & Λ) usually combined with pure luminosity evolution; Differential luminosity evolution – evolution in the shape of the luminosity function; Number density evolution – via mergers or addition of a new population of sources. Taking these in order:

• Increasing the volume at high redshift either by using a low q_o open geometry and luminosity evolution (Koo & Kron 1992) or a flat geometry (Cowie 1991, Fukugita *et al.* 1991) with a non-zero Λ, allow the no evolution model to almost fit B_j counts. However, the former model then has difficulty fitting the observed redshift distribution – it develops a high-z tail – and is aesthetically unappealing in an inflationary cosmology. The latter model has been ruled out by the K band counts (Gardner *et al.* 1993).

• Differential evolution in the shape of the luminosity function was used to explain the apparent increase in the number of faint galaxies observed to $B_j = 21.5$ (Broadhurst *et al.* 1988). This was motivated by the observation that the proportion of galaxies undergoing a strong burst of star formation – measured by their [OII] equivalent widths – is close to that needed to explain the slight excess in the counts at this depth (30% abone N.E.). In this model the excess comprises galaxies that would normally be fainter than the survey's absolute magnitude cut-off for at a given redshift, but have been temporarily brightened by a burst of star formation. This naturally explains both the excess and the fact that it has a similar redshift distribution to the overlying population. However, when extended to the much larger number count excesses seen at fainter limits this approach may lead to infeasibly fast duty cycles for the bursts.

• The additional population hypothesis was prompted by results from a small spectroscopic sample of galaxies to $B_j = 24$ (Cowie *et al.* 1991). It appeared that there was an excess number of low luminosity galaxies at $z \sim 0.3$ where the no evolution $N(z)$ peaks. These were hypothesised to be dwarf galaxies undergoing a burst of star formation before either destroying themselves or fading beyond detection by the present. Theoretical models have been proposed (Babul & Rees 1992) which provide a justification for this rather unusual behaviour by invoking changes in the extra-galactic UV background which allow large numbers of dwarf galaxies to form in a very short interval. The fading route for the remanents may not be available as very strong dimming is required for them to be unobserved in current near-infrared surveys (Zepf, priv. comm.).

• Finally, we can change the space density of galaxies as a function of redshift. Such a result is expected in a scenario where galaxies grow by merging of sub-units. In these models galaxies consist of less massive sub-units at earlier epochs. This model has some success in accounting for the current observations (Broadhurst *et al.* 1992, Rocca-Volmerange & Guiderdoni 1990). The attraction of the merger hypothesis is that it is a process which

we know to be occurring on a range of scales at the present epoch. However, the lack of a strong two-point correlation function on small scales may be difficult to account for in this model – as well as in others. It has also been argued that the apparent preponderance of thin disks is incompatible with a high merger rate (Toth & Ostriker 1992).

To distinguish between these various theories it is apparent that we must observe galaxies at fainter limits where the number counts are much higher. At deeper limits we would expect the differences between the models to become more obvious: the low q_o models give a very extended redshift distribution, the burst model would resemble the no evolution prediction while the second population model has a strong excess of low redshift galaxies. The most important observations are therefore redshift distribution as a function of magnitude, the average star formation rate as a function of redshift and the average mass or luminosity as a function of redshift. Gravitational lensing provides a very promising method to attack these goals.

1.3   The Lenses: Rich Clusters

As stated above, to use the gravitational lensing of the faint field population by clusters it is important to understand the lens as well as the sources. Gravitational lensing is a unique probe of the shape and depth of a cluster's potential and thus provides us with a powerful tool to test models of cluster evolution.

The current leader amongst such models for the growth of structure in the universe is the cold dark matter model (CDM, Blumenthal *et al.* 1984, Davis *et al.* 1985). This is a hierarchical (bottom-up) model for the formation of structure – large structures are created through the merging of smaller sub-units. The distribution of fluctuations in the

intial mass field is proposed to be gaussian; these fluctuations grow linearly until they reach a critical density contrast compared to the background at which point they start to collapse. The distribution of fluctuations means that there is always a range of masses of objects which are just reaching the threshold density. Merging is therefore a continous process characterised by a single mass scale – at a particular time we can ask what is the characteristic mass of an object which is currently turning around and uncoupling from the Hubble flow. At the present epoch this characteristic mass is about the mass of a small group (10 galaxies). Larger systems, such as rich clusters, may go non-linear earlier but the more massive the system the rarer the initial fluctuation required to cause it. We would therefore predict that most structures seen today which are more massive than a group have not been in existence as a bound system for very long. They are therefore dynamically young; only their centres being virialised. At $z \gtrsim 0.2$ rich clusters would be predicted to be even rarer, younger and less relaxed then they are today.

Optically selected catalogues of distant clusters show that the space density of rich clusters (as determined from their optical richness and velocity dispersions) does not appear to decrease to $z \sim 0.5$ (Gunn *et al.* 1989, Couch *et al.* 1991). This is in stark contrast to the predictions of CDM which give a strong decline in the number of these very rare structures at intermediate redshifts. The existance of these distant galaxy clusters and in particular their high dynamically-estimated masses is a grave problem for the CDM model. This being the case a solution has been found. The much referenced explanation is that projection effects both artificially enhance the optical contrast of such systems and also contaminate the velocity dispersion of the distant clusters with interlopers producing spuriously high velocity dispersions (Frenk *et al.* 1990). It is not immediately apparent that more elaborate statistical tests applied to the observations would be unable to distinguish the type of contamination accused of causing the high dispersion tail (White 1992).

However, at the moment the explanation still stands – to determine if the distant clusters are massive systems we need an independent estimate of the cluster mass. The obvious method is to look at the X-ray luminosities of these clusters ($L_X \propto M\rho_g T^{\frac{1}{2}}$). However, even at relatively modest redshift ($z \sim 0.2$), where there is no evolution in the number of optically selected clusters, a strong decline is seen in the number of bright X-ray clusters (Edge *et al.* 1990, Gioia *et al.* 1991). This is actually in the opposite sense to the simple prediction from hierachical models – including CDM (Kaiser 1992) – which would have a strong increase in the number of X-ray clusters seen at relatively recent look-back times. This arises because although the typical cluster mass goes down with increasing redshift the density goes up and thus the characteristic X-ray luminosity is approximately constant. However, the number of sources is increasing with look-back time, giving an overall increase in the number of bright X-ray clusters. Large scale hydrodynamical simulations are needed to provide more robust theoretical predictions.

There are also good reasons why the study of cluster mass profiles at large radii is interesting. From the central mass estimates for clusters ($\Omega \sim 0.2$) we are still left with the problem of where the remainder of the mass resides if we are to have a flat universe, as predicted by inflationary cosmologies ($\Omega = 1$). A possible solution has been proposed (West & Richstone 1988, West 1990) in which the galaxies in a cluster are dynamically segregated from the dark matter. This causes them to exhibit a lower velocity dispersion than the cluster as a whole. The best regime to test this proposal is at large radii – a technically demanding region for both optical spectroscopy (due to contamination) and X-ray imaging (due to low flux) – but relatively accesible to weak gravitational lensing studies.

We now discuss a gravitational lensing technique for deriving mass estimates for distant rich clusters – the class of objects of most interest. These techniques are relatively insensitive to projection effects which have plagued other methods.

In gravitational lensing the cluster's potential field remaps the sky seen behind it: this remapping distorts the image of any source seen beyond the cluster (see Appendix A for definitions). For a source a given distance behind the lens the remapping creates a web of connected lines of infinite image amplification (caustics) on the plane of the sky. The mapping of the caustics onto the observed sky (image plane) are termed critical lines. The highly elongated giant arcs are only produced by a source close to a lens caustic – the arc actually traces the associated critical line in the image plane allowing a direct measurement of both the cluster centre and the critical line's radius and hence b (Appendix A) – if the source redshift is known this can be converted into a projected mass within the critical line.

Modelling of the potential using giant arcs has been undertaken for a number of clusters (*e.g.* A370 Grossman & Narayan 1988) giving mass to light ratios of M/L $\sim$ 100 for the central parts of the clusters ($\Omega \sim 0.2$). This value is similar to that derived from dynamical techniques and independent of the assumption required in the dynamical estimates. The high value confirms that there exists a large amount of non-luminous mass in the centres of clusters ($\Omega \gg \Omega_{gal} + \Omega_{gas}$). Furthermore, the basic conclusion is that at least in the very centres of clusters we are neither over estimating the cluster masses nor missing a large amount of dark matter by employing dynamical tracers. The full implication of these observations is actually more complex – the giant arcs provide an estimate of the mass within a cylinder through the cluster and is thus dependent upon the radial mass profile.

We can also use the statistics of the rate of occurrence of giant arcs to probe the distribution of cluster masses. However, it is important to bear in mind that the creation of the most extreme giant arcs (*e.g.* A370 A0, Cl2244−02) is dependent upon both the depth of the cluster potential well and its structure – in that a compact mass distribution will more easily create a giant arc than a diffuse cluster. Thus the observed number of giant arcs in rich clusters can be used to constrain models of the cluster masses and could in principle

be used to trace their evolution at relatively recent epochs. To quantify the term 'rich cluster' we refer to Fitchett (1990) who claims that only the most centrally condensed of the various mass models available for Coma, one of the richest local clusters ($\sigma \sim 1000$ km/sec), would be capable of strong lensing.

Although detailed modelling has been undertaken for most of the giant arcs discovered to date, very few of these models have predicted mass distributions strongly at odds with the observed light distribution. This view has been challenged in a recent paper by Boute & Canizares (1992) who attempted to look at the relative distribution of galaxies and mass in 5 low redshift clusters. The mass distributions were calculated from X-ray maps using deprojection techniques. This paper concludes that although the two distributions are orientated in the same direction the ellipticity of the mass distribution is much lower than the light. Unfortunately the Authors are forced to employ a number of assumptions to make this conclusion – of which the most damaging is that the clusters are isothermal. Note that as they purposefully selected clusters with highly elliptical light distributions – which may indicate a merging system (3 out of their 5 clusters have substructure) this assumption appears untenable.

While the giant arcs provide a probe of the mass distribution in the central regions of clusters analysis of the coherent pattern of weakly distorted arclets promises to provide a similar test in the outskirts of clusters. Tyson *et al.* (1990) attempted such analysis using deep imaging of two clusters with high velocity dispersions and X-ray luminosities: Abell 1689 at $z = 0.18$ has $L_X = 1.7 \ 10^{45}$ ergs/sec and $\sigma_{cl} = 1800\pm200$ km/sec and Cl1409+52 at $z = 0.46$ has $L_X = 9.2 \ 10^{44}$ ergs/sec and the unreasonably high dispersion of $\sigma_{cl} \sim 3000$ km/sec. The regions imaged in the two clusters were restricted by the small CCD formats: reaching to a radius of 380 kpc in the low redshift cluster and 500 kpc in the more distant system. The histograms of image orientation for the two clusters show excesses of tangentially aligned images for the blue samples in both clusters. The samples

used were selected with $B_j \in [22,26]$ roughly equivalent to $I \in [20,24]$ and were split on colour: for Abell 1689 blue was $B - R < 0.7$ and for Cl1409+52 blue was defined as $B - I < 2$. The red samples were claimed to be dominated by cluster members. Indeed, only the blue samples show the aligned excess – infact for Cl1409+52 it appears that the red galaxies are preferentially aligned radially. However, the excess blue aligned component in both clusters is small: about 30-40 galaxies in the low redshift cluster and a mere 12 in the high redshift cluster. Using these excesses Tyson *et al.* claim that at least 70% of the $B_j \in [22,26]$ galaxy population are beyond $z = 0.9$. Using a test based on the alignment signal they derive radial 'mass' profiles for the clusters and compare these with the light profiles – it transpires that the 'mass' profiles they derived were not for the mass as they claimed but were closer to the surface potential (Kaiser & Squires 1992). Clearly this analysis while promising should be repeated with larger samples all observed in the same bands and the correct surface mass estimator applied.

A new technique developed by Kaiser & Squires (1992) allows us to use the information inherent in the arclet distortion pattern to derive the full two dimensional mass distribution in the lens (see Appendix A). This marks an important step forward in the investigation of mass in clusters. The mass reconstruction is in theory only limited by the surface density of background galaxies that can be acquired – compared to spectroscopic tracers which are limited by the number of galaxies sampling the potential. In reality other effects such as projected large scale structure will effect the outer parts of the mass maps at a distance where the two contributions to the surface mass density are equal. Miralda-Escudé (1991b) has argued that this should occur at a radius around 1-2 Mpc in a typical cluster – beyond this radius it would still be possible to construct a surface density profile for the cluster but the two dimensional information would be lost. Using the full two dimensional mass map it should be possible to survey intermediate redshift clusters for the presence of substructure in their mass distributions. Substructure is to be expected in

clusters within hierachical models as these clusters should be growing via accretion events at the observed epoch – the prevelance of substructure can be used, for example, as an indicator of the density of the universe (Richstone *et al.* 1992).

The observations of arcs and arclets therefore appear to be relatively clean probes of cluster potentials – allowing us a detailed view of the distribution of mass in the cores of rich clusters and a more statistical view of the form of the mass distribution on larger scales. It is this latter approach which may provide answers about the growth of clusters and the evolution of their mass distributions. We also hope to learn something about the nature of the faint field galaxies behind the lensing clusters and so constrain models for their evolution.

1.4   Summary

We give a brief summary of the structure of this thesis:

Chapter 2: The research set out here covers the observations of a double arc structure in the rich cluster Abell 963 ($z = 0.206$) – the arcs lie in the stellar halo either side of the dominant cluster galaxy. Deep spectroscopic observations show a single emission line in the spectra of both arcs confirming that they both originate from the same source. Identification of this line with [OII]3727 gives a redshift for the source of $z = 0.771$ – using near-infrared imaging we conclude that the source is a dwarf galaxy undergoing a burst of star formation.

Chapter 3: This chapter describes the first attempt to construct a statistically complete sample of gravitational arcs. The catalogue is selected from a homogenous archive of cluster images using well defined criteria and contains a total of 20 arcs in 19 clusters.

This arc catalogue is then employed in a number of new tests to study the lensing ability of an ensemble of intermediate redshift clusters in an attempt to determine the redshift distribution of the background galaxies. The sensitivity of the lensing signal to slight differences in the lensing clusters makes application of the tests to the entire sample infeasible. Nevertheless, we show that the tests could be successfully applied to very deep observations of a single rich cluster.

Chapter 4: Using near-infrared imaging of a complete sample of 7 spectroscopically-confirmed giant arcs we extensively model the photometric characteristics of high redshift field galaxies in order to understand their star formation histories. We find that the majority of the light emitted by the most distant arc sources arises from recent star formation. Using a number of independent approaches we conclude that a constant star formation rate in sub-L^* systems is most consistent with the observations (L^* is the characteristic luminosity of a Schecter luminosity function). If the star formation remains at its observed rate these systems would be the precursors of today's spiral galaxies.

Chapter 5: In this chapter we describe the acquisition and analysis of a set of very deep optical images of three moderate and distant redshift clusters (Cl1455+22; $z = 0.259$, Cl0016+16; $z = 0.546$ and Cl1603+43; $z = 0.895$). The clusters have been selected on either X-ray luminosity or optical richness. Using well defined selection criteria we create robust samples of faint galaxies suitable for lensing studies. These are used in two separate analytic methods to study both the redshift distribution of the faint field galaxy population and the mass in the lensing clusters. Relatively simple tests rule out redshift distributions for the faint field galaxies which depart significantly, at either low or high redshift, from the no evolution prediction. The mass analysis uses newly-developed techniques to reconstruct the two dimensional mass distribution in the lens from the gravitationally distorted images of galaxies seen through the clusters. We conclude that the morphology of the mass distribution is accurately traced by the cluster galaxies.

Chapter 6: This chapter presents a unique gravitationally lensed system recently discovered in deep Hubble Space Telescope images of the rich cluster AC114 ($z = 0.31$). We also discuss observations of a number of gravitational arcs and arclets seen in the same data. Spectroscopic evidence for the lensed nature of the multiply imaged system is shown and a probable redshift of $z = 1.87$ is derived for the source. We also present an initial attempt to constrain the mass distribution in the lensing cluster by modelling of the multiply imaged source.

Chapter 7: Here we restate the main conclusions arising from the work and indicate where fruitful areas of further research may lie.

Appendix A: This gives a glossary of terms and explanations for some of the general results of gravitational lensing.

2 SPECTROSCOPY OF THE GIANT ARCS IN ABELL 963

2.1 Introduction

At the time when these observations were first published the number of gravitational arc candidates with secure spectroscopic redshifts was very small. The intention was therefore to enlarge the sample by observing one of the candidate arcs which were being serendipitously discovered by workers in other fields. The spectroscopic observation of the pair of arcs in the rich cluster Abell 963 was a unique opportunity to confirm the gravitational lensed nature of the arcs and in doing so test the prediction that both objects were images of the same background source.

Although existing spectroscopy for giant arcs supported the lensing hypothesis in all published cases (see Soucail 1992), it was important to continue spectroscopic follow-up for the fainter arclets and those arcs embedded in galaxy halos before assuming that *all* highly distorted features in deep cluster images represent lensed galaxies. This is especially important for the embedded arc candidates where there already exists a class of morphologically similar structures; shells, physically associated with the dominant galaxy (Malin & Carter 1989). When spectroscopy does confirm the lensing hypothesis the derived redshift removes the ambiguity in the intepretation of the source colours (*q.v.* Chapter 4)

and is a vital parameter in modelling the mass distribution in the lens. In this chapter we discuss spectroscopic and imaging observations of the two arcs in Abell 963 seen close to the central cD galaxy.

The structure of this chapter is as follows: Section 2 describes the photometry of the two arcs, Section 3 lays out the spectroscopic observations and their reduction, including the identification of a single emission line in the spectra of *both* arcs. Discussion of the nature of the source and the current modelling of the lensing cluster is given in Section 4 with our conclusions in Section 5.

2.2 Photometry

The two arcs in the rich cluster Abell 963 ($z = 0.206$) were first noted in B and R frames taken by Lavery & Henry (1988; LH). In fact, the arcs are just visible in earlier SIT Vidicon data published by Butcher, Oemler & Wells (1983; BOW). A B image of the cluster taken on the 2.5m Isaac Newton telescope is shown in Figure 2.1(a) and a colour-subtracted ($B - R$) frame, scaled to remove the cD envelope, is shown in Figure 2.1(b). The contrast of the blue arcs is striking. There appears to be significant structure in both arcs, in particular both arcs show two bright knots, whilst the remainder is of lower surface brightness.

Lavery & Henry commented on the fact that the arcs are both substantially bluer ($B - R \simeq 0.6 \pm 0.1$) than the cluster ellipticals ($B - R \simeq 2.5$) and near-concentric about the central cD. This represented the first example of an arc and counter arc in a single cluster. Lavery & Henry concluded that the most likely mechanism responsible for creation of the pair of arcs is gravitational lensing of a single high redshift galaxy by the cD and cluster core.
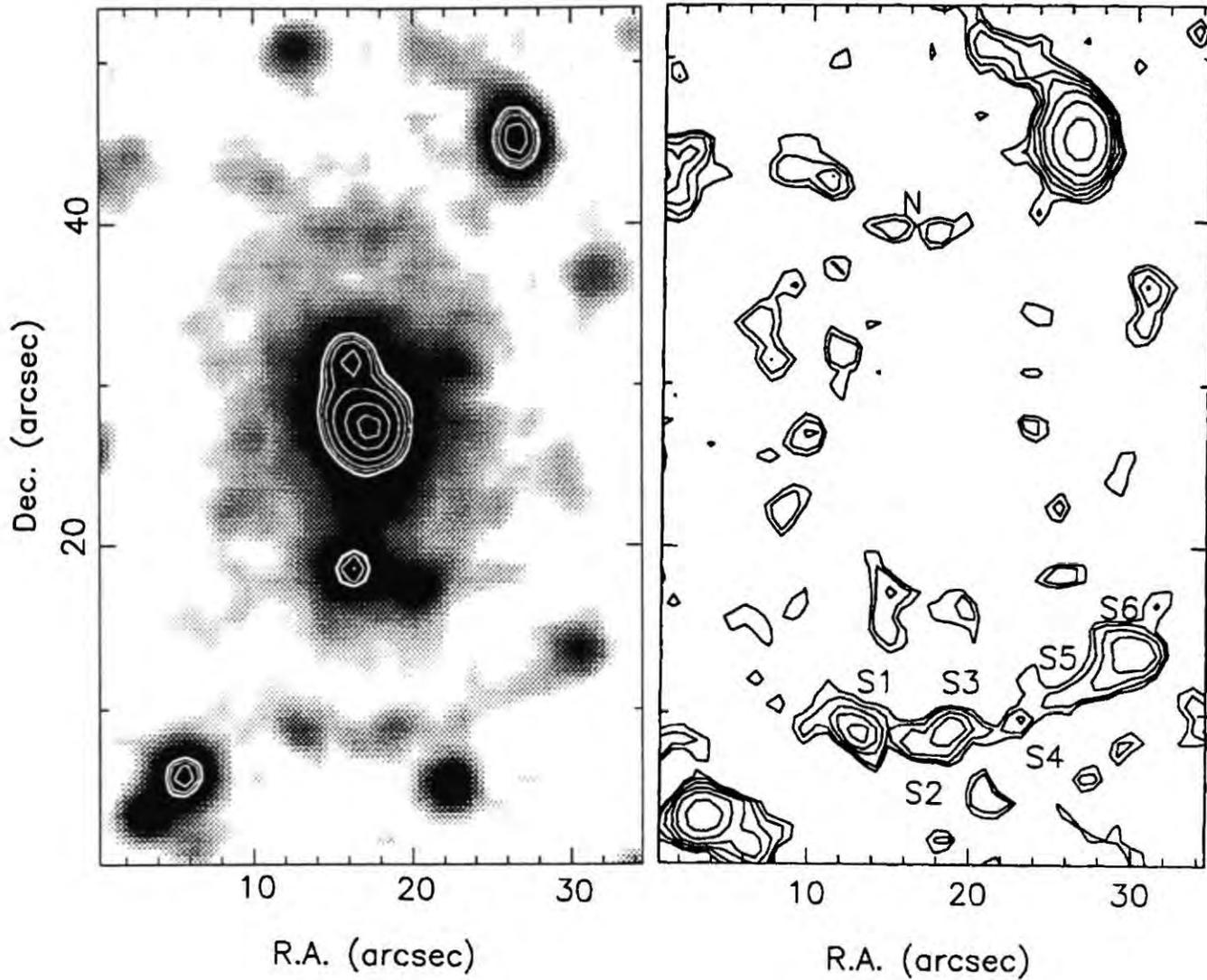
Figure 2.1 (a) A *B* band image of the core of Abell 963. North is up and east is to the left. (b) Composite $B - R$ image with the intensity in the each band scaled so that the cD envelope has zero intensity. The field orientation and size is the same as in (a). The northern arc is marked by N and the individual sub-components of the southern arc as S1–S6. BOW's object #238 is S6.

Table 2.1 Photometry of Abell 963 arcs

			Observing Log		
Filter	R.A. (1950)	Dec. (1950)	Date	Seeing	Exposure (s)
B	$10^h13^m59\overset{s}{.}0$	$39°17'20\overset{''}{.}0$	17/18 April 1990	$\sim 1\overset{''}{.}6$	2500
R			17/18 April 1990	$\sim 1\overset{''}{.}6$	1500

Telescope: 2.5m INT

Instrument: Prime

Detector: RCA (385 × 578 pixels)

Pixel size: $0\overset{''}{.}75$ /pixel

	Arc Colours	
Object	$B - R$	
	This work	Lavery & Henry
N arc	$0.3^{+0.8}_{-0.8}$	0.5
S arc (S1–S3)	$0.3^{+0.3}_{-0.4}$	0.7
S1	$0.7^{+0.2}_{-0.3}$	
S2	$0.1^{+0.6}_{-0.8}$	
S3	$-0.4^{+0.4}_{-0.5}$	
S5	$0.5^{+0.3}_{-0.3}$	
S6 (BOW #238)	$1.7^{+0.1}_{-0.1}$	
cD		2.47

Photometry is clearly important in determining whether the arc and counter-arc arise from the same background source. Unfortunately, due to the faintness of the features and the proximity of the cD envelope this is not straightforward. Although Lavery & Henry determined mean arc colours, they did not examine colours for individual portions. This is particularly important for the southern arc which is in a photometrically complex region with contamination by a number of unrelated sources. It is for this reason we secured new B and R images referred to above. These were service observations taken on the 2.5m Issac Newton Telescope (INT) in mediocre seeing. Although conditions were not photometric, our relative photometry can be calibrated to the required precision using the colour-magnitude relation of early-type cluster members and the colour of the cD envelope (both assuming a redshifted spectral energy distribution of a present day L^* elliptical; $B - R = 2.47$) and Lavery & Henry's colour for BOW object #238. These zero points differ by less than 0.1 mag in $B - R$.

Since the arcs are embedded in the envelope of the cD, it is necessary to consider carefully how to determine the background contribution when measuring colours. Lavery & Henry determined the background level from an equivalent portion of the image obtained by *reflection* about the centre of the cD. This method can only be applied to the southern arc since the mirror image of the northern arc falls on another cluster galaxy. Using this method we can reproduce Lavery & Henry's colour for the southern arc but believe it unnecessarily assumes symmetry in the envelope. Instead, we determined the background in the vicinity of both arcs by linear interpolation between regions immediately inside and outside the arcs along a radius from the cD centre; unless the variation of $B - R$ with radius in the cD envelope is strongly non-linear, this should give a more realistic estimate of the background and associated errors.

Our results for the northern arc and various portions of the southern arc are summarised in Table 2.1. The mean colours ($B - R \simeq 0.3$) are slightly bluer than Lavery & Henry's

except for S4, for which we could not obtain a reliable colour because of contamination of the background by a nearby galaxy. However, both arcs are consistent with a single colour. The variations across the southern arc (e.g. at the west end) are probably not significant. Despite the large photometric uncertainties, the low probability of unrelated objects having colours so remarkably blue in a crowded field of red ellipticals, strongly suggests both arcs are related to the same phenomenon.

2.3 Spectroscopy

During February 20–21 1990, we secured spectra for the two arcs (north and south) using the ISIS spectrograph on the 4.2m William Herschel Telescope (WHT); the observing configuration and log is summarised in Table 2.2.

Figure 2.2 shows the integrated light profiles derived from the spectra (without sky subtraction) for the 3 position angles secured on the WHT. From the spectra obtained for each arc (Figure 2.2(a) & (b)), the arc signals are found to be about 20-30% of the cD envelope at that radius. For the northern arc an extent of $\sim$5 arcsec is found (Figure 2.2(a)) in agreement with the size estimated from Figure 2.1. The profile of the southern arc (Figure 2.2(b)) shows evidence for three objects which we identify with S1, S3 and S4. S2 and S5 did not fall on the slit.

For the northern arc, spectral sky subtraction was performed using parabolic interpolation from adjacent regions, this also served to remove the contribution from the cD. The resulting spectrum has a single strong emission line at 6600Å (Figure 2.3) but no other obvious features. To demonstrate that this line comes from the arc rather than from a superimposed object or bad sky subtraction, we show the sky subtracted *image* in the

Table 2.2 Abell 963 Spectroscopic Observations

Observing Log				
Date	Seeing	Source	Slit PA	Exposure (s)
20 Feb 1990	0.8	Northern arc	90	12000
20 Feb 1990	0.8	cD	0	1500
21 Feb 1990	1.0	Southern arc	87	13000

Instrumental Setup	
Instrument	4.2m WHT + ISIS + EEV CCD (800 × 1180)
Dispersion	124 Å mm^{-1}, 2.72 Å pixel^{-1}, 8 Å resolution
Slit format	264 arcsec × 1.5 arcsec
Wavelength range	4800 – 7800 Å
Spatial resolution	0.″33 /pixel
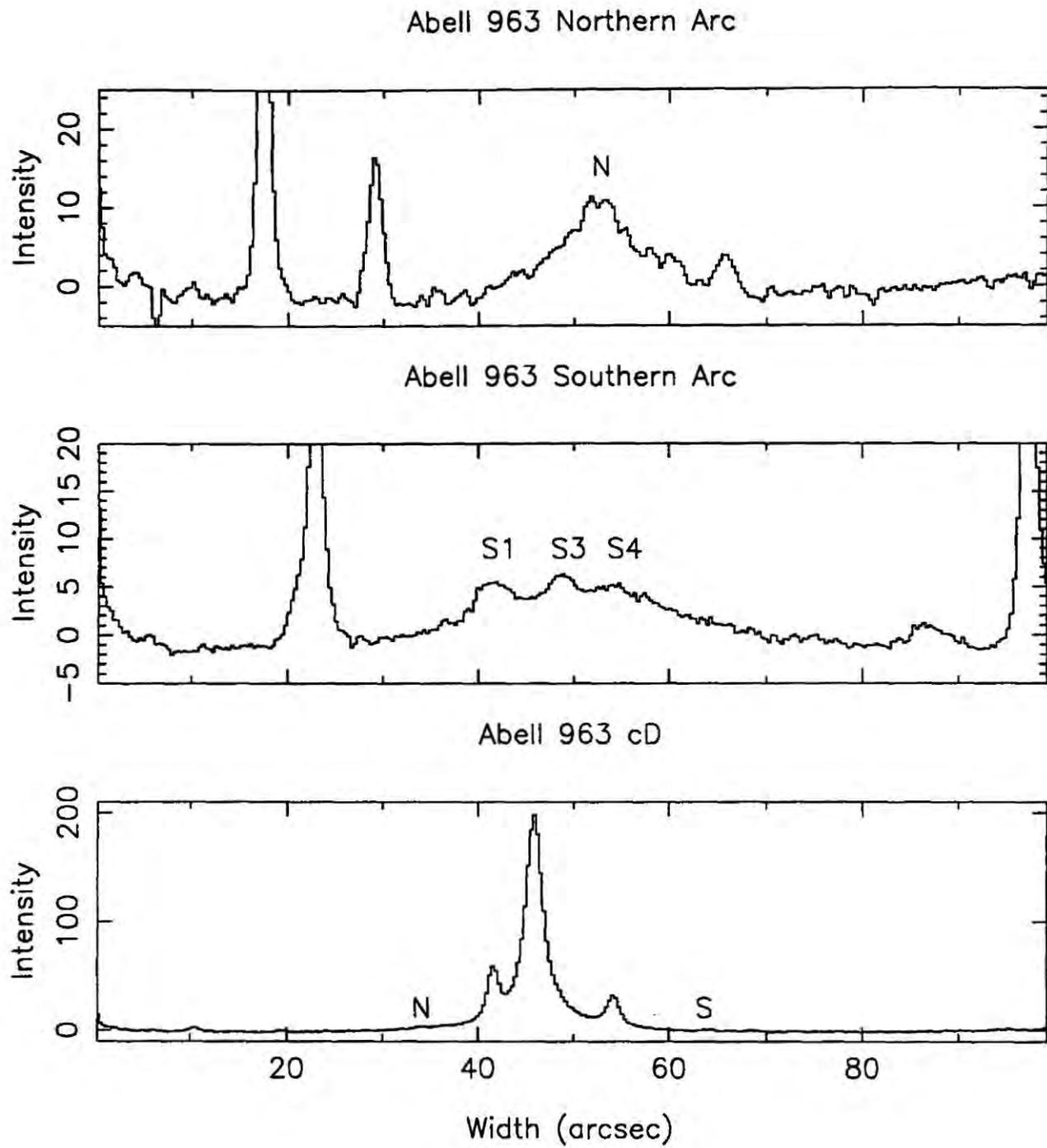
Figure 2.2 Sky brightness profiles derived from the spectral data with objects marked as in Figure 2.1: (a) E–W along northern arc, (b) E–W along southern arc, (c) N–S profile slit position angle intersecting both arcs and the cD's nucleus.

vicinity of the arc in Figure 2.4(b). The emission line clearly extends along the full length of the arc but no further. This line shows no observable velocity gradient across the arc. For the southern arc, we applied linear interpolation to estimate the sky subtraction and therefore retained the light of the cD's halo. Of the three objects, S1, S3 and S4, both S1 (Figure 2.4(c)) and S3 show a very weak emission line at 6600Å. The lack of any such feature in the cD's spectrum allows us to conclude that the lines originate from the southern arc and therefore confirms that at least certain regions of the southern arc are from the same source as the northern arc. These arcs therefore constitute the first spectroscopically confirmed multiply imaged galaxy – a fact which can be used as a powerful tool to differentiate between lensing models for the cluster. This detection lends support to those models of the cluster lens which identify both arcs as originating from the same source (Angonin $et\ al.$ 1992, see Angonin 1992).

Given the presence of only a single strong feature in the northern arc's spectrum, a reliable redshift is hard to justify. However, to support the lensing hypothesis it is sufficient to demonstrate, firstly, that the light is consistent with that from a single object (as is clearly the case – Figure 2.4(b)) and secondly, that the object is behind the cluster. If the light was due to a source foreground to the cluster, the only likely identification for the line at 6600Å would be Hα at $z = 0.0056$. Given the blue colour one would expect to see Hβ at 4888Å. Additionally, the object would be only be 4 h^{-1} kpc across. This hypothesis is thus unlikely.

At the cluster redshift itself, the line has no sensible identification. If the line is [O$\textsc{iii}$]5007 at $z = 0.318$, the absence of Hβ and [O$\textsc{iii}$]4959 is puzzling, as is the absence of Hγ for this colour if the strong line is Hβ at $z = 0.358$. Most probably the line is [O$\textsc{ii}$]3727 at $z = 0.771$ in which case no other strong emission lines would be expected in the 4800-7800Å window. The most likely additional feature expected for a galaxy of this colour would then be the Balmer line Hϵ plus Ca$\textsc{ii}$ H at $\lambda_{rest} = 3968$ Å, for which there is little evidence.
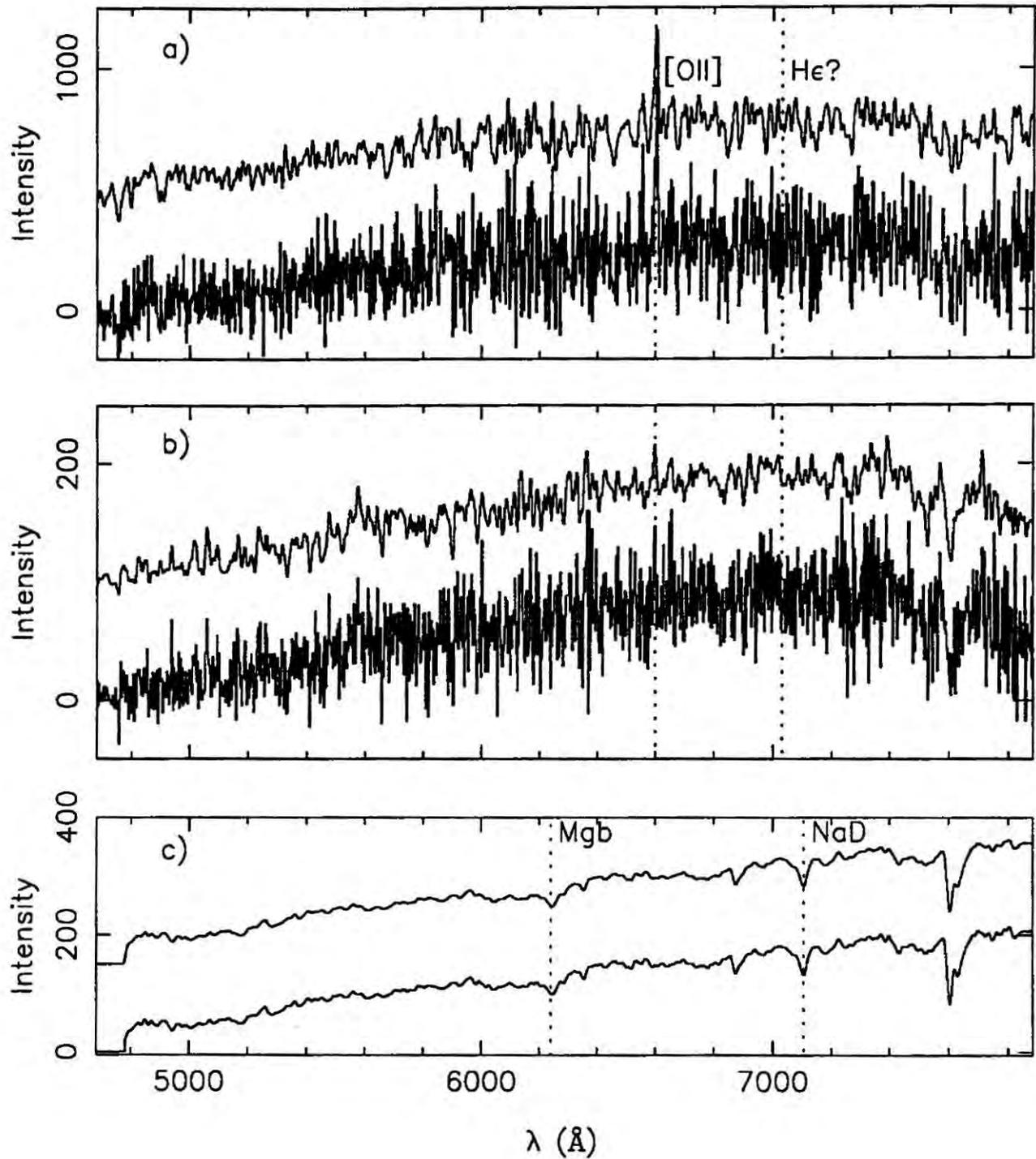
Figure 2.3 (a) Sky subtracted spectrum of the northern arc in Abell 963 with features marked for the measured redshift of $z = 0.771$. (b) Spectrum of the object S1 from the southern arc in Abell 963 showing the position of features detected in the northern arc spectrum. (c) Sky subtracted spectrum of the cD galaxy for comparison. In each case the upper of the two spectra has been smoothed to the instrumental resolution.
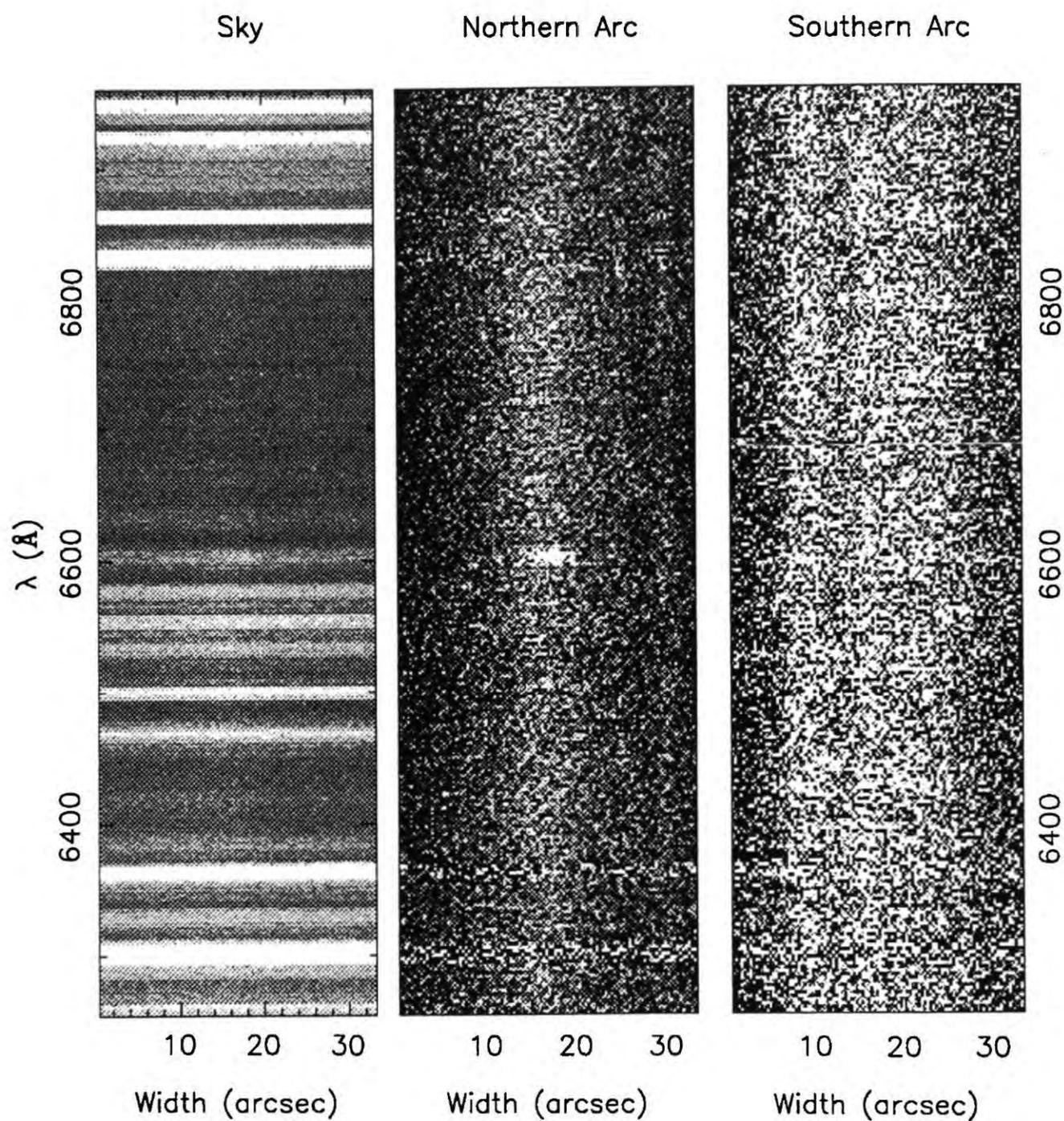
Figure 2.4 2-D spectral images for the region of the slit containing the emission line. (a) Northern arc before sky subtraction. (b) Sky subtracted northern arc, notice that the emission line at 6600Å extends along just that portion of the slit occupied by the arc in Figure 2.2(a). (c) Sky subtracted southern arc showing structure corresponding to S1, S3 & S4.

Higher redshift identifications cannot be ruled out, but in each case one would expect to see other lines or discontinuities present. The rest frame equivalent width of the [OII]3727 line is 12Å, although this is a lower limit due to possible residual contamination from the cD's envelope.

The spectrum of the southern arc is not as satisfactory as the northern arc primarily because the weather, whilst good, was not as exceptional as on the previous night. This is reflected in the relative flux of the [OII] line in the two spectra, the significance of the line in the southern arc spectrum being less than would be expected from the source brightnesses. In the original publication of this work (Ellis *et al.* 1991) we did not claim any detection of this line in any subset of the southern arc. This lack of detection was due to non-optimal reduction techniques applied to the data used in that paper. These consisted of median combining, rather than averaging, of the raw data and the use of parabolic interpolation in an attempt to remove both the sky and cD contamination from the southern spectrum. This necessitated the use of a smaller region to define the background sky flux creating larger errors. Both of these degraded the final signal to noise. Further spectroscopic work on the southern arc to confirm this line identification is highly desirable but would benefit from a purpose-made curved slit.

2.4   Discussion

We can place some limits on the source if we accept that both arcs are gravitationally-lensed images of a single background object at $z = 0.771$ with $B - R \simeq 0.3 \pm 0.5$ (Table 2.1). This average colour is marginally bluer than that expected from redshifted spirals. Even the bluest Sdm/Irr galaxies today (Chapter 4) would have $B - R \geq 0.7$ for all redshifts of interest, $z < 2$.

At the time the observations were taken, the most secure spectroscopically-confirmed arc was the giant arc in Abell 370, which was found to be a lensed background source at $z = 0.72$ (Soucail $et\,al.$ 1988). In this case the arc's blue optical colour probably arises from a relatively mild ultraviolet upturn in an otherwise normal Sbc spiral (Aragón Salamanca & Ellis 1990). Could the blue $B - R$ colours in Abell 963 reflect a similar burst of star formation in an otherwise old system?

The arcs in Abell 963 are considerably bluer than the giant arc in Abell 370 but a strong detection at 2μm would clearly indicate the presence of an old population. Because of the lower surface brightness and the overwhelming presence of the cD envelope at infrared wavelengths, this was a very difficult observation. A 5 hour integration undertaken in May 1990 using UKIRT's IRCAM detected the northern arc at a mean surface brightness contour of $\mu_K \simeq 22.0$ mag/arcsec^2 (Chapter 4). The derived $R - K \sim 2.7{\pm}0.3$ supports the interpretation of the arc source as a blue strongly star-forming galaxy. Clearly more accurate photometry is desirable before the overall spectral energy distribution is modelled further. Given the faintness and location of the arcs this will, however, be very difficult.

The arc's blue optical colours are typical of a sizeable fraction of the faint field population (Tyson 1988) and it is tempting to assign the lensed source to this population. However, the [OII] equivalent width limit of the northern arc is at the lower end of those measured by Broadhurst $et\,al.$ (1988) for their faint sample ($b_j \leq 21.5$). Combined with the calculated $M_K \simeq -21.$ (Chapter 4) this implies we are seeing a dwarf system in a phase of relatively vigorous star formation similar to those seen in field redshift surveys at $z \sim 0.3$ (Cowie $et\,al.$ 1992).

The presence of strong star-forming dwarf galaxies at $z \sim 0.5$–1 is not unexpected in many evolutionary pictures including those invoking recent galaxy formation (Babul & Rees 1992). However, the detection of a few examples implies little about any general increase

in the star formation rate for the *overall* galaxy population without some consideration of the selection processes involved. The same biases which render a galaxy visible in the redshift surveys (c.f. Colless *et al* 1990, 1992) are quite likely to affect the detection of arcs in surface brightness limited surveys. A proper understanding of the means by which arcs are detected and a statistical study of their rates of occurrence is required to properly exploit this interesting phenomenon in unravelling both the properties of high redshift galaxies and of the clusters which lens them (Chapter 3).

The current theoretical modelling of the arcs in Abell 963 appears to support a model in which the two arcs originate from different sources. Angonin *et al.* (1991) initially claimed that it was possible to model the two arcs as arising from the same source. However, Kovner (1989) has voiced concern that the mass distribution in the lens needed to form the two arcs from a single source has to be very close to circular. This is at odds with both the X-ray surface brightness distribution of the cluster (Kellogg *et al.* 1990) and the light distribution of the cD (Figure 2.1(a)) both of which are strongly elliptical. He therefore favours a model with two sources – with the longer southern arc originating from the more distant. More recently Angonin (priv. comm.) has stated that their previous model has problems recreating the widths of the two arcs. At the present moment it is not clear whether it will be possible to manipulate the models to overcome this difficulty.

One possible recourse is indicated by a comparison of the X-ray map and the cluster member's distribution – selected by colour from our CCD frames. Neither of these distributions is centered on the cD galaxy – both centres being approximately 0.5 arcmin due east. A cD spatially offset from the cluster centre is not unexpected, detailed study of the velocity distributions of several local clusters shows that their cD's have significant velocity offsets from the cluster mean. A less naive lens with non-concentric potentials for the cluster and cD may be capable of successfully accounting for both arcs using a single source. To determine if the centre of mass of the cluster does indeed lie off the cD it will

be necessary to either acquire higher resolution X-ray images of the cluster or perform deep optical imaging to detect the statistical alignment of the background faint galaxy population caused by gravitational lensing.

2.5 Conclusions

• The presence of an emission line at the same wavelength in the spectra of both the northern and southern arcs in Abell 963 indicates that both arcs most likely represent images of a single source. These arcs therefore constitute the first spectroscopically-confirmed multiply imaged galaxy discovered. The identification of the line as [OII]3727 gives the redshift of the source as $z = 0.771$.

• The combined optical and infrared photometry for the arcs show that the lensed galaxy must be currently undergoing a burst of star formation. Moreover, the very low intrinsic absolute K magnitude points towards the source being a dwarf galaxy – similar to those seen at lower redshift in the field (Chapter 4).

• Finally we note that the identification of both arcs as arising from the same source requires a re-evaluation of the current lensing models for the mass distribution in the cluster. One possible solution is indicated by the optical and X-ray images of the cluster which show that the cD does not appear to lie at the centre of mass of the system.

3 A STATISTICALLY-COMPLETE SURVEY FOR ARCS IN DISTANT RICH CLUSTERS OF GALAXIES

3.1 Introduction

To date the arc phenomenon is sufficiently new that it has been regarded largely as a demonstration of gravitational lensing. However, our aim in this chapter is to test the *use* of arcs as a cosmological tool. If the majority of arc-like features seen in intermediate redshift clusters arise from gravitational lensing of background sources, their statistics may be used to constrain not only the redshift distribution of the population of very faint field galaxies, unobtainable by conventional spectroscopy, but also the mass distribution in the lensing clusters – which is difficult to obtain even by indirect methods. The application of gravitational lensing to these tests has been hampered by the lack of a statistically-complete sample of giant arcs. The aim of the work presented in this chapter is to create such a sample and to test its usefulness in differentiating between different proposed redshift distributions of the background field population.

It can be easily demonstrated (Appendix A, Nemiroff & Dekel 1989) that for each highly distorted giant arc there should be many less elongated arclets. The relative rate of *occurrence* of arcs of different sizes further tests the lensing hypothesis, and would be a new probe of the mass distribution in the cluster lenses. However, any attempt to explore the various probability distributions was impossible because of the absence of any well-defined observational sample thus precluding any definitive conclusions.

The purpose of this chapter is to examine such theoretical arguments in the context of a new sample of cluster images which has been systematically analysed for arc-like images. The resulting catalogue of *candidate* arcs allows us to examine their potential for constraining the redshift distribution of faint field galaxies and the cluster mass distribution. We also compare this strategy of surveying a reasonably large number of clusters to moderate depth with the alternative approach where the surface density of background galaxies is raised to a significant level in a single cluster via much deeper integrations (c.f. Tyson *et al.* 1990, Chapter 5).

A plan of this chapter follows: in Section 2 we describe a new observational database of distant clusters which has been constructed in such a way as to maintain as uniform a detection limit for arcs and arclets as possible. Section 3 discusses the motivation for the statistical tests we have developed and demonstrates their application to our sample. We find that the number of arcs found is consistent with the lensing hypothesis, but that our cluster properties would need to be understood in considerably greater detail before strong constraints could be placed on the proportion of faint galaxies beyond the clusters. We develop a new technique that might resolve this problem but show that the current sample is too diverse for an effective application and briefly discuss how this could be applied to a more detailed analysis of one or more clusters. In Section 4 we discuss the implications of this work and the prospective role arcs may play in faint object cosmology. We summarise the main conclusions in Section 5.

3.2 Observations

3.2.1 The Danish Distant Cluster Sample

As part of the Danish distant supernova search (Hansen *et al.* 1987, Couch *et al.* 1989), many V CCD frames of average exposure time $\sim$1 hour were taken on the Danish 1.5m telescope at La Silla, Chile for $\sim$60 clusters with redshifts 0.2<z<0.5 during the years 1987–1989. Clusters were selected from the Abell catalogue (Abell 1958), its southern counterpart (Abell *et al.* 1989) and the southern AAO distant cluster catalogue (Couch *et al.* 1990). The principal aim was to compare photometric observations of the clusters at different epochs in a search for faint supernovae (SNe). Since a Type Ia supernova could occur at any lunation, limiting magnitudes of $V \sim 24$ were essential for each exposure. Hansen *et al.* (1989) and Nørgaard-Nielsen *et al.* (1989) discuss the faint SNe discovered and the implications for cosmology and the SN rate. Over the many runs at La Silla, the observing conditions varied somewhat. In the SN search, new frames were compared with those whose seeing matched most closely the current conditions. Different transparencies and small seeing mismatches were then allowed for by rescaling and smoothing one image using fiducial stars as calibrators prior to eventual comparison.

The most direct determination of the application of the survey data to the discovery of faint arcs is to test the detectability of a previously discovered arc as a function of both the limiting detection isophote and seeing. The strong role played by the latter effect in the detection of giant arcs has been stressed by Fort (1992), as the majority of arcs are unresolved even in good seeing, degrading the seeing eventually reduces the peak surface brightness below the isophotal detection limit.

Fortunately the surveyed clusters included Abell 370 which contains the spectroscopically-confirmed arcs A0 and A5 (Soucail *et al.* 1990). The arc A5 (Figure 3.1) is the fainter
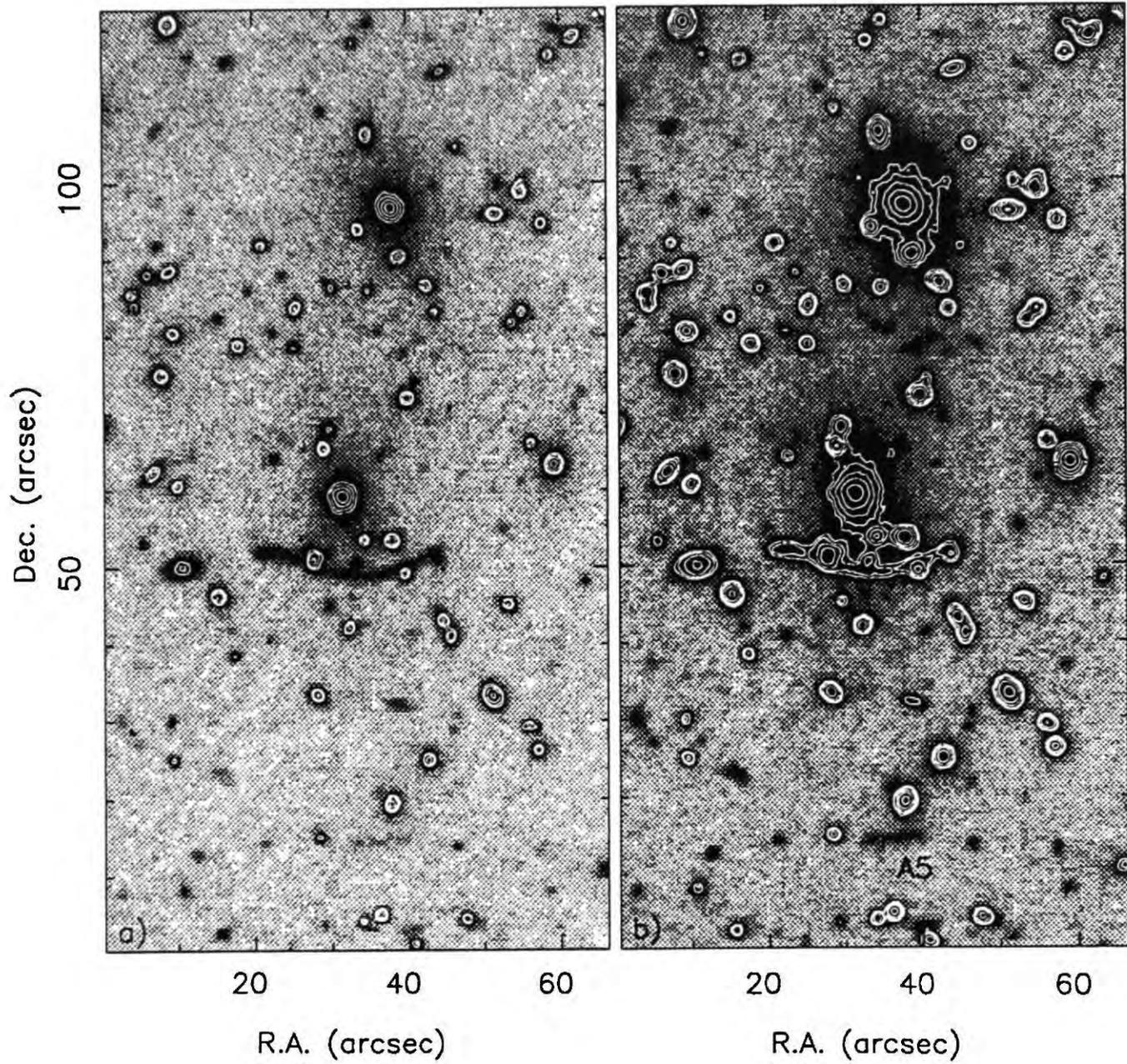
Figure 3.1 Examples of the co-addition of Danish CCD frames taken at different epochs: (a) The central section of a single 1 hour exposure. (b) 8 × 1 hour exposures median combined of the same region.

of these two and is probably more representative of the bulk of the lensed population. Therefore to test the application of the Danish frames for finding faint arcs, we registered and median combined a varying number of frames of the cluster Abell 370 testing for the detection of the arc A5 (Figure 3.1). We found that provided the frames were restricted to those with measured seeings $\lesssim$1.5 arcsec FWHM and that an effective total integration time of $\geq$ 4-5 hours on the Danish 1.5m telescope was secured, the arc could be readily detected as an extended object. From photometry in several clusters, we determined that a 4 hour V integration in typical conditions can reliably reach a limiting surface brightness of $\mu_V \sim 26.0$ mag/arcsec^2.

Our cluster sample for this study consists, therefore, of those in the SN programme for which the total V integration time with seeing $\leq$1.5 arcsec is $\geq$4 hours. The 19 clusters that fall into this category are listed with their redshifts in Table 3.1.

The typical richness of a cluster entering this subset of the supernova search cluster sample can be estimated from the source material for the clusters. The 4 Abell clusters are all distance class 6, richness class 1 clusters comparable to, or exceeding, Coma in richness. However, only Abell 370 has a reliable velocity dispersion ($\sigma_o = 1367^{+310}_{-184}$ km/sec). Velocity dispersions are available for 3 of the 6 southern Abell-Corwin clusters from the extensive fibre spectroscopy of Couch & Sharples (1988). For these the mean line of sight dispersion in the rest frame is σ_o= 1483$\pm$566 km/sec – in excess of that for Coma. The richnesses of the 7 AAO clusters (J sequence numbers) can be estimated from their optical contrast against the background at their known redshift (c.f. Couch *et al.* 1990). Several of these are somewhat weaker than Coma, so the mean is reduced slightly. Overall, it seems reasonable at this stage to conclude that the sample is statistically equivalent to 19 clusters comparable to Coma ($\sigma_o \approx$800-1000 km/sec) at a mean redshift of $<z>$=0.32$\pm$0.09.

Table 3.1 Danish Archive Sample

Cluster	R.A. (1950)	Dec. (1950)	Redshift	Exp. (hrs)
AC118	$00^h 11^m 48\!\!\overset{s}{.}0$	$-30°42'00\!\!\overset{''}{.}0$	0.31	8
Abell 222	$01^h 35^m 04\!\!\overset{s}{.}0$	$-13°14'48\!\!\overset{''}{.}0$	0.21	6
Abell 370	$02^h 37^m 20\!\!\overset{s}{.}0$	$-01°47'51\!\!\overset{''}{.}0$	0.37	8
J2175.23C	$03^h 31^m 08\!\!\overset{s}{.}0$	$-39°16'49\!\!\overset{''}{.}0$	0.43	8
J2183.27TL	$03^h 45^m 37\!\!\overset{s}{.}0$	$-34°46'46\!\!\overset{''}{.}0$	0.28	6
0346-45	$03^h 46^m 49\!\!\overset{s}{.}0$	$-45°24'30\!\!\overset{''}{.}0$	0.33	8
AC122	$04^h 00^m 54\!\!\overset{s}{.}0$	$-27°20'49\!\!\overset{''}{.}0$	0.21	8
J2001.21C	$05^h 12^m 14\!\!\overset{s}{.}0$	$-48°21'54\!\!\overset{''}{.}0$	0.42	8
J2090.7CL	$10^h 02^m 12\!\!\overset{s}{.}0$	$-07°06'12\!\!\overset{''}{.}0$	0.38	5
J1834.2TC	$10^h 42^m 14\!\!\overset{s}{.}0$	$+00°14'12\!\!\overset{''}{.}0$	0.38	6
1141-28	$11^h 41^m 40\!\!\overset{s}{.}0$	$-28°18'24\!\!\overset{''}{.}0$	0.54	5
J1836.23T	$13^h 40^m 35\!\!\overset{s}{.}0$	$+00°13'20\!\!\overset{''}{.}0$	0.42	5
J1836.14BC	$13^h 41^m 11\!\!\overset{s}{.}0$	$-00°15'46\!\!\overset{''}{.}0$	0.28	5
Abell 1942	$14^h 35^m 55\!\!\overset{s}{.}0$	$+03°52'24\!\!\overset{''}{.}0$	0.22	6
AC106	$20^h 06^m 00\!\!\overset{s}{.}0$	$-53°18'50\!\!\overset{''}{.}0$	0.24	5
AC103	$20^h 54^m 52\!\!\overset{s}{.}0$	$-64°51'22\!\!\overset{''}{.}0$	0.31	5
Abell 2397	$21^h 53^m 37\!\!\overset{s}{.}0$	$+01°08'32\!\!\overset{''}{.}0$	0.24	7
AC113	$22^h 50^m 43\!\!\overset{s}{.}0$	$-33°59'27\!\!\overset{''}{.}0$	0.22	6
AC114	$22^h 50^m 96\!\!\overset{s}{.}0$	$-35°04'44\!\!\overset{''}{.}0$	0.31	6

3.2.2   Homogeneity of the CCD Survey

The individual V frames were first registered by a generalised rotation using the fiducial positions of typically 7-10 stars. The resampled images were scaled to the same total sky count, stacked and median combined to produce a single deep image free from cosmic rays and defects. The frame centres do not align perfectly but the common field is at least $\sim 2 \times 3$ arcmin in all clusters. The gain in depth by this coaddition is illustrated in Figure 3.1 where the central region of both the final Abell 370 image and a single 1 hour integration are compared. The arc A5, labelled in the figure, clearly emerges.

Before describing how the final cluster frames are searched for arc-like features, we first need to define a self-consistent limiting surface brightness value and discuss how this might vary from frame to frame. Since the smallest arc that we can hope to recognise (axial ratio of $a/b \geq 2$) in frames of 1.5 arcsec seeing will occupy ~ 10 arcsec^2, we choose to cut all combined frames at a threshold of 2σ of the sky brightness on these scales: this corresponds typically to 1% of the background sky.

Although the clusters were always observed in dark time, the varying night sky brightness and difference in total exposure time from one cluster to another will ensure such a limiting surface brightness cut varies from cluster to cluster. This cannot be eliminated entirely without accurate photometric zero points which are not available in every cluster. However, we demonstrate that the variation in the limiting surface brightness is small enough for the catalogue to be useful for our purposes. Of course, by virtue of averaging at least 4 frames taken at different times for each cluster, the sky brightness will approach the overall average value at La Silla during 1986-1988.

The mean exposure time of 6.4 hrs has a 1σ scatter of $\sim 20\%$ which together with airmass differences on the meridian implies a spread of less than 0.2 mag in the surface brightness that corresponds to a constant signal/noise. The absolute value of the sky brightness can

be checked for 4 clusters containing good V photometric zero points (Abell 1942, Abell 370, AC114 and AC118) and these confirm a mean sky value of $\mu_V = 21.0 \pm 0.3$ mag/arcsec^2. We take this range as representative of the 16 other clusters observed during the same period. In summary, therefore, by cutting at 2σ of the median sky value across the co-added image, our survey should maintain a surface brightness limit of $\mu_V = 26.0 \pm 0.3$ mag/arcsec^2.

3.2.3   Identification of Arc Candidates

In Appendix A we demonstrated how, for a simple potential, lensing elongates an image by an amount that depends on the source and lens distances (z_s, z_{cl}), the lens mass (which can be represented by the line of sight velocity dispersion; σ_{cl}), and the true angular separation of the source and lens, θ_s. For a circular singular isothermal cluster an intrinsically circular background source appears elongated such that the *minor* axis of the image equals the undistorted radius of the galaxy, and the *major* axis is elongated perpendicularly to the line joining the source and lens centre. Two observational parameters are crucial to any statistical analysis: the axial ratio $A = a/b$ of the lensed image, and the angular distance, d_c, of the arc candidate from the cluster centre.

Each processed frame was cut at a threshold of 2σ above the sky level (as discussed in §2.2) and examined visually for objects with axial ratios $A \geq 2$. This was deemed more appropriate than a blind automatic image analysis for several reasons. Firstly such algorithms find it extremely difficult to cope with the crowded fields and extensive envelopes near the cluster centres where arcs have often been found (*e.g.* Abell 963, Chapter 2). Secondly, by examining the frames visually, the curvature of the arcs can also be assessed. Finally, in confusing situations the frames can be readily pushed to a lower threshold to clarify the reality or otherwise of weak features.

Table 3.2 Candidate Arc Catalogue

| Arc Catalogue ($A \geq 2$)				
Cluster	Redshift	Arc ID	A	$d_c^\dagger$
AC118	0.31	AC118-1	2.9	13.7
AC118	0.31	AC118-2	3.6	21.4
AC118	0.31	AC118-3	2.5	10.9
A222	0.21	A222-1	4.7	12.2
A222	0.21	A222-2	2.6	14.1
A370	0.37	A370-1	12.3	26.3
A370	0.37	A370-2	4.0	63.7
J2183-27T	0.28	J2183-1	2.2	6.1
J2090-7CL	0.38	J2090-1	2.7	3.1
J2090-7CL	0.38	J2090-2	2.3	5.1
A1942	0.22	A1942-1	3.0	8.1
A1942	0.22	A1942-2	2.0	55.4
A1942	0.22	A1942-3	2.6	23.2
A2397	0.24	A2397-1	2.4	14.6
AC113	0.22	AC113-1	2.2	32.4
AC113	0.22	AC113-2	2.2	30.5
AC113	0.22	AC113-3	2.6	25.3
AC114	0.31	AC114-1	2.3	27.1
AC114	0.31	AC114-2	4.6	25.8
AC114	0.31	AC114-3	4.1	61.9

†: Radius from cluster centre in arcsec.

The complete list of candidate arcs and their parameters is given in Table 3.2. In this list, the radius vector is calculated using the estimated optical centre of the cluster, but it should be emphasised that this was done *after selection*. Since Abell 370 was included in the Danish SN search without any regard for its spectacular giant arc, we consider it appropriate to include this cluster in the sample.

Figure 3.2 shows the V images for 4 of those clusters which, besides Abell 370, contain the arc candidates with the largest distortions ($A \geq 3.5$). Images of the candidate arcs in the fifth cluster, AC114, are presented in Chapter 6. Whilst the majority of the candidates do, in fact, lie approximately tangential to the cluster radius vector, it is clear that some do not. These could be spurious detections, or cases where the cluster potential has strong substructure.

To check the reliability of the candidate list we can devise a number of tests. The most direct is to examine images in other passbands to look for the arcs. Although B and R images were occasionally taken during the SN search, they are few in number and consequently their mean depth cannot match that of the prime V-band material. However, for a small subset of the arc candidates we have obtained follow-up multi-colour observations to confirm the candidate arcs. Only for one cluster, AC114, are these images sufficiently deep in all bands to be capable of detecting the candidate arcs and these images will be presented in Chapter 6.

We can also test our completeness level by comparing our detection rate with that of other observers using multi-colour data of the same clusters. A search was made in Abell 370 for all arcs and arclets down to the noise limit of the image, irrespective of their axial ratios – a comparison with the list of arcs in Fort *et al.* 1988, selected on the basis of their colour, shows that we identify 5 (A0, A1, A2, A5, A6) of the 7 arcs presented in that work. We also identify 2 other candiates not in Fort *et al.* list. These latter 2 candidates along with
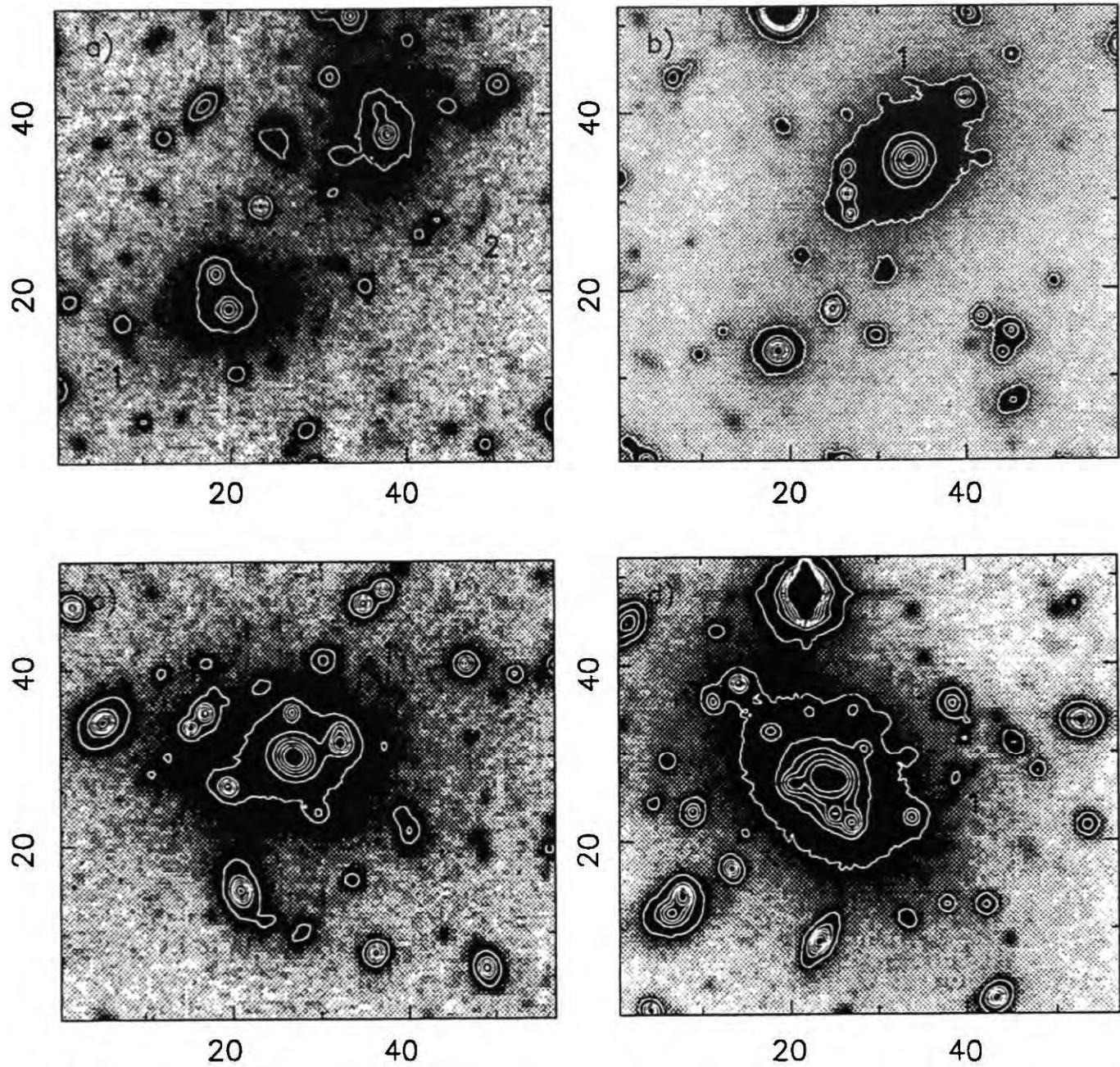
Figure 3.2 Examples of candidate arcs in 4 clusters processed according to the precepts of Section 3.2: a) AC 118, b) Abell 1942, c) Abell 222 and d) Abell 2397. The arc IDs correspond to those given in Table 3.2. North is up and east is left. The scale is in arcsecs.

A1 and A2 from the Fort *et al.* arcs are fainter than our surface brightness limit and so were discarded. Of the remaining 3 arcs A6 is merged with two cluster galaxies making evaluation of its axial ratio impossible, it was also discarded leaving the final list of 2 arcs: A0 and A5. Given our combined selection on surface brightness and axial ratio we have only failed to identify 1 of the 3 arcs that ought to be in our sample and that failure was due to crowding rather than non-detection.

Finally, the expected contamination rate in our sample can been estimated by applying the same analysis and detection criteria to deep B band CCD images of two blank fields in the SGP. These frames were taken on the 3.5m NTT, Chile by Richard Ellis and Matthew Colless in $\sim 1\rlap{.}''5$ seeing. The two fields contain a total of ~ 1500 objects to $V \simeq 25$ covering 105 sq. arcmin. There is only one object that would classify as an arc using our selection criteria. This gives a contamination rate of 1 interloper in every 18 clusters, adopting our mean cluster field size. We would therefore expect that 1 of the objects in Table 3.2 would be spurious. Further evidence for the lack of contamination is given by the fact that even though we have not considered the orientation of the arc candidates, the majority are tangentially aligned.

The only similar attempt to generate a statistically-complete sample of arc candidates was that of Lynds & Petrosian (1989) who comment in their analysis of the Abell 370 and Cl2244−02 giant arcs, that during an examination of 58 clusters they found only two examples of such giant arcs. Their 58 clusters covered a very much wider range in redshift and they pointed out that both arcs found occur in clusters with redshift well above the median value for their sample ($<z>$=0.23). If their sample is restricted to the 27 clusters with $0.2<z<0.4$, the rate for the giant arcs would be such that one is seen in $\sim 8\%$ of the Abell clusters. This is somewhat higher than our rate for the largest arcs (which already depends heavily on the presence of Abell 370) but is probably within the statistical uncertainties. Since Lynds & Petrosian's images were taken in a variety of

passbands with a much greater range of exposure times *depending on the cluster redshift*, our survey should be more homogeneous and more useful for the analysis below.

3.3 Analysis

3.3.1 Motivation and Modelling

A major hope with gravitational lensing is that the arc statistics will provide new constraints on the redshift distribution of background sources. In this section we develop techniques to address this question, using our new sample as an example to demonstrate the sensitivity of various statistical probes to assumptions *e.g.* about the lensing clusters themselves.

Whereas galaxies are selected by apparent magnitude in the number counts and spectroscopic studies, the candidate arcs in Table 3.2 are found by virtue of their *surface brightness*, which is conserved in the lensing process. For the magnitude-limited samples, a *selection function* $\phi(z)$ is usually modelled on the basis of the present-day luminosity function of galaxies (Efstathiou *et al.* 1988) and certain assumptions about the effects of redshift and evolution. $\phi(z)$ quatifies the observability of a sample of galaxies as a function of their redshift. In this way the form of the observed redshift distribution $N(z)$ can be estimated for any magnitude-limited sample, including one slightly fainter than the current limit of the redshift surveys.

Although it is possible, in principle, to calculate the selection function for a sample limited by surface brightness we adopt a much simpler approach. At the most basic level, the arc statistics are required to test whether the majority of faint blue objects are behind or

in front of the clusters; the precise form of $N(z)$ is not required. As far as the limiting observational parameters are concerned, we can also estimate that a sample limited at μ_V=26.0 mag/arcsec^2 approximates an apparent magnitude limited sample with $V \leq 26 - 5\log(r_{sec})$. In 1.5 arcsec seeing, our maximum limit, this becomes $V \leq 25$. We have of course ignored the effects of amplification bias on the $N(z)$. If we assume for simplicity that all the arcs have axial ratios, and therefore magnifications, equal to our minimum criterion (A=2) then we estimate the increase in the median redshift of the sources to be $\Delta z \leq 0.1$. However, a $V \leq 25$ sample does provide us with the shallowest likely redshift distribution for the source population and we therefore choose to use this as our null hypothesis.

At this limit Tyson's (1988) b_J and R counts imply a surface density of 13.6 objects arcmin^{-2} of which 35% have colours in the *flat-spectrum* category $b_J - I \leq 1.0$ (Chapter 5). To examine whether arcs can place useful constraints on the likely redshift distribution of various subsets of the faint galaxy population we first propose two illustrative (and extreme) hypotheses:

H_0 The flat spectrum galaxies broadly share the same $N(z)$ as the non-evolving distribution as suggested by Broadhurst *et al.* (1988) and Colless *et al.* (1990,1992). Roughly speaking this would imply $<z> \sim 0.55$ and the bulk of the population having $z < 1$.

H_1 The flat spectrum galaxies all lie between z=1 and 4 as suggested originally by Cowie *et al.* (1989). We will explore various distributions that place these galaxies within these redshift limits.

We parameterise the fraction of flat spectrum objects to V=25 as f_b. Cowie *et al.* (1989) claim that regardless of their redshift, the surface density of this fraction of blue sources implies the bulk of the metals were formed in this population. The null hypothesis, H_0,

implies that the population coexists with the remainder and is temporary in nature (*e.g.* by virtue of short-term bursts of star formation); the overall $N(z)$ being close to the no evolution prediction. The alternative hypothesis, H_1, amounts to the statement that the flat-spectrum component is a cosmologically important one, perhaps associated with galaxy or disk formation in the remote past. In this case the fraction, $(1 - f_b)$ without flat-spectrum colours is assumed to be a non-evolving population. Of course a host of intermediate possibilities exist. Our purpose here is to examine the sensitivity of various tests to these extreme hypotheses.

3.3.2 Lens models and robust arc parameters

The simplest cluster potential that might be considered is the singular isothermal sphere. In this case the lensing geometry is straightforward – every light ray from the source plane appears to be deflected an angular distance $\Delta = \alpha_0 (D_{ls}/D_{os})$ away from the cluster centre, where D are the angular diameter distances assuming a $\Omega = 1$ universe with matter inside the beam to the cluster (*e.g.* Turner *et al.* 1984) and

$$\alpha_0 = 4\pi \left(\frac{\sigma_{cl}}{c}\right)^2 \sim 29'' \left(\frac{\sigma_{cl}}{10^3 \text{kms}^{-1}}\right)^2 \tag{1}$$

Intrinsically circular sources whose impact parameter lies close to the cluster centre will be distorted considerably, while sources with larger impact parameters will be distorted less. This simple lensing model does not affect the width of the source. The singular isothermal sphere model is used in this paper to show the type of analysis that might be carried out. In Section 4 we will discuss its validity and other possible mass distributions.

This model gives the final shape of the image, A, and its distance from the cluster centre, d_c, as a function of the source redshift z_s, the lens redshift z_l, the source impact parameter, θ_s, and the cluster velocity dispersion, σ_{cl}. Given a set of clusters with known or assumed velocity dispersions and a hypothesized $N(z)$ this model predicts the observed number of

arcs as a function of their distortion A, their radial distribution from the cluster centre and their lengths (with some assumption on the intrinsic source size). Each of these quantities can be compared with the available data. The arc length distribution is probably not useful for comparing theory with observations since little is currently known about the intrinsic source size (Wu & Hammer 1992, Chapter 4). The quantities A and d_c are however fairly easy to measure and not so sensitive to such unknowns.

Calculating the expected number of arcs is straightforward. Following Nemiroff and Dekel (1989), for a single cluster with a singular isothermal sphere mass distribution

$$N_{arc}(A > A_c) = \pi \alpha_0^2 (A_c - 1)^{-2} \Sigma_s J(\hat{N}, z_{cl}) \tag{2}$$

$$J(\hat{N}, z_{cl}) = \int_{z_{cl}}^{\infty} \hat{N}(z_s)(1 - r(z_{cl})/r(z_s))^2 dz_s$$

Here Σ_s is the surface density of objects down to the surface brightness limit of the sample and $\hat{N}(z_s)$ is the normalized redshift distribution of these sources (i.e. $\int \hat{N}(z_s)dz_s = 1$). It is trivial to calculate from this formula the expected number of arcs for an ensemble of clusters, and for different hypothesized $\hat{N}(z_s)$. Notice that the integral is linear in $\hat{N}(z_s)$. Therefore a mixture of populations with a fraction f_b of galaxies drawn from $\hat{N}_b(z_s)$ and the remaining $(1 - f_b)$ drawn from $\hat{N}(z_s)$ would give

$$N_{arc}(A > A_c) = \pi \alpha_0^2 (A_c - 1)^{-2} \Sigma_s ((1 - f_b)J(\hat{N}, z_{cl}) + f_b J(\hat{N}_b, z_{cl})) \tag{3}$$

If σ_{cl} is known (from X-ray data or a large sample of velocities for the cluster members) and the cluster mass distribution is described by the singular isothermal sphere model then the number of arcs seen with distortions greater than some specified value could determine f_b.

Predicting the distribution of d_c is not quite so simple. The first step to note is that images of circular sources at z_s with distortions $A > A_c$ must lie in the annulus $d_c \in (\Delta, \Delta(1 + (A_c - 1)^{-1}))$. Given that sources uniformly populate the available volume behind the

cluster, one can then calculate the probability distribution for d_c within this annulus, and convolving that with the source redshift distribution gives the final probability distribution of d_c for arcs with distortion $A > A_c$ as

$$\Phi(d_c) = \beta \int_{z_1(d_c)}^{z_2(d_c)} \frac{2\hat{N}(z_s)(d_c - \Delta(z_l, z_s, \sigma_{cl}))}{\Delta(z_l, z_s, \sigma_{cl})^2} dz_s \qquad (4)$$

where β is the normalizing constant and $z_1(d_c), z_2(d_c)$ are respectively the solutions of the equations $d_c = (1 + (A_c - 1)^{-1})\Delta(z_l, z_1, \sigma_{cl})$ and $d_c = \Delta(z_l, z_2, \sigma_{cl})$. We have solved this integral by simulating the effect of our clusters on a background population using a Monte Carlo technique.

3.3.3 Comparison of models with the Danish sample

There are two possible tests that can be carried out with the Danish arc sample. The simplest is to compare the number of arcs, $N_{arc}(A > A_c)$ detected with $A > A_c$, with that expected under the two hypotheses discussed above. The second is based on the distribution of the arc distances, $\Phi(d_c)$, from their cluster centres.

Suppose for example that one places a fraction f_b of galaxies at $z = 2$ with the remaining $(1 - f_b)$ distributed according to the standard no evolution $N(z)$ predicted for a $V = 25$ magnitude limited sample. Using the formula from the previous section, we can calculate the number of arcs with $A > 2$ expected for our ensemble of clusters in the simple case where each cluster has the same velocity dispersion; σ_{cl}, at the mean redshift of the sample. Adopting a source surface density of 13.6 arcmin^{-2} (Tyson 1988), the results for various σ_{cl} are shown in Figure 3.3. The observed number of arcs, 20, is consistent with these predictions. Indeed one might be tempted to infer from this plot that a small fraction of high redshift galaxies is preferred. However, we will show that it is very unlikely that all the clusters have similar velocity dispersions, and one can see from Figure 3.3 that the relation between $N_{arc}(A > A_c)$ and f_b depends strongly on the cluster velocity dispersion. The
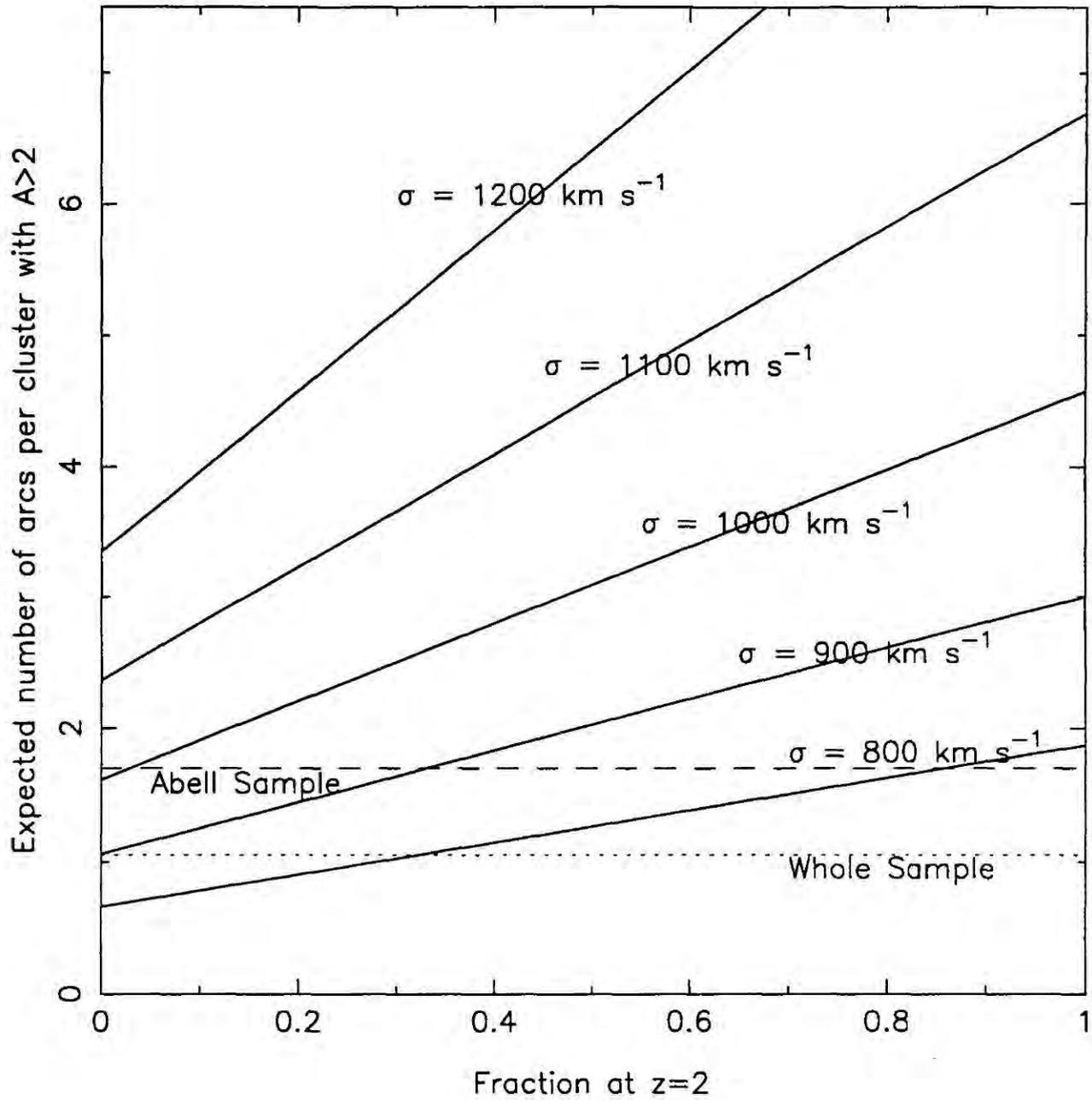
Figure 3.3 The predicted number of arcs with $A > 2$ as a function of the fraction of sources, f_b, placed at $z_b = 2$, plotted for various cluster velocity dispersions. The dotted line shows the average number of such arcs detected per cluster in the complete sample, while the dashed line marks the number detected in the Abell and Abell & Corwin subsample.

predicted number of arcs with $A > 2$ varies by a factor ~ 2 as f_b increases from 0 to 1, but $N_{arc} \propto \alpha_0^2 \propto \sigma_{cl}^4$. Thus small differences ($\sim 20\%$) in the cluster velocity dispersion would easily mask the increased number of arcs expected due to the high redshift population.

For the second test we again suppose that each cluster has the same (unknown) velocity dispersion and lies at the mean redshift of the sample. The probability distribution of d_c for those arcs with $A > 2$ has then been calculated for a range of redshift distributions comprising the null distribution and four other distributions where a variable fraction f_b of the sources are placed at various fixed redshifts z_b. These probability distributions, $\Phi(d_c)$, are shown in Figure 3.4 for a cluster velocity dispersion of $\sigma_{cl} = 1000$ km/sec. On the same figure the Danish arc data probability distribution is shown. Clearly there is little agreement between any of these models and the data. Indeed there is no agreement for any single velocity dispersion. The most likely cause of this discrepancy is the range of cluster velocity dispersions. The sample will be likely to contain both high velocity dispersion clusters, which give rise to large values of d_c, and low velocity dispersion clusters which will not act as significant lenses at all. For this sample the distribution of d_c does not act to constrain the $N(z)$ of the faint sources. However, we note that the *shape* of $\Phi(d_c)$ is different for each of these hypotheses and one might therefore, with a large sample of arcs in one cluster, be able to constrain $N(z)$ using the shape of this function. The larger the fraction of high z objects the more skew this function becomes. This approach will be discussed in the next section.

One can show that in order to obtain f_b to accuracy δf_b, the error on σ_{cl}, $\delta \sigma_{cl}$ must satisfy

$$\frac{\delta \sigma_{cl}}{\sigma_{cl}} \leq \frac{1}{4} \left(\frac{R \delta f_b}{1 + f_b R} \right) \qquad (5)$$

where $R = (N_{arc}(f_b = 1) - N_{arc}(f_b = 0))/N_{arc}(f_b = 0)$. For instance if $R \sim 2$ and $f_b = 0.4$ and we require $\delta f_b \leq 0.2$ then $\delta \sigma_{cl}/\sigma_{cl} \leq 0.045$. This measurement would require in excess of ~ 1000 redshifts (Danese *et al.* 1980), a formidable task even in a local cluster, let
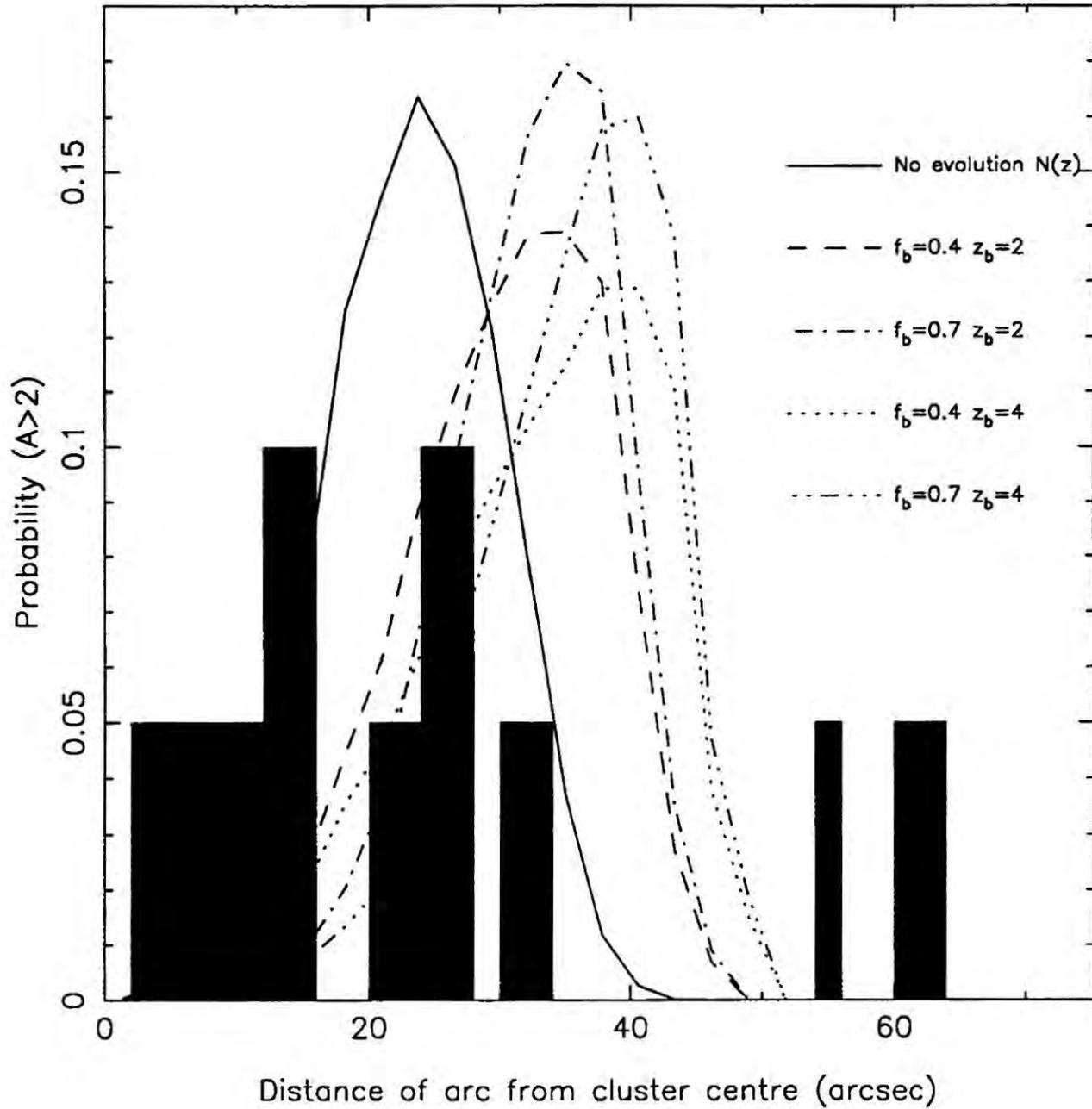
Figure 3.4 Predictions for the radial distribution of arcs with $A > 2$ for a cluster with velocity dispersion 1000 km/sec and various hypothesized $N(z)$: the solid curve is for a no-evolution $N(z)$, while the other curves place various fractions, f_b, of the sources at various redshifts, z_b, and distribute the remainder according to the no-evolution prediction. The probability distribution of radial distances for the Danish data is also shown.

alone one at $z \sim 0.4$. X-ray temperature measurements to high precision might allow a determination of f_b to this accuracy.

There are other simple questions one can ask about this sample: for example, is the distribution of A consistent with that expected from lensing and are the number of arcs in each cluster consistent with the clusters having equal velocity dispersions? Independent of the cluster velocity dispersion we should find $N_{arc}(> A) \propto (A - 1)^{-2}$ assuming that the clusters act as singular isothermal lenses, and the lack of dependence on σ_{cl} means that this should hold for the entire sample. A K-S test on the observed distribution of A shows that the probability that it was drawn from the $N_{arc}(> A) \propto (A - 1)^{-2}$ distribution is $\sim 9\%$. Whilst a low value, it remains consistent with the lensing hypothesis. Removing the large arc in Abell 370 has little effect on this probability.

On the second question, if all of the clusters did have the same velocity dispersion then the number of arcs seen in any cluster should have a Poisson distribution with a mean value of 20/19. The number of arcs in these clusters varies from 0 in several to maximally 3. A χ^2 test shows that this distribution is *not* consistent with the Poisson distribution at the $< 0.5\%$ level. We have therefore effectively demonstrated why the above tests will not work on our sample in the absence of detailed knowledge about the clusters themselves. This can be quantified by using a K-S test to compare the distribution of number of arcs seen in the Abell and Abell & Corwin clusters ($<z>= 0.26$) with that seen in the rest of the sample ($<z>= 0.38$). We find that the probability that the two distributions are drawn from the same parent population is $< 2\%$ showing that the sample of clusters may be relatively inhomogenous in its lensing strength, including a large fraction of sub-critical lenses.

Another test for lensing in the clusters can be performed by looking for an excess number of tangentially-aligned objects in the cluster fields. Furthermore measuring the relative
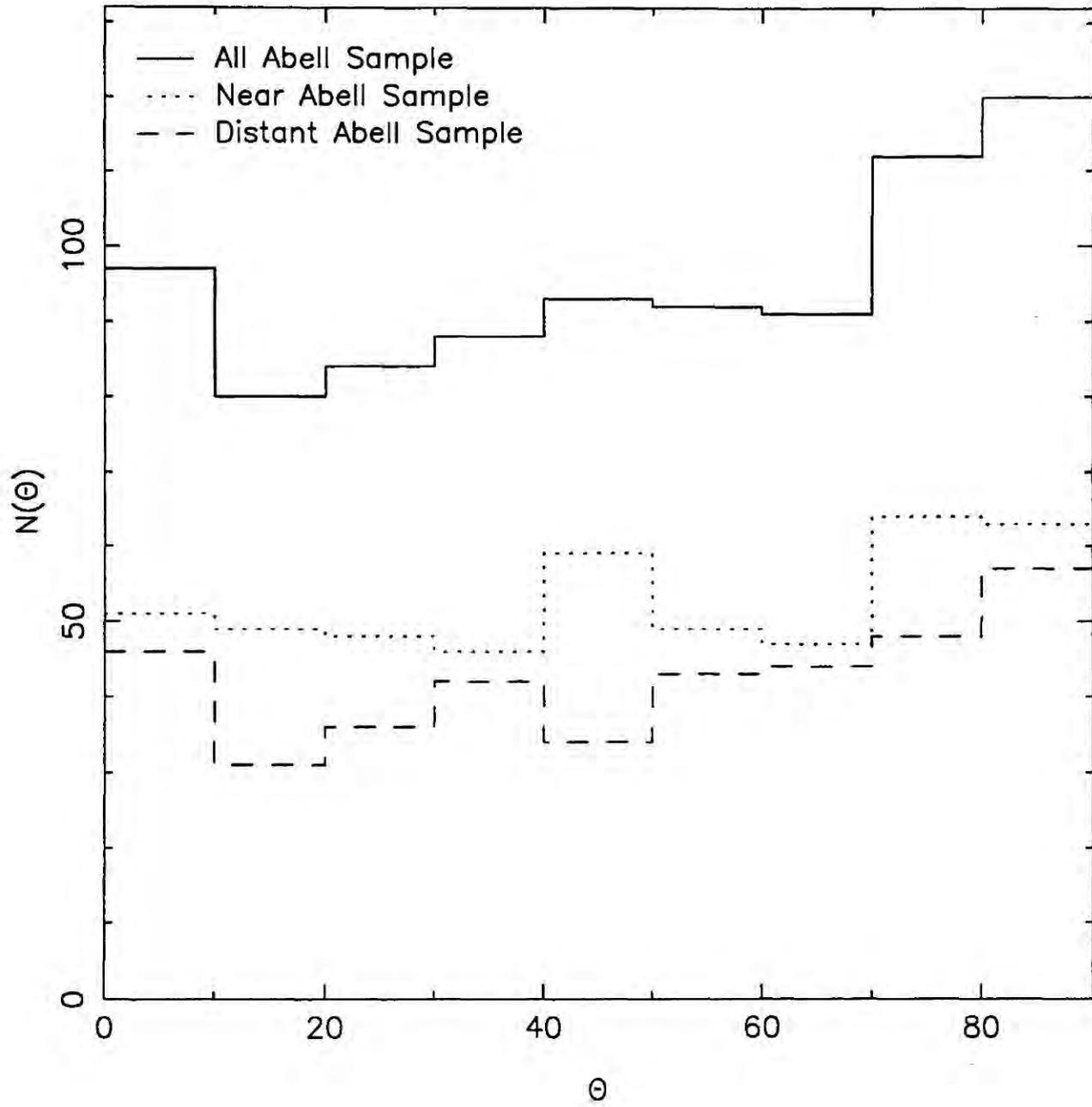
Figure 3.5 The histogram of image orientation for all the galaxies with $A > 1.5$ and $22 \lesssim V \lesssim 25$ in the Abell cluster sample. The orientation (θ) is measured relative to the vector to the cluster centre, hence 90° is tangential.

numbers of arcs and arclets in a single cluster with greater than a given distortion – if the lenses have singular isothermal mass profiles this will scale as:

$$R_{arc} = \frac{N_{arc}(A > A_c^1)}{N_{arc}(A > A_c^2)} = \left(\frac{A_c^2 - 1}{A_c^1 - 1}\right)^2 \qquad (6)$$

We have already shown that the observed arc lengths for arcs with $A > 2$ are in rough agreement with this distibution. We can extend this test by measuring the statistical excess of tangentially-aligned objects with $A > 1.5$ seen in the cluster frames. Comparing the ratio of observed number of arcs to the excess number of aligned images ('arclets') with that predicted by various mass distributions for the clusters will enable us to differentiate between the possible lens models. Bearing in mind the large difference between the number of arcs seen in the Abell and non-Abell clusters we split the sample into these two groups. This gives 10 clusters in the Abell sample ($< z > = 0.26$) and 9 in the non-Abell sample ($< z > = 0.38$). We discard one of the clusters in the Abell sample (AC103) as the image is fringed making it difficult to analyse, leaving us with 9 clusters in each sample with 17 $A > 2$ arcs observed in the Abell sample and 3 arcs in the non-Abell sample.

To measure the tangential excess we analysed the frames using the FOCAS image-analysis software (Jarvis & Tyson 1981) to produce catalogues containing photometry and shape information on all objects above the detection isophote. After applying an ellipticity cut ($A > 1.5$), a magnitude cut ($22 \lesssim V \lesssim 25$) was applied to remove the bulk of cluster members ($V = 22$ is 2.5 magnitudes fainter than the characteristic magnitude of a cluster member, M_V^*, at $z = 0.26$). The orientation relative to the cluster radius vector is calculated for the remaining objects in each cluster and the resulting orientation histograms are combined. The histogram for the Abell sample is shown in Figure 3.5. Clearly there is a significant excess (53 galaxies) in the tangential bins confirming that these clusters are acting as gravitational lenses, a χ^2 test gives a probability of less than 0.1% that the

excess occurs by chance. Also plotted are the relative contributions to the signal from clusters with redshifts either below or above $z = 0.26$ showing no obvious trend. A similar analysis applied to the non-Abell sample gives a marginal excess of aligned objects, but this is not statistically significant at the 10% level. A detailed analysis of the excess of aligned images cannot be made as the lack of colour information on the galaxies makes the removal of the remaining contamination from cluster members impossible.

The absence of a signal in the more distant non-Abell sample could arise from one of two factors. The clusters may be sub-critical, either because of strong evolution in the total mass bound in the cluster or due to changes in the distribution of mass within the clusters. Alternatively the lack of an aligned excess in this more distant sample could be due to a drop in the space density of sources behind the clusters, *i.e.* the redshift distribution of $V = 25$ galaxies does not exhibit a high redshift tail. Deep pointed ROSAT observations of selected clusters from the AAO catalogue shows that the clusters while being optically as rich as Coma have significantly lower X-ray luminosities than Coma (Bower *et al.* 1993). An inspection of the orientation histograms for the rich $z = 0.55$ cluster Cl0016+16 (Figure 5.24) shows an excess of aligned images in the $I \in 20 - 23$ sample – equivalent to $V \in 22 - 25$. This argues for at least 20% of the galaxy population to this depth being beyond $z = 0.55$. The implications of this observation for the non-Abell cluster sample are discussed below.

A comparison of the relative number of arcs and arclets seen in the Abell sample with that predicted by different mass models for the clusters may be capable of distinguishing between the various models. We illustrate its application assuming circular sources and perfect seeing. In the Abell sample we have 17 arcs with $A > 2$ in 10 clusters and 53 arclets ($A > 1.5$) in 9 clusters. This gives an observed ratio of $R_{arc} = 3.5 \pm 0.9$ where the errors assume Poisson statistics. The predicted ratio for a singular isothermal lens is $R_{arc} = 4.0$ (a non-singular isothermal lens would have $R_{arc} \gtrsim 4$), while for a point mass the

value is $R_{arc} = 2.7$. Even under our simplified assumptions we cannot clearly differentiate between these two models. The two assumptions we made affect the model R_{arc} values in different ways. The instrinsic source ellipticity distribution increases the observed scatter in R_{arc} for a given mass model, while the seeing would tend to systematically reduce R_{arc}. This is because the effect of seeing depends upon the slope of the axial ratio distribution, $dN_{arc}(A > A_c)/dA_c$, near the lower cutoff, A_c. The relative effect therefore depends upon the slope for the two values of A_c and this decreases with increasing A_c. The model values of R_{arc} would therefore decrease if seeing was included in the modelling, bringing the value for the isothermal lenses closer to that observed.

3.3.4   A likelihood ratio test based on $\Phi(d_c)$

Suppose a cluster has arcs with distortions larger than some chosen critical value A_c at distances $(d_1, d_2, ...d_n)$ from the cluster centre. For an assumed σ_{cl} the singular isothermal sphere model can be used to predict the expected d_c distribution $\Phi(d_c|H_i, \sigma_{cl})$ under the hypothesis of a no evolution $N(z)$ (H_0) or one with a fraction, f_b, of galaxies at high redshift (H_1). This $\Phi(d_c)$ yields the probability of observing the data $(d_1, d_2,...d_n)$, $p(d_1,....d_n|H_i, \sigma_{cl}) = p_i$ for short. Using the standard maximum likelihood method (Silvey 1975) one can estimate the cluster velocity dispersion. The σ_{cl} which yields the greatest likelihood of observing the set of arcs is the *maximum likelihood estimator* $\hat{\sigma}_{cl}$ of the cluster velocity dispersion. This estimator will depend on the assumed $N(z)$.

As an example consider the 7 arcs in Abell 370 with $A > 1.5$ (Fort *et al.* 1988). For a no-evolution $N(z)$ the radial positions of these arcs yield $\hat{\sigma} = 1230$ km/sec, gratifyingly close to the optically determined value of 1367^{+310}_{-184} km/sec for the red galaxies in Abell 370 (the blue galaxies yield a larger velocity dispersion but there is some evidence that these are subclustered in velocity space, see Mellier *et al.* 1988.) The radial arc distribution therefore

offers an independent method for estimating cluster velocity dispersions – however the calculations rely on the assumed cluster potential and $N(z)$. Additionally we might have been fortunate in our estimate of the velocity dispersion of Abell 370 since, for a small number of arcs (~ 7), the errors on the estimate of the velocity dispersion by this method can be as large as the errors in the dynamical estimate. However, as we will show, with a larger sample of arcs this estimator could be very accurate providing a useful means of determining velocity dispersions of clusters at high redshift.

As before the null hypothesis will be that the sources are distributed according to the no evolution model to $V = 25$, and the alternate hypothesis will place a fraction f_b of the sources at $z = 2$ with the remainder distributed according to the no evolution $N(z)$. Applying the maximum likelihood method to each hypothesis will yield two estimates of σ_{cl}, denoted $\hat{\sigma}_0$ and $\hat{\sigma}_1$, and two probabilities $\hat{p}_0$, $\hat{p}_1$. If one of the inferred velocity dispersions is clearly unreasonable then the other hypothesis would be favoured. However, since such a clear distinction is unlikely (for Abell 370 H_0 yields 1230 km/sec and for H_1 1050 km/sec), the most sensible method for comparing the hypotheses is to construct the ratio $\Lambda = \hat{p}_0/\hat{p}_1$, the standard statistical likelihood ratio test of one hypothesis against another. If this ratio is large one can safely reject the alternate hypothesis (a large fraction of sources at high redshift) in favour of the null (no evolution) hypothesis.

The important question now is how many arcs would be needed to confidently distinguish between these two hypotheses. In order to answer this question several simulations have been made. These are described stepwise below:

1) Choose the cluster velocity dispersion σ_{cl}, at random, and place the cluster at $z_{cl} = 0.4$.

2) Generate N_{arc} arcs (with distortions above a specified critical value A_c) using a singular isothermal sphere model with this velocity dispersion and the null $N(z)$ distribution (no evolution).

3) Now calculate the likelihood of observing this set of arcs for a range of cluster velocity dispersions with the null hypothesis $N(z)$ **and** for a range of cluster velocity dispersions with the alternate redshift distribution described above.

4) For each hypothesis determine the maximum likelihood estimates of σ_{cl} ($\hat{\sigma}_0$ and $\hat{\sigma}_1$). Calculate $\log \Lambda = \log(\hat{p}_0/\hat{p}_1)$ and $S = \hat{\sigma}_0/\sigma_{cl}$.

5) Repeat the above procedure several times, resulting in a set of $(S, \log \Lambda)$ pairs.

6) Now repeat the above simulations but in this case generate the set of N_{arc} arcs (Stage 2) using the $N(z)$ of the alternate hypothesis. In this case the ratio S is defined as $S = \hat{\sigma}_1/\sigma_{cl}$ and $\log \Lambda = \log(\hat{p}_0/\hat{p}_1)$ as before.

Ideally then the values of $\log \Lambda$ in the first set of simulations should be greater than those in the second set, and the values of S in either case should be close to unity. Figure 3.6(a) shows a plot of the 100 $(S, log\Lambda)$ pairs for each type of simulation with $N_{arc} = 7$. The values of $\log \Lambda$ are similar for each hypothesis. Therefore a measurement of $\log \Lambda$ from a data set consisting of 7 arcs would be incapable of differentiating between H_0 and H_1. Figure 3.6(b) shows the results for $N_{arc} = 60$, which clearly differentiate between the two hypotheses. Moreover this approach also provides a very good estimate of the cluster velocity dispersion (typically to better than 5%). In terms of defining precise significance levels for this test a larger simulation would be needed. However by inspection one can see that a value of $\log \Lambda > 1.0$ arises for only $\sim 1\%$ of the simulations with the redshift distribution of H_1, and thus if the data has a measured value of $\log \Lambda > 1.0$, there is only at most a 1% chance that we would be in error in choosing the null over the alternate hypothesis. Thus with a set of 60 arcs in a single cluster it should be possible to discriminate with some confidence between a no evolution $N(z)$ and a $N(z)$ with 40% of objects at $z = 2$. If f_b or z_b are larger then this test becomes even more powerful.
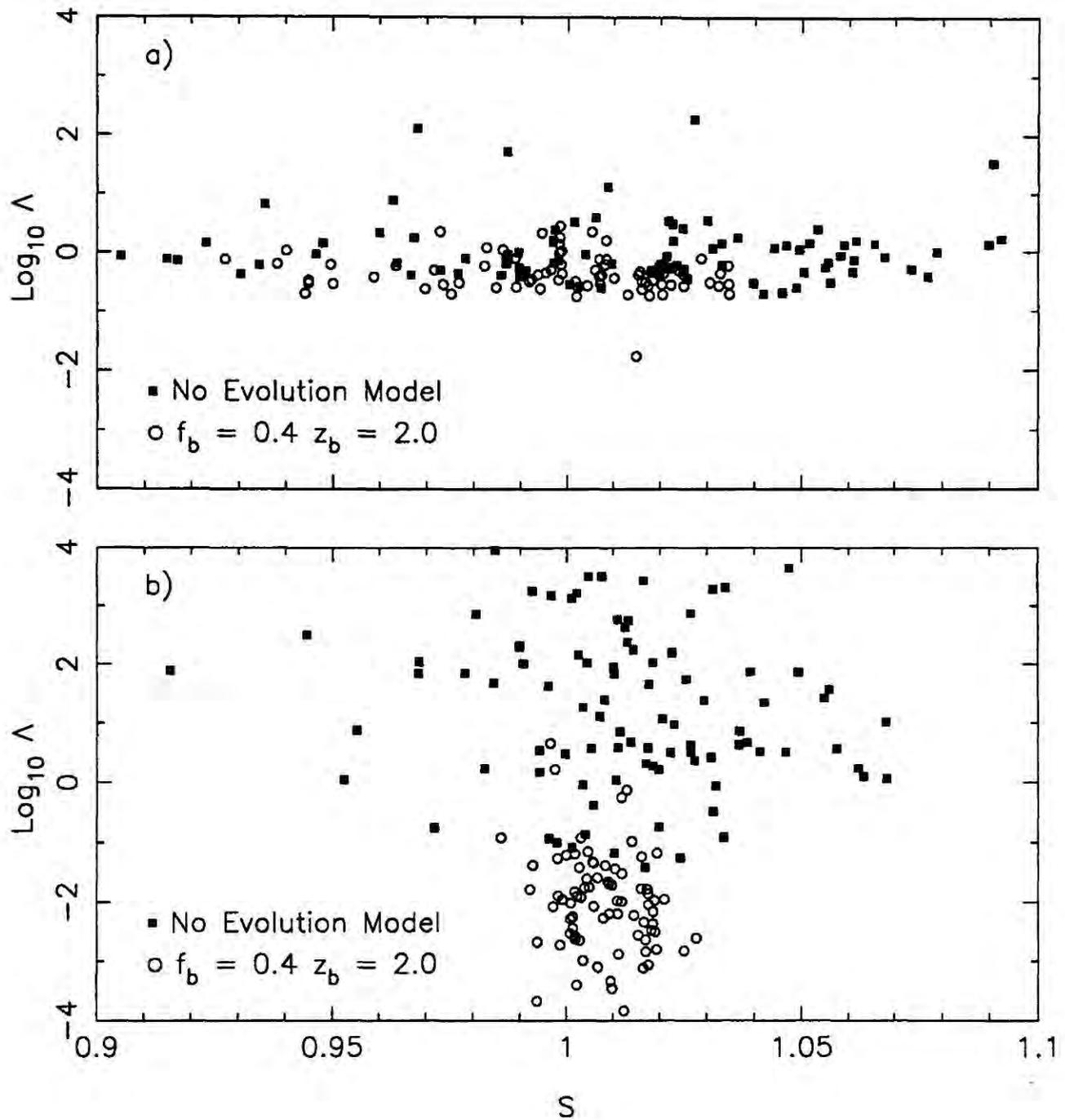
Figure 3.6 (a) The distribution of likelihood ratios and estimates of the cluster velocity dispersion for $N_{arc} = 7$ and $A \geq 1.5$. Square symbols correspond to arcs generated from a no-evolution $N(z)$ while the stars correspond to arcs generated with $f_b = 0.4$ and $z_b = 2.0$. (b) The distribution of likelihood ratios and estimates of the cluster velocity dispersion for $N_{arc} = 60$ and $A \geq 1.25$. Notice there is a much clearer separation of the components.

3.4 Discussion

There are several assumptions we have made that need to be discussed here. The first is our use of the singular isothermal sphere model as the lens model. It is well known that determining the mass distribution in clusters in an assumption-free way as possible is very difficult (see Fitchett 1990 for a review). Even the best studied rich cluster, Coma, has a poorly constrained mass distribution (Hughes 1989). On the other hand, Beers and Tonry (1986) have shown that clusters have galaxy surface density distributions that fall off as r^{-1}. This finding is consistent with a singular isothermal sphere mass distribution if mass traces light in the centres of clusters.

If clusters really do have cores of constant density then their effect on our analysis will depend on their extent. We assume that the core has a size; r_c, and outside of this region the cluster has an approximately isothermal density distribution $\rho \propto r^{-2}$. The important scale is the angular size of the cluster core $\theta_{core} = r_c/r(z_{cl})$ compared with the lensing scale θ_{lens}. The lens scale depends on the cluster velocity dispersion, its redshift, the redshift of the source population and on the size of the cutoff A_c. For an intrinsically circular source to be distorted $> A$ its impact parameter must lie at $\theta_s < \theta_{lens} = \Delta(A-1)^{-1} \sim 42''(\sigma_{cl}/1200\mathrm{km/sec})^2(A_c-1)^{-1}D_{ls}/D_{os}$. This is the scale that must be compared to θ_{core}. For a cluster at $z_{cl} = 0.4$ and a source redshift of $z \sim 1.0$ this gives $\theta_{lens} \sim 20''(\sigma_{cl}/1200\mathrm{km/sec})^2(A_c-1)^{-1}$, which for $A = 1.25$ gives $\theta_{lens} \sim 80''(\sigma_{cl}/1200\mathrm{km/sec})^2$. Now for a cluster at $z = 0.4$ the angular scale of the core is $\theta_{core} \sim 22''(r_c/100\mathrm{kpc})$. There is evidence from the distribution of observed arc widths (Wu & Hammer 1992) that the core sizes of super-critical clusters must be small ($r_c \leq 100$ kpc) and that the clusters should be at least as centrally condensed as an isothermal model. This canonical core size is approximately a quarter of the lensing scale, and thus one would expect approximately 5% of the images to have been lensed by the core. Such a

small fraction would not significantly alter the application of our method. This is because the core region will distort background objects less than in the singular case, and so some lensed images close to the cluster centre will not satisfy the distortion criteria and so not be in the sample on which the d_c distribution is based. However, since the skewness of the $\Phi(d_c)$ distribution is towards large d_c this should be preserved.

Of course if the actual mass distribution was known in one cluster the likelihood ratio test could be straightforwardly applied with confidence. An estimate of the mass distribution in a cluster could be made by using spatially resolved measurements of the temperature and density profile of the hot X-ray emitting gas under the assumption that it is in equilibrium in the cluster potential. There are two other possible lensing-based techniques that could be used to determine the mass distribution in a single cluster. One of these relies on the discovery of the rare multiply-lensed images created by lensing by a compact cluster potential. Such systems contain enough observational constraints that they may be used to derive the mass profile in the centres of rich clusters, we present an example of such a system in Chapter 6. The final technique relies on obtaining deep observations of the arclet populations in a large sample of clusters – these may then be modelled as the redshift distribution of the arclets must be the same in all clusters the only differences must reflect the structure in the lensing clusters (Chapter 5).

We now discuss the optimal strategy for carrying out our test. In principle the method can be applied with similar ease to clusters at a range of redshifts since arc detection requires securing a certain signal to noise for the *background* population. However, there are several competing effects which suggest that the test is close to optimal for a cluster at $z_{cl} = 0.4$. For a low redshift cluster ($z_{cl} = 0.1$) the shapes of the $\Phi(d_c)$ curves are not as different for different values of f_b and z_b as they are for higher redshift clusters. This suggests using the highest redshift clusters known for such a test. However, at higher redshift the number of arcs produced decreases whatever the postulated $N(z)$. This is shown in Figure 3.7
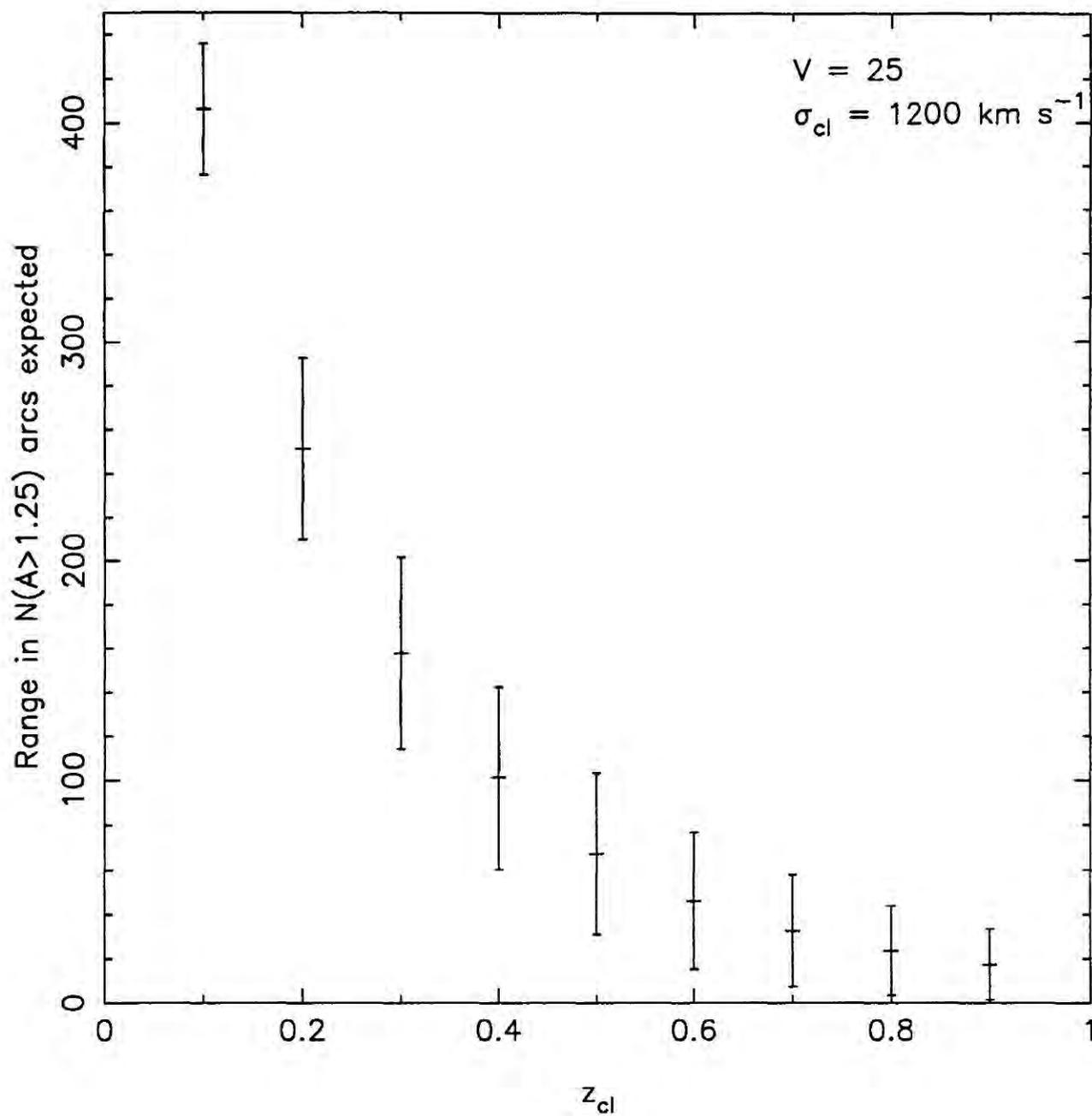
Figure 3.7 The range in the expected number of arcs with $A > 1.25$ seen in a cluster at various redshifts. The cluster has $\sigma_{cl} = 1200$ km/sec and the range in the number of arcs corresponds to f_b increasing from 0 to 0.4 at $z_b = 2.0$ with the remaining fraction of galaxies, $(1 - f_b)$, distributed according to the usual no evolution $N(z)$ to V=25.

where the range in the number of arcs produced with $A > 1.25$ as the fraction, f_b, of sources at $z_b = 2$ varies from 0 to 1 is plotted against the cluster redshift. Here the model cluster has a velocity dispersion of 1200 km/sec and the source surface density is taken to be 27.6 arcmin^{-2}. This limit is readily achievable on a 4m class telescope (Chapter 5). The declining number of arcs produced in clusters of higher redshift suggests that unless a very massive cluster is available (recall $N_{arc} \propto \sigma_{cl}^4$) the optimal cluster for this test has $z_{cl} \sim 0.4$. The effect of contamination by foreground and cluster members can be quite strong depending upon the sample selection. Even when basing the definition of an arclet on a combined colour and surface brightness profile requirement it is still possible to pick up a large fraction of interlopers. Unfortunately, the fraction of cluster members falling into these catagories – so called Butcher-Oemler galaxies – is a strongly increasing function of cluster redshift and appears to peak at $z_{cl} \sim 0.4$.

One aim of this chapter was to explore whether a few arcs in each of many rich clusters could be used to set constraints on the redshift distribution of the faint background sources. We have shown that the number of arcs discovered above some critical distortion or their radial distribution about the cluster centres, could constrain the redshift distribution of the sources if the cluster properties were well known. We have also shown that our sample is too diverse for these tests to be applied with confidence. We have therefore explored the use of the radial distribution about the cluster centre of a larger sample of arcs as a possible probe of the faint galaxy redshift distribution. A high redshift component of the faint galaxy population leads to a large fraction of arcs at large distances from the cluster centre, and a consequent skewness in the distribution of arc distances. We have devised a likelihood ratio test based on the *shape* of the radial distribution of arcs around the cluster centre. This test can discriminate between different redshift distributions for the background objects if $N_{arc} \gtrsim 60$ arclets can be found in one cluster.

Finally there is the possibility of using clusters to probe to greater distances than in the field. The magnification of a galaxy induced by lensing will always make it brighter – even if the resulting image is not obviously distorted. This will tend to extend the observed redshift distribution for a field sample viewed through a gravitational lens beyond a 'plain' field sample. This effect may already have been seen in a sample of faint field galaxies uncovered in the fields of distant rich clusters during a survey of the clusters (Dressler & Gunn 1992). The median redshift of this sample is deeper than equivalent field surveys (Koo & Kron 1992) – as would be expected if we are seeing deeper into the universe by virtue of the magnifying power of the centres of the rich clusters. However, the colour selection used to construct the sample makes the comparison somewhat ambigous so this result awaits confirmation.

The role of selection effects in surveys for giant arcs must be born in mind, especially when trying to use such surveys to make statements about the colours of high redshift galaxies. As we have stated a survey for arcs is effectively surface brightness limited and this will determine what mix of galaxies appear in the survey when compared to a simple magnitude limited sample. The strong surface brightness dimming with redshift biases the sample towards the highest surface brightness, therefore strongest star-forming, galaxies at any redshift. Even if only small regions of the galaxy were undergoing strong star formation these small areas could appear as a giant arc given a sufficiently high distortion and magnification. These regions are even more dominant as at high redshift optical passbands sample the rest-frame ultraviolet, dominated by light from short-lived massive stars created in star bursts. Currently it does appear that the giant arcs are optically bluer than a random sample of galaxies at the present epoch. However, it is *not* apparent whether this reflects a real increase in star formation activity in galaxies at high redshift or the action of the selection effect discussed above (Chapter 4).

In addition to detailed information on high redshift galaxies this method could also yield a very accurate measure (typically to better than 5%) of the cluster velocity dispersion, which can be achieved for a cluster at *any* redshift (provided only that there are enough arclets). This approach to determining cluster velocity dispersions may prove extremely powerful as a means of constraining current theories of large scale structure since it has been claimed that the abundance of high redshift clusters with high purported velocity dispersions provide a strong argument against the cold dark matter theory of galaxy formation (Evrard 1989, Peebles *et al.* 1990). These analyses, based on spectroscopically determined velocity dispersions, are subject to the usual projection effect problems. It had been hoped that X-ray observations of such distant clusters would be capable of determining whether they were real or not. However, the strong evolution in the space density of luminous X-ray clusters at relatively recent epochs ($z \sim 0.2$) seen by Edge *et al.* 1990 and Gioia *et al.* 1990 casts some doubt on this approach. Such strong evolution may reflect changes in the state of the X-ray gas, rather than the depth of the cluster potential in which it is lying (Kaiser 1992).

3.5   Conclusions

• We have searched a homogeneous set of deep V images of 19 moderate redshift rich clusters for arc-like features. 20 candidate arcs with $A > 2$ and 6 with $A > 3.5$ have been found to a surface brightness of $\mu_V = 26$ mag/arcsec^2.

• We have modelled the gravitational lensing effect of our ensemble of clusters on a background population of sources and find that the number of arcs and their shapes and orientations are consistent with the lensing hypothesis. Moreover, a statistical test using

the less distorted arclets in a subset of the sample shows a significant signal, indicating that at least these clusters are acting as gravitational lenses.

• However, the same test applied to the remaining, more distant, part of the sample produces a null result. Deep observations of the cluster Cl0016+16 ($z = 0.55$, Chapter 5) may provide the information necessary to determine whether this is due to evolution in the cluster properties or due to a shallow redshift distribution for the faint galaxy population. The Cl0016+16 observations show that at least 20% of the $V \sim 25$ field population lies beyond $z = 0.55$ – supporting the former explanation for the lack of lensing signal. In addition deep ROSAT X-ray observations of the catalogue from which the distant clusters were selected shows that all the clusters are under-luminous in X-rays for their optical richness (Castander *et al.* 1993). The implication is that the changes in both the lensing and X-ray properties of these clusters arises from the same source – evolution in the depth and shape of cluster potential wells. Such changes are to be expected if we are observing clusters at an epoch where they are still dynamically young.

• The analysis of the gravitational lensing strength of a cluster can provide an accurate measure of the cluster mass for distant clusters. Both of the classical approaches to this problem – spectroscopic and X-ray – rely on dynamical tracers of the mass in the system – the only technique which directly measures the depth of the cluster potential is gravitational lensing. It is this fact which explains why gravitational lensing may prove to be the cleanest probe into the evolution of clusters and structure in the universe.

4 GIANT GRAVITATIONAL ARCS:
STAR FORMATION IN HIGH REDSHIFT GALAXIES

4.1 Introduction

From an observational perspective the most useful feature of gravitational lensing occurs when the potential well of a foreground cluster of galaxies highly magnifies and distorts the image of a background galaxy into a giant arc. This provides an easily identifiable signature which may be used to preferentially select objects at high redshift. Since the lensing process conserves surface brightness, the resulting magnification enables information to be gathered about the dynamics and colours of a distant source on spatial scales normally unattainable.

There has been a steady increase in the number of spectroscopically-confirmed giant arcs (see Soucail 1992 for a recent update). However, these have been largely serendipitous discoveries and do not yet constitute a complete sample. To overcome this problem we undertook a limited survey of 19 clusters, maintaining a constant surface brightness limit for their detection (Chapter 3). This survey indicates that giant arcs (*i.e.* those bright enough for spectroscopy with 4m-class telescopes) are rather rare ($N_{arc} \lesssim 1$ per rich cluster). Nevertheless, since lensed sources *must* be reasonably distant, even a small sample will be useful and will complement data on field galaxies derived from magnitude-limited redshift surveys (Colless *et al.* 1990, 1992, Cowie *et al.* 1991). Indeed, although the latter surveys now reach $b_J \sim 23$–24, the median depth is only $\bar{z} \sim 0.3$; few galaxies

are found with $z > 1$. Furthermore, for many applications in galaxy evolution, precise redshifts are not required: it would be sufficient to know the bulk properties of sources lying substantially beyond the distance of the lensing cluster.

An important motivation for this chapter is the observation (Fort 1990, Mellier *et al.* 1991) that most of the spectroscopic arcs have optical colours similar to the *flat spectrum* blue galaxies that dominate the faint field population (Tyson 1988, Cowie *et al.* 1991). If correct, a careful study of a few arcs would throw valuable light on the origin of this puzzling population.

When observing high redshift galaxies, the three most useful parameters to measure are the mass, the current star formation rate and a time-averaged star formation rate. A comparison of the latter two parameters gives some indication of whether we are witnessing the source in an important phase of its lifetime *e.g.* during a major episode of star formation. Our approach here will be to examine the colours of the most reliable giant arcs across a wide wavelength range, extending Mellier *et al.*'s study to infrared wavelengths. In particular, the combination of optical *and* infrared colours allows us to probe the ratio of present to past star formation, while the infrared luminosity is closely related to the mass of the galaxy. Using these results we address the question of whether the current optically-discovered sample is likely to be representative of high redshift field galaxies in general and to link our observational results with those found from the field redshift surveys.

A plan of this chapter follows. In Section 2 we discuss the role that selection biases may play in terms of optical and optical-infrared colours and demonstrate using spectral modelling the value of infrared photometry in resolving such questions. In Section 3 we review the observational material and present new infrared images and photometry for the sample under consideration. The optical-infrared colours are presented in Section 4

where we conclude that the most distant arcs represent extreme star forming galaxies. We also discuss in this section spatially-resolved photometric information for individual arcs. Finally, we summarise the implications our results in the general context of the faint galaxy population in Section 5 and present the main conclusions in Section 6.

4.2   Optical and Infrared Selection Effects

It is well-known that star forming galaxies are more readily visible than those dominated by old stellar populations at modest redshifts when surveyed in optical bands. This selection bias occurs because the rest-frame ultraviolet (dominated by light from hot young stars) is redshifted into the observing passband. Although the blue colour of many of the arcs discussed in Mellier *et al.* indicate sources with strong star formation, the implications for galaxy evolution are unclear. For example, a massive spiral galaxy with continuous star formation would appear similar, in terms of its rest-frame ultraviolet spectral energy distribution, to a less massive galaxy undergoing a more intense, but short-lived, burst of star formation. Optical data alone cannot readily disentangle these very different scenarios.

The distinction is important because deep redshift surveys (Colless *et al* 1990, 1992, Cowie *et al.* 1991) find that the bulk of the faintest bluest sources are at surprisingly modest redshifts $z \simeq 0.3\text{-}0.5$. It has thus been argued that these are *not* the evolving precursors of L^* galaxies (Cowie *et al.* 1991, Babul & Rees 1992) but an entirely independent dwarf population. Alternatively, Broadhurst *et al.* (1992) have suggested such star-forming low luminosity sources at moderate redshift may evolve via merging to form the present day

population of massive galaxies. In either case, independent data on systems at $z \simeq 1$ from lensing studies would be highly valuable.

In examining an optically blue arc, the critical question is whether we are witnessing a low mass dwarf made temporarily luminous by a burst of star formation, a massive system whose bulk star formation was much higher in the past, or a normal late-type galaxy with a moderate but continuous star formation rate. In the final model the arcs could be representative of present-day massive late-type spirals whose properties can be modelled rather well via a continuous star formation rate.

To illustrate the role that infrared photometry can offer in resolving these possibilities, we examine in Figure 4.1 the optical and optical-infrared colour evolution of a set of model galaxies. The calculations were made using Bruzual's most recent evolutionary code (Bruzual & Charlot 1992). Their new models follow in detail all the relevant stages of stellar evolution, including the red and asymptotic giant branches and post-AGB stars. These authors claim that the models correctly reproduce the colours of stellar populations from the UV to the near-IR over a broad range of ages. They can be computed for an arbitrary star formation history. A standard Salpeter (1955) IMF with an upper mass limit of $125 \, M_{\odot}$ was used.

The model galaxies are presented as viewed using standard passbands but at a redshift $z=1$ for three contrasting situations. First we consider a family of primaeval galaxies undergoing their first major star forming episode. The bursts are arranged to occur 0.2–5.0 Gyr before $z=1$ (we adopt $H_o=50$ km s^{-1} Mpc^{-1}, $q_o=0.5$ throughout). The second family of models has a smaller instantaneous burst superimposed upon an older ($\simeq 5$ Gyr) evolved population. In this case, the secondary burst occurs between 0.2–5.0 Gyr before $z=1$ and compirses 10% of the total gas+stellar mass. The final model has a constant star formation rate and a variable epoch of formation. Ignoring, for the moment, the
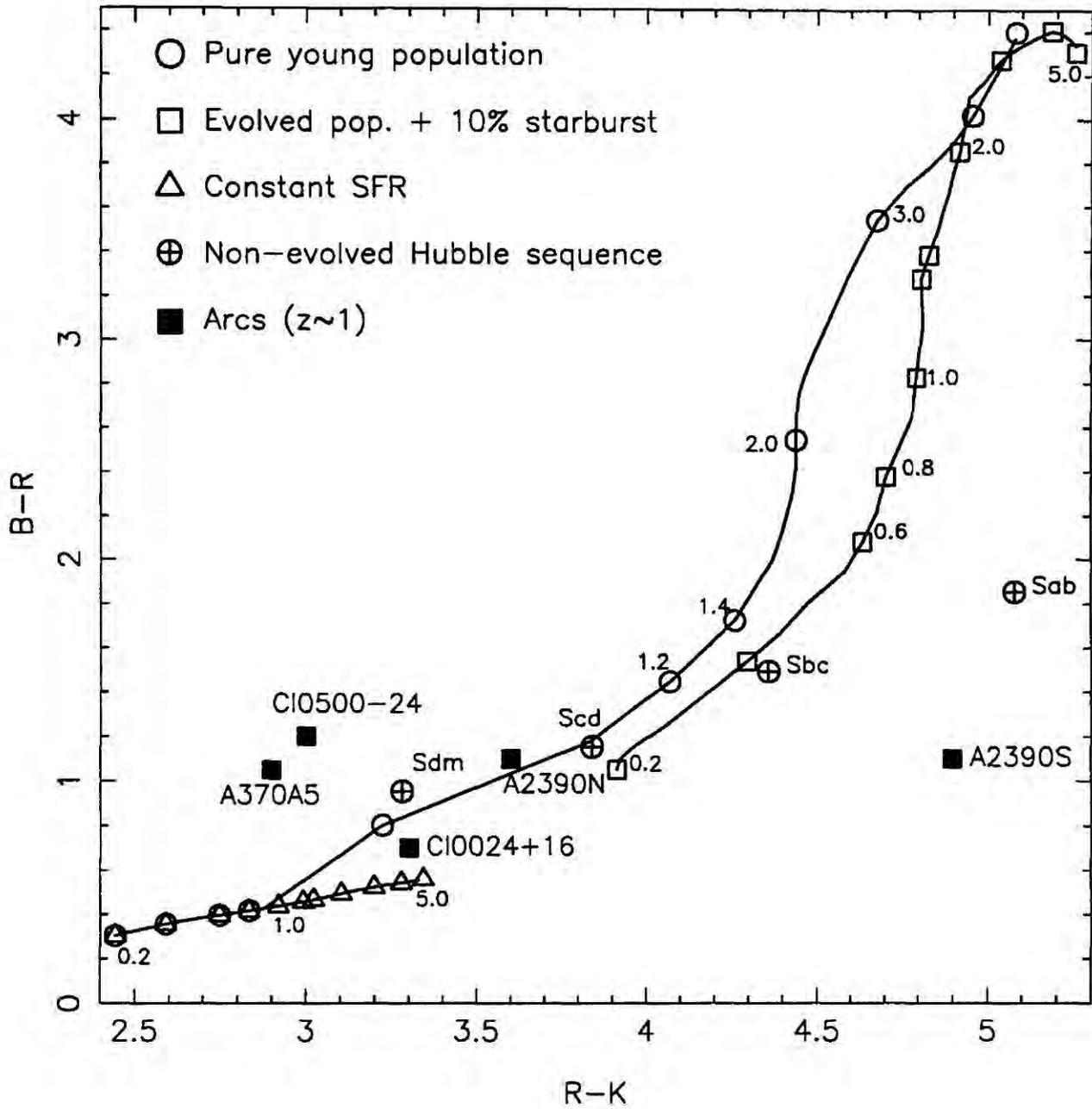
Figure 4.1 $(B-R) - (R-K)$ diagram for galaxies viewed at $z=1$ according to three different star formation histories. The tracks refer to a family of galaxies whose burst of star formation occured at the marked time *before* $z=1$. The first symbol is for 0.2 Gyr before $z=1$ and they are then every 0.2 Gyr until 1.4 Gyr and after that every 1 Gyr to 5 Gyr. The model details are described in the text. The superimposed burst models consist of an old population which encounters a secondary instantaneous burst involving 10% of the stellar mass at the given time prior to $z=1$. The present day Hubble sequence as observed at $z=1$ is also shown. Data points refer to high redshift arcs, the northern and southern sections of Abell 2390 are plotted separately.
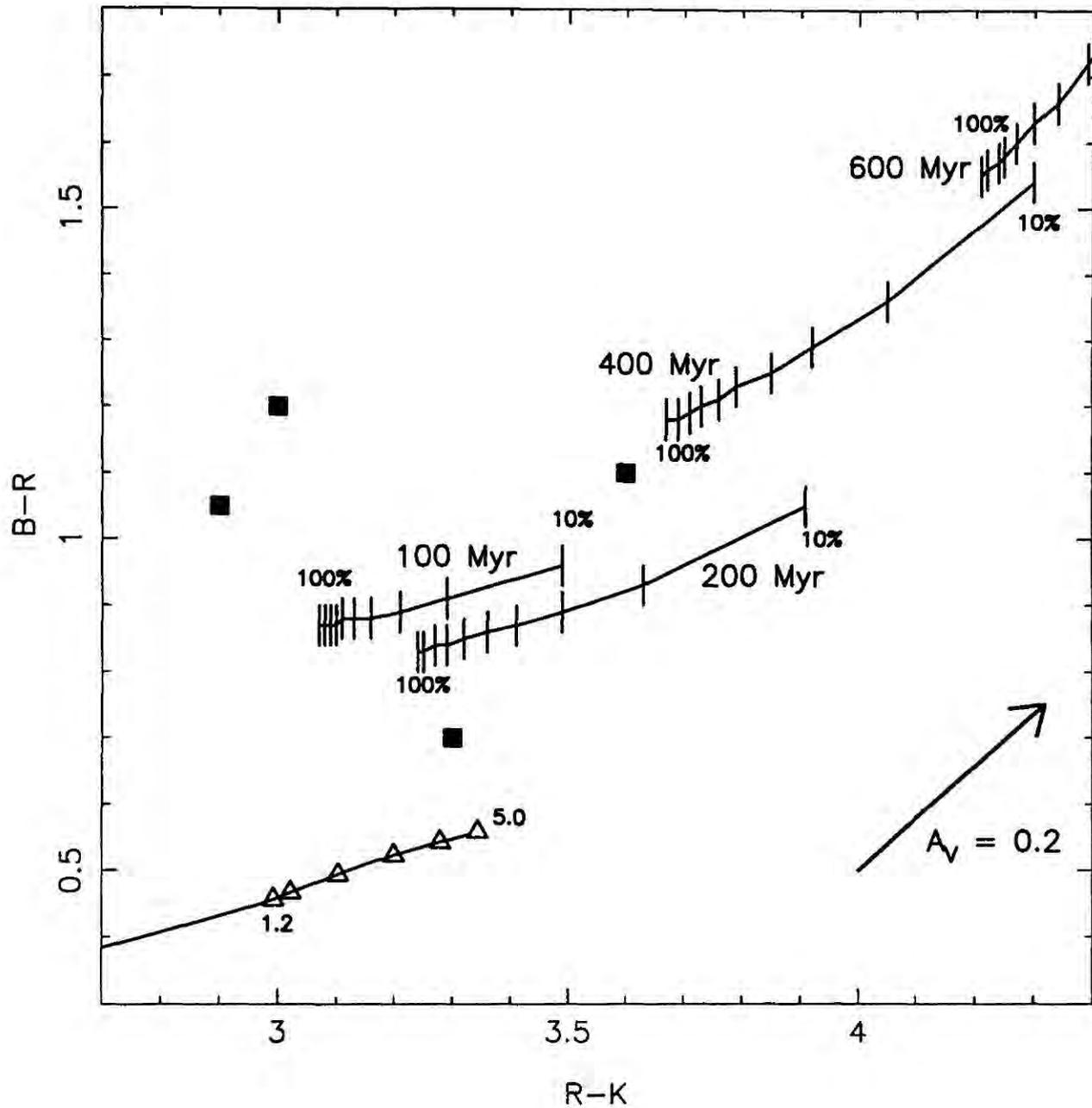
Figure 4.2 $(B-R) - (R-K)$ diagram as in Figure 4.1 but showing the tracks of different burst fractions for a given age in the secondary burst model. The remainder is comprised of an evolved population as above. The separate curves correspond to burst occuring the stated time before $z=1$, the increments show the fraction of the stellar mass of the system created in the burst (from 10% to 100% in 10% steps). The 100 Myr track is heavily influenced by individual stellar evolution phases in the instantaneous burst. Also plotted using the same symbols as in Figure 4.1 are the observations of the giant arcs, the continuous star formation track and the extinction vector for solar abundance dust.

intrinsic luminosity of the source, we see that all three models render the galaxy very blue in $B - R$. At high redshift, optical colours cannot differentiate between a forming galaxy and an evolved system suffering a secondary event of less significance *i.e.* optical colours alone could not differentiate between the very different scenarios. The argument can be extended to conclude that optical colours alone provide few constraints on *any* form of evolution in the star formation rate at high redshifts *unless* perhaps the mass of the system it is known *a priori*.

However, Figure 4.1 shows that an optical-infrared colour such as $R - K$ allows a ready discrimination between the burst models in the range of interest. This is primarily because the K light is sensitive to any underlying evolved stellar population. Only a secondary burst model seen immediately after a short intense burst can become as blue in $R - K$ as the primeval model. The relationship between the $B - R$ and $R - K$ colours offers a straightforward way to estimate the contribution recent star formation may have made to the optical colours. No assumptions need be made about the structural state of the source. The distinction between a secondary burst model and a constant SFR model is also clear in $R - K$, but it is much harder to differentiate between a 'single-burst' galaxy viewed close to its formation and the constant SFR case. Figure 4.1 shows, nonetheless, that to obtain a representative view of the stellar populations of the distant arc sample discussed by Mellier *et al*, near-infrared photometry will be particularly valuable.

Furthermore, if the lensing magnification can be understood, infrared photometry provides a robust estimate of the mass in stars of the system, since it is sensitive to light from long-lived stars that dominate the stellar mass function. At $z \sim 1$ the K band samples rest-frame wavelengths of $\lambda \sim 1\mu m$ whereas the optical colours sample the rest-frame UV. For conventional initial mass functions and stellar populations older than a few 10^8 yrs, the majority of the $1\mu m$ radiation comes from stars which are on either the main sequence or the red giant branch, the progenitors of the latter group are long-lived main sequence stars

(Buzzoni 1989). In a 0.5 Gyr population the relative contributions to the $1\mu m$ light are: MS 30%, Core He burning stars 30% and AGB 40% (Bruzual & Charlot 1992). Therefore, the K band flux gives a better indication of the long-term star formation rate (and hence, indirectly, the stellar mass of the galaxy) than the optical colours which measure the instantaneous star formation rate, since the UV flux is dominated by hot, young stellar populations.

4.3 Observations and Data Reduction

Our sample consists of those available giant arcs with either genuine redshifts or redshift constraints from spectral information; the complete list and the sources for the photometry are summarised in Table 4.1. Our strategy has been to measure $2\mu m$ K band photometry with an infrared array in conjunction with optical CCD photometry in B and R, some of which was published by Mellier *et al.* (1991). In certain cases, the spectral data is inconclusive, as we will discuss in more detail below.

The crowded fields in many clusters and the relative brightness of the cluster members compared to the arcs in the K band makes measurement of 'total' magnitudes very difficult because of contamination from close by objects. We have chosen therefore to measure aperture magnitudes in K and use associated aperture photometry at shorter wavelengths to compute aperture colours. Ideally, we would prefer to measure a total K magnitude in order to estimate its intrinsic luminosity. However, as the magnification factors associated with the gravitational lensing are somewhat model-dependent (Wu & Hammer 1992) we adopt a more realistic approach and measure an average surface brightness for each arc. These are used in conjunction with an assumed angular size and the source redshifts to calculate their luminosities.

Table 4.1 Spectroscopic Arc Sample

Arc	R.A. (1950)	Dec. (1950)	z_{cl}	z_{arc}	T_{exp}
Cl0024+16	$00^h23^m58.5$	$+16°52'51\rlap{.}''0$	0.39	>1[1]	11760
Abell 370 A0	$02^h37^m20.4$	$-01°47'51\rlap{.}''0$	0.375	0.725[2]	6120
Abell 370 A5	$02^h37^m20.8$	$-01°48'15\rlap{.}''8$	0.375	1.308[1]	12420
Cl0500−24	$04^h59^m02.1$	$-24°29'18\rlap{.}''0$	0.321	0.913[3]	11700
Abell 963 N	$10^h13^m58.0$	$+39°17'18\rlap{.}''0$	0.206	0.771[4]	14720
Abell 2390	$21^h51^m15.5$	$+17°27'51\rlap{.}''0$	0.230	0.913[5]	10720
Cl2244−02	$22^h44^m38.3$	$-02°21'30\rlap{.}''0$	0.329	2.238[1]	16320

1) Mellier *et al.* 1991

2) Soucail *et al.* 1988

3) Giraud 1992

4) Ellis *et al.* 1991

5) Pelló *et al.* 1991

The new data consists of deep K band images obtained on the 3.8m UK Infrared Telescope (UKIRT) on Mauna Kea, using the 58×62 InSb array IRCAM (McLean *et al.* 1985). IRCAM offers a choice of pixel scales (0.62, 1.24 or 2.4 arcsec/pixel). Since the data was taken over a series of runs, occasionally during allocations made to other programmes, we used both the smaller scales (see Table 4.1 for details). In general, the smallest pixel scale is best matched to the seeing, allowing more accurate photometry in the crowded cluster environments. However, the field of view is then restricted especially when using in-field dithering methods (*c.f.* Cowie *et al.* 1989) to flatfield the data to the required precision for detecting the low surface brightness arcs against the bright sky in K. In some cases more than one arc could be secured with a wider field, making it profitable to use a larger pixel scale.

The in-field dithering technique constructs a sky flatfield for a particular frame from a number of disregistered object frames spanning the frame. The actual number of frames used depends upon the unit exposure time but was usually $\simeq$8–9. Each frame was dithered on a rectangular 3×3 grid with 5 arcsec spacing. This method allows maximum on-source integration whilst providing a coeval flatfield – which is particularly advantageous in the near-infrared where the sky structure varies on a time scale of minutes. In crowded fields, however, we used the alternative procedure of using separate offset sky flats interleaved with the object frames (*c.f.* Aragón-Salamanca *et al.* 1991). Here, the exposure times depended upon the observing conditions but were typically $\simeq$40 secs for background-limited operation at the 0.62 arcsec scale.

Both sky and object frames were linearised, dark-subtracted and bad pixels removed by interpolation. Flatfielding was accomplished by dividing each object frame by the scaled skyflat frame (regardless of whether it was produced by the in-field dithering or offset sky technique). The flatfielded image frames were registered using fractional pixel shifts

and median-combined to remove cosmic-ray events. All reduction was carried out on the Durham node of STARLINK using IRCAM and purpose-written software.

The in-field dithering technique produces the most impressive results, penetrating to fainter surface brightness limits than those quoted in earlier work (*c.f.* Aragón-Salamanca *et al.* 1991). In a 3.3 hrs dithered exposure, we obtain virtually photon-noise limited performance, a sky flat to better than 4 parts in 10^5 and a 1σ surface brightness limit of $\mu_K = 23.5$ mag/arcsec^2. Representative K images are reproduced along with some optical CCD frames in Figure 4.3 & 4.4.

Calibrations were obtained via defocussed exposures of bright standard stars taken from the list of Elias *et al* (1982). These were interspersed with the observations according to the conditions and reduced using similar procedures. Photometry was performed using large synthetic apertures to give independent zero points for each night. Photometric comparisons for arcs taken on different nights and between different runs shows that the zero point errors are below 0.05 mag.

One arc (Cl0500−24) was taken through a K' filter whose long wavelength edge is curtailed to reduce the rising thermal background across the passband. The effective wavelength is $\lambda_{\mathrm{eff}} \sim 2.1 \mu m$. To convert this measurement onto the standard K system, colour relations were calculated from standard stars with a wide range of $H - K$ colours and the infrared colours of different galaxy classes using the known filter transmissions. A linear relation $K' = K - 0.2(H - K)$ was determined and for the arc in question, an average colour of $H - K = 0.8$ was used for the transformation. This $H - K$ colour is representative of all morphological types beyond $z \sim 0.6$.

As described above, the arcs are often irregular or embedded in the envelopes of cluster ellipticals so precise integrated photometry is not always practical. Since we are principally interested in colours, we chose to measure within fixed apertures. To standardise across

the optical and infrared, the optical frames were resampled onto the infrared pixel scale, rotated and aligned. Images were also smoothed when there was significant differences in the seeing conditions amongst the various filters. This latter step produces only a small correction to the actual colours and the uncertainty is incorporated in our formal photometric error.

Aperture sizes and background subtraction techniques were chosen on an individual basis for each arc. Some arcs (those in Cl0017−20, Abell 370 A5 and Cl0500−24) are relatively uncontaminated by cluster members and photometric measures were taken inside the faintest isophote unaffected by other objects. However, others (Abell 2390 and Cl0024+16) are merged with bright cluster galaxies. For Abell 2390 the contaminating light was removed by rotating, recentring and subtracting the image from the original. While for Cl0024+16 we quote colours for only the most southern of the three arc sections. Yet others (*e.g.* Abell 370 A0) have projected sources superimposed and here colours were measured in all uncontaminated regions. The most critical are the arcs in Cl2244−02 and Abell 963 which are embedded in the halos of several galaxies. To measure colours for these we calculate the halo contribution in the appropriate aperture by interpolation.

Systematic sources of photometric error are, of course, a concern, there may be contaminating unresolved sources whose colour is quite different to the arcs. In a few cases the K light is sufficiently faint that a small error in sky-subtraction might produce a significant change in the optical-infrared colour. Rather than make general statements about the precision achieved, we discuss uncertainties for individual cases in Section 4. For the brighter arcs it is also possible to measure colours as a function of spatial position along the arc. This provides important additional information, *e.g.* on the likely lensing magnification.

For those clusters with optical images, we have measured optical $B - R$ and optical-infrared $R - K$ colours using the same aperture adopted in K. Although our optical
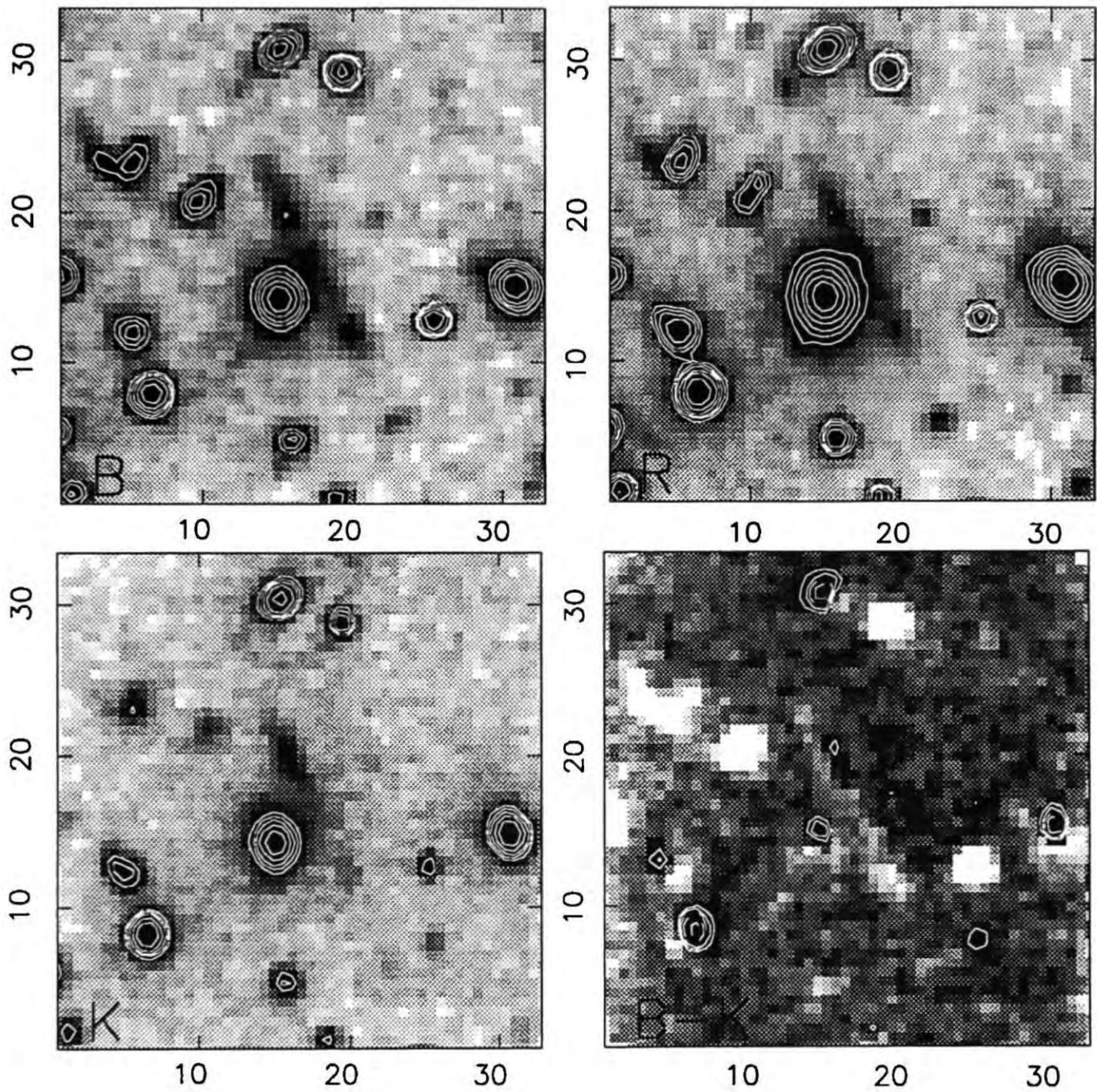
Figure 4.3 Broad band images of selected arcs in our sample. North is at the top, East is at the left. B, R, K and $B - K$ images of Abell 2390. The images are 29 × 27 arcsec. The $B - K$ image was constructed by scaling the two images to remove the cluster ellipticals and shows the strong colour gradient along the arc.
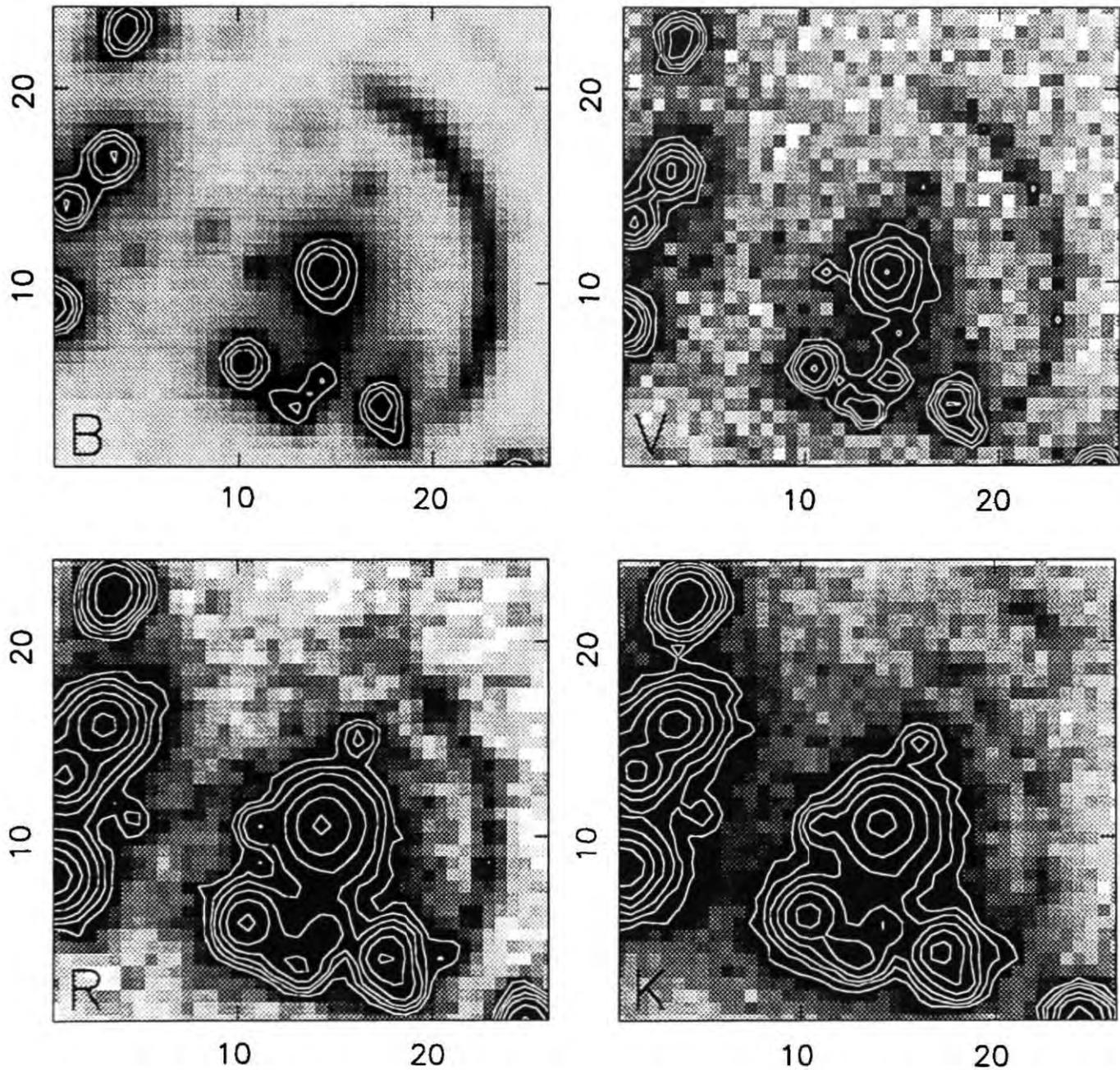
Figure 4.4 Broad band images of selected arcs in our sample. North is at the top, East is at the left. B, V, R and K images of Cl2244−02, the giant arc is clearly detected in the K image. The second infrared arc is concentric with the giant arc and north-west of it. The vast difference in the arcs' colours can be seen by comparing the B and K images. The frames are 25 arcsec square.

Table 4.2 Spectroscopic Arc Sample Colours

Arc	$B - R$	$R - K$	$B - K$	μ_K	M_K
Cl0024+16	0.7[1]	3.3±0.1	4.0	21.7	−22.1
Abell 370 A0	1.97[2]	4.1[3]	6.1	18.5	−24.1
Abell 370 A5	1.05[4]	2.9±0.2	3.9	21.6	−22.1
Cl0500−24	1.2[5]	<3	<4.2	>22.0	< −21.1
Abell 963 N	0.7±0.3	2.7±0.3	3.4	22.0	−20.8
Abell 2390	1.1±0.1	4.6±0.1	5.7	20.0	−23.1
Cl2244−02	1.0±0.1	2.5±0.2	3.5	21.8	−22.8

1) Koo 1989

2) Fort *et al.* 1988

3) Aragón-Salamanca & Ellis 1990

4) Hammer *et al.* 1989

5) Pelló *et al.* 1991

data is often taken from the frames analysed by Mellier *et al.*, we have reduced these completely independently. A comparison of our $B - R$ colours with those of Mellier *et al.* (1991) shows good agreement within our quoted errors with the exception of Abell 2390 where our $B - R$ colour is significantly bluer. In this particular arc, there is a strong optical-infrared colour gradient but no gradient in $B - R$. This disagreement cannot then be due to the use of different apertures. We return to this problem in Section 4.4.2. Our photometric results are summarised in Table 4.2.

Finally, we report the dicovery of a new giant arc candidate, *discovered* in the near-infrared. The deep K image of Cl2244−02 revealed a second, shorter, arc further from the cluster centre than the main arc with a similar centre of curvature (Figure 4.4). This detection prompted the acquisition of a much deeper B image which shows the second arc at a surface brightness of μ_B =27.6 mag/arcsec^2. The optical detection suggests the Lyman limit has not reached the B band and thus z<3.8. In contrast to the main sample, although this arc appears blue in the optical ($B - R \leq 1$), it is prominent in K and hence very red in the optical-infrared region ($B - K = 7.3$ and $R - K \geq 6.3$). An early-type galaxy placed at the cluster's redshift (z=0.329) has $B - K \sim 6.2$ and reaches $B - K = 7.3$ at $z \sim 0.6$, when $R - K = 4.3$. However, the unusual feature of the arc is the faintness in R – the limits given by this in $R - K$ require the source to have $z \geq 1.2$ and the $B - R$ colour then needs a strong upturn in the SED below 2000 Å. However, the arc is sufficiently faint, especially in the optical, that these colours must be viewed with some caution. In the deep high resolution B data, the second arc is approximately 10 arcsec long and appears unresolved.

A simple geometrical lensing model suggests the second arc should be at least as distant as the primary arc, and possibly at an even more distant. The colours are consistent to those expected for an E/S0–Sab with a strong UV upturn observed at the redshift of the primary arc; in this case the source would be luminous with $M_K \sim -25.7$. The red

optical-infrared colour is important, however, in view of the near uniform optical-infrared colours for the optically-selected arcs. It suggests there might be very strong selection effects operating in the identification of arcs.

4.4 Photometric Results for Distant Galaxies

4.4.1 Broad-band Colours and SEDs

In Figure 4.5 we plot the observed $B - R$ and $R - K$ colours versus redshift for our sample. For comparison, we also plot the $B - R$ – redshift distribution measured by Colless *et al.* (1990,1992) for their samples of faint field galaxies with $21 < b_j < 24$. The important point, originally noted by Fort (1990), is that *both* datasets include objects with very blue optical colours ($B - R \leq 1$) typical of the most extreme star forming galaxies present today (*e.g.* NGC 4449). However, to the redshifts probed with the field population ($z \simeq 0.5$), objects are found with colours as red as present-day ellipticals. It would appear that the arcs sample a population of galaxies at $z \simeq 1$ whose star formation activity is much more vigorous than a random cross-section of the present Hubble sequence and, possibly, than the lower redshift field galaxies in current field surveys.

In Figure 4.5(c) we compare the data with the colours of the faint field galaxies in the recent survey of Cowie *et al.* (1991) limited at $b_j \leq 24$. It has been suggested that the latter sources, whose spectra show strong [OII] emission, are either dwarf galaxies undergoing disruptive star formation or merging to form the present-day galaxy population (Broadhurst *et al.* 1992, Babul & Rees 1992). The similarity in colours is striking, stressing the importance of the K band measures as well as the need to estimate the lensing magnification so that the K luminosities can be derived. For example, in the merger picture one
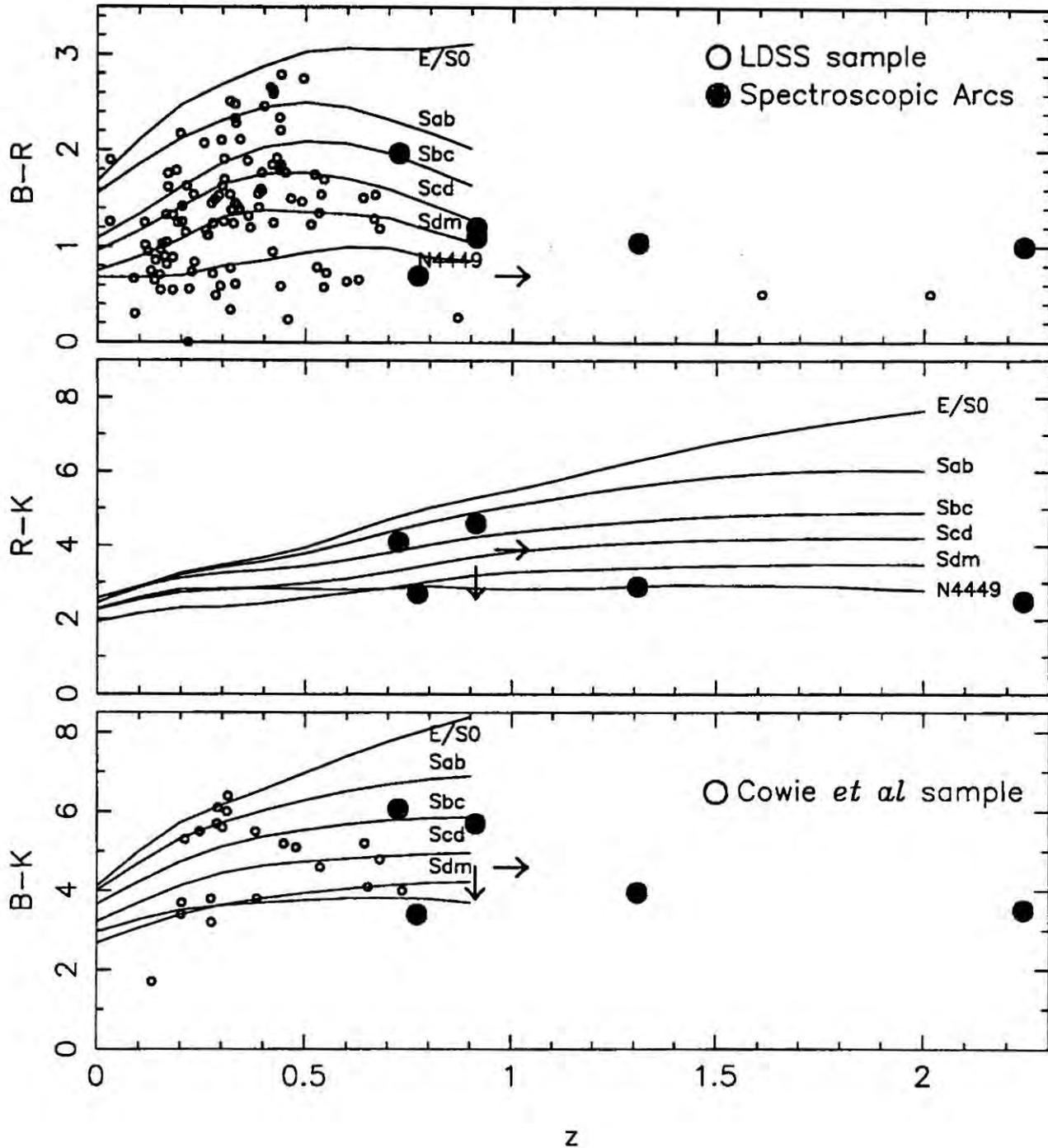
Figure 4.5 (a) $B - R$ versus redshift for the arc sample ($\bullet$) compared to the distribution of $B - R$ for the Colless *et al.* samples of faint field galaxies (o). The horizontal arrow shows the probable redshift range of Cl0024+16. (b) $R - K$ colour versus redshift for the arc sample. The vertical arrow denotes the upper limit for the arc in Cl0500+24, converted from K' to K. (c) $B - K$ colour versus redshift for the arc sample compared to the colours of field galaxies in the faint optical survey of Cowie *et al.* 1991 (o). Curves denote the expected colours of the non-evolving Hubble sequence.

expects a gradual decline in K luminosity with redshift as each galaxy has formed from less massive sub-units, with the K light tracking the mass. In Babul & Rees' scenario, dwarfs commence their eventual dramatic star formation only when the confining ultraviolet background flux falls below a critical threshold. Presumably the redshift at which this occurs is uncertain, although an extended era of dwarf formation $e.g.$ $0.3 < z < 2$, might be difficult to accommodate.

In Section 2 we demonstrated how optical colours can mislead at high redshift because of biases introduced by ultraviolet flux which enters the optical region. Indeed, several of the arcs with $z < 1$ which are blue in $B - R$ turn out to have fairly reasonable colours in $R - K$ indicative of precisely this effect. Only a small amount of additional star formation in a normal spiral would be needed to explain the combined BRK colours. However, more interestingly, the 5 arcs claimed to be the most distant – Abell 2390 N (z_{arc}=0.913), Cl0500−24 (z_{arc}=0.913), Abell 370 A5 (z_{arc}=1.3), Cl2244−02 (z_{arc}=2.24) and Cl0024+16 (z_{arc} >1) – are blue in *all* colours suggesting a genuinely young stellar population is dominating the light.

We plot the colours of the $z \sim 1$ arcs on the $B - R$ versus $R - K$ diagram in Figure 4.1. *The most striking conclusion is the clear demonstration that the 4 arcs with $z \sim 1$ have no significant contributions from an evolved population and cannot, therefore, readily be explained via subsidiary star bursts of a minor nature superimposed on a pre-existing stellar population.* Either we are witnessing constant star formation in late-type galaxies, or a significant burst of star formation in a genuinely young population.

To quantify this statement we plot in Figure 4.2 the colours of a family of secondary burst models as a function of the fraction of mass in the second burst. Each curve is for an instantaneous burst occuring at the stated time before z=1 – the remaining fraction of the system being composed of an evolved population. Given the instantaneous nature of

the burst the 100 Myr locus is strongly effected by individual stellar evolution phases and should be taken as illustrative only. Nevertheless, the older tracks show that agreement with the arc colours can only be achieved by viewing the system very soon after the burst occured. The earliest burst which could reasonably explain all the arc colours needs to occur less than 400 Myr before $z=1$ and would have to create at least 50% of the stellar mass of the system. Later bursts allow smaller mass fractions. Given such stong star bursts the distinction between the secondary burst model and the primeval galaxy model then becomes somewhat semantic. For reasonable burst fractions agreement seems unlikely given the region defined by the distribution of the arcs on the colour-colour plane and the small time scale during which the secondary burst models enter this area. Neither the constant star formation model nor the primeval galaxy model have such a grave problem with the time scales. At $z=1$ both B and R are sampling the rest-frame ultraviolet and may therefore be subject to strong reddening. To illustrate the upper limit on the possible role of dust we plot the extinction vector for solar abundances.

For a subset of our sample we have secured photometric data in a variety of passbands and can thus construct spectral energy distributions (SEDs) which allows us to demonstrate the above result more clearly. The arcs with suitable data are Abell 370 A0, Abell 370 A5, Cl0500−24 and Cl2244−02 and we present their rest-frame SEDs in Figures 4.6 together with those of the present-day Hubble types as would be observed at the redshift of the arc. As Aragón-Salamanca & Ellis (1990) showed, the giant arc A0 in Abell 370 ($z_{arc} = 0.72$) is fitted well by a normal spiral of class Sbc, but the higher redshift systems are clearly dominated by young stars, closely matching the SED of NGC4449 − an intense star forming system. Whilst the spectroscopic identifications for Abell 370 A5 and Cl2244−02 remain somewhat uncertain, we would like to stress that this redshift uncertainty does not significantly affect our conclusion about the nature of these sources because the SED for the
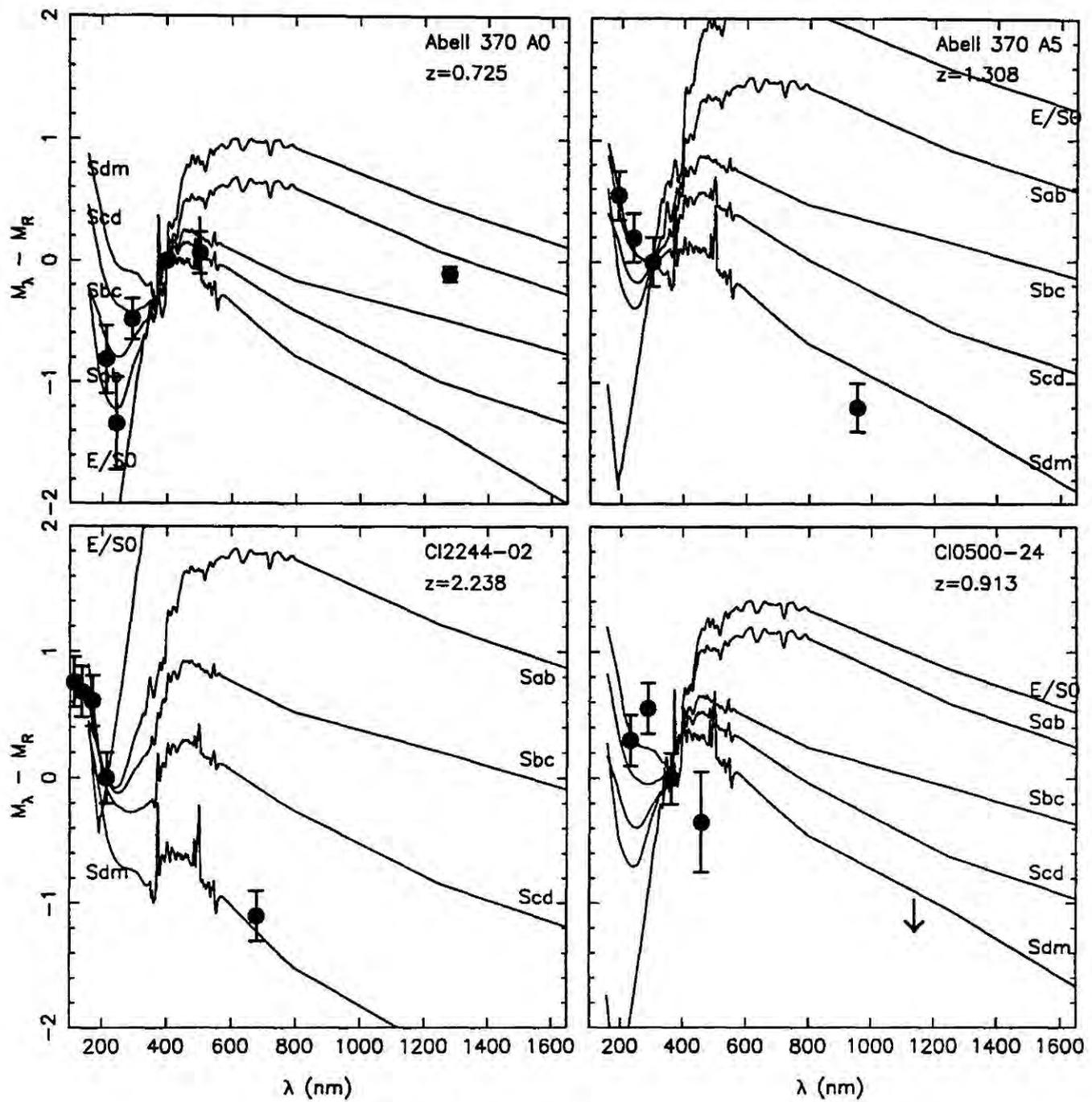
Figure 4.6 Spectral energy distributions for those arcs with extensive broad-band data. Data points are compared in the rest-frame with the present-day Hubble sequence.

bluest Sdm/Irr classes maintains its shape more or less independently of redshift (*c.f.* the flatness of the colour-redshift relations for NGC4449 in Figure 4.5).

4.4.2 Intrinsic Luminosities and Colour Gradients

The gravitational magnification for the arcs in our sample is an issue central to resolving the question of whether we are witnessing vigorous star formation in massive ($\sim L^*$) systems or simply seeing individual star forming clumps, either in isolation (*e.g.* as in the dwarf hypotheses discussed earlier), or star forming portions of fairly normal systems. The latter point was raised in discussion in Chapter 3 where we suggested that strong surface brightness dimming with redshift may render only the star forming 'peaks' of distant galaxies visible.

In Table 4.2 the absolute K luminosity of each arc has been estimated from its integrated apparent K magnitude assuming an unresolved source with an intrinsic angular size equal to the seeing disk and the spectroscopic redshift. Since all are blue in colour, we determined a k-correction assuming a flat ($f_\nu \simeq$ constant) spectrum (Cowie *et al.* 1989). Where comparisons can be made, these magnifications agree with those calculated for individual arcs from detailed lensing geometries: magnification factors of $\sim$10 are found. We return to possible systematic sources of error in this calculation in the next section. This result tends to support the suggestion that the lensed galaxies are sub-L^* systems. The present day remanents of these systems will depend critically upon their subsequent star formation. In the single burst model they undergo purely passive evolution leading to present day counterparts with $M_K \sim -20$. If the constant star formation model is valid and star formation continues at the same rate then the final $z = 0$ objects have $M_K \sim -25$.

Whereas it may ultimately be possible to derive quantitative estimates of the magnification by constraining the lensing geometry in clusters where there are a useful number of arcs

and arclets (Chapters 5 & 6), another approach towards resolving this ambiguity is to search for colour gradients along the arcs. If the source is a highly-magnified compact HII region, taking an extreme example, one might expect a remarkably uniform colour, whereas a more massive system might show a variation in colour representative of resolved portions each exhibiting different star formation rates.

Unfortunately, measuring reliable optical-infrared colour gradients is an exceedingly difficult task because of the inherent faintness of the sources and their location in the dense cluster cores. In the case of Cl0024+16 and the giant arc Abell 370 A0, no perceptible colour gradient is seen in either the optical or optical-infrared. A gradient might have been expected for the latter given the earlier comments about its spectral energy distribution, but the situation is confused by a number of galaxies superimposed on this giant feature (Figure 3.1, Aragón-Salamanca & Ellis 1990). Those authors measured colours in four uncontaminated regions and found no variations within their photometric errors. In the case of Abell 370 A5 and Cl0500−24, the K signal is either too faint or not detected and no optical-infrared variations can thus be measured, no optical colour gradients are reported for these arcs. Finally, for Abell 963, the northern arc is embedded in the envelope of the massive cD and the southern arc has too low a surface brightness for a K detection in the present data – the absence of an optical colour gradient is discussed in Chapter 2.

The only two arcs worthy of consideration for colour gradient studies are Abell 2390 and Cl2244−02. The former has probably the most reliable spectroscopic redshift (z_{arc}=0.91, Pelló *et al.* 1991) whereas the latter is representative of the star forming high redshift systems discussed above. Surface K photometry, in terms of μ_K mags/arcsec^2, and optical and optical-infrared colours as a function of position for these two cases are presented in Figures 4.7 and 4.8. We discuss the two cases in turn:
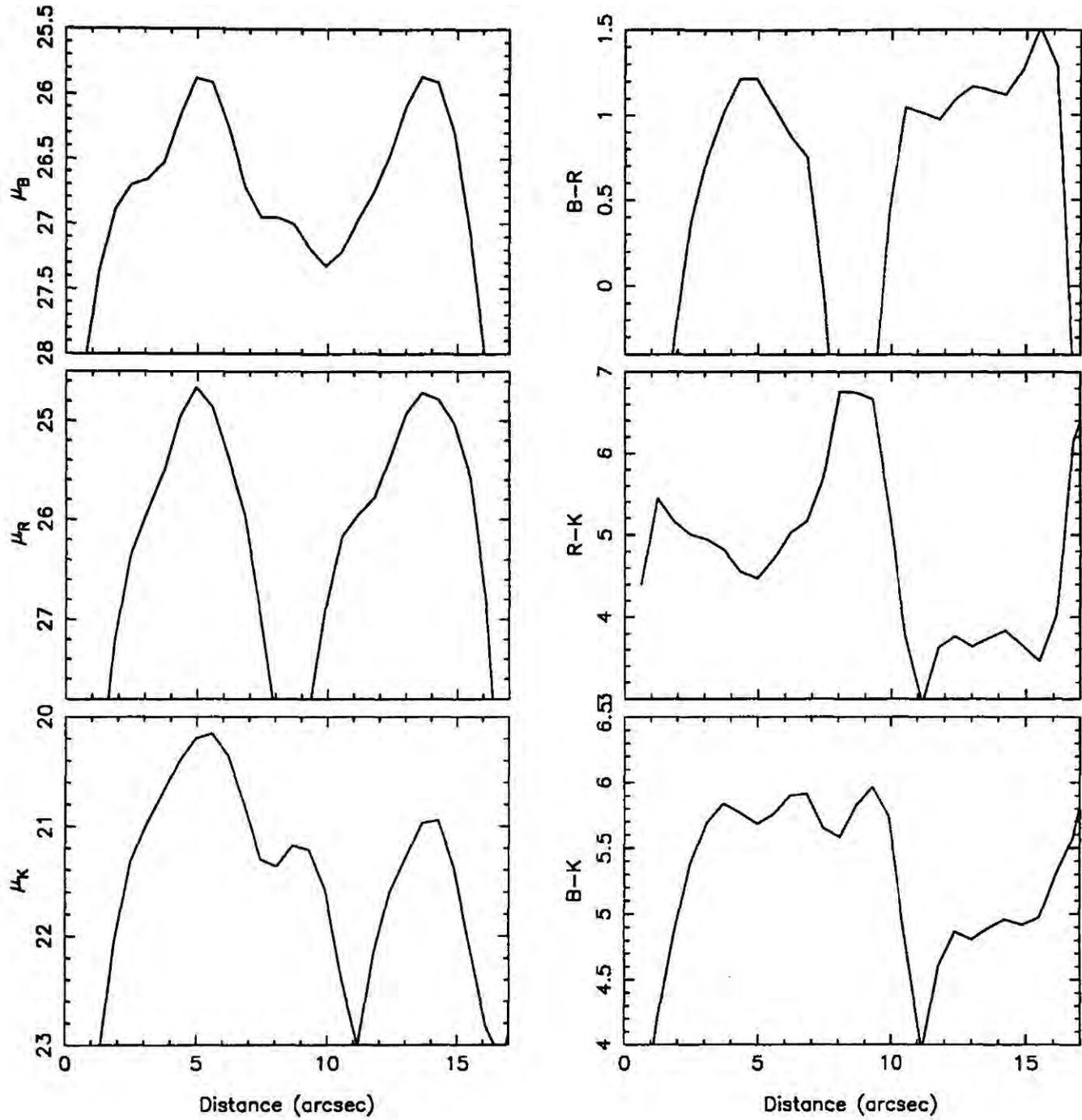
Figure 4.7 Surface brightness and colour profiles for the giant arc in Abell 2390. North is at the left handside. The strong $B - K$ colour gradient between the northern and southern sections of the arc is readily apparent.
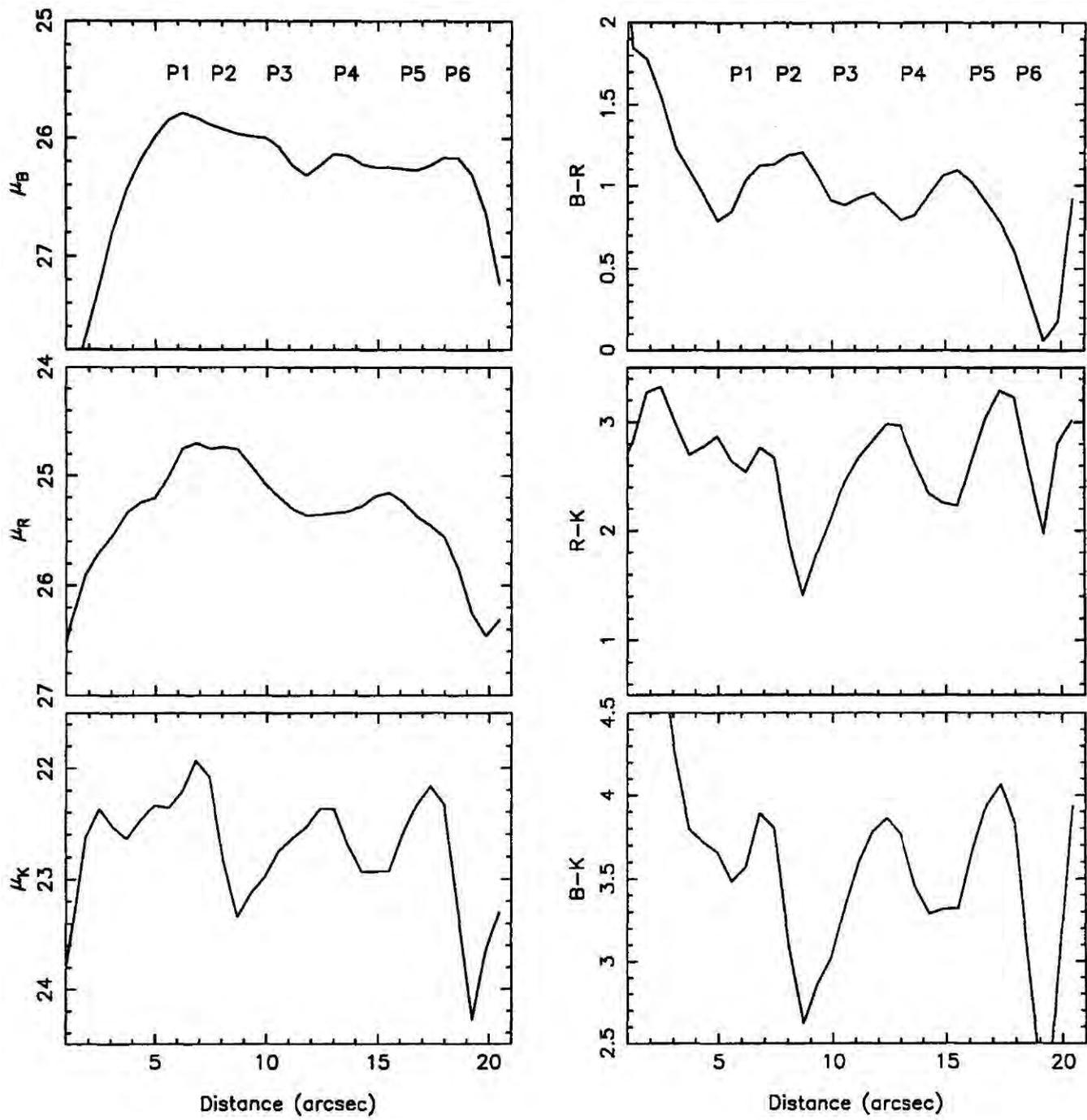
Figure 4.8 Surface brightness and colour profiles for the giant arc in Cl2244−02. The features marked refer to those discussed by Hammer *et al.* 1989. The profiles run have south at the left. Notice the symmetrical shape of the $B - R$ and $B - K$ profiles around the break between P3 and P4.

Abell 2390: The arc is surprisingly straight and lensing geometries based on two potentials have been suggested by Pelló *et al* and Blandford (1991) based on a strong velocity gradient seen in [OII] 3727Å of $\simeq 400$ km/sec indicative of a massive star forming system. Although this line is prominent across the entire arc, we find a striking optical-infrared colour gradient. Whereas the northern section shows a blue ($R - K = 3.6 \pm 0.2$) colour representative of a spiral disk at $z_{arc}=0.91$, the southern region is substantially redder ($R - K = 4.9 \pm 0.3$) as would be the case for an associated spheroidal component. Both sections of the arc are plotted on Figure 4.1. The northern section is a member of the group of arcs which are blue in both optical and optical-infrared colours, while the southern section lies in a part of the plane occupied by old evolved populations which have superimposed young secondary star formation.

However, since there is no observed $B - R$ gradient, the likelihood of contamination from an unrelated very red source at the southern tip must be considered. The resolution of this paradox is not yet clear because even the coolest M star would not distort the $R - K$ colour to the extent required without being visible as a source in the B image. Another factor is the discrepant $B - R$ colour obtained by Mellier *et al.* (1991) noted earlier. Their optical colour, whilst not reproducible by us, would support the bulge+disk picture for a normal system at $z = 0.91$.

Kassiola *et al.* (1992) have suggested, on the basis of the velocity gradient data and stable lensing configurations, *two* lensed sources may be involved. In this case, the similar $B - R$ colours of the two sources could result from a starburst induced by their interaction, while the different $R - K$ colours would reflect different pre-burst stellar populations. Higher resolution and deeper optical data is needed to make progress, but given the current information, the last explanation is the most consistent with the data.

Cl2244−02: Although the redshift of this arc is less well-determined, the rising ultraviolet continuum does indicate a high redshift. Mellier *et al.* (1991) showed that if the emission line feature seen in their spectrum *is* Lyα, its strength implies a high star formation rate per unit mass, consistent with the colours. Some structure is seen in the optical data (Figure 4.4) and these variations have been modelled by Hammer and Rigaut (1991) who concluded that the arc comprises two images, with opposite parities, of a single face-on spiral galaxy with the surface brightness peaks corresponding to disk and bulge components. The $B - K$ colour variations show a symmetrical pattern across the break between the two supposed images providing independent support for this lensing model.

4.5 Discussion

There are two possible biases that may weaken the conclusions we can make from our dataset. These are our lack of knowledge of the exact lensing magnification, this effects our derived source luminosities, and the bias caused by the arcs being selected in blue optical passbands, primarily B. We now address these two concerns:

The intrinsic K luminosities derived above imply that we are seeing significantly sub-L^* systems compared to the present day field population. For a resolved arc the axial ratio gives a good estimate of the magnification factor, the main uncertainties being the original source orientation and the core size of the lensing potential. Unfortunately a majority of the arcs are unresolved (see Chapter 6) and this results in uncertain magnifications as has recently been discussed by Wu & Hammer (1992) and Miralda-Escude (1992). The ambiguity arises because for a given observed radial distance, r_{arc}, from the centre of the

lens, the arc's width depends upon both the original source dimensions and the core size of the lensing potential (Wu & Hammer 1992). For large elongations:

$$\frac{d_{arc}}{d_{source}} \propto \frac{1}{(1 - \kappa(r_{core}))}. \qquad (1)$$

Where d_{arc} and d_{source} are the arc and source widths, $\kappa(r_{core})$ is dependent upon the lens' mass surface density at the position of the arc image. For a given arc position and cluster velocity dispersion, σ_{cl}, the larger the core radius, r_{core}, the larger the value of κ ($\kappa = 0$ for $r_{core} = 0$). The magnification, A, is given by:

$$A \propto \frac{l_{arc}}{\pi d_{arc}} \frac{1}{(1 - \kappa(r_{core}))^2}. \qquad (2)$$

where l_{arc} is the observed arc length. We can therefore postulate two scenarios:

Model 1: A singular lens producing a moderate magnification event ($A \sim l_{arc}/d_{arc} \sim 10$) from a marginally unresolved source, $d_{source} \sim 1$ arcsec,

Model 2: A non-singular lens with $r_{core} \sim 100$ kpc giving a high magnification ($A \sim 5l_{arc}/d_{arc} \sim 50$) with an intrinsically small source, $d_{source} \sim 0.1$ arcsec.

To distinguish between these two possibilities we can draw upon two additional arguments: 1) we examine the angular sizes of faint field sources and 2) we consider the implications of the lensing cross-section.

A large fraction of $B \leq 26$ sources are resolved in good seeing with FWHM of 0.6 arcsec (Chapter 6). This result has recently been corroborated using HST for a sample of faint field galaxies with measured scale lengths of 0.3-0.8 arcsec (Griffith's *et al.* 1992). The former observation was used by Wu & Hammer (1992) to argue that the lensing potentials must be very compact if a typical giant arc arises from a $B = 25$-26 source. For the low magnification model everything is then consistent with calculated source sizes and magnitudes. However, for the high magnification model the intrinsic source magnitudes

would lie fainter than the $B = 26$ limit – where we have no knowledge of the source sizes. We can therefore only claim tentative support for Model 1 from the self-consistency of the observations.

The probability of a high magnification event ($A_c \gg 1$) is (Blandford & Kochanek 1987):

$$P(A > A_c) \propto \frac{1}{A_c^2}. \tag{3}$$

If we require that the total mass in galaxies, and hence K luminosity, per unit volume is conserved with redshift (c.f. Broadhurst et al. 1992) then we can derive a simple relation between luminosity, L, and space density, N, of sources at a given epoch for the two models: $N_1 L_1 = N_2 L_2 = constant$. We also have that $A_1 L_1 = A_2 L_2 = L_{arc}$ as both models must recreate the observed arc luminosity. As the cross-section for the creation of a luminous arc in a particular model is given by the product of the space density of sources and the lensing probability:

$$P(L_{obs} \geq L_{arc}) \propto N_i \frac{1}{A_i^2} \propto \frac{1}{A_i} \propto L_i. \tag{4}$$

Therefore the probability of observing a bright arc from a given source decreases with decreasing source luminosity. It should be noted that this line of argument is not applicable to the optical observations where the luminosity is seriously affected by the star formation and dynamical histories. Although no complete sample of infrared-selected arcs has yet been constructed, the absence of small arcs of comparable surface brightness in our fields supports for Model 1; indeed for Model 2 to be valid, the optical surveys would have to miss the majority of intermediate magnification arcs while finding only the extreme events.

Although neither conclusion is particular convincing, given the small sample size and possible selection biases, we conclude that the most likely scenario is that in which the sources are $B = 25$–26 galaxies undergoing moderate magnification, supporting our earlier calculations of source luminosities. In Figure 4.9 we compare the distribution of intrinsic
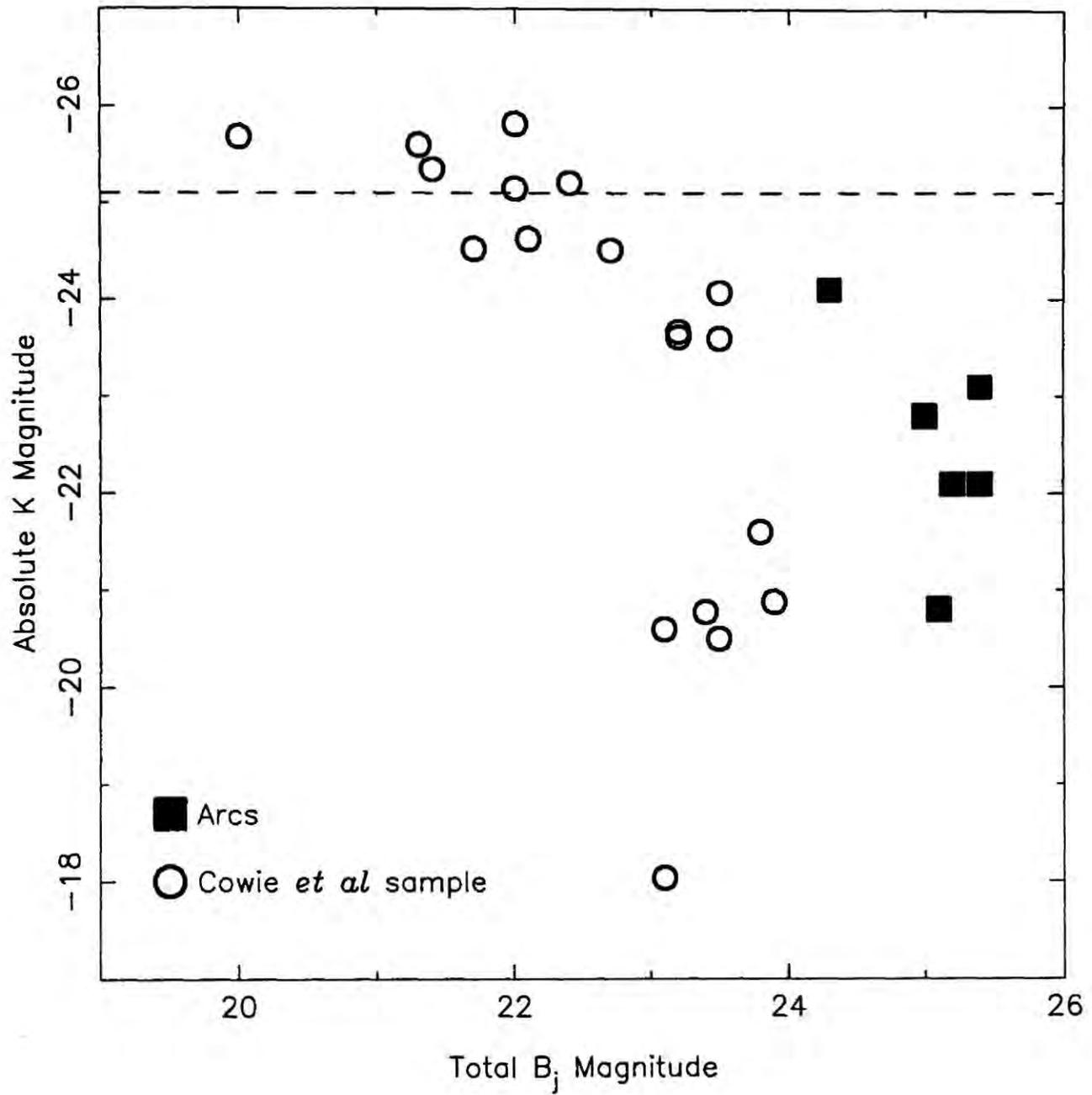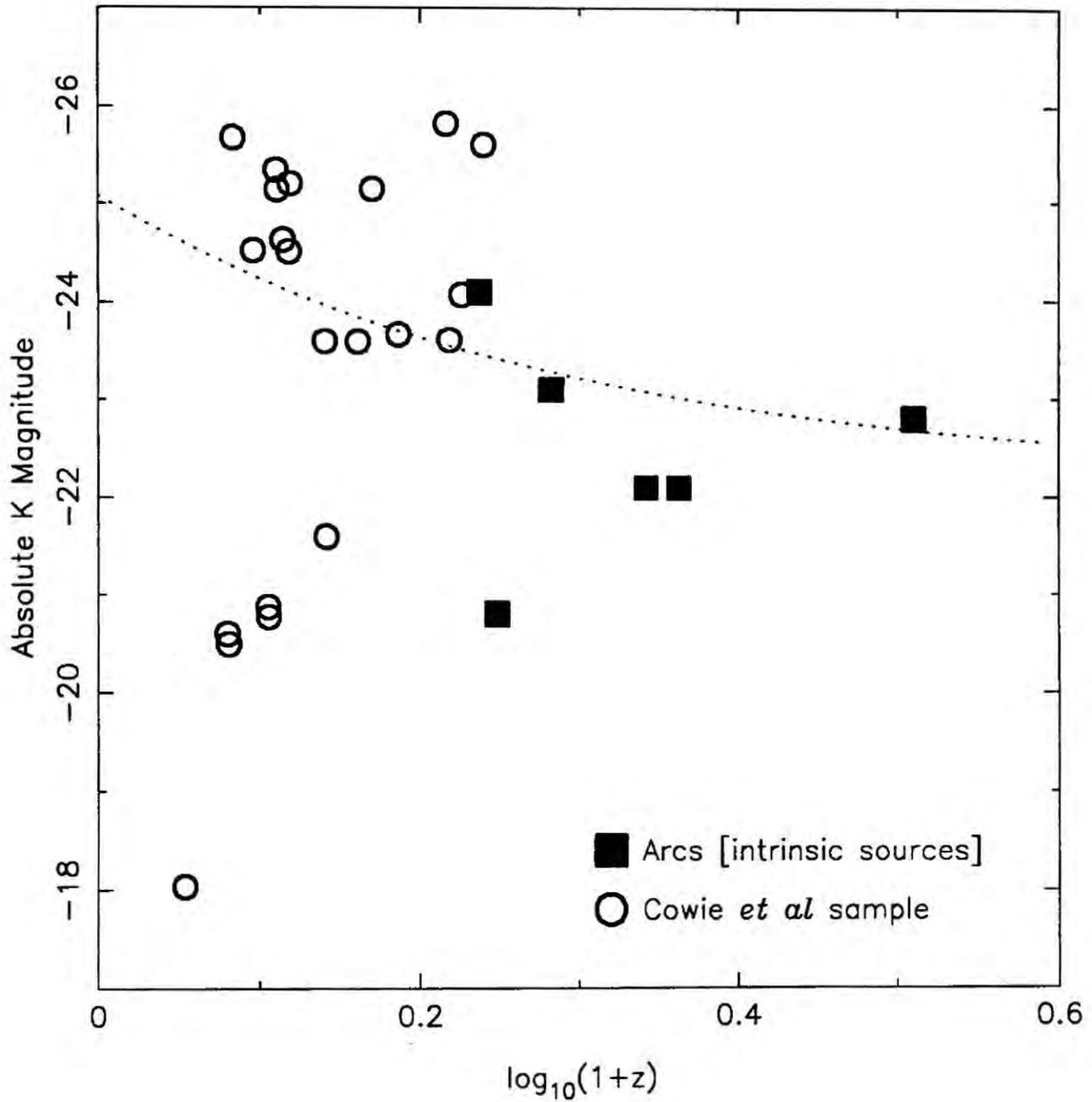
Figure 4.9 M_K-B diagram for the arc sample together with that for the $B \leq 24$ field sample of Cowie *et al.* (1991). A slow decrease in the mean K luminosity of systems at fainter optical limits is apparent. The dashed line shows M_K^* for a present day field sample.

source magnitudes and absolute luminosities of the arcs with the $b_j < 24$, spectroscopic sample of Cowie *et al.* (1991). A Kolmogorov-Smirov test shows that there is a 12% probability that the distribution of M_K in the two samples are drawn from the same parent population. This drops to 2% if we adopt the extreme magnification model. This is equivalent to the statement that there is marginal evidence that the bright end of the K luminosity function in our prefered model evolves between $B = 22$–24 and $B \sim 25$–26. This is seen as a slight trend to lower absolute luminosities at fainter magnitudes, which is in the direction expected in the merger hypothesis. If we plot M_K versus z this evolution becomes more apparent (Figure 4.10), with an absence of the brightest galaxies in the more distant arc sample. We also plot the prediction M_K^* for the prefered Q=4 model of Broadhurst *et al.*(1992) – arbitrarily normalised to the local field M_K^*. The rapid evolution seen in the luminosity of the brightest galaxies is approximately fit by: $L_K \propto (1+z)^{-2.9\pm0.7}$. This assumes that the arc sample crudely represents a magnitude-limited sample. This rapid evolution is predicted under the merger scenario of Broadhurst *et al.*(1992) – within the errors allowed by the likely selection effects in the arc sample.

The present dataset was not homogenously selected and in many ways does not resemble a classical magnitude-limited sample. Indeed, it may be impossible to construct a well-defined sample given the nature of the lensing process. More likely the arcs represent a *surface brightness limited* sample (*c.f* Chapter 3). Such samples are prone to strong selection effects as emphasised by Phillipps *et al.* (1990) in addition to problems associated with ultraviolet bias (see Section 4.2).

One way of examining the possibility of selection biases, at least in the optical-infrared colours of the arc sample, is to compare it with a K-limited sample of faint field galaxies from the photometric survey of Cowie *et al.* (1991) which is statistically complete to $K = 22$. Cowie *et al.* find the bulk of the K-selected galaxies are blue and representative of those found to $B \simeq 25$–26, *i.e.* there are few intrinsically red sources. A comparison of

Figure 4.10 M_K–z diagram for the arc sample together with that for the $B \leq 24$ field sample of Cowie *et al.* (1991). The lack of distant counterparts to the luminous local galaxies is obvious. The plotted line shows an Q=4 model from Broadhurst *et al*(1992) normalised to the local M_K^*.

the $B - K$ colour distribution for the arcs and the field objects with $21 < K < 22$ shows agreement at the 99% significance level using a two sample K-S test. In the event that a strong selection effect was at work in the arc sample we might have expected our colour distribution to be skewed blueward. This gives us some confidence that the arcs are no more biased towards extremely blue objects than a normal field survey. The remaining thorn in this argument is, of course, the untypical colours of the only infrared-selected arc in Cl2244−02. More examples are clearly needed to understand the significance of this unusual object.

Although our two-colour plane (Figure 4.1 & 4.2) argues against scenarios where blue light is produced by secondary star formation in evolved galaxies, it was not possible to distinguish between the models involving a primaeval burst and a more pedestrian history of continuous star formation as would be seen, for example, in a late-type spiral. However, the absence of $z > 1$ galaxies in the flat-spectrum field survey of Colless *et al* (1992) is a strong argument against the former scenario. For example, in the primaeval burst model where the stars are formed in ~ 1 Gyr before $z = 1$, a model galaxy with a culminating luminosity of $M_K \sim -23$ must reach an apparent magnitude in its most luminous phase of $B \sim 23$. The current dearth of such galaxies in the Colless *et al.* (1992) survey is strong observational evidence against this picture. In the continuous star formation picture, the peak B magnitude for equally blue sources can be arranged not to exceed $B \simeq 26$ (see also Baron & White 1987). Moreover, while the primeval burst model would require all the systems to be formed within ~ 1 Gyr of $z=1$ (*i.e.* $z \leq 1.5$) creating the possibility of a feature in the B counts, the continous star formation model allows a much more extended formation epoch while still being consistent with the distribution of arc colours.

The final observation to make is that the redshift distribution for the giant arcs is peaked at relatively low redshifts; ignoring the uncertain case of Cl2244−02, 75% lie below $z = 1$. The low redshift cut off clearly arises because of the redshifts of the lensing clusters. The

apparent lack of high z galaxies is however surprising. Although few high z sources are found in deep spectroscopic surveys to $B = 24$, the equivalent result from the arc samples implies 2–3 magnitudes fainter we are still not uncovering a population of strongly evolving galaxies (*c.f.* Chapter 6).

4.6 Conclusions

From infrared photometry of a spectroscopic sample of giant arcs we find that:

• Giant arcs provide us with a unique and easily recognisable probe of the nature of field galaxies at high redshifts. Their optical-infrared colours are representative of galaxies found in the deepest field surveys. Although not yet constituting a statistically-complete sample, their colour distribution shows no evidence of any bias arising from surface brightness or ultraviolet selection effects peculiar to the lensing process. As such, they can be regarded as a useful sub-sample of very faint field galaxies.

• From a number of independent approaches we show that the distribution of intrinsic K luminosities of the arcs indicates the sources are marginally less luminous in K than a field sample to z$\simeq$0.5. This evolution is primarily evident as a deficit of luminous galaxies in the arc sample compared to the local field. Using a model devised to account for the B and K number counts and the observed B selected N(z) we can adequately reproduce the observed strength of evolution. Depending upon their subsequent star formation these systems may either appear as faint red dwarf systems or large star forming spirals at the present epoch.

• The optical-infrared colours of the giant arc sample shows strong evidence for enhanced star formation. The blue colours cannot, however, arise from secondary bursts superimposed upon pre-existing evolved systems. Neither can the star formation seen be a dramatic single event associated with galaxy formation. Such an event in massive systems would render typical sources visible in current deep spectroscopic field surveys. Most likely we are witnessing an extended formation phase which culminates at redshifts $z \simeq 1$. If correct, we would not expect to see any features in the galaxy counts associated with the formation phase to $B \simeq 26$.

5 STATISTICAL GRAVITATIONAL LENSING OF THE FAINT GALAXY POPULATION

5.1 Introduction

In the previous chapters we have explored the possible application of gravitational lensing to determine both the redshift distribution of the faint blue galaxy population and the mass distribution in the lensing clusters. In this chapter we extend this study to an observational field which promises to provide the strongest constraints on both of these areas. This field is the study of the weak distortion of distant galaxies by massive foreground clusters (Tyson *et al.* 1990). The distortion has a coherent pattern in the form of an alignment of the elongated galaxy images, perpendicular to the local radius vector. In the ideal case of a circular lensing potential this results in an excess of objects aligned tangentially to the radius vector from the cluster centre (Figure 8.1, Appendix A). This alignment can be used as a tracer to study the statistical properties of galaxies seen through the lens. The strength of the alignment signal depends upon both the redshift distribution of the source galaxies ($N(z)$) and the mass profile of the cluster ($M(r)$). By studying a well defined sample of clusters at different redshifts we intend to decouple these two effects to independently study the $N(z)$ and $M(r)$. The statistics we use require a functional form for the faint galaxy $N(z)$ and to this end we will test a number of theoretically-motivated $N(z)$

against a null hypothesis: that the galaxies are distributed as predicted by a no evolution model.

We chose to test three redshift distributions – the no evolution model ('N.E.'), one shallower than the no evolution model ('Shallow') and one deeper ('Deep'). The form of the Shallow model follows the no evolution prediction until $I = 21$, beyond this the galaxies are distributed as in the $I = 21.5$ N(z). This model is motivated by both observations and theory. Preliminary results from deep spectroscopic samples are interpreted (Cowie *et al.* 1991) as showing that the excess galaxies seen in the number counts consists of star forming dwarf galaxies at intermediate redshift ($z \sim 0.2$-0.4) – this is the so-called second population hypothesis. In the model of Babul & Rees (1992) these bursting dwarf galaxies are triggered by changes in the UV background – allowing large numbers of these systems to form in a relatively small redshift interval at these recent epochs. This is shown in Figure 5.1(b) – the median redshift of the Shallow model does not increase as the observations go deeper.

Redshift distributions close to the no evolution case are predicted by two of the models refered to in Chapter 1. These models are the burst model proposed by Broadhurst *et al.* (1988) and the merger model of Broadhurst *et al.* (1992). Both of these models are specifically conceived to recreate both the no evolution N(z) observed in faint spectroscopic samples and the slope of the number counts using physically plausible mechanisms. The merger model is also consistent with the observations presented in Chapter 4 for the evolution in the mass of galactic systems with redshift.

Finally, the Deep model represents any model with a large fraction of the faint galaxy population beyond $z = 1$ – where our most distant cluster lies. This model is a combination of theoretical predictions of the distribution of galaxies at faint limits and the observed distributions at brighter magnitudes ($I \leq 23$). The theoretical distributions used are from
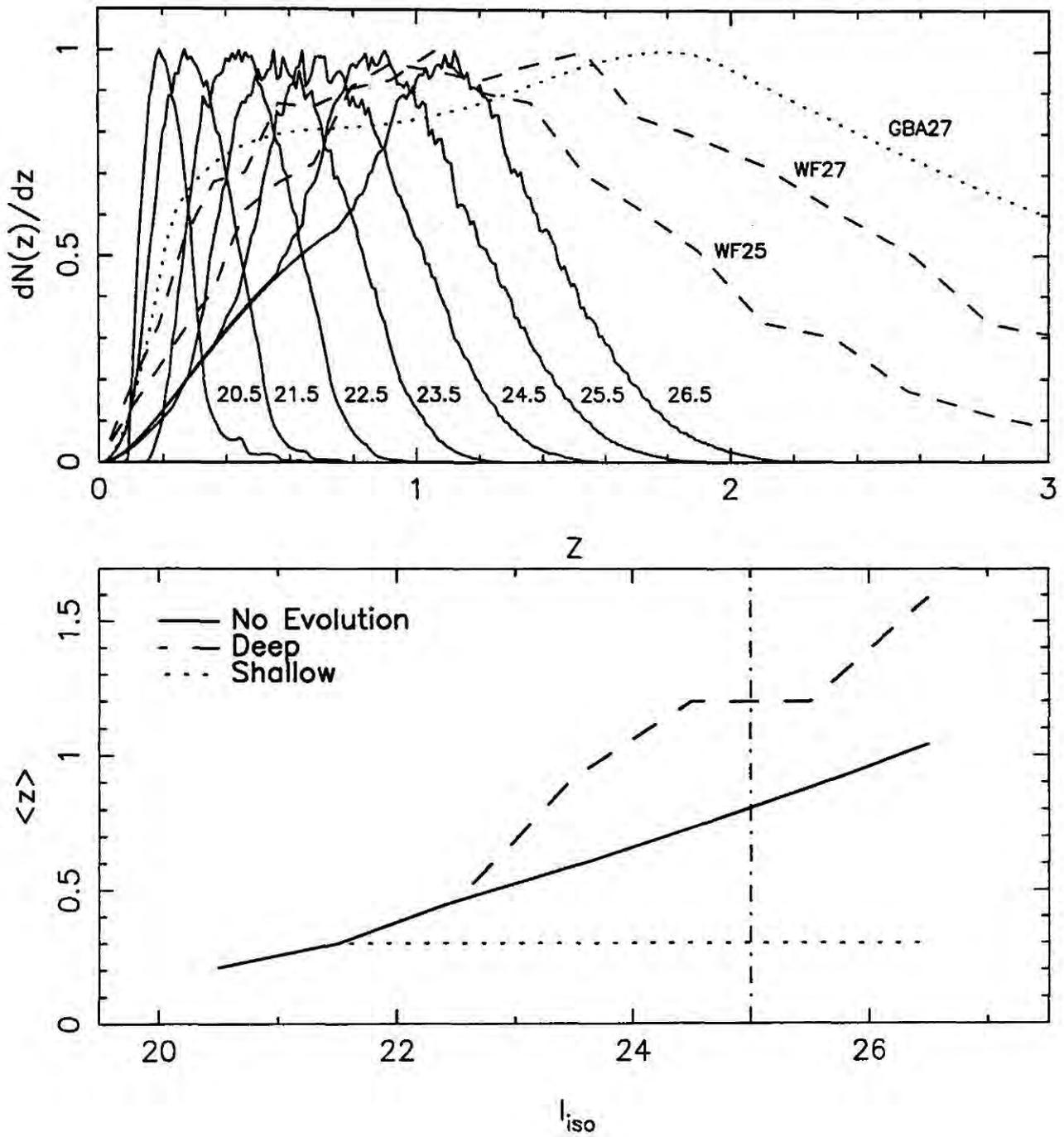
Figure 5.1 (a) The various normalised redshift distributions used in the analysis. The dashed curves marked WF25 and WF27 are the B_j =25 and B_j =27 distributions from White & Frenk 1991. The curve shown as dotted is a Bruzual B_j =27 cumulative $N(z)$. The remaining solid curves show the no evolution differential $N(z)$ centred on the I magnitude marked – these were calculated for observations in R band and then converted using a fixed colour term. (b) The run of median redshift with I magnitude for the three hypotheses.

White & Frenk (1991). This paper uses a hierachical model for galaxy formation and self-consistent models for star formation within the galaxies to predict the distribution and number of galaxies as a function of magnitude. The White & Frenk models have been crudely transformed from B_j to I using a fixed colour term. As our tests are unlikely to be sensitive to anything more than the median redshift of the cumulative distributions such simplifications are allowable. For the Deep distribution the Bruzual model is used to describe objects fainter than the catalogue limit – the reason for this is explained below. The White & Frenk distributions were kindly provided by Carlos Frenk, while Nathan Roche produced the Bruzual model. The cumulative Deep $N(z)$ is also reasonably representative of the predictions of pure luminosity evolution models (Koo & Kron 1992) given the probable sensitivity of our tests.

Our study was designed to both extend the results of Tyson *et al.* (1990), detailed in Chapter 1, by creating a large robust sample of faint galaxies and apply a variety of new analytic techniques to this sample. In particular in the analysis undertaken by Tyson *et al.* the redshift distribution of the faint field galaxy was fixed. The signal we are attempting to measure is intrinsically weak and so great care must be taken to remove systematic sources of error. In addition the complexity of the analysis requires that in order to fully model all possible sources of error, we need to simulate images of clusters, including all likely observational effects (seeing, crowding, etc.). These are used to calibrate the statistics which are applied to the actual datasets. Tyson *et al.*'s sample was selected in a blue band, taken under conditions of average seeing using B and R or I observations of two clusters. Even at relatively low redshift the B band becomes highly sensitive to the amount of current star formation in the galaxies sampled. Our intention is firstly to produce a well-defined deep sample of galaxies selected in a red passband to circumvent possible star formation biases, complete with long baseline colours to allow removal of contamination by cluster members. The surface density of sources must be high enough

to allow resolution of possible substructure in the cluster mass distribution. The minimum detectable induced ellipticity in a background galaxy is a strong function of both the seeing and the image sampling. It is therefore critically important that the observations are well sampled and taken in very good conditions.

A plan of this chapter follows: in Section 2 we describe the sample selection. Section 3 details the data acquisition and reduction. In Section 4 we discuss the object catalogue construction selection and analysis using the FOCAS image analysis package. While in Section 5 we describe the modelling with the discussion of results from the catalogues in Section 6 and the conclusions in Section 7.

5.2   Cluster and Sample Selection

The long integration periods of 4m dark time required to produce reliable samples of faint galaxies precludes the observation of more than a handful of clusters. The choice of telescope was determined by both the aperture, the site and the available instrumentation. Given that the seeing in the passband used for object selection must be sub-arcsecond and the need to critically sample the seeing disk – we have a maximum allowed pixel scale of 0.3 arcsec, preferably over a wide field. The only available site which can guarantee consistent sub-arcsecond seeing is La Palma, the telescope used was therefore the William Herschel Telescope (WHT). The TAURUSII imaging Fabry-Perot acting as an f/4 focal reducer is capable of providing 0.27 arcsec/pixel sampling over a 5 × 5 arcmin field, making it ideally suited to this project.

The choice of passbands was determined by both the need for a long colour baseline and the sensitivity of the available large format CCDs. These were GEC EEV's which have

Table 5.1 WHT Cluster Sample

Cluster	z	R.A. (1950)	Dec. (1950)	L_X	σ_{cl}	Scale (kpc/arcsec)
Cl1455+22	0.259	$14^h 55^m 00\overset{s}{.}6$	$22°32'20\overset{''}{.}7$	$1.60\ 10^{45}$	~ 700	5.0
Cl0016+16	0.546	$00^h 15^m 56\overset{s}{.}0$	$16°09'36\overset{''}{.}0$	$1.43\ 10^{45}$	1324	7.4
Cl1603+43	0.895	$16^h 02^m 45\overset{s}{.}0$	$43°12'54\overset{''}{.}0$	$1.1\ 10^{44}$	—	8.4

excellent cosmetic properties but relatively low sensitivity in the blue. This necessitated our using V and I observations rather than the prefered longer baseline B and I. To reach a surface density of objects of 40 arcmin^{-2} in the I band requires a completeness limit of $I = 25$ (Lilly et al. 1991). To ensure accurate colours for the bulk of the galaxies seen at these faint limits ($V - I \sim 1.5$) requires a V completeness limit of $V = 26.5$. We need the detections of the faintest objects to be good enough to estimate robust image parameters for the object. This translates into a requirement that the average signal to noise per pixel for the image exceed 2.5 over the galaxy's area. For a galaxy with FWHM of 1.5 arcsec that corresponds to 50 sigma (measured pixel to pixel). To achieve this signal to noise at the quoted completeness limits with WHT+TAURUSII+EEV requires integrations of 20 ksec in I and 10 ksec in V. Given our maximum likely allocation of dark time from PATT of 6-8 nights this restricted us to observations of only three clusters even when using in-field dithering to create the sky flatfield frames.

The choice of the three clusters depends upon the hypothesis to be tested. The clusters must be massive and preferably regular systems at three different redshifts, available from the northern hemisphere. Current moderate and high-z cluster samples have been constructed either from peaks in the projected surface density of galaxies identified in optical surveys (Abell 1958, Gunn et al. 1989, Couch et al. 1991) or serendipitous deep X-ray observations (Henry et al. 1992).

Strong negative evolution has been claimed for the number density of luminous X-ray clusters at relatively low redshifts (Edge et al. 1990), in contrast to that for rich optically-selected clusters (see Kaiser 1992). Nevertheless, X-ray observations hopefully provide us with a tracer of the most massive systems at any given epoch. Additionally the X-ray catalogues should be less sensitive to projection effects. We therefore chose our low Cl1455+22 ($z = 0.26$) and intermediate redshift Cl0016+16 ($z = 0.55$) clusters on the basis of their X-ray luminosities – they being respectively the first and third most luminous

clusters in the EMSS sample (Henry *et al.* 1992). The choice of our final high redshift cluster was determined by our desire to test evolutionary models then in vogue which predicted a large fraction of faint galaxies should lie at high redshift (Chapter 1). As illustrated below the strongest test of these models is obtained by using a $z \sim 1$ cluster, there is only one good candidate for a cluster at this redshift: Cl1603+43 ($z = 0.89$) from the survey of Gunn *et al.* (1989). Recent deep ROSAT observations of this cluster confirm its reality and support our choice. For our three model N(z)'s the following proportions of $I \in [20, 25]$ galaxies lie behind the three clusters (Cl1455+22, Cl0016+16, Cl1603+43): Shallow (63%, 2%, 0%), N.E. (96%, 69%, 20%) and Deep (97%, 83%, 65%). The Deep N(z) is qualitatively close to that proposed by Tyson *et al.* (1990) with $\sim 70\%$ of the $B_j \leq 26$ population beyond $z = 0.9$. We list details of the three target clusters in Table 5.1 the X-ray luminosities are in ergs/sec and the velocity dispersions are in km/sec.

5.3 Observations and Data Reduction

The observations were made in two runs in July 1990 and May 1991 on the WHT. The first run produced data which was photometric with very good seeing. However, during the second run the seeing deteriorated and exceeded the project limit for the final part of the run, as a result less data was taken. However, the data from the first part of this run is of very good quality. As we use the I band data for image analysis the seeing on these frames is the important quantity – for all three clusters the seeing measured off the final frames is sub-arcsecond. The observing technique employed was to take multiple $\lesssim 1000$ sec exposures of the target clusters in one passband each night. These exposures were dithered on a rectangular grid with 10-15 arcsecond spacing. With two clusters imaged each night the data frames can be used to create a sky flatfield for the entire night which

Table 5.2 Observing Logs

WHT Run #1 Observing Log						
Cluster	Filter	R.A. (1950)	Dec. (1950)	Date	Seeing	Exposure (s)
Cl0016+16	V	$00^h15^m56\!\!.\!\!^s0$	$16°09'36\!\!.\!\!''0$	21/22 July 1990	$1\!\!.\!\!''05$	11000
Cl0016+16	I	$00^h15^m56\!\!.\!\!^s0$	$16°09'36\!\!.\!\!''0$	22/23-24/25 July 1990	$0\!\!.\!\!''95$	25500
Cl1603+43	V	$16^h02^m45\!\!.\!\!^s0$	$43°12'54\!\!.\!\!''0$	21/22 July 1990	$1\!\!.\!\!''00$	9000
Cl1603+43	I	$16^h02^m45\!\!.\!\!^s0$	$43°12'54\!\!.\!\!''0$	22/23-24/25 July 1990	$0\!\!.\!\!''90$	20500

Telescope:	4.2m WHT
Instrument:	TAURUSII f/4
Detector:	GEC EEV (880 × 1180 pixels)
Pixel size:	$0\!\!.\!\!''27$ /pixel

WHT Run #2 Observing Log						
Cluster	Filter	R.A. (1950)	Dec. (1950)	Date	Seeing	Exposure (s)
Cl1455+22	V	$14^h55^m00\!\!.\!\!^s6$	$22°32'20\!\!.\!\!''7$	11/12-12/13 May 1991	$1\!\!.\!\!''00$	12000
Cl1455+22	I	$14^h55^m00\!\!.\!\!^s6$	$22°32'20\!\!.\!\!''7$	11/12-12/13 May 1991	$0\!\!.\!\!''90$	20850
Cl1603+43	V	$16^h02^m45\!\!.\!\!^s0$	$43°12'54\!\!.\!\!''0$	13/14 May 1991	$1\!\!.\!\!''5$	11500
Cl1603+43	I	$16^h02^m45\!\!.\!\!^s0$	$43°12'54\!\!.\!\!''0$	12/13 May 1991	$0\!\!.\!\!''85$	4800

Telescope:	4.2m WHT
Instrument:	TAURUSII f/4
Detector:	GEC EEV (1280 × 1180 pixels)
Pixel size:	$0\!\!.\!\!''27$ /pixel

can then be used to process the images. Numerous shorter exposures of standard stars were also taken at regular intervals through out the night to track variations in the transparency of the atmosphere. Finally, in twilight at the beginning and end of the night exposures were made of blank fields to facilitate flatfielding. The atmospheric transparency at La Palma is very stable and this is shown by the photometry – the zero point errors on the final frames are all below 0.01 mag. This stability also ensures that the master flatfield created each night is representative of the entire night.

The reduction of in-field dithered images is a more complex affair than normal image reduction, especially when the images are of a rich cluster, with the many bright galaxies that such a system includes. The reduction consisted of the following steps:

1) Bias subtraction and trimming – the median bias level for each exposure was obtained from the overscan regions of the chip and subtracted off. The images were then trimmed to remove the overscan strips.

2) Initial flatfielding using the twilight flatfields. These removed the bulk of the large scale gradients that were obvious on the exposures (vignetting, etc).

3) An object detection algorithm (FOCAS, Jarvis & Valdes 1981) was used to remove all the bright objects in the field and replace them with random sky values drawn from regions around the objects. This process succeeded in removing most of the flux from bright stars and galaxies in the final cleaned frame.

4) These cleaned frames were then combined using a broad median algorithm to give an image containing both the pixel-to-pixel sensitivity variations and any residual large scale variations from the mismatch of the twilight flatfield and the actual flatfield.

5) The pre-cleaned images were then flatfielded using this sensitivity image to produce the final reduced images.

At this point a problem was detected. A comparison of offset frames of the same field after aligning showed large mismatches between the positions of objects near the frame edge. This was a result of the focal reducer not correcting the optical distortion over the entire field covered by the chip. The net result of this is that images of the same field taken at two different pointings on the sky will show positional variations of ~ 1 arcsec for objects near the chip edge. These errors increase outwards from the chip centre and when combining images with different pointings using a shift-and-add method it drastically reduces the image quality off-axis. The solution was to geometrically remap every image to coincide with one fiducial reference frame, these could then be combined to give final images for each passband. The remapping used the positions of a large number ($\gtrsim 100$) of objects distributed over the frame to define a spline surface for each of the X and Y distortion vectors. This vector map was then applied to the data in conjunction with a linear interpolation routine to correct for the distortion. The remapping successfully removed the distortion to a level below 0.1 arcsec over the entire frame.

Unfortunately, the remapping then introduces large scale variations in the sky level – because the original flatfield applied contained effects due to both vignetting and the field distortion. By applying the flatfield we have effectively 'corrected' for the effects of the field distortion on the sky brightness – so that when we finally remove the focal corrector distortion we reintroduce variations in the sky level. These variations are removed by a multiplicative correction. To calculate the correction we again removed all objects from the frames using FOCAS and replaced them with sky values. The cleaned frame was then smoothed with a large median filter and the remapped frame divided by this image to correct for the sky distortion.

These processed frames are then suitable for combination using a broad median algorithm with an additive scaling offset to account for variations in sky brightness. The broad

median algorithm is less efficient than a pure average but has the advantage that it removes all cosmic-ray events and makes more efficient use of the data than a normal median.

We then have two final frames, one in each passband, for each of the three clusters. The 1 sigma isophotal limits for the shallowest data in each of the two bands are: $\mu_V = 28.9$ mag/arcsec^2 and $\mu_I = 27.8$ mag/arcsec^2. The next step is to create catalogues of objects detected in these images. Once again we turn to the FOCAS image analysis package.

5.4 Catalogue Selection and Sample Analysis

The size and depth of the frames obtained are such that, when optimising the analysis technique, it is far quicker and easier to run tests on a small, but representative, region of the whole field. The regions chosen in each cluster were random 1×1 arcmin fields (Figure 5.2). The object detection algorithm used by FOCAS is described in detail in Jarvis & Tyson (1981). The two main parameters which control the detection characteristics of the algorithm are the threshold cut (in units of the global sky sigma) and the minimum object area (in pixels). Here we just state the main features of the technique:

Sky Estimation: Starting from an initial estimate based on the first few lines of the image FOCAS builds up a coarse map of the sky values in the image. Pixels belonging to both bright and dark objects are excluded from the sky estimate.

Object Detection: The image is then filtered using a built-in 5×5 filter and thresholded at a level above the local sky. The threshold is calculated using the global sigma of the sky and the input threshold cut. An object is a region with a number of connected filtered pixels above the threshold value, only objects with at least the minimum area requirement
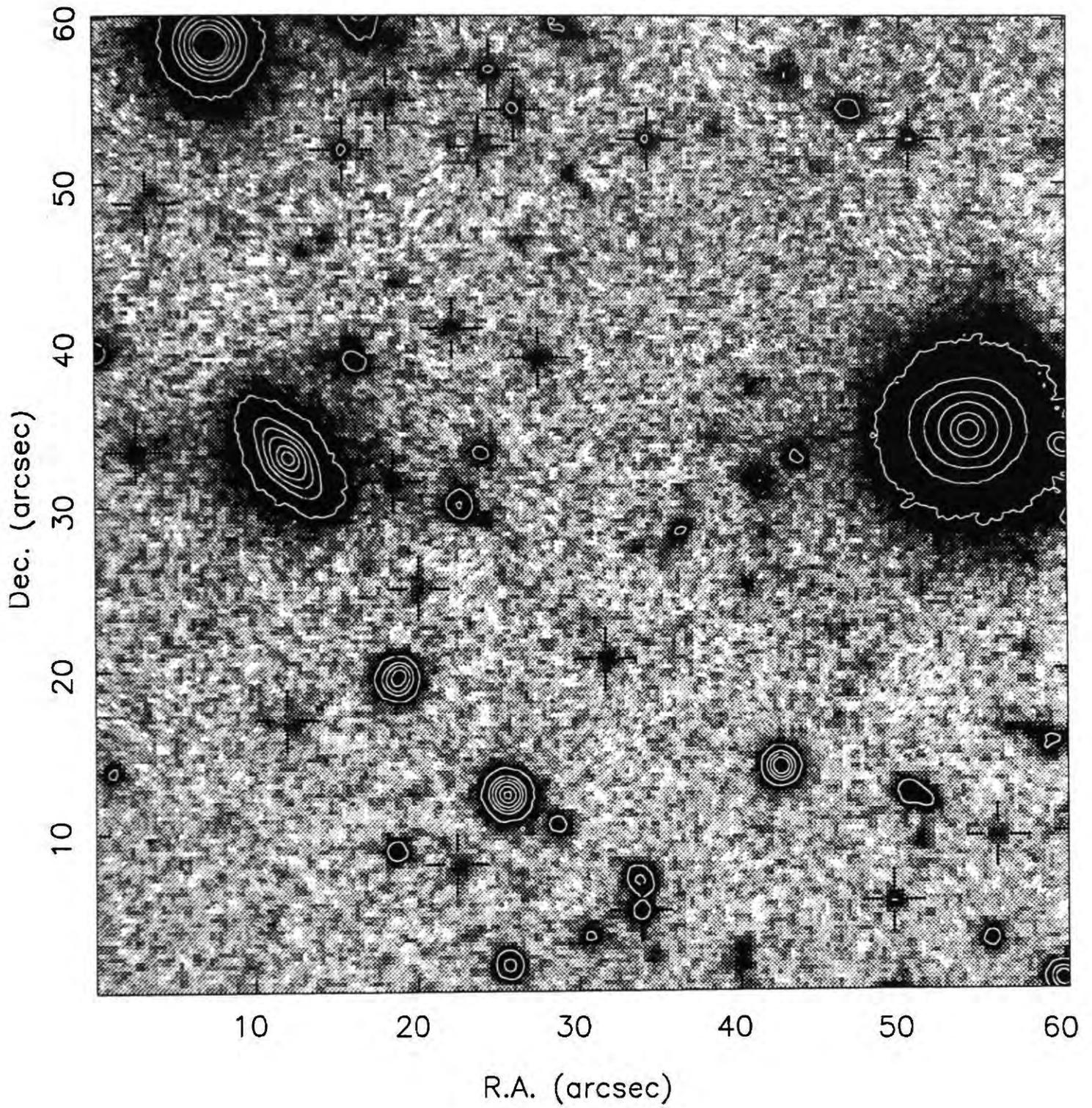
Figure 5.2 A 1×1 arcmin test area in the Cl1455+22 frame. This is a 20.8 ksec I exposure with 40 objects detected above $I = 25$. Those objects in the faintest analysis sample ($I_{iso} \in 24 - 25$) are marked.

are retained. Objects are also detected as negative fluctuations from the sky level – these are termed 'dark' objects.

Object Evaluation: The object parameters (magnitudes, second moments, etc.) are now evaluated using an improved local sky estimate.

Object Splitting: FOCAS then attempts to split every image by thresholding the image at brighter and brighter isophotal contours and determining if the image breaks into multiple peaks or not. If the image does split each of the fragments is classed as an object, evaluated and the splitting continued.

Object Classification: Finally all the detected images are compared with a fiducial stellar point spread function using a multi-dimensional non-parametric test on their intensity maps to determine its classification. The default classes available are: star, galaxy, stellar feature, noise, long and diffuse.

Catalogue Merging: Having produced a catalogue for each passband we then merge these by pairing the nearest detected objects in each catalogue, subject to the requirement that they are closer than 1 arcsec. Unpaired images are discarded. This produces a final matched catalogue of objects detected in both frames.

The search parameters were optimised by repeated analysis of the test regions. The catalogues were visually checked for the success rate of detecting very faint objects compared to spurious detections. The optimal combination of search parameters finally chosen was a threshold of 2.5 sigma per pixel over 10 pixels. This corresponds to roughly a 25 sigma detection within the seeing disk – measured in terms of the pixel-to-pixel variation. We performed the object detection on the coadded $V + I$ images, these were combined so that a flat spectrum object (whose colour is typical of the faintest field sources) has equal flux contributions from each filter. Tests showed that this approach both provides a fainter

detection limit for images and improves our ability to detect objects with very extreme colours. The second point is illustrated in the colour-magnitude diagrams for the three clusters (Figures 5.5, 5.8 & 5.11) which show that we successfully detect faint very red objects in part of the plane far beyond the pure V detection limit. After initial detection on the $V + I$ image the object areas are evaluated and analysed from the individual V and I images. These catalogues are then merged to create a final list of objects detected in both images. Standard aperture photometry in a 3 arcsec aperture was then performed on all the detected objects using seeing-matched images and aperture colours calculated. We choose to measure colours in apertures to overcome possible differences in the object isophotes in the two frames. The important parameters for each object are then its position, intensity weighted second moments calculated from the better seeing I image, isophotal I magnitudes and $V - I$ aperture colours.

Simulations were performed to determine the effective completeness limit for the detection of a compact image in each of the two passbands for each cluster. We create a representative high signal to noise faint galaxy by median combining a large number of faint galaxy images from the data. This can then be scaled and repeatedly added into a region of the cluster frame, the detection process is then run and the success of detection of the images as a function of magnitude gives the completeness limit for the catalogue. We then apply a fixed I isophotal magnitude cut to all three cluster catalogues so that we can compare the same well-defined redshift distribution for all clusters. The drawback with this approach is that the detection limit only applies to objects with profiles similar to those already detected.

We illustrate in Figure 5.2 one of the random 1×1 arcmin test fields, from the Cl1455+22 field. There are 40 objects brighter than $I_{iso} = 25$ in the field and we have marked those with $I_{iso} \in 24 - 25$. The lensing technique relies upon our ability to robustly estimate the ellipticities of these faint objects. The problem of measuring reliable ellipticities for

faint objects has already been tackled (Bernstein priv. comm.) but an ideal solution has yet to be found. The main criticism of the use of intensity weighted second moments to estimate the ellipticity and orientation of an object is that they are dominated by the noise on the outer image isophote – this is illustrated by the fact that for the faintest objects they give very similar results to the unweighted moments. To circumvent this we do two things: instead of using the detection isophote to define pixel membership for an object we use a circular aperture and to reduce the noise from the outer regions we apply a radial weighting function when calculating the second moments in this aperture. The optimal weighting function for a particular object has the same profile as the object. To simplify matters the weighting applied was a generic circular gaussian with a variable width, the width being determined from the intensity weighted radius of the object broadened by convolving with the seeing.

We undertook two separate tests to estimate both our ability to measure the ellipticities of $I = 25$ galaxies using simulations and the scatter in an individual measurement from two independent observations of one field. The simulations consisted of the analysis of a large number of artificial frames populated by objects with known ellipticities. For the comparison test the individual exposures comprising the final Cl1455+22 I frame were arranged to create two independent frames each with a total exposure time of 9.5 ksec. These were then analysed and the resulting catalogues matched to allow comparison of the measured image parameters (Figure 5.3). Both of these tests have drawbacks – the simulation results are dependent upon the form of the galaxy profile used, while the real observations are by necessity only half as deep as the final image.

In the simulations the raw FOCAS ellipticities provide an unbiased and relatively accurate estimate of the input object ellipticity ($< \Delta\epsilon >= 0.16$). While the optimally-weighted ellipticities are systematically rounder by about 0.1 than the input (Figure 5.3). However, the comparison test showed that the weighted ellipticities had a roughly four-fold reduction
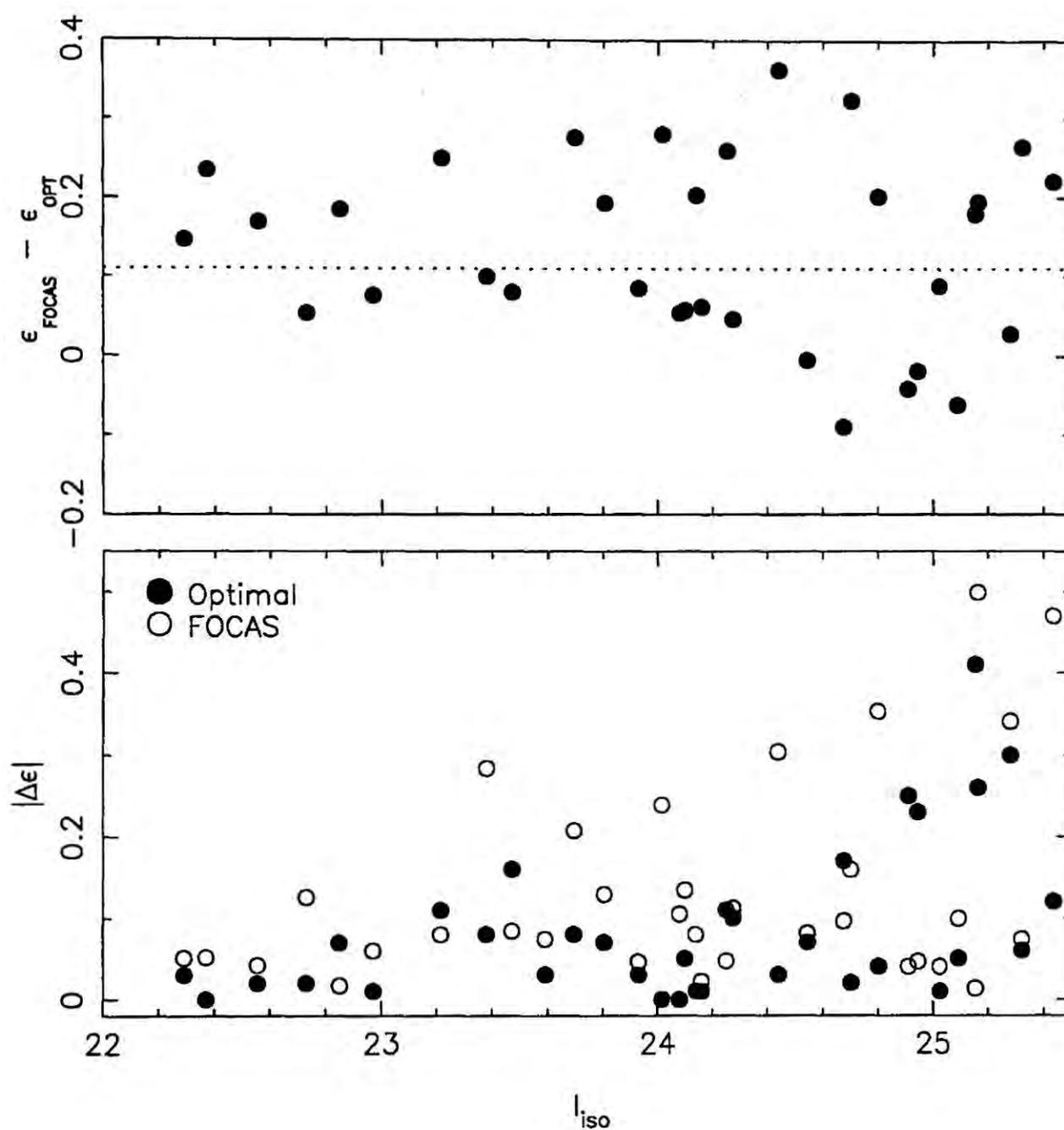
Figure 5.3 The two panels show the comparison of the raw (FOCAS) and optimally weighted ellipiticites for the Cl1455+22 test area. The top panel illustrates the systematic offset (dotted line) introduced in the ellipticity measurement when using the optimal weighting scheme. The lower panel compares the ellipticities of objects measured on the two independent frames. It is apparent that the optimal weighting reduces the scatter in individual ellipticity measurements for $I_{iso} \in [24, 25]$ objects.

in the scatter in the ellipticities measured for an object from both frames ($<\Delta\epsilon>= 0.04$ versus $<\Delta\epsilon>= 0.16$ for the objects with $I_{iso} \in 24-25$). A similar reduction in scatter and introduction of a systematic offset was reported by Bernstein. We therefore chose to use the optimally-weighted moments in our analysis where we could model the systematic effects on the measured ellipticity (*e.g.* simulated images), otherwise we use the raw FOCAS moments – the 15-20% errors in these measurements are small enough that a coherent distortion should be observable with the large number of galaxies sampled.

5.4.1   Cl1455+22

This cluster was discovered as a serendipitous source in the EINSTEIN Medium Sensistivity Survey (Henry *et al.* 1992). The identification of this source was a subject of some dispute, initially being identified using broad-band colours as a $z = 0.7$ cluster (Schild *et al.* 1980) and subsequently being associated with a spectroscopically identified $z = 0.259$ cluster (Mason *et al.* 1981). The latter group measured redshifts for four cluster members including the central dominant galaxy ($z =0.258$), which give a velocity dispersion of only $\sim$700 km/sec. With such a small sample it is impossible to get a fair estimate of the true velocity dispersion. Simulations show that with only four members it is possible to get the observed dispersion from a sample with an intrinsic dispersion of 1500 km/sec 40% of the time. In contrast to the apparently low velocity dispersion the cluster redshift gives it a very high intrinsic luminosity of $L_x \sim 1.598\ 10^{45}$ ergs/sec in the 0.3–3.5 keV band. The cluster was part of a proposal for deep ROSAT High Resolution Imager observations in parallel to our gravitational lensing study and Sunyaev-Zel'dovich observations with the Ryle Telescope. The latter observations have been delayed due to problems with the system development of the telescope. The ROSAT observations were undertaken, although the spacecraft had a gyro failure during the exposure resulting in a total integration of only 4 ksec compared to the requested 20 ksec – the remaining part
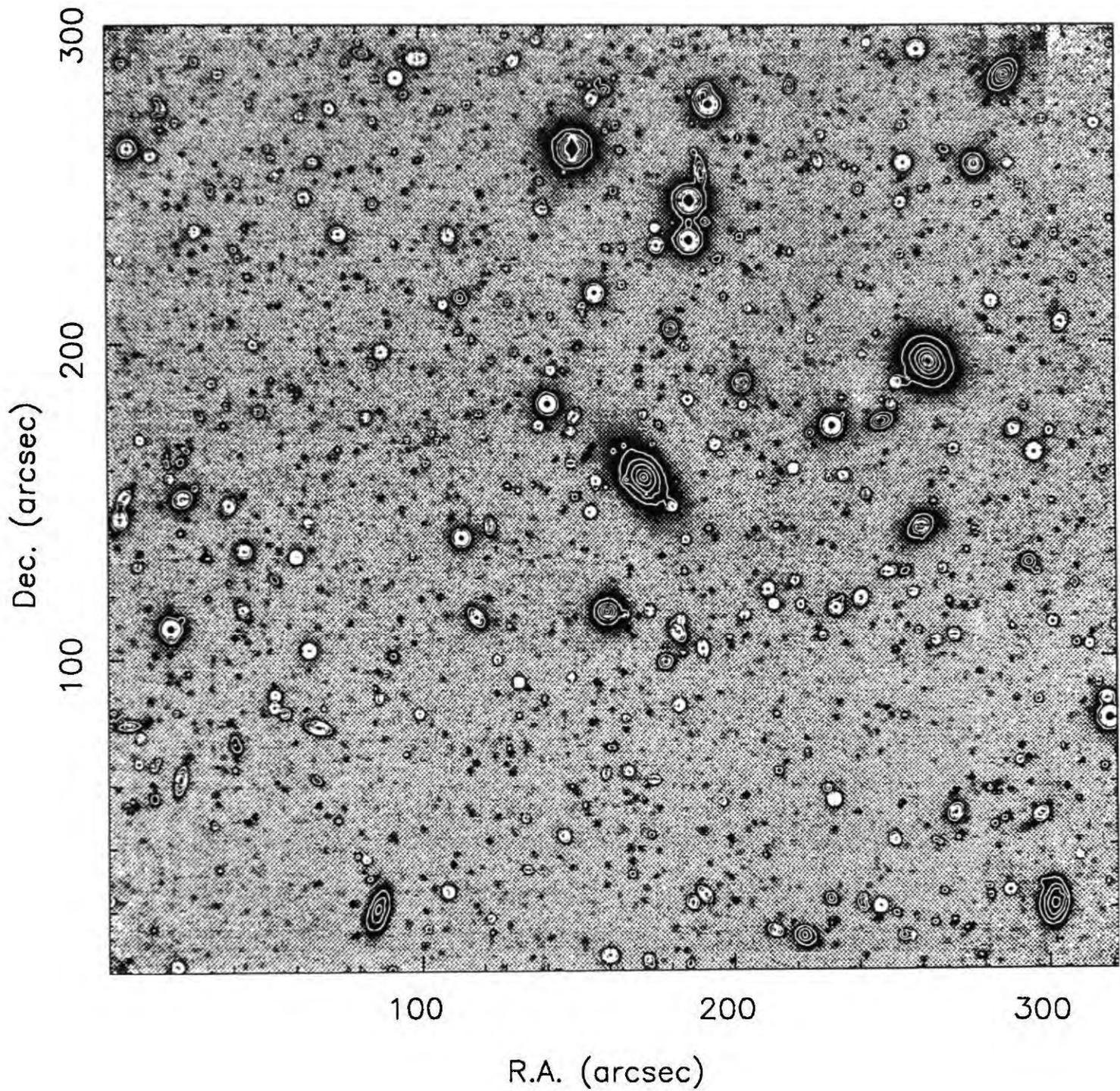
Figure 5.4 A composite $V + I$ image of the cluster Cl1455+22 (z =0.26). The total exposure time is ~33 ksec and the scale is in arcseconds with east to the left and north at top. The faintest reliable detections have $B \simeq 28$.

of the exposure is planned for early 1993. The present data is therefore unusable for the original intention of detecting very low luminosity features associated with substructure in the cluster. However, we can still derive a reliable gas profile for the cluster.

The reduction and analysis of the ROSAT observations was kindly undertaken by Alastair Edge at the IOA: for details of the analysis procedure see Arnaud (1988). The main assumption of the X-ray analysis is a form for the profile of the cluster potential well – this is a King profile with a core radius of 230 kpc – the canonical value from low redshift clusters. Below we test this assumption through a direct comparison of the predicted mass profiles from the lensing and the X-ray gas. The analysis deprojects the X-ray surface brightness distribution assuming a given potential. A large cooling flow is detected associated with a strong extended source centred close on the cD ($L_{bol} \sim 1.97\ 10^{45}$ ergs/sec) with $\dot{M} = 530^{+301}_{-976} M_\odot/yr$ within a cooling radius 210±76 kpc. Such a strong inferred cooling flow is relatively rare ($\lesssim 5\%$ of rich clusters) and may indicate that the cluster is both massive and dynamically stable. Combined with the sharply peaked central potential associated with the cD this makes this cluster a very good candidate for deep lensing studies.

The cluster shows a well defined tight colour-magnitude relation ($\sigma = 0.05$ mag, Figure 5.5) which extends into the bulk of the field population. The 80% completeness limits for the I and V catalogues are $I = 25.3$ and $V = 26.5$. The chosen limit of $I = 25$ then corresponds to a 17 sigma detection in the seeing disk. To remove the cluster members from the sample we must first determine how faint the cluster reaches. This faint magnitude cut-off for the cluster colour-magnitude relation was determined by a comparison of the object density on the colour-magnitude plane for Cl1455+22 with that for Cl0016+16 and Cl1603+43 after scaling the total number of objects in the region blueward of $V - I = 1.5$ and brighter than $I = 25$ to be the same in all frames. This shows no excess in the field beyond $I = 22$ associated with galaxies on the colour-magnitude relation. Those galaxies lying on
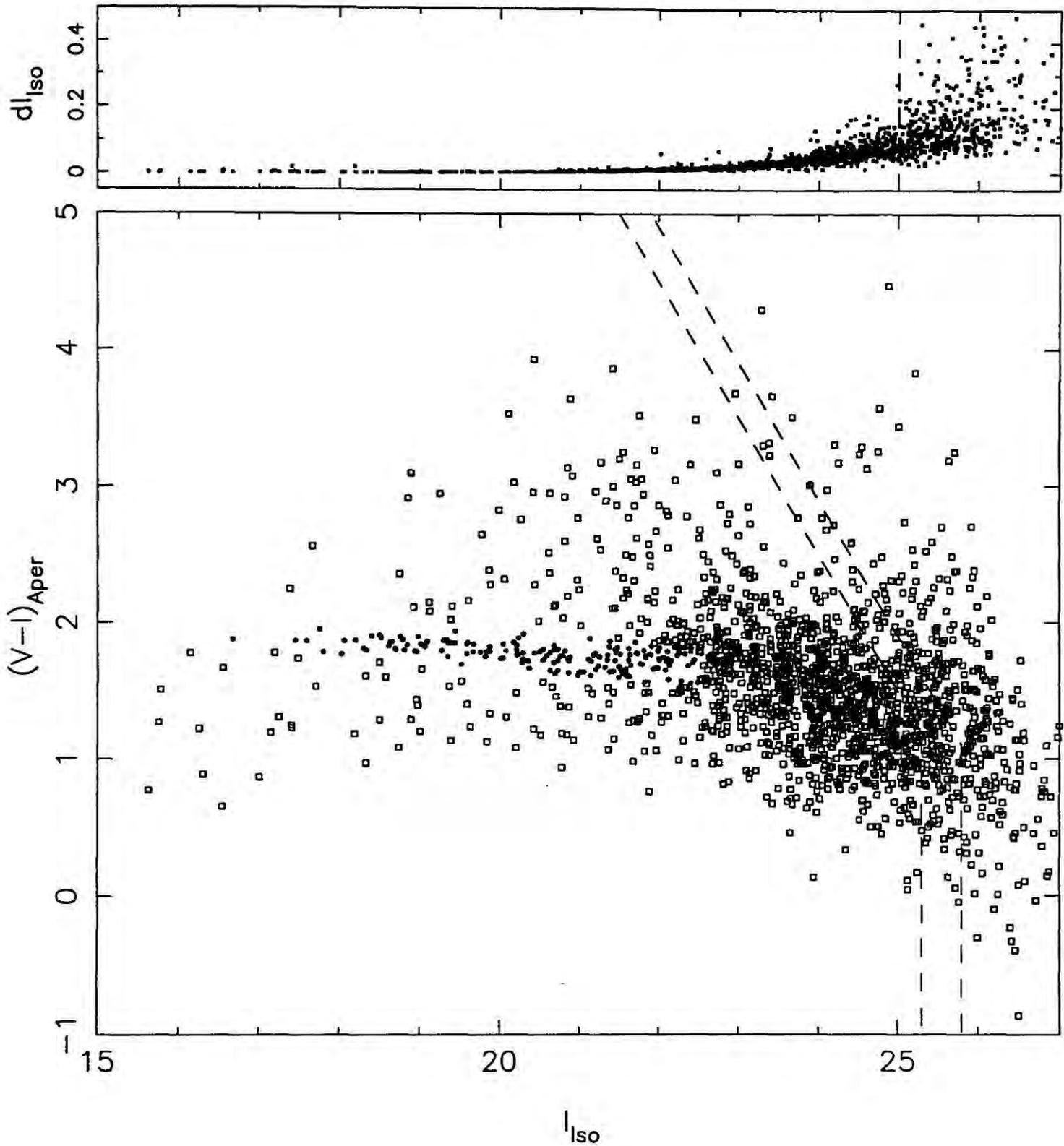
Figure 5.5 The $V - I$ colour-magnitude diagram for the cluster Cl1455+22. Galaxies with colours similar to an E/S0 in the cluster are shown (•), as well as the 80% and 50% completeness limits for the catalogue, calculated from simulations. Also shown are the photometric errors as a function of magnitude for the entire sample, the line marked is the chosen magnitude limit for the final sample $I = 25$.
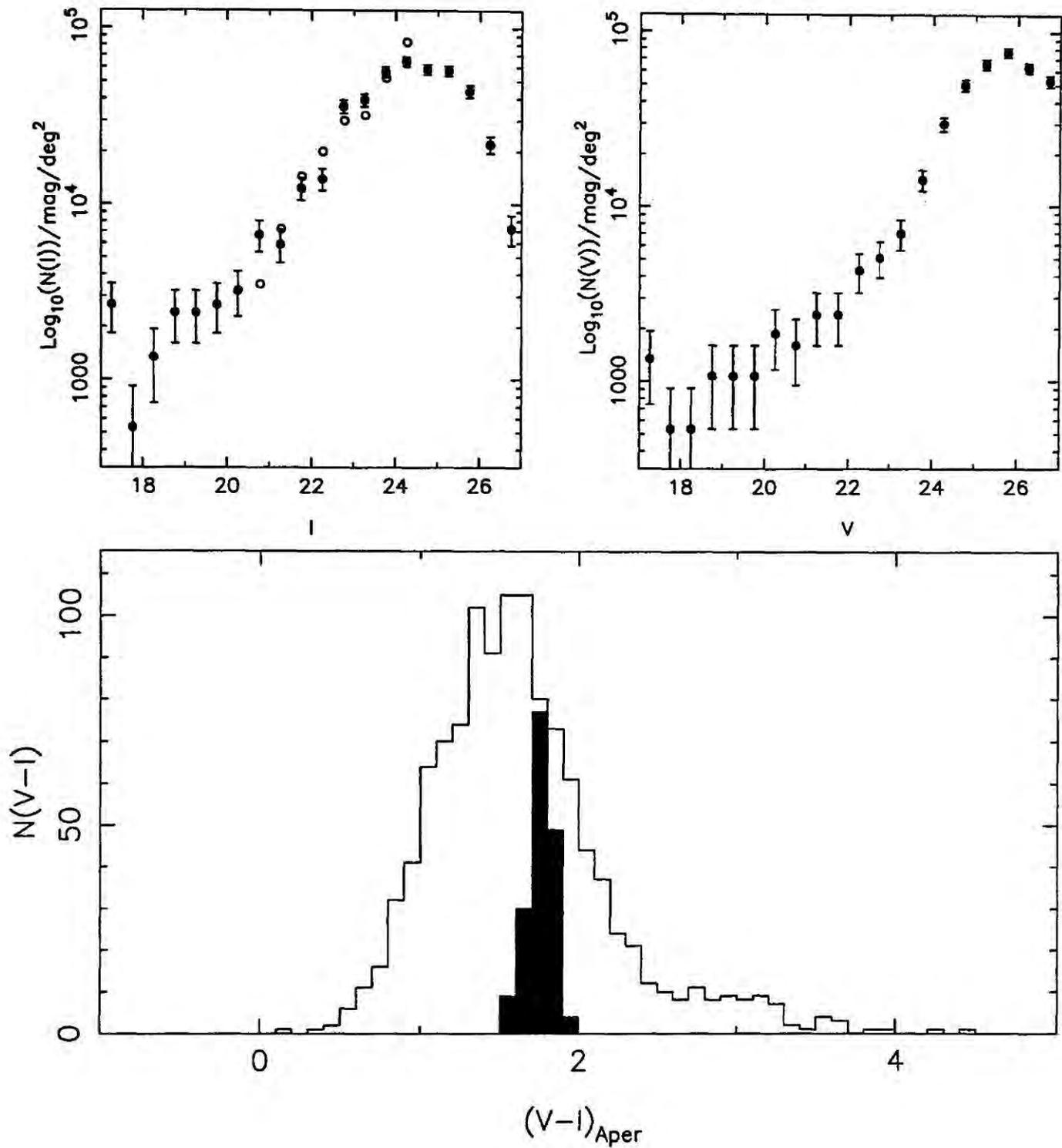
Figure 5.6 a) Differential number counts in I and V of Cl1455+22 after removal of the cluster members ($\bullet$) compared to the Lilly *et al.* (1991) field counts ($\circ$). b) $V - I$ Colour distributions for the cluster (filled) and field galaxies (open) brighter than $I = 25$.

the colour-magnitude relation to $I = 22.5$ were classed as cluster members and removed, the remainder being termed the field sample. Figure 5.6 shows that both the slope and normalisation of the I field sample counts agrees well with that measured from blank fields surveys (Lilly *et al.* 1991) supporting the view that we are successfully removing the bulk of the contamination due to cluster members.

The cluster sample contains $\sim$180 galaxies brighter than $I = 22$ over the 5×5 arcmin field with colours similar to those of an unevolved E/S0 at the cluster's redshift. Of these only 17 have I magnitudes in the range $[m_3, m_3 + 2]$ and lie within 500 kpc of the centre, compared to the value for Coma of 28 (Bahcall 1981) this makes Cl1455+22 about half as rich as Coma. This optical richness is in better agreement with the optically derived velocity dispersion than the high X-ray luminosity. The spatial distribution of colour-selected cluster members is fairly flat across the field – showing a slight elliptical peak near the cD. The lack of a strong central concentration of galaxies is a concern when appraising the lensing strength of this cluster. However, the very high X-ray luminosity and the presence of a large cD galaxy both point to a deep and centrally concentrated cluster potential. It should be noted that all five objects originally thought by Schild *et al.* to be members of a $z = 0.7$ cluster lie on the colour-magnitude relation for the cluster.

5.4.2 Cl0016+16

This cluster was discovered by Kron on a 4-m Mayall prime focus plate. The cluster's redshift is $z = 0.545$ (Dressler & Gunn 1992) and it has a rest frame velocity dispersion of $\sigma = 1324$ km/sec from 30 members. The cluster has been extensively observed in optical and near-infrared passbands (Koo 1981, Ellis *et al.* 1985, Aragón-Salamanca 1991) and was the subject of a deep EINSTEIN High Resolution Imager (HRI) exposure (White *et al.* 1981). The main conclusions of these studies are as follows:
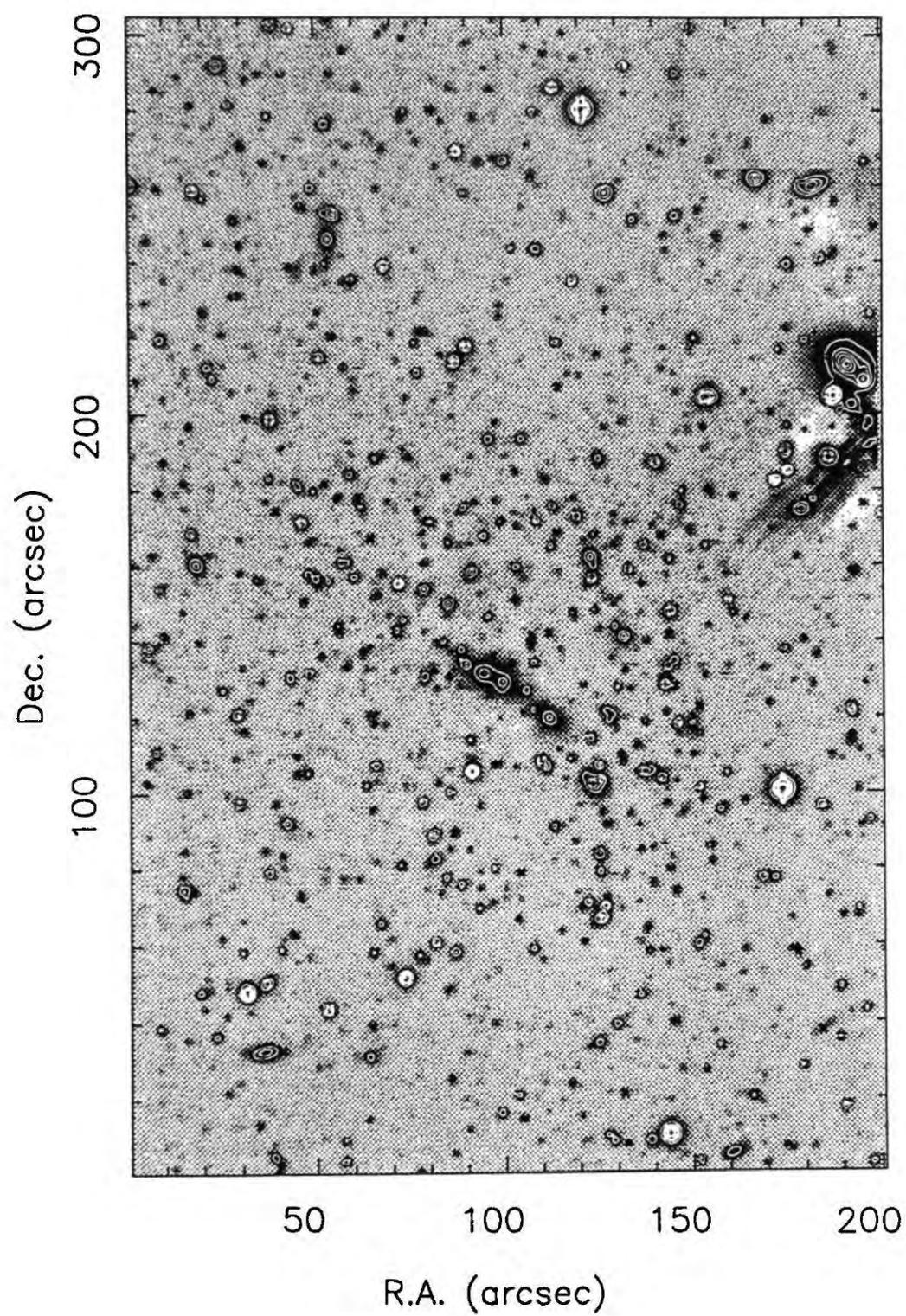
Figure 5.7 A composite $V + I$ image of the cluster Cl0016+16 (z =0.55). The total exposure time is $\sim$36.5 ksec and the scale is in arcseconds with east to the left and north at top.
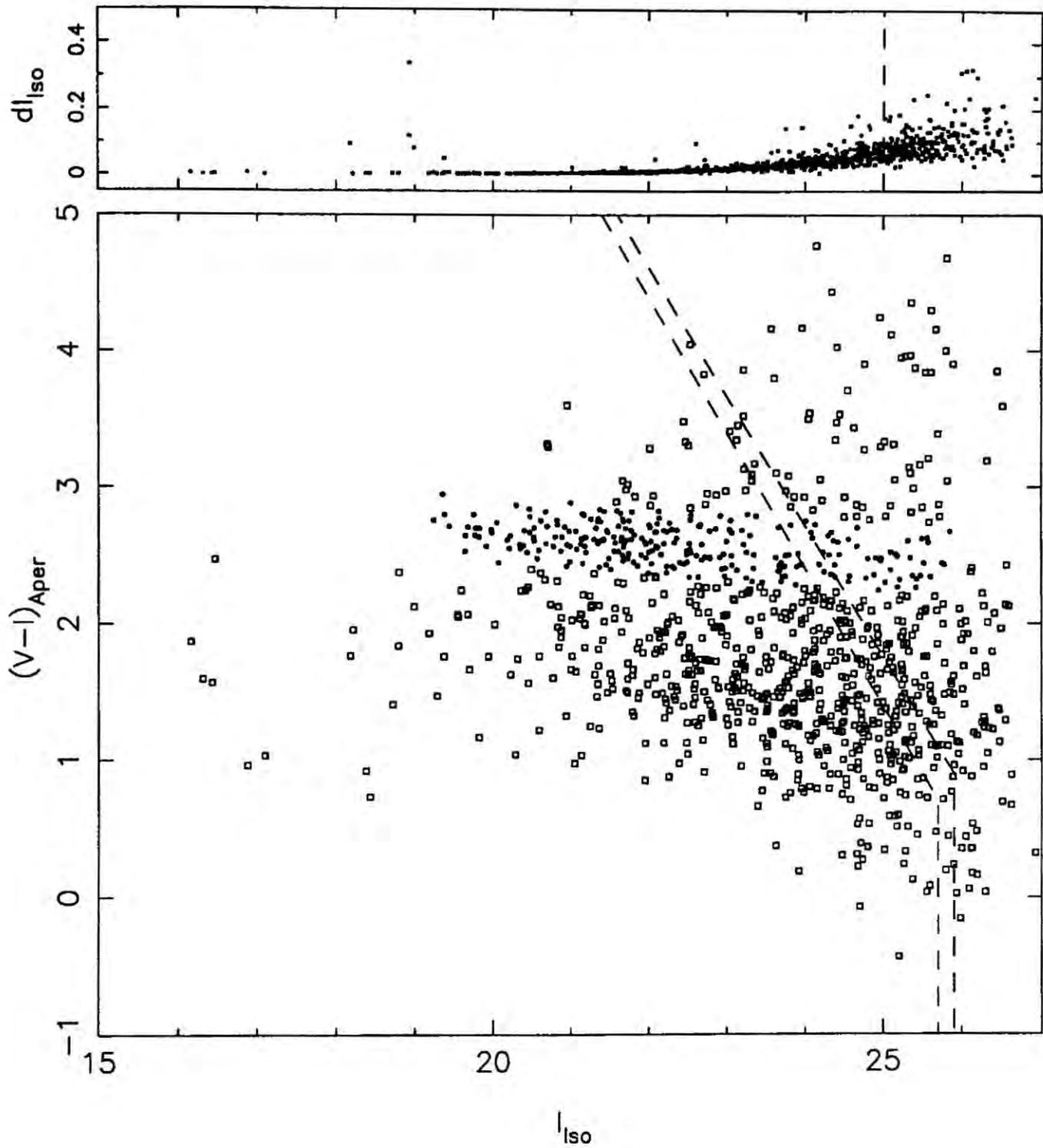
Figure 5.8 The $V - I$ colour-magnitude diagram for the cluster Cl0016+16. Galaxies with colours similar to an E/S0 in the cluster are shown (●), as well as the 80% and 50% completeness limits for the catalogue, calculated from simulations. Also shown are the photometric errors as a function of magnitude for the entire sample, the line marked is the chosen magnitude limit for the final sample $I = 25$.

The cluster has no central dominant galaxy – the centre being defined by a linear structure comprised of three bright galaxies (Koo 1981). The peak in the galaxy surface density lies slightly to the south-west of this structure. The raw optical counts would make the system about twice the richness of Coma, however, this is complicated by contamination by a number of weak foreground systems at $z \sim 0.3$ (Ellis *et al.* 1985). The cluster does not exhibit a Butcher-Oemler effect – in that there is no excess of blue galaxies in the cluster core as compared to similar clusters at low redshift. The central members of the cluster are concentrated in a highly elliptical structure (axial ratio ~ 0.6, Figure 5.7). As expected for an optically-selected cluster it shows very strong contrast against the field, with a measured core radius of 330 kpc. The pronounced annular structure inhabited by the cluster members (radius 370 kpc) has been noted by previous workers. The cluster was detected in a deep EINSTEIN HRI exposure at a luminosity of $L_X \sim 1.43 \ 10^{45}$ergs/sec in the 0.5–4.5 keV band, the best fitting isothermal β-model has an X-ray core radius of 220 kpc and $\beta = 0.5$ (White *et al.* 1981). The published X-ray map has only a 30 arcsec (220 kpc) resolution, however it too shows a roughly elliptical structure centred on the optical cluster centre and orientated at a position angle of roughly 135° (White *et al.* 1981) – similar to the orientation of the galaxy distribution on the same scale and on smaller scales the orientation of the central linear structure. The cluster has also a detectable Sunyaev-Zel'dovich decrement (Birkinshaw *et al.* 1992). In conclusion therefore this cluster appears to be a very rich and centrally condensed structure ideally suited for lensing studies.

The individual V and I catalogues have 80% completeness limits from simulations of $V = 26.4$ and $I = 25.7$ – the $I = 25$ limit imposed on the data thus gives a 17 sigma detection in the seeing disk. The cluster membership was determined from a comparison of the distributions on the colour-magnitude plane as described for Cl1455+22. There appeared to be a slight excess of objects on the cluster's colour-magnitude relation down
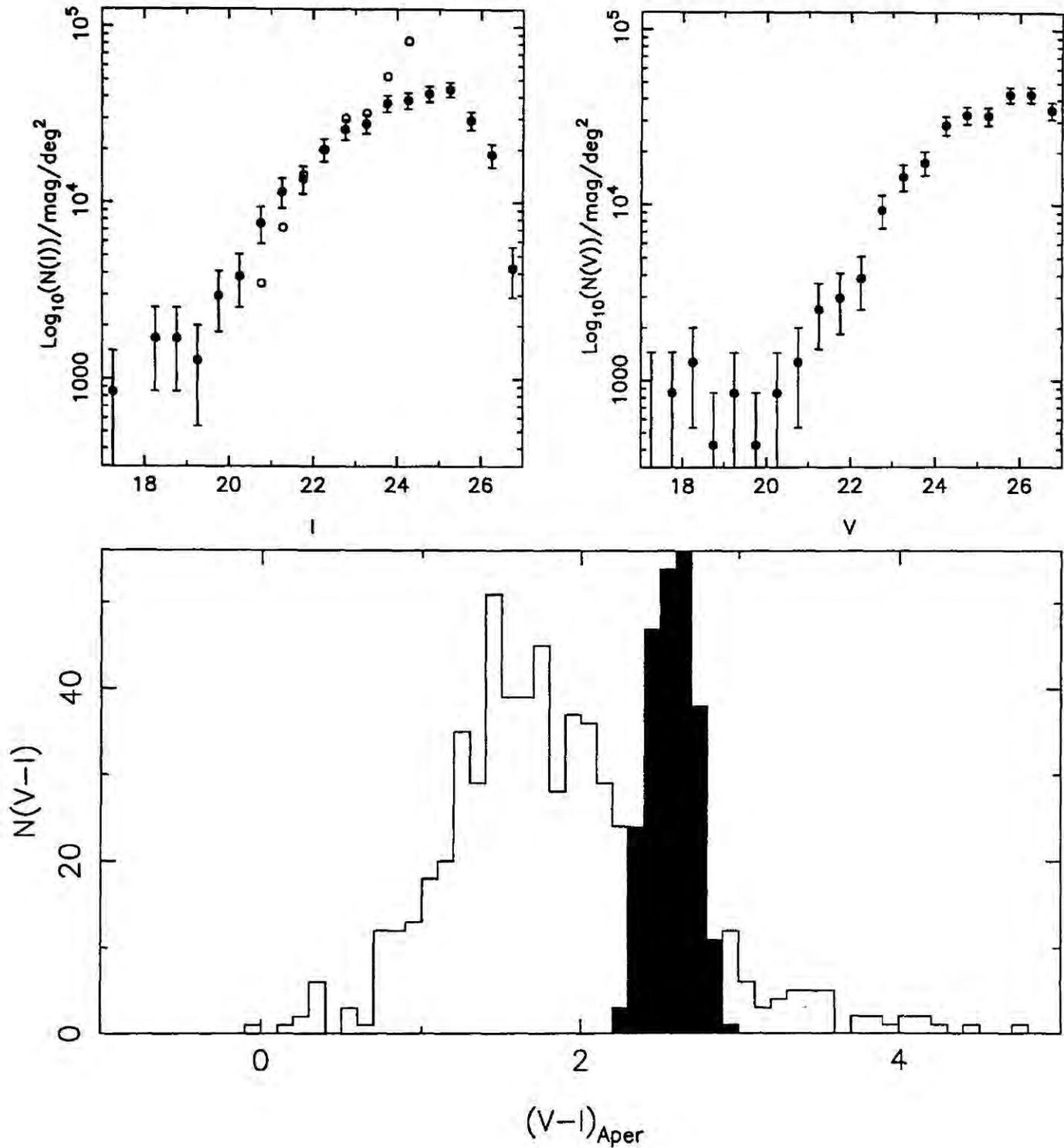
Figure 5.9 a) Differential number counts in I and V of Cl0016+16 after removal of the cluster members (•) compared to the Lilly *et al.* (1991) field counts (○). b) $V - I$ Colour distributions for the cluster (filled) and field galaxies (open) brighter than $I = 25$. Notice the flattening of the slope at the faint end due to the misclassification of field galaxies and the excess at bright magnitudes due to the large colour range of cluster members.

to the catalogue completeness limit so all objects lying along the relation were removed. A comparison of the widths of the two colour-magnitude relations for Cl1455+22 and Cl0016+16 shows the increased intrinsic scatter which appears in clusters at moderate redshift. This increased scatter makes cluster member identification using colour selection very difficult – as illustrated by the excess of bright objects in the field sample (Figure 5.9). We will therefore make comparisons with both a pure magnitude limited selected and colour selected samples to define cluster membership. The rather liberal colour definition of cluster membership results in the field I counts flattening at faint magnitudes due to misclassification of field galaxies (Figure 5.9). A comparison of the two membership lists shows that the colour selection predominantly highlights the ring structure in the cluster while the magnitude selected members populate an elliptical distribution orientated in the same direction as both the bright line of galaxies in the cluster centre and the X-ray map.

5.4.3 Cl1603+43

At the time of its discovery this was the most distant optically-selected cluster known. It was uncovered as part of a programme by Gunn and co-workers to discover high redshift clusters (Gunn *et al.* 1989). The subsequent spectroscopic follow-up provided redshifts for ~5 cluster members, giving a mean redshift of $z = 0.895$. The cluster was included in the study of high redshift cluster populations undertaken by Aragón-Salamanca (1991). The very long exposure times mean that the catalogues have relatively faint completeness limits: $I = 25.9$ and $V = 26.3$ for 80% detection. The corresponding $I = 25$ detection limit is for a 21 sigma detection within the seeing disk. An inspection of the colour-magnitude diagram for the field and the associated error plot (Figure 5.11) illustrates the trend of increasing *intrinsic* scatter in the colours of cluster members with increasing redshift – there being a very weak colour-magnitude relation. Aragón-Salamanca came to a similar conclusion – in that the $V - I$ colour distribution for the cluster was very close to the
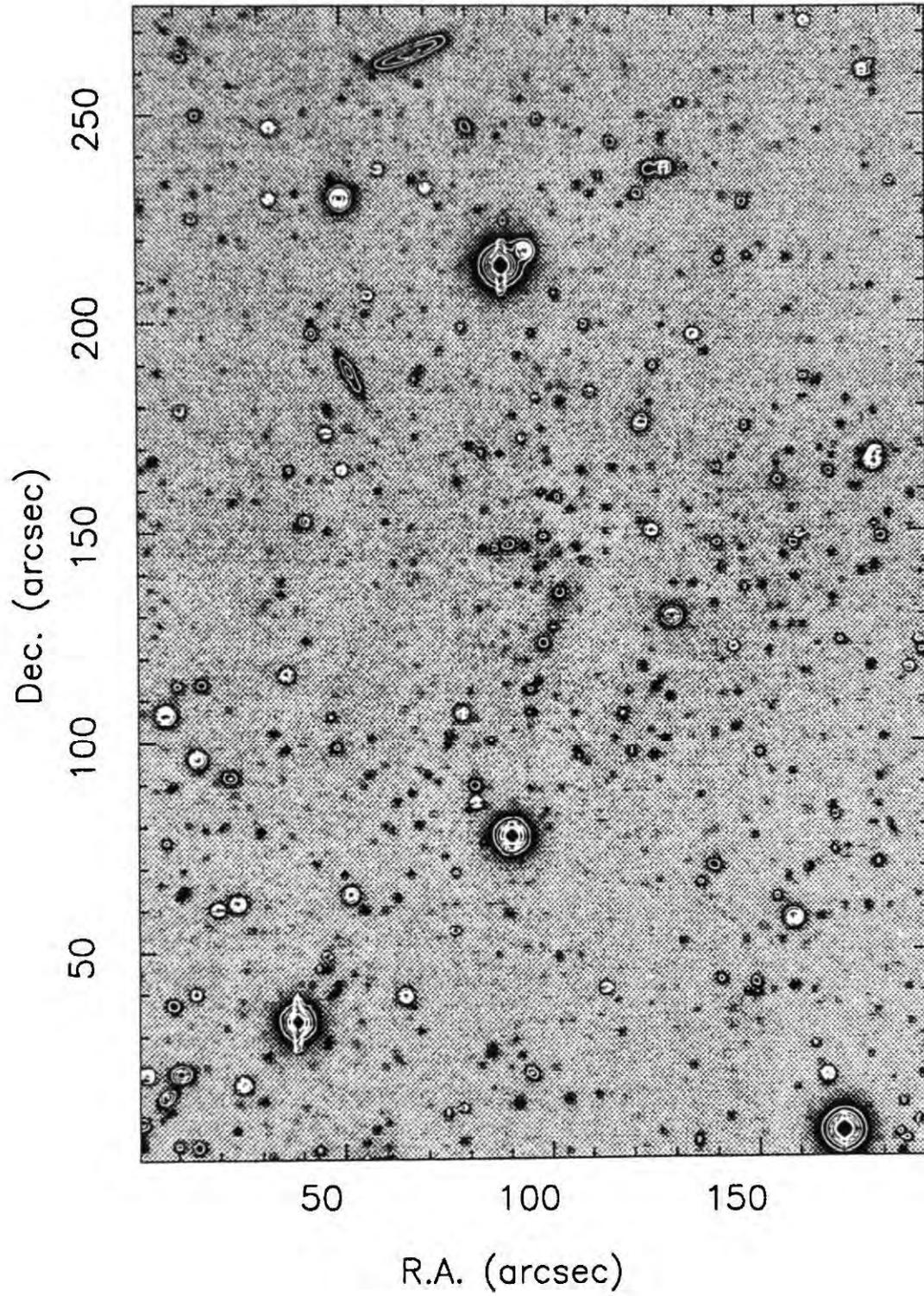
Figure 5.10 A composite $V + I$ image of the cluster Cl1603+43 ($z = 0.89$). The total exposure time is $\sim$45.8 ksec and the scale is in arcseconds with east to the left and north at top.

field distribution. To remove cluster members we have therefore adopted a very broad colour criterion to define cluster membership – resulting in the underestimation of the field counts at faint limits (Figure 5.12).

This cluster was one of four high-z cluster targets chosen by Dressler and co-workers to image with the PSPC aboard ROSAT. The reduction and analysis of this image was kindly undertaken by Franscico Castander at Durham. The cluster was detected within a 2×2 arcmin aperture at a 6.5 sigma significance level in a total exposure time of 28 ksec. This corresponds to an instrumental absolute luminosity of $L_X \sim 1.1 \pm 0.2 \ 10^{44}$ ergs/sec. Given the likely richness of a cluster which was discovered at such high redshift this low X-ray luminosity is surprising, unless the evolution in the cluster X-ray properties seen at low redshift (Edge *et al.* 1990) continues in more distant samples. This does indeed seem to be the case as X-ray studies of the more homogeneously selected AAO distant cluster sample (Couch *et al.* 1990) show (Castander *et al.* 1993). Cl1603+43 has a higher X-ray luminosity than the bulk of the lower redshift AAO sample studied – some of which have gravitational arc candidates (Chapter 3).

The reasonably high spectroscopic identification rate for cluster members combined with the cluster's X-ray luminosity provide ample evidence that the cluster represents a bound system which is probably massive ($\sigma_{cl} \gtrsim 800$ km/sec using the low redshift σ–L_X relation). Given the identification of giant arc candidates in distant clusters with lower X-ray luminosities (Chapter 3) it is likely that if there are galaxies beyond this cluster they will be gravitationally lensed.

5.4.4 Field Colour-Magnitude Distributions

The cluster-subtracted field colour-magnitude distributions for all three clusters show the now well known trend to bluer colours at fainter magnitudes. The median colour for the
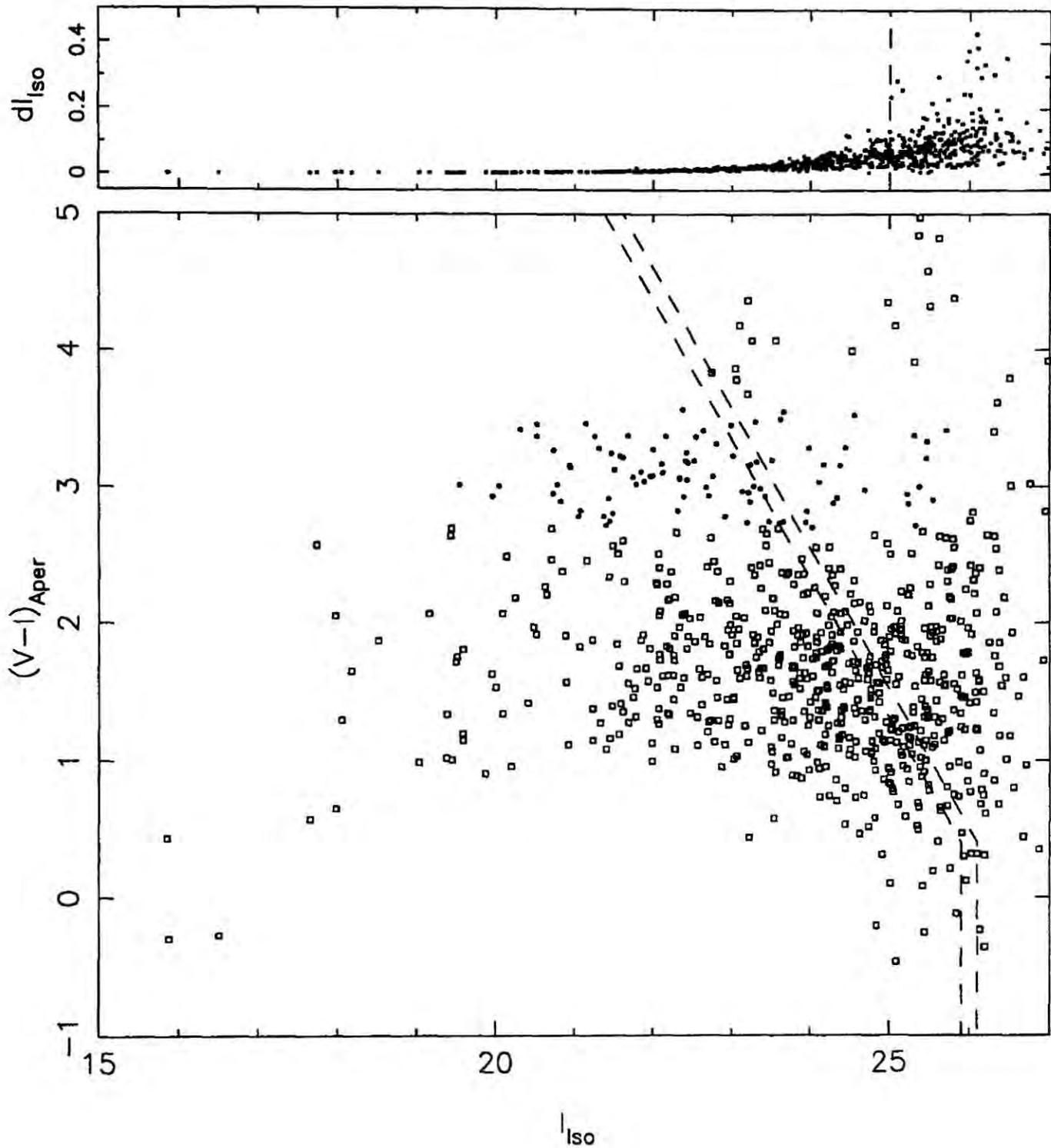
Figure 5.11 The $V - I$ colour-magnitude diagram for the cluster Cl1603+43. Galaxies with colours similar to an E/S0 in the cluster are shown (•), as well as the 80% and 50% completeness limits for the catalogue, calculated from simulations. Also shown are the photometric errors as a function of magnitude for the entire sample, the line marked is the chosen magnitude limit for the final sample $I = 25$.
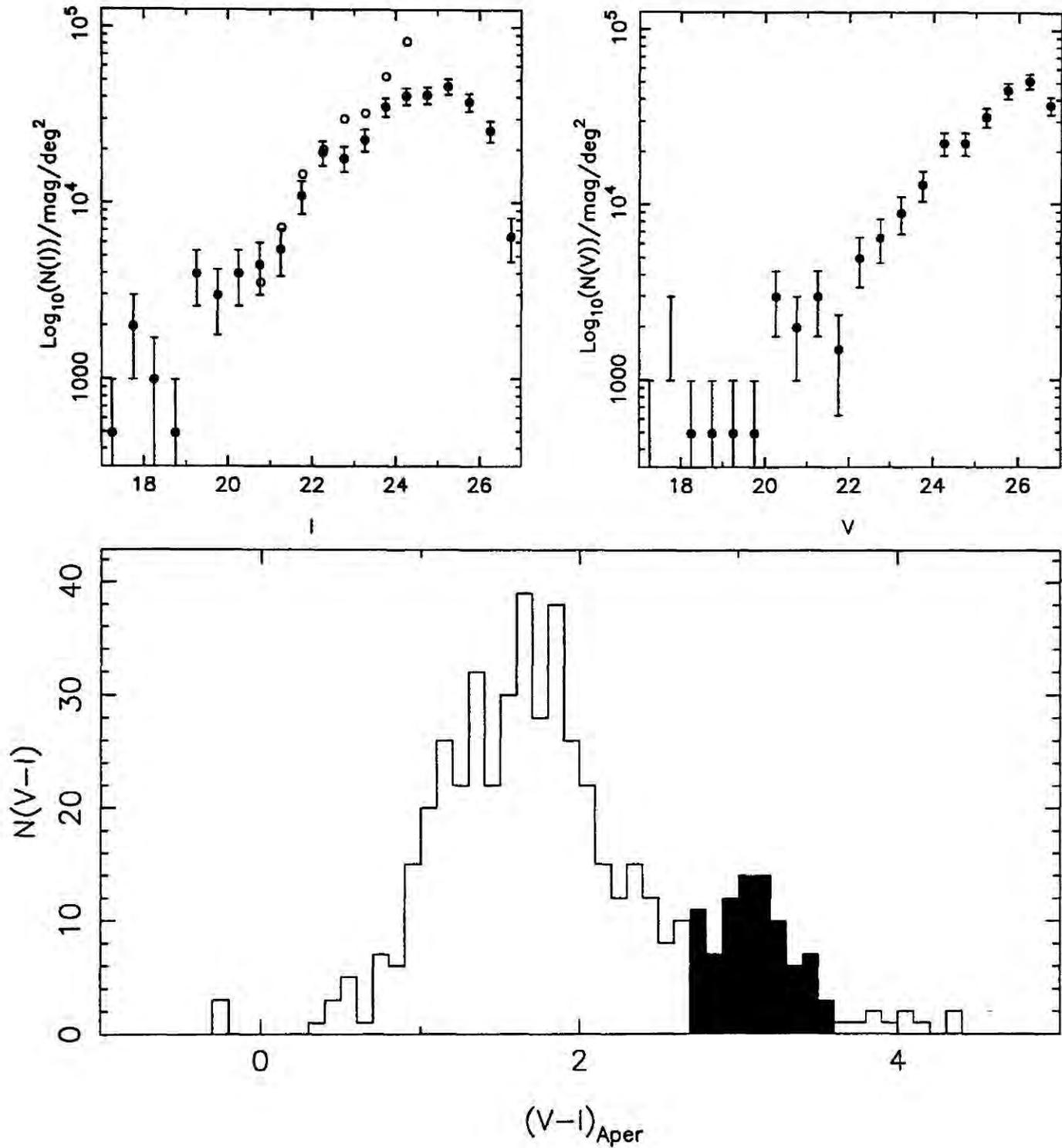
Figure 5.12 a) Differential number counts in I and V of Cl1603+43 after removal of the cluster members (•) compared to the Lilly *et al.* (1991) field counts (o). The deficit of field galaxies at faint magnitudes arises from the cluster selection criteria. b) $V - I$ colour distributions for the cluster (filled) and field galaxies (open) brighter than $I = 25$.

entire field sample brighter than $I = 25$ is $V - I = 1.55 \pm 0.10$. There appears to be a lower envelope to the bluest observed colour $V - I \sim 0.9$, similar to the colour of a flat spectrum source. This lower bound is only breached at $I \sim 23$ and even then the number of objects below is consistent with the scattering from above with the measured photometric errors. What is apparent is that the number of objects on the boundary (*i.e.* with flat spectrum colours) increases rapidly beyond $I \sim 23$ ($B \sim 25$) as illustrated in Figure 5.13. The colour distributions in the intervals a magnitude brighter and fainter than $I = 23$ are totally inconsistent with being drawn from the sample parent population ($P_{KS} = 6 \ 10^{-7}$). However, if allowance is made for the bluing of the entire population at fainter limits the shapes of the two distributions are very similar.

A population of very red objects is obvious in Figure 5.13, these have $V - I \sim 3$ and they first appear around $I = 20$. Morphological classification of this sample shows that the majority are compact/stellar. Both their colours and morphologies are compatible with these being faint galactic M stars. As such they constitute foreground contamination and are excluded from the analysis. Faint stars may well remain in the sample, however general arguments show that their number is strongly decreasing as we go to fainter limits. A combination of an ellipticity cut to remove circular images and a bright magnitude cut should therefore considerably reduce, if not eliminate, this source of contamination.

Finally, a comparison of the I band differential number counts in the three clusters with those of Lilly *et al.* (1991) shows an apparent deficit of galaxies fainter than $I \gtrsim 24$ in all three clusters. For Cl0016+16 and Cl1603+43 this can be accounted for by the cluster sample selection. However, in Cl1455+22 this deficit must be real as it occurs nearly a magnitude brighter than our 80% completeness limit. The equivalent B_j limit is $B_j \gtrsim 25.5 - 26$ where a change in the slope of the B counts has been observed (Metcalfe, priv. comm.). Such a feature may account for some of the apparent turn-over.
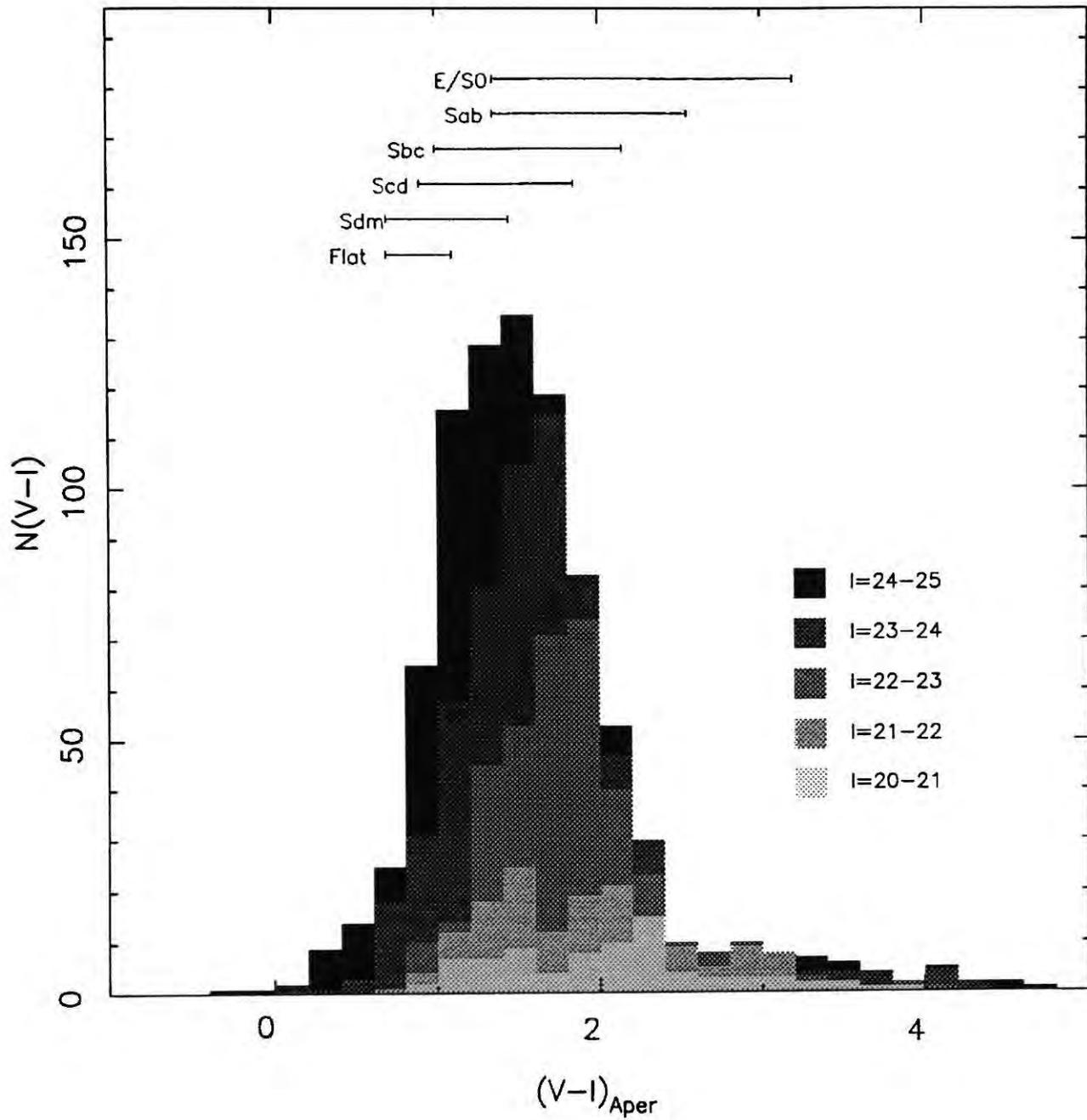
Figure 5.13 The $V - I$ colour distribution of the combined field samples from the three clusters, split into the various magnitude slices. The bars at the top show the range of colours covered by the non-evolved morphological types as a function of redshift. The galaxy colours generally start at the left side for $z = 0$ and move right until $z \sim 0.5$ at which point they start becoming bluer again.

5.4.5 Final Samples

The comparison of the completeness limits for the three clusters and the estimated measurement errors on the object ellipticities requires that we apply a faint magnitude cut-off at $I_{iso} = 25.0$. The depth of the V data then makes the resulting samples incomplete for objects redder than $V - I \sim 2$ – a weakly populated region of the colour magnitude plane. This limit corresponds to a minimum detection significance in the I band of ~ 17 sigma in the seeing disk, when combined with the requirement that the object has a similar detection in the V frame this creates a very robust sample with which to work. We also apply a bright magnitude cut-off to reduce foreground contamination, the exact value of this cut-off is discussed below.

5.5   Statistical Analysis of Gravitational Lensing

5.5.1   Statistics

Over the last couple of years a number of statistical tools have been developed to analyse the weak lensing of faint galaxies by rich clusters (Kochanek 1990, Miralda-Escudé 1991a, 1991b, Kaiser & Squires 1992). These tools were intended in the main to be used to look at the mass profile of the lensing cluster, rather than the properties of the faint galaxy population – which is assumed to be known. The tests fall into two main classes: parameteric likelihood tests which assume some form for the distribution of mass in the lens and then attempt to determine the most likely values of the model parameters (Kochanek 1990, Miralda-Escudé 1991a, 1991b) and non-parametric tests which directly derive the mass distribution (Kaiser & Squires 1992, Appendix A). The former are capable of testing the faint galaxy properties, while the latter is better suited for investigating the lensing cluster.

These two classes are complementary and they can be combined to overcome each other's weaknesses – by first applying the non-parametric test we can determine the morphology of the mass distribution to be used in the parametric test. This is especially important when dealing with real data where the assumptions input into the parameteric tests are based on little more than extreme optimism.

We can directly apply the non-parametric test to the data, however the parametric likelihood tests need simulated datasets to calibrate the statistics used to determine the maximum likelihood solution. The more detail that is incorporated into the model datasets the more reliable the test will become. We have therefore combined two approaches – analytic simulations which assume that the data has simple noise properties and simulated images to calibrate these. The simulated images can include all the likely sources of observational

noise but are computationally intensive to produce. In addition to calibrating the statistical tests the simulated images provide us with an easy method to view the effects of varying the sample definition and measurement technique.

5.5.2 Likelihood Test

The parametric test we apply to the data consists of a simple maximum likelihood test. We determine the probability that a given observational dataset could have been selected from galaxies distributed according to one of two redshift distributions $N(z)$, which have been lensed by a family of lens models. The probabilities are determined by comparison of the distributions of image orientations, ellipticities and radial distance from the lens centre. All three of these distributions are skewed by lensing (c.f. Chapter 3). The strength of this skewing on the observed distributions depends upon the number of galaxies in front and behind the lensing cluster – the $N(z)$.

In each of our tests the null hypothesis $N(z)$ is that the faint galaxies are distributed according to the no evolution prediction (Figure 5.1). The ratio of the maximum likelihoods for each $N(z)$ determines which is prefered. In addition we also obtain the maximum likelihood values of the lens parameters which best fit the data for each cluster. Depending upon the $N(z)$ and the redshift of the cluster a fraction of these objects are foreground to the cluster and therefore weaken the observed lensing signal, additional unlensed objects can be added to model residual cluster contamination. The lens is modelled by a spherically-symmetric non-singular isothermal sphere parameterised by a core radius and a one dimensional velocity dispersion.

For each $N(z)$ we take a combination of core radius and velocity dispersion for the lens and use these to lens galaxies at distances selected from the hypothesised distribution – this is termed an 'analytic' model. Each galaxy from the distribution is randomly, but

uniformly, placed on the source plane with an ellipticity drawn from a distribution and a random orientation. The image distortion is calculated using the analytic framework of Miralda-Escudé (1991a). We then solve the lensing equations to give the final position, orientation and ellipticity of this object. This is repeated until there are enough objects to give well populated parameter distributions (ellipticity, orientation relative to lens centre and radial distance from centre) to allow a fair comparison with the observations. The statistics used to compare the distributions are either combinations of linear or multidimensional Kolmogorov-Smirnov tests. The combined probabilities from the comparison of the three distributions give the likelihood of the model being correct. This test is extremely powerful when applied to strong lensing systems. However, as the signal weakens the test's distinguishing power between the lens models diminishes.

An example test is shown in Figure 5.14. Here we compare an analytically-simulated observation with a family of analytic models (top panel) and a numerically-simulation observation with a family of analytic models (bottom panel). The details of the simulation techniques are given below. Each plot shows the probability contours assuming that the sources are drawn from one of two redshift distributions: the no evolution (N.E.; H_0) or the Shallow model (H_1). The probability contours are logarithmically spaced from the peak. The input parameters of the simulation were σ_{cl} =1400 km/s, r_c = 100 kpc and the redshift distribution used was the no evolution model (N.E.) for $I \in [20, 25]$. The observation parameters (lens redshift, frame size, galaxy surface density etc.) are those for Cl1455+22. The distribution of ellipticities used for the sources was obtained from the analysis of a number of deep high resolution images of blank fields taken with the New Technology Telescope (NTT) in Chile by Matthew Colless and Richard Ellis (see below).

The test very easily distinguishes between the two hypotheses when comparing an analytic simulation with other analytic simulations: the probability ratio is $\log \hat{p}_1 / \hat{p}_0 \equiv \log \Lambda < -10$ (see Chapter 3 for notation). In addition the input lens parameters are correctly

recovered. The shape of the likelihood contours can be understood as a trade-off between an increase in the lens velocity dispersion – which produces a stronger lens – against an increase in the core radius of the lens – which weakens it. The shifts between the contours for the various redshift distributions arise from more distant distributions being more easily distorted (Appendix A). The majority of the distinguishing power of this test arises from the comparison of the orientation distributions – this constrains the solution to lie somewhere along the slanted locus (Figure 5.14). The other two probability distributions then confine the best solution to a point on this locus.

For the numerically-simulated observations the test still correctly distinguishes between the two possible redshift distributions with $\log \Lambda = -1.8$. However, there is now a systematic offset in the best fit lens parameters. The calibration and correction for this offset is one of the main motivations for undertaking the numerical simulations and we discuss its source below. Nevertheless, it should be noted that the test is still capable of correctly distinguishing between the redshift distributions even in the presence of this offset. The ability of the test to determine the correct lens parameters is very sensitive to the strength of the observed lensing signal. For weak signals the likelihood peak flattens and while the test can still differentiate between the redshift distributions the lens parameters are meaningless.

The analytically-simulated observations (created in the same manner as the analytic models) obviously disregard a number of complications. The effects of noise on the image measurements and the degradation of the induced distortion by seeing are ignored. Both these effects will introduce a systematic error in the measured ellipticity. However, their effect on the image orientations will be random – by concentrating on the image orientation and radial distributions we can hope to minimise the effects of these systematic errors. Also the uniform distribution on the source plane results in a paucity of objects in the lens centre on the image plane. This is because we have neglected the amplification bias which acts
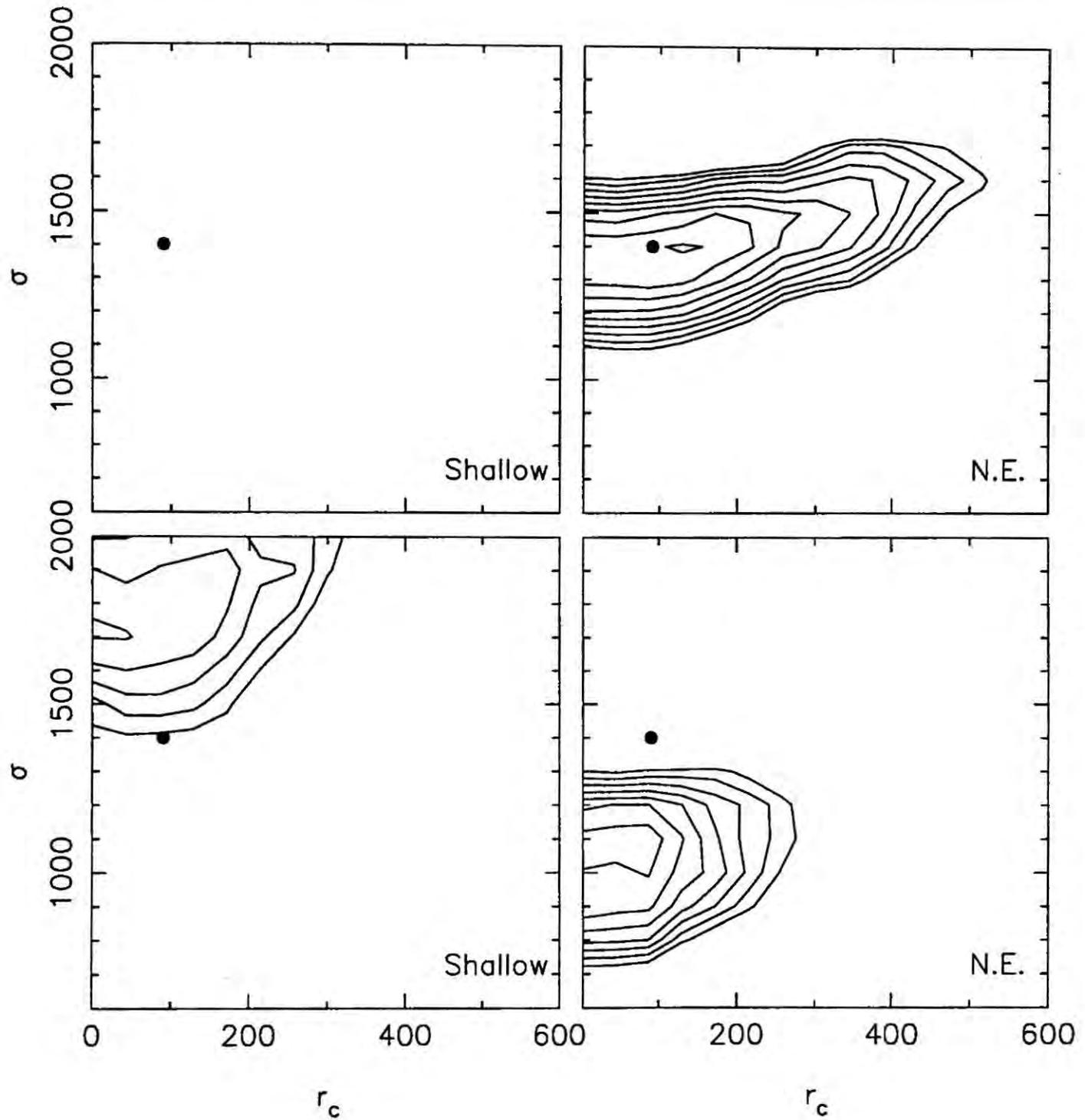
Figure 5.14 The top panels show the likelihood contours of a test of an analytic simulation while the bottom panels show the contours for a numerical simulation with the same lens parameters. The probability contours are logarithmic and spaced every factor of 10 – starting at 10^{-10} below the peak probability. Details of the simulations are given in the text, the input redshift distribution was the no evolution model and the lens parameters are marked (•). the core radius (r_c) is in kpc and the velocity dispersion (σ) is in km/sec.

to populate this region by magnifying galaxies fainter than the observation's magnitude limit into the sample. However, all these effects would tend to reduce the observed lensing signal in the simulations (Figure 5.14). By using numerically-simulated observations we can hope to calibrate this degradation and so correct the observations for it.

The final likelihood is derived assuming that the probabilities from the three K-S tests are independent. While this is not entirely valid, neither is it an unreasonable assumption to make, as has been stated the distinguishing power of the test mainly arises from one single distribution (orientation).

5.5.3 Numerical Simulations

The numerically-simulated observations each consist of a set of simulated images which are analysed in the same manner as the real data using FOCAS. The detected image parameters can then be used to calibrate the statistical test used on the observations. This approach allows us to model most effects that are likely to be present in the data. There are a number of effects in the data which are not covered in the analytic modelling and these may play an important role in degrading the strength of the lensing signal seen in the simulations. These will cause systematic errors in the derived lens parameters (Figure 5.14). Processes which affect the isophotal shape of the galaxies are of the most concern, these include seeing, sky noise and undetected merged galaxy images. Underlying correlations in the data due to redshift dependency of certain image charactersistics are also a concern unless properly modelled. The object lensing is performed using the same technique as in the analytic simulations with a number of additional features:

• Instead of using a cumulative $N(z)$ to a given magnitude limit we use differential $N(z)$ for objects in a given magnitude interval. A mapping is then possible between apparent magnitude and the family of differential $N(z)$'s. This allows empirical changes to the

form of the N(z) as a function of magnitude without requiring a detailed model of the luminosity and density evolution. This approach has another advantage, the strength of the distortion at a particular radius on the source plane is an increasing function of redshift. As the signal to noise in a given ellipticity measurement decreases for fainter objects it is important that the faintest, distant and hence most strongly lensed objects are most effectively degraded. There is a similar effect related to the possible correlation of source scale size with distance and the effect of seeing on the measured ellipticity. However, we choose not to couple the scale size to the redshift as there is no observational data on this correlation. We randomly select scale lengths from a distribution measured off a deep HST Wide Field Camera Medium Deep Survey (MDS) image of a blank field (Griffiths *et al.* 1992). This distribution has the advantage of being unaffected by atmospheric seeing. A choice of image profile is also available but we normally restrict ourselves to exponential disks.

• The effects of crowding on image detection and the distortion of image isophotes by undetected faint images are also included. The latter is modelled by lensing galaxies fainter than the adopted magnitude limit, the number being determined by extrapolating the observed counts. Those objects which are fainter than the magnitude limit and detected are then discarded after the FOCAS analysis. The sources are uniformly distributed on the source plane and the inclusion of the fainter sources thus allows us to model the effects of amplification – as intrinsically faint galaxies are magnified into the sample. The source's spatial distribution is taken to be uniformly random as current data (Efstathiou *et al.* 1991) implies a very weak two point correlation function for these faint objects and so we will not appreciably underestimate the crowding effects.

• The effects of seeing, pixelation and sky noise on the measurements are easily included in the simulated image to match those in a particular observation. The effect of isophote

distortion of objects lying close to frame edge is also automatically included – although these are removed from the catalogue.

Again, there are some apparent shortcomings with these simulations. The most obvious is that the technique used to lens the galaxies does not produce any curvature in the final images. This is unimportant for the majority of images, but the rare very strongly lensed images (giant arcs) close to the cluster centre are not well modelled. None of our three datasets contains such a giant arc and so we apply an upper ellipticity cut-off to both the simulations and real data to remove this effect. We are already applying a lower cut-off due to the intrinsic scatter in the orientation measurements of near circular images.

Another possible weakness is that we rely on an ellipticity distribution taken from ground-based NTT data (limited at $I \sim 24$). This has already been effected by both seeing and noise and so does not represent the intrinsic source ellipticity distribution. We also have the recurrent problem that the data which we are using to define the intrinsic source characteristics is shallower than the observations. This means that we have to assume continuity in the samples from brighter magnitudes. Fortunately, the MDS data while covering a smaller area than the NTT data goes to a comparable depth and is unaffected by seeing. We therefore used the very high resolution WFC sample to test the validity of the ellipticity distribution derived from the NTT data. A two sample K-S test shows a 85% probability that the two distributions came from the same parent population – giving us strong justification for using the ground-based distribution.

Finally, there is the question of the accuracy of the scale length distribution used. A similar concern arises in the observations of giant arcs (Wu & Hammer 1992, Chapter 4). The small area and brighter limiting magnitude of the MDS data makes a definitive statement impossible. However, the derived scale lengths from the HST data ($r \sim 0.3$-0.7 arcsec) at $I = 23$ are comparable to those measured from our cluster observations when allowance

has been made for the effect of seeing. When applied to the fainter $I \sim 25$ sample this technique gives a similar range of scale sizes. This quantifies the visual impression that the model faint galaxy images appear very similar to the real data.

5.6 Results and Discussion

As discussed above we first applied the non-parametric technique to both determine the cluster mass distribution and optimise the sample selection. The samples were then analysed to select the most likely redshift distribution for the faint galaxies and the best fit model parameters for the lensing cluster.

Before discussing the analysis of the weakly lensed arclets we note that in none of the three clusters is there a good candidate for a giant arc ($A \geq 3.5$) as defined in the survey presented in Chapter 3. This is in spite of the fact that the surface density of sources is at least four times higher than in that survey. We found 6 arcs satisfying this criteria in 19 clusters – scaling that to the depth of these observations we should see at least one such arc per cluster – rather than none. Given that we might also expect to pick up more distant galaxies (than a $V = 25$ or $I = 23$ sample) which are more easily distorted as we go deeper this result is interesting. As we shall show below the two lower redshift clusters do show lensing signals from the analysis of the arclets – this result is compatible with the absence of giant arcs if there is either a relatively low surface density of distant galaxies or both of the clusters have very soft potentials.

5.6.1 Cluster Mass Distributions

The non-parametric method developed by Kaiser & Squires (1992, Appendix A) produces a map of the mass distribution in the lens. It does this by comparing the observed alignment of images around a selected position in the cluster with that expected from a point mass centred there. The ellipticities and alignments for the field sample are measured using the optimal weighting scheme outlined above. The strength of the similarity between the two patterns is a direct estimate of the mass surface density at that point. This statistic is evaluated on a grid of centres (20×20) to produce a map of the mass in the cluster. The random intrinsic orientations of the galaxies are a source of noise and to remove this the map is filtered using the filter outlined in Kaiser & Squires (1992). Kaiser & Squires give an analytic formula for the noise level in the reconstructed map which can be used to judge the significance of any structures.

Cl1455+22

In Figure 5.15 we compare the derived mass map from the lensing analysis with the smoothed distribution of cluster members. The choice of limits for the sample was determined by the need at the bright end to reduce foreground contamination and at the faint limit to have reliable ellipticity measurements. Both the cluster galaxy and mass distributions have similar ellipticities and orientations $\epsilon_{gal} \sim 0.44 \pm 0.15$, p.a. $\sim 141 \pm 5$ degrees and $\epsilon_{mass} \sim 0.52 \pm 0.07$, p.a. $\sim 141 \pm 5$ degrees. Indeed on smaller scales the orientation of the cD (p.a.$\sim$135 degrees) closely matches that of the larger scale mass distributions as would be expected from dynamical arguments for its growth. While in Figure 5.16 we make a similar comparison between the mass map and the X-ray surface brightness distribution, again both distributions have similar orientations ($\epsilon_{X,b} \sim 0.17 \pm 0.03$, p.a. $\sim$ 137±5 degrees). To convert the X-ray surface brightness distribution into the ellipticity of the surface density we assume that the X-ray surface brightness reflects the potential and
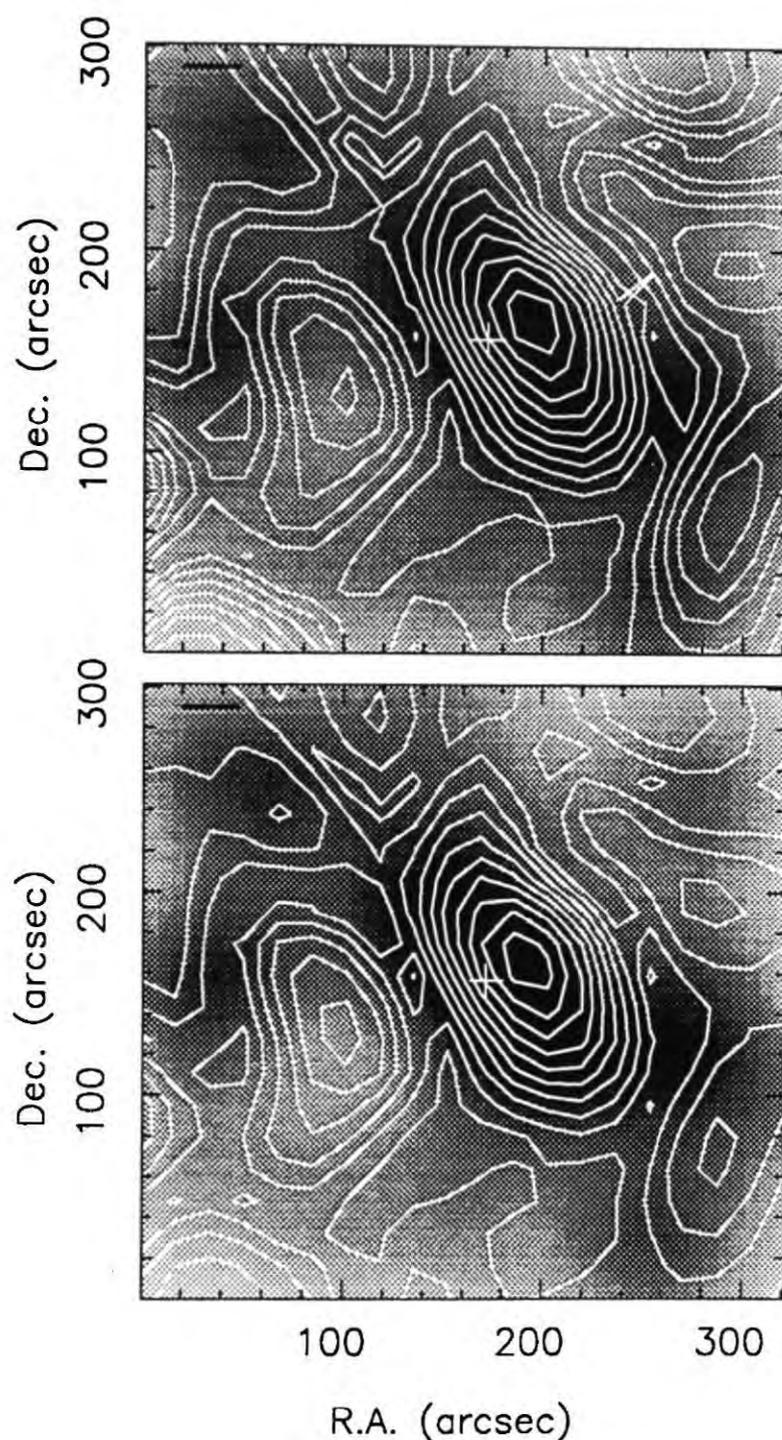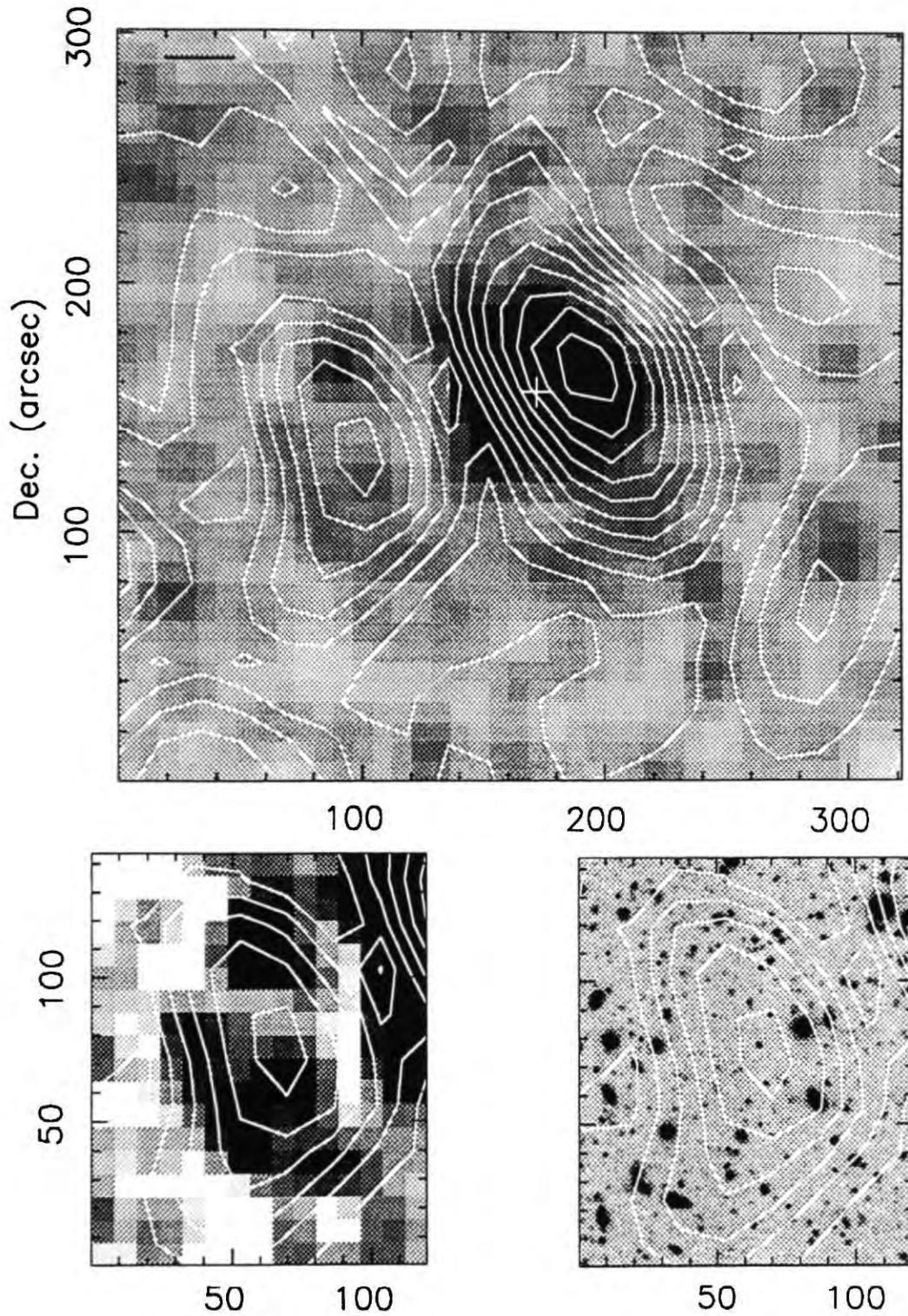
Figure 5.15 (a) The derived mass map from the Cl1455+22 FOCAS catalogue overlayed on the smoothed distribution of cluster members. The map was constructed with all objects with $I \in [23, 25]$ and $V - I \in [-1.0, 2.5]$ using the optimally weighted ellipticities. The contours start at zero surface density and are spaced every 2 sigma. The smoothing scale used to construct the mass map is marked and the position of the cluster cD is indicated $(+)$. (b) The same map as above but weighted by the local error to show the reality of structures near the map edge.

assuming that this is isothermal we have: $\epsilon_{mass} = 3\epsilon_{pot}$ hence $\epsilon_{X mass} \sim 0.5 \pm 0.1$. There is obviously excellent agreement between the orientations and ellipticities of the all three distributions. However, there appears to be slight offsets between the peaks of the X-ray, optical and mass distributions. In particular the light distribution does not appear to be centred on the cD but is offset in the same sense as the mass peak. The size of the various offsets between the mass peak and the other distributions is within the filtering scale and is therefore unlikely to be significant.

The contour significance used for the mass contours in Figure 5.15(a) assume errors as calculated using the prescription of Kaiser & Squires – these are purely dependent upon the average number of background galaxies within the smoothing scale. However, such a formulation is invalid within a smoothing length or so of the frame edges. This explains the large amount of apparently significant structure within a smoothing scale of the field edges. This structure is insensitive to the removal of objects close to the chip boundary showing that it is not isophote truncation that is creating the spurious signal. We show in Figure 5.15 (b) the mass map using a local surface density weighting scheme – this shows that the structures on the frame boundary are much less significant than they would appear in Figure 5.15 (a). The other fact to note is that the errors are dependent upon the form of the N(z) chosen for the faint galaxy population and the redshift of the cluster.

However, there is one significant secondary maximum ($\sim 10\sigma$) in both maps, nearly due east of the cluster centre, that is clear of the field edges (Figure 5.16). Moreover, this peak does not lie close to any feature in either the cluster member distribution or the field distribution on the frame – it does, however, correspond to a structure in the X-ray image. This structure consists of four merged knots, has an average surface brightness 2 sigma above the background and appears marginally elongated in the same direction as the main X-ray peak. The northern-most knot coincides with a small group of objects all fainter than $I = 22.5$ – of the brightest five objects, four may be cluster members and the fifth

Figure 5.16 (a) The surface brightness distribution of X-ray gas from the ROSAT HRI image of Cl1455+22 which is overlayed on the derived mass map. The X-ray distribution's morphology is very similar to both the mass and the light. The marked symbols correspond to those in the previous figure. (b) The region around the mass subclump, enhanced to show the associated X-ray component. This is a low surface brightness region which roughly corresponds to the mass peak. (c) The same region overlayed on the $V + I$ image.

is a red stellar object – possibly a galactic M star. The whole structure has an integrated luminosity, above the local background, of $L_{bol} \sim 7 \pm 3\ 10^{43}$ ergs/sec assuming the same temperature as the cluster centre. This luminosity is too large for a single galaxy and is more typical of a small group. The projected separation of the secondary peak from the cluster centre is $r \sim 0.5$ Mpc.

Shown in Figure 5.17 are the mass profiles derived from the three distributions centred on their respective maxima. The profiles have been normalised to the inner-most bin, the error-bars on the lensing derived profile show the spread in values at that radius. There appears to be good agreement within 1.5 arcmin between the mass distributions derived from the lensing with that arising from the potential used as input into the X-ray analysis: a King model with a 230 kpc core. Outside of 450 kpc the X-ray surface brightness in our shallow image falls away rapidly, while the lensing signal becomes confused by edge effects in the small field.

We fit a modified Hubble profile ($\Sigma(r) \propto 1/(1+(r/r_c)^2)$) to the projected mass and galaxy distributions giving maximum likelihood estimates for the core radius of: $r_c^{mass} = 195^{+45}_{-35}$ kpc and $r_c^{gal} = 285^{+100}_{-100}$ kpc respectively. The errors are 5% likelihood limits. For the galaxy distribution we assume that there is no background contamination and remove the inner-most bin. The turn-over seen in the lensing derived M(r) occurs at a radius close to the weighting scale ($R = 135$ kpc, $\log R \sim -0.35$). The reality of the feature is confirmed by inspection of lensing profiles produced using a smaller smoothing scale, which while noisier also have a turn-over at $r_c \sim 200$ kpc. These core radii values should be treated as upper limits given that the effects of both the weighting filter used to construct the maps and the ellipticities of the distributions have been ignored. Fitting the core radius of the mass distribution along its major and minor axes gives smaller values as expected: $r_c = 165^{+35}_{-25}$ kpc and $r_c = 130^{+45}_{-30}$ kpc although the fits are not as good.
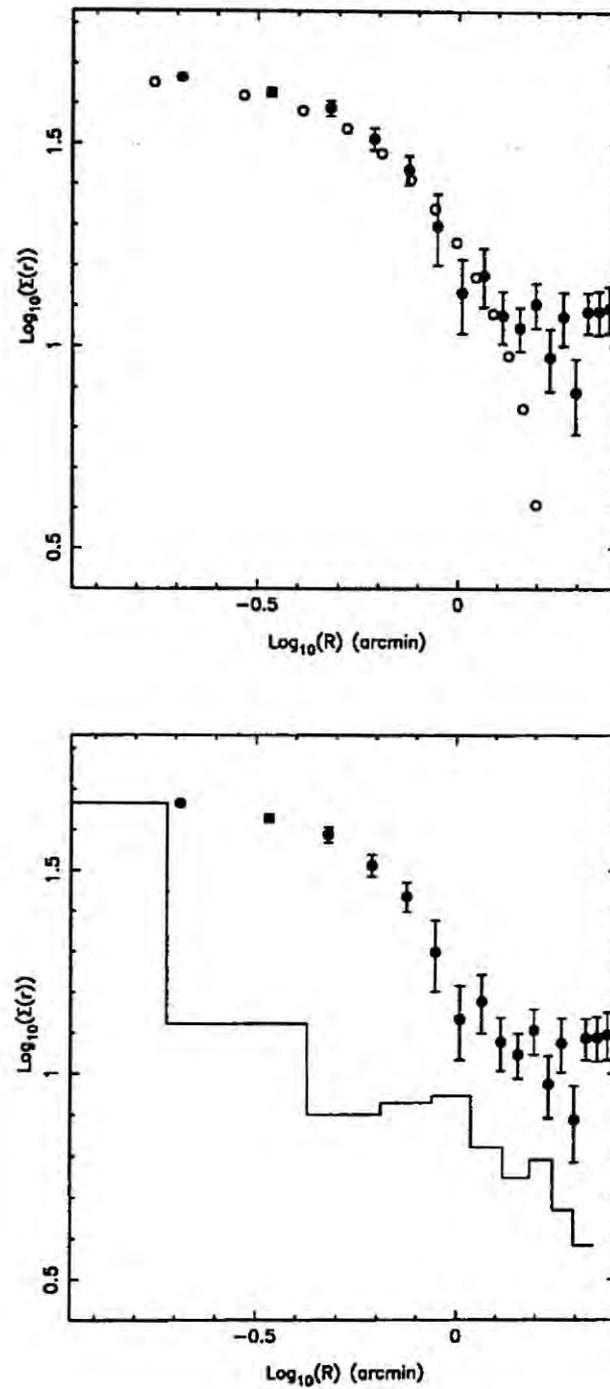
Figure 5.17 The derived mass profiles for Cl1455+22 from the two dimensional maps shown previously (lensing: •, X-ray: o and the histogram shows the cluster galaxy surface density). The profiles are centred on the respective distribution maxima, except for the galaxy counts which use the cD as centre. No allowance has been made for the ellipticity of the distributions. Notice the good agreement shown between the lensing and X-ray mass derived profiles – confirming the validity of the model assumptions used in the X-ray analysis.
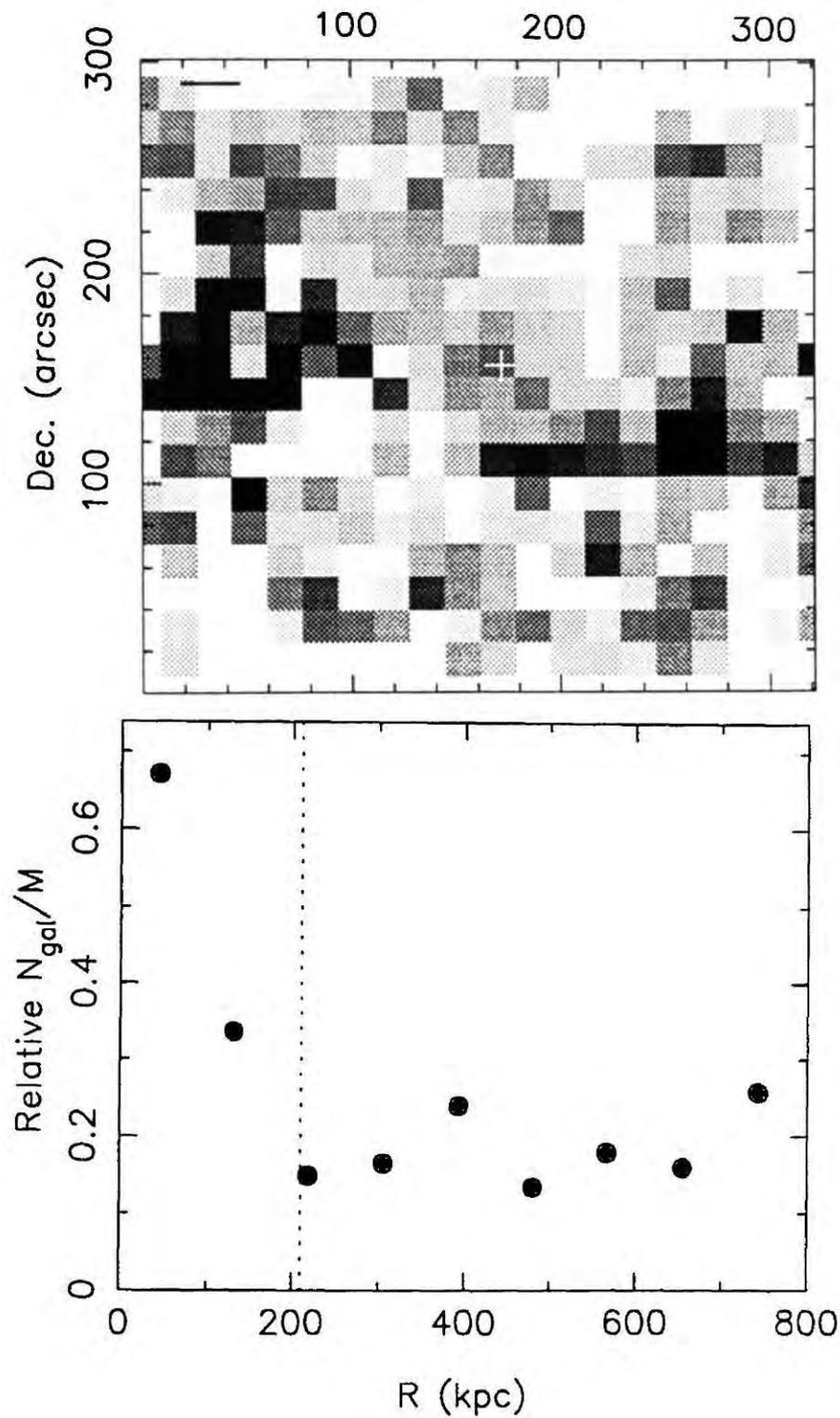
**Figure 5.18** a) The relative distribution of mass and galaxies for Cl1455+22. Black shows a low ratio of mass to galaxy surface density. The smoothing scale used is marked and the position of the cluster cD is indicated (+). b) The median radial profile derived from the above distribution centred on the cD. The dotted line shows the cooling radius from the X-ray analysis – the potential's core radius has a similar scale.

From Figure 5.17 it is apparent that the distributions of the mass and galaxies cannot both be well described by a single parametric form on all scales. A more informative approach to understanding the relative distribution of mass and galaxies in the cluster is to take the two dimensional mass and galaxy maps and calculate the ratio of the mass to galaxy surface density (Figure 5.18(a)) - the radial profile extracted from this map is more sensitive to large scale differences in the two distributions. Figure 5.18(b) shows the median relative galaxy surface density to mass surface density ratio (N_{gal}/M) as a function of radius in the cluster. The ratio of mass to galaxies appears relatively constant outside of the cluster centre, as would be expected if the galaxies were acting as tracers of the mass. However, within 200 kpc of the centre the number of galaxies increases relative to the mass. This is the same scale as both the inferred cooling radius of the cluster and the measured mass core radius.

The relative concentration of the galaxies towards the cluster centre compared to the mass could arise from a variety of processes. One such process, which has been discussed recently, is dynamical segregation (West 1990, West & Richstone 1988). Using N-body simulations West & Richstone showed that dynamical friction between the heavy galaxies and the lighter dark matter would lead to the galaxies being more centrally condensed than the mass. Dynamical friction should be more effective in small subclumps rather than in rich clusters - although any existing segregation may carry over from subclumps into the larger systems with which they merge. If this is what we are seeing then it would also go someway to explaining the low dynamical mass estimate for the cluster - as the central galaxies are both spatially and dynamically segregated giving spuriously low values for the measured velocity dispersion.

We have demonstrated that the potential used in the X-ray analysis is representative of the actual cluster potential. We can therefore compare the total cluster mass, within a radius of 450 kpc, derived from the X-ray analysis with the lensing analysis to give an
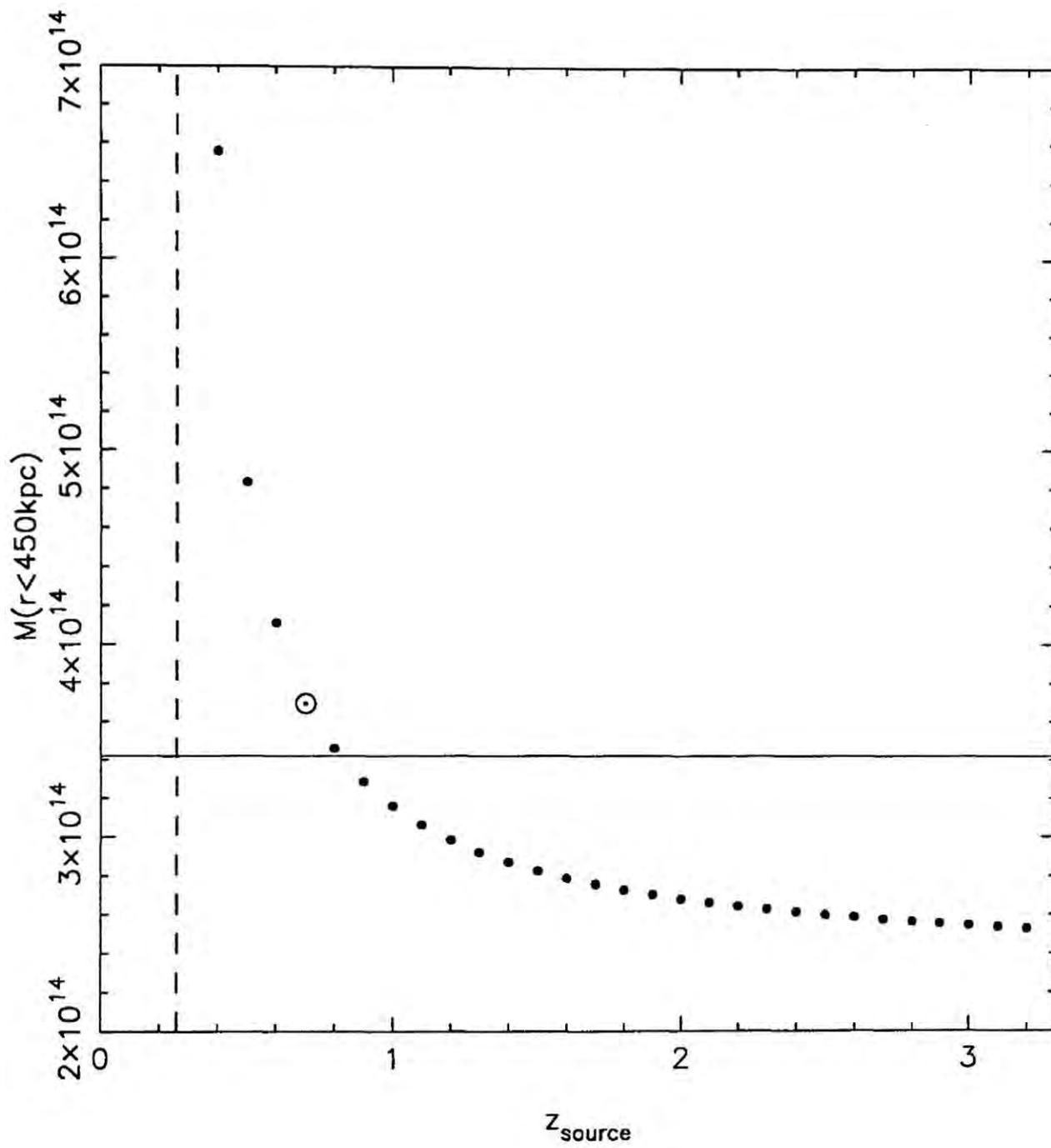
Figure 5.19 The total mass, in solar units, interior to 450 kpc from the lensing analysis as a function of the median redshift of the background galaxy distribution (•). This is compared to the mass derived from the analysis of the X-ray image within the same radius (solid line). The predicted value for a no-evolution $N(z)$ to $I = 25$ is also marked (⊙) – in close agreement to the X-ray measurement. The redshift of the cluster is shown by the vertical dashed line.

estimate of the redshift of the background sources. In Figure 5.19 we compare the variation in the cluster mass derived from the lensing analysis as a function of the source redshift with the X-ray derived mass. The lensing derived mass is for the excess *projected* mass within 450 kpc of the centre compared to the projected mass at larger radii. To directly compare this with the X-ray value we should deproject the mass distribution using the ill-determined cluster mass profile at large radii. Nevertheless, we note that the median z_{source} for an $I = 25$ no-evolution model gives very good agreement between the two mass estimates – however, the flatness of the curve combined with the probable errors in the X-ray mass estimate make this an insensitive tool to use to derive an upper limit to the background source redshift. It does provide a rigorous lower limit of $M \geq 2.5 \ 10^{14} M_{\odot}$ for the projected cluster mass in the central 1 Mpc or so – roughly twice the equivalent mass for Coma (Hughes 1989). This plot can also be used to rule out very shallow redshift distributions as will be shown later.

As previously stated the cluster is optically poor with a total luminosity of $L_B \sim 2.6 \ 10^{11} L_{\odot}$ within a 450 kpc aperture. This is a lower limit due to possibly significant contributions from cluster galaxies with colours bluer than the cluster ellipticals – using all galaxies within this aperture gives an upper limit of $L_B \sim 1.1 \ 10^{12} L_{\odot}$ for the cluster. Combining these estimates with the measured velocity dispersion gives a mass to light ratio in solar units of $M/L \in [35{:}150]$ while the X-ray mass gives the higher values of $M/L \in [300{:}1250]$. The upper X-ray limit corresponds to closure density, while the lower is similar to that derived using dynamical methods on local clusters.
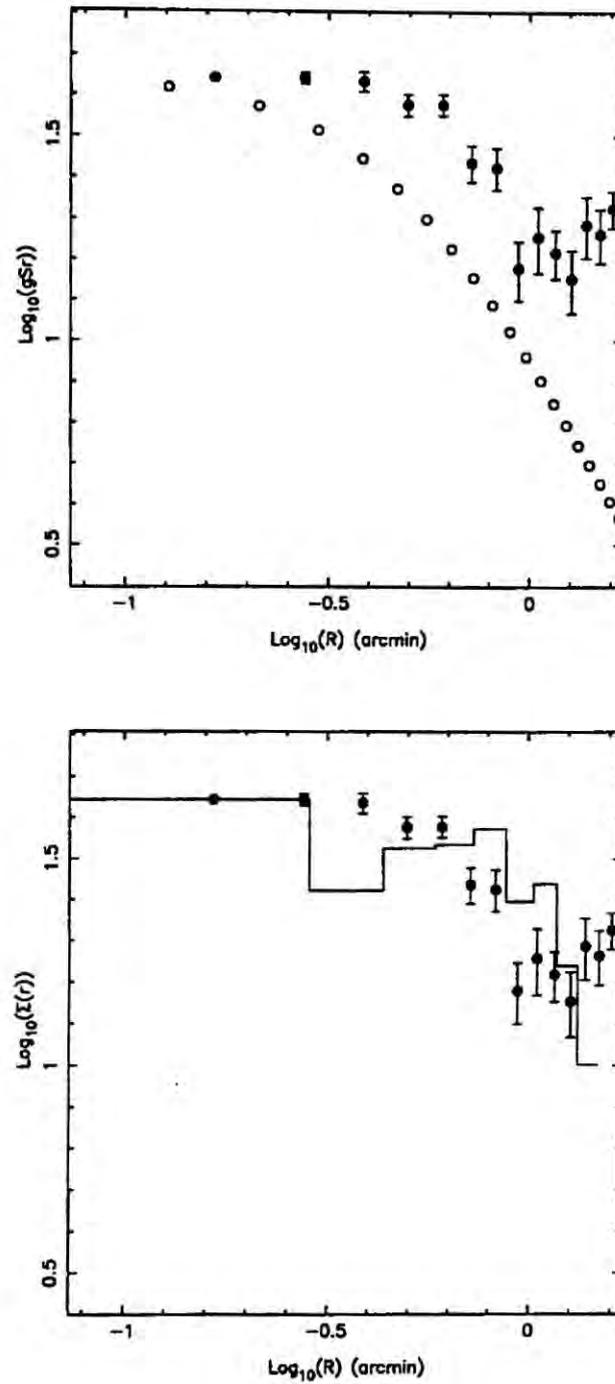
Cl0016+16

The comparison in Figure 5.20 of the lensing derived mass map with the distribution of cluster members selected by magnitude shows a large degree of similarity. The features at the top and bottom of the mass map are likely to be artifacts due to edge effects. For
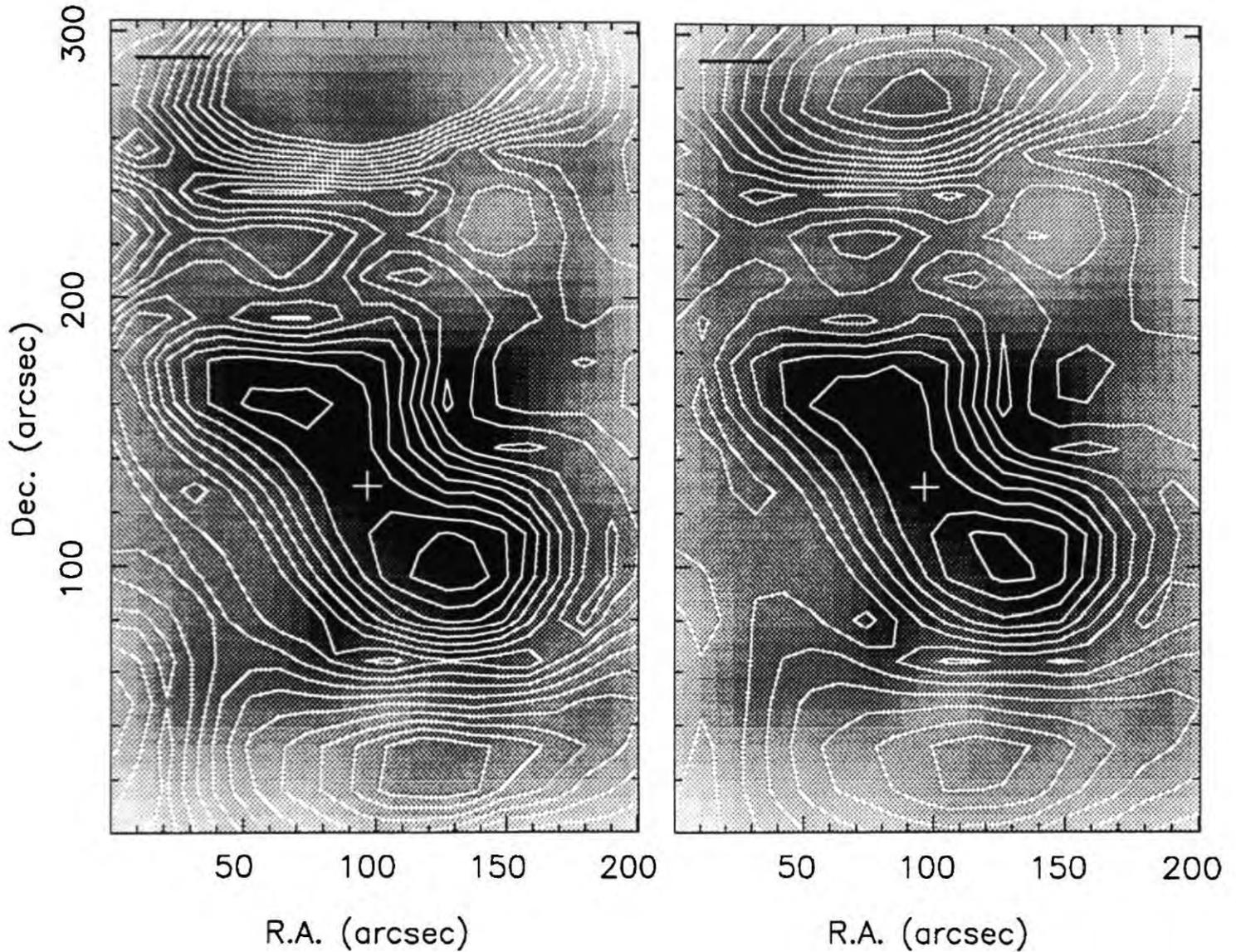
Figure 5.20 (a) The mass map of Cl0016+16 overlayed on the distribution of magnitude-selected cluster members. The map was constructed with all objects with $I \in [23, 25.5]$ and $V - I \in [-1.0, 2.5]$ using the optimally weighted ellipticities. The contour levels are in 0.5 sigma steps from zero surface density. The smoothing scale used for the mass map and the position of the structure defining the cluster centre (+) are shown. (b) The same map as above but normalised by the local estimated error.

this reason we will mainly concentrate on the structure in the centre of the field. Both distributions show an extended feature with roughly the same orientation (p.a.^{mass} ~130 and p.a.^{light} ~125). The X-ray map also shows the emission to be extended in the same direction, albeit on larger scales (White *et al.* 1981). The structure in the mass maps is strongly bimodal with the two peaks straddling the optically defined cluster centre. The galaxy distribution also shows some bimodality with the dominant mass peak corresponding to the maximum peak in the galaxy surface density. The projected separation of the two mass peaks is 0.7 Mpc. Although there is no significant velocity difference between the two clumps in the spectroscopic data of Dressler & Gunn (1992). The low resolution of the X-ray map precludes any direct comparison of the mass morphology with that of the X-ray gas on these scales, but the centre is within 15 arcsec of the optical cluster centre which would place it over the mass distribution. To compensate for the smaller field of view of this observation compared to that presented for Cl1455+22 we have taken advantage of the greater depth of this data by using a fainter magnitude limit to increase the source surface density.

Shown in Figure 5.21 are the profiles derived from the three distributions centred on their respective maxima. The X-ray profile is the fit to the surface brightness distribution given by White *et al.* (1981) and so is only included for illustration. The curves have all been normalised to the inner-most bin, the error-bars on the lensing derived profile show the spread in values at that radius. It is quite apparent that the complex core structure, the restricted field of view and the associated edge effects necessitates that any comparison of these distributions be preliminary. The galaxy distribution clearly shows a core structure with a size of ~ 350 kpc – larger than the turn-over radius for the lensing mass profile which has a scale of ~ 200 kpc. Although a blind fit for a Hubble profile to the mass gives $r_c = 295^{+95}_{-50}$ kpc – the fit is very poor with a formal probability of only 0.7%. The scale of the turn-over in the mass profile is very close to the 220 kpc core size measured

Figure 5.21 The profiles derived for Cl0016+16, the lensing mass profile is from the two dimensional map above. The X-ray profile is fit to the surface brightness profile from White *et al.* (1981). The profiles are centred on the respective distribution maxima, except for the galaxy counts which use the centre as defined by Koo (1981). The distributions are shown as: lensing derived mass (●), X-ray surface brightness (○) and galaxy surface density (histogram). No allowance has been made for the ellipticity of any of the distributions.

by White *et al.* (1981) from their EINSTEIN HRI image. A direct comparison of the mass
and galaxy distributions does not uncover any additional features in this complex system
beyond those visible in Figure 5.20. The most obvious feature is extension to the north-
west seen in the galaxy surface density distribution of the cluster centre which is *not* seen
in the mass map.

Cl1603+43

By utilising the deep completeness limit for this data via a faint magnitude cut we can
attempt to compensate for the small area coverage in this field. A reconstruction of the
mass surface density using a sample selected with $I \in [23, 25.5]$ and $V - I \in [-1.0, 2.5]$
shows a maximum surface density detection of 3.4 sigma on the edge of our field. The
highest peak in regions away from the chip edge is 2 sigma – as there are 400 grid centres
this is consistent with the noise. There is no apparent correlation between the mass map
and galaxy surface density distribution. The quoted errors are estimated using the pre-
dicted no evolution distribution for the magnitude limit and do not take into account the
edge effects. This non-detection of a lensing signal effectively rules out models combining
a massive cluster and a large fraction of distant galaxies ($z \gg 1$). The lack of lensed
galaxies may therefore arise from one of three different sources:

(1) The cluster is not sufficiently massive or compact – the very low X-ray luminosity
may indicate this. However, as we have previously noted all of the optically selected high
redshift clusters have very low X-ray luminosities compared to local clusters with similar
apparent richnesses.

(2) The data has too restricted a field of view. The maximum in the galaxy surface density
lies at the western edge of our frame, rather than being centred upon the bright wedge
of objects near the frame centre. This surface density maximum is also close to the peak
in the detected X-ray emission. As the redshift identifications have concentrated on the

wedge of objects it may be that the galaxy surface density peak to the west is associated with a foreground structure.

(3) If neither (1) nor (2) is correct then we must conclude that there are very few field galaxies beyond the cluster. An $I \in [23, 25.5]$ sample has a median redshift of: $\bar{z} \sim 0.7$ with only a quarter of the population beyond $z = 0.89$. This factor is taken into account when calculating the error. For redshift distributions with high-z tails the background fraction increases thus reducing the formal errors and making the detection more significant.

We discuss possible techniques to differentiate between the various explanations in the next section.

5.6.2   Faint Galaxy Redshift Distributions

We now turn to the comparison of the data with the simulations described earlier. We use a number of tests including a maximum likelihood technique to estimate the most likely redshift distribution for the faint galaxies in each cluster. These independent measurements are then combined to give probabilities for each of our hypotheses. This method also provides an estimate of the core radius and velocity dispersion for each cluster – we can compare the former to the value derived from the non-parametric analysis applied in the previous section.

It is apparent from the cluster mass maps that a spherically symmetric lens is not a good representation of the mass in the clusters. However, in this section we are only interested in the coarse properties of the redshift distribution of the faint galaxies. We will therefore use spherical models for the cluster simulation and compare these with observations. This will probably result in the best fit core radius being larger than reality, while the cluster's velocity dispersion fit will be lower. It would be preferable to correct the observations for

the cluster's ellipticity. However, this is not possible as the correction remaps the image positions and in doing so distorts the chip boundaries making comparisons with models very difficult.

Orientation Histograms

The simplest test to apply is to measure the fraction of galaxies aligned tangentially to the cluster centre in each of the clusters. If we make the gross simplification that the clusters are all identical lenses this directly provides the fraction of galaxies behind each cluster and hence N(z). The strong dependence of the number of observed arcs on the velocity dispersion of the lens ($N_{arc} \propto \sigma^4$, Chapter 3) probably invalidates this assumption.

We employ elliptical annuli aligned with the cluster to remove the effect of the lens ellipticity on the orientation histogram. We show in Figure 5.22 the orientation histograms for each of the three clusters. Both of the lower redshift clusters show obvious excesses of tangentially aligned images. The excess in Cl1455+22 is 189 from a total of 810 objects – a surface density of 7.0 galaxies arcmin^{-2}. While for Cl0016+16 the excess accounts for 76 out of the 356 galaxies – or 4.5 arcmin^{-2}. As stated earlier Cl1603+43 shows no aligned excess: in Figure 5.22 the histogram was constructed with circular annuli. The total aligned fractions for the two nearby clusters are Cl1455+22: 23±2% and Cl0016+16: 21±2%. These are lower limits on the fraction of galaxies behind the clusters – the Cl0016+16 observation for an $I \in [20, 25]$ sample already rules out unimodal redshift distributions which are shallower than the $I = 22.5$ distribution in Figure 5.1. While the Cl1603+43 result means the cumulative $I \in [20, 25]$ distribution cannot be much deeper than the $I = 25.5$ N(z).

We can compare these orientation histograms with analytic models of the three clusters on our three hypothetical N(z). Using a K-S test to compare the orientation distributions we rule out the Shallow distribution at the 99.7% level using the combined result from
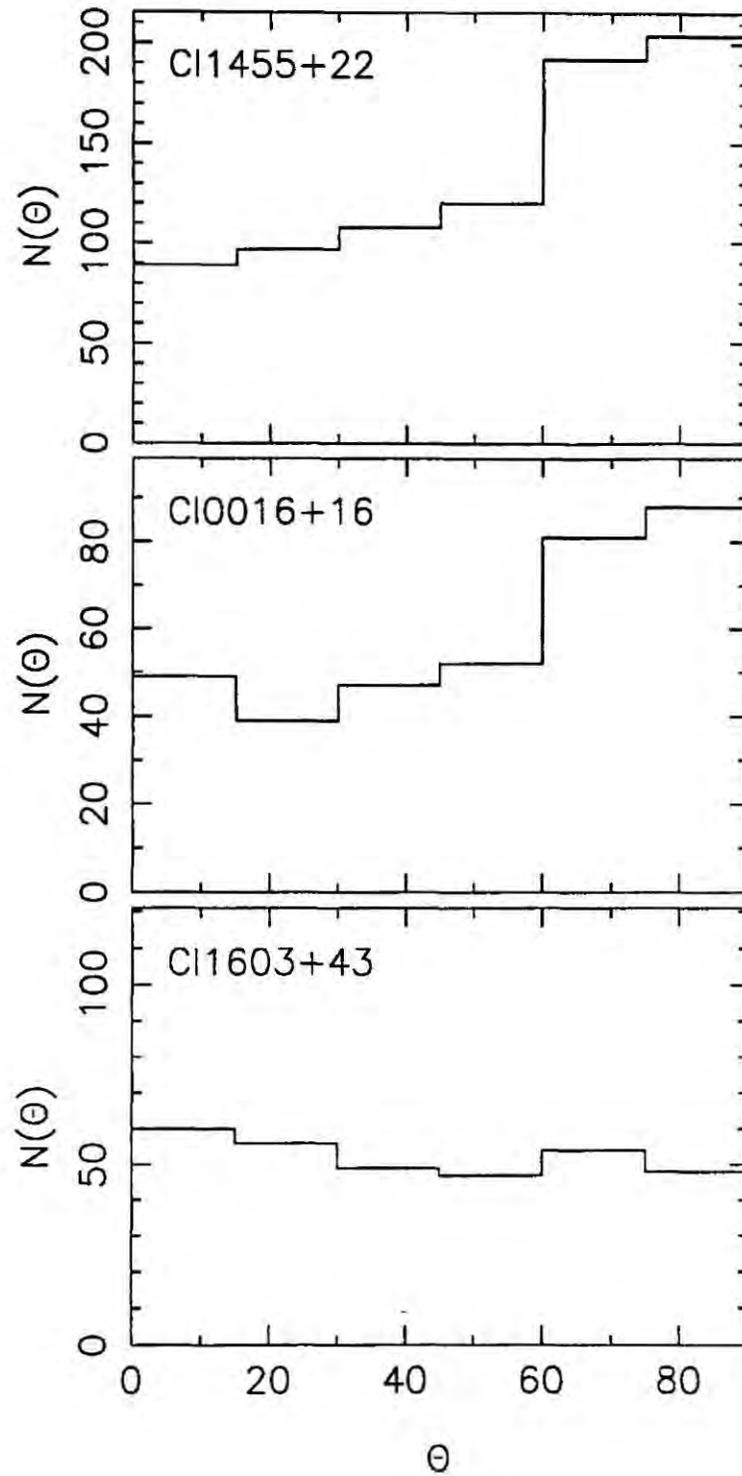
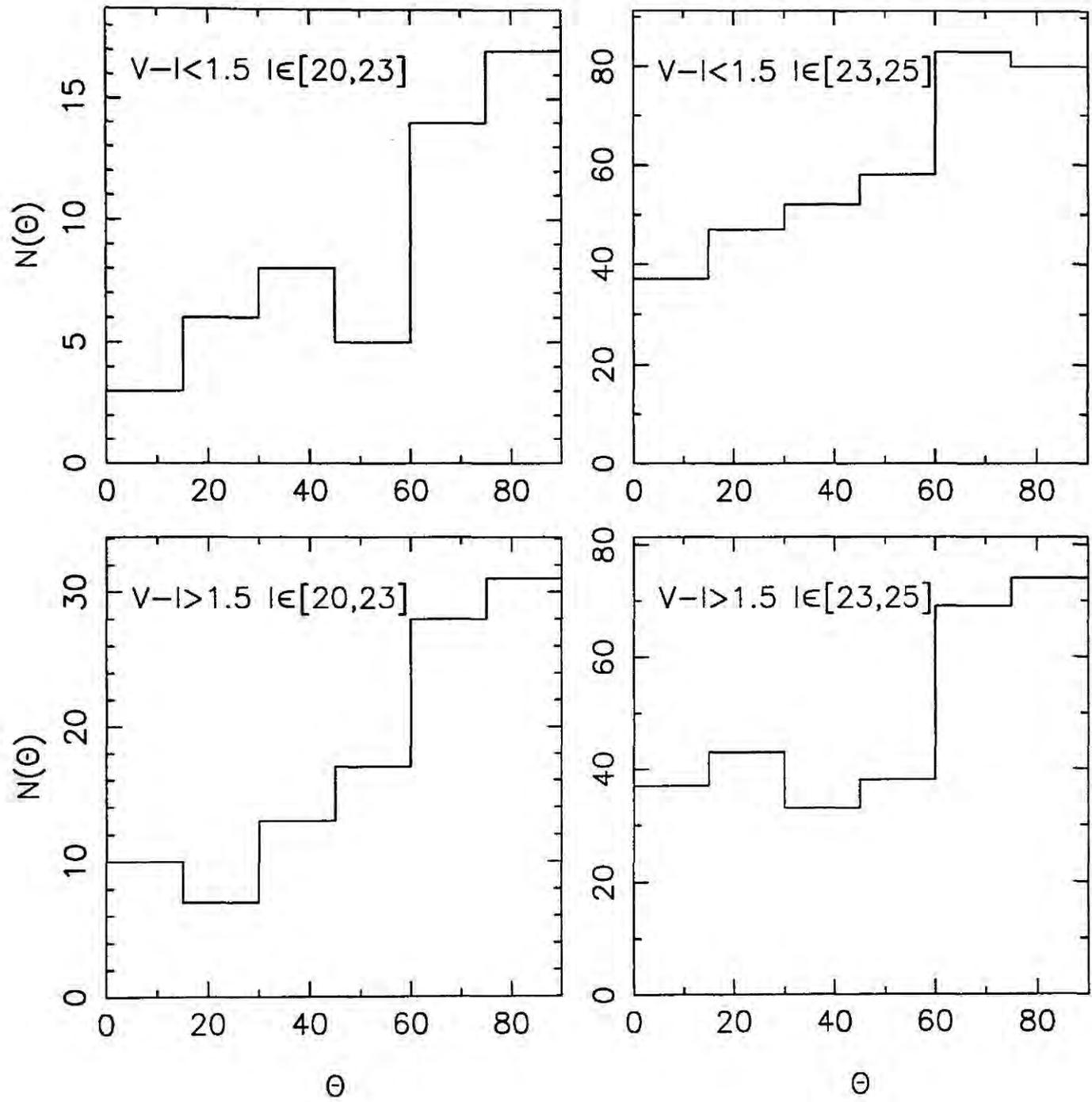**Figure 5.22** Orientation histograms for Cl1455+22, Cl0016+16 and Cl1603+43. The histograms were constructed using all objects in the field samples with $I \in [20, 25]$ and $V - I \in [-1, 2.5]$ with optimally weighted ellipticities above a cutoff of $\epsilon \geq 0.05$. The orientations and ellipticities used for the annular bins were those quoted in the text and the optically determined lens centres were used.

all three clusters (Cl0016+16 provides by far the strongest rejection). We are unable to differentiate between the Deep and N.E. models because of the possibility of a low mass for the Cl1603+43 cluster. However, if Cl1603+43 does represent a compact rich cluster we can reject the Deep model (see next section).

The signal in the two lower redshift clusters is sufficiently strong that we can sub-divide the sample to try to determine if the excess is being predominantly caused by a particular class of object. We split the samples into bluer or redder than the mean sample colour $V - I = 1.5$ and brighter or fainter than $I_{i,o} = 23$ – the point at which the colour distribution rapidly begins to shift to the blue (Figure 5.13). The four sub-classes are shown in Figure 5.23 for Cl1455+22 and Figure 5.24 for Cl0016+16.

It is readily apparent that all four classes for both clusters show a similar aligned excess and so we cannot improve the signal contrast by applying simple colour or magnitude cuts. This result can be rephrased and quantified by comparing the colour and magnitude distributions for the aligned bins ($\theta > 60$ degrees) with the other bins. Both the colour and magnitude distributions are completely consistent for the aligned and unaligned orientation bins. This is graphically illustrated in Cl1455+22 where the two most obvious arclets have colours which fall either side of the cluster member's colour. The radial distribution of the aligned component shows no variation of colour with radius in the Cl1455+22 catalogue.

We can place a strict limit on the maximum possible colour difference for the excess aligned population if we assume that they are drawn from a population with a colour distribution similar in shape to that observed in the unaligned bins but shifted to the blue. The upper limits refer to the maximum shift which could be allowed before it would have been seen. For Cl1455+22 the 90% confidence limit is $\Delta(V - I) = -0.2$, the equivalent limit for Cl0016+16 is also $\Delta(V - I) = -0.2$. Hence the aligned component cannot be drawn
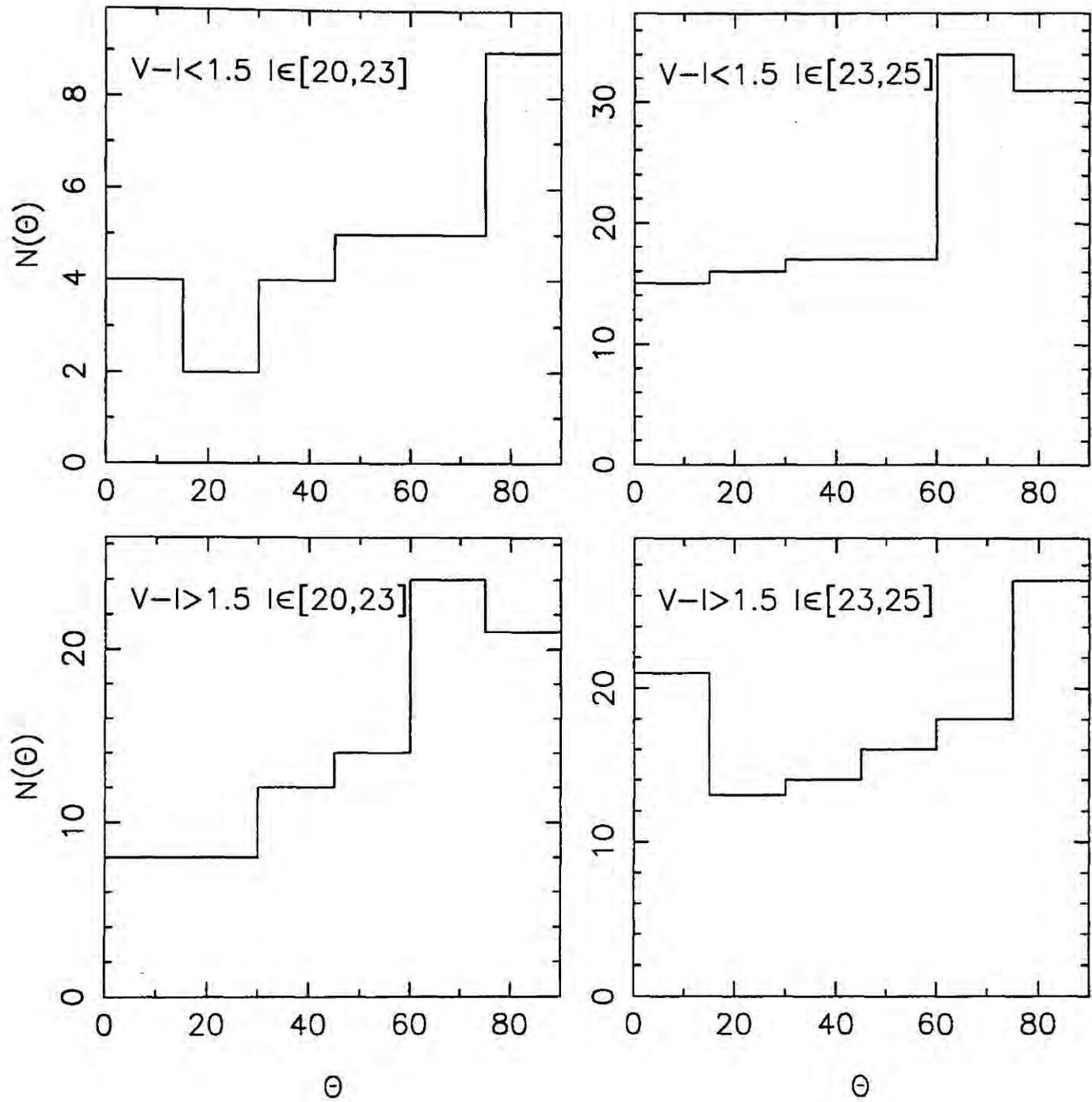
Figure 5.23 The orientation histograms for Cl1455+22 separated in terms of colour and magnitude. The aligned excess has a similar strength in all four samples showing that it has no strong colour or magnitude dependency.

from a population which is very much bluer in $V - I$ than the bulk of the population – alternatively, the strong shift to the blue seen in the field colours beyond $I = 23$ is not wholly caused by the appearence of a new distant galaxy population. This observation weighs heavily against the Deep models which have large fractions of very blue high redshift galaxies (Tyson 1988).

The relatively strong signal in the bright samples allows us to test a boot-strap method for determing the redshift of the faint galaxy population. The redshift distribution of field galaxies has been measured to $I \leq 22$ (Lilly 1992, Tresse *et al.* 1993). By applying a maximum likelihood analysis we can both test these observed distributions and use them to find maximum likelihood fits for the velocity dispersion and core radius of the two clusters. These fits can then be used to constrain the redshift distribution of fainter galaxies distorted by the clusters.

For this analysis we use all galaxies with $I \in [20, 22]$ and $\epsilon_{opt} \geq 0.05$. We apply a combined maximum likelihood estimator on their radial distribution (see Chapter 3) and orientations using K-S tests. The two input redshift distributions are the observed one (hypothesis: H_0) and a foreshortened distribution with the majority of objects between $z = 0.3$-0.4, similar to that observed in blue selected surveys (hypothesis: H_1, the $I = 21.5$ distribution from Figure 5.1). As expected the more distant cluster (Cl0016+16) is a better discriminator of the two possible redshift distributions. The foreshortened distribution is rejected at the 95% level using the combined limits from both clusters: confirming that the I selected redshift distribution probes deeper than a B selected survey. The maximum likelihood estimates for the Cl1455+22 lens parameters are $\sigma_{cl} = 1300$ km/sec and $r_c = 400$ kpc, these give a reasonable fit to the observations: $\log \hat{p}_0 = -0.1$. The velocity dispersion is also close to that estimated from X-ray mass: $\sigma_X \sim 1400$ km/sec. For Cl0016+16 the most likely fit has $\sigma_{cl} = 1800$ km/sec and $r_c = 70$ kpc with a probability of $\log \hat{p}_0 = -1.9$. Given the bimodal mass distribution seen in Cl0016+16 the low likelihood is not surprising

Figure 5.24 The separate orientation histograms for the Cl0016+16 sample. As in Figure 5.23 all four samples contain an excess of tangentially aligned objects confirming that this arises from a population of objects with similar characteristics to the bulk of the faint field population.

– although the combination of a very high velocity dispersion and very small core implies that the observed N(z) may in fact be slightly shorter than the real redshift distribution. The incompleteness in Lilly's observed N(z) is of order 10%, placing this all above the median redshift of the distribution would both solve this discrepancy and bring it closer to the no evolution prediction.

However, the maximum likelihood values for the cluster parameters from the small bright samples are sufficiently uncertain to make the boot-strap approach hazardous. A similar method using redshift information for many galaxies seen behind an ensemble of rich clusters at similar distances may provide us with a technique for probing the shape of the potential in an 'average' rich cluster. For the moment we instead move on to a single-step fit for the cumulative redshift distribution of the entire sample in each cluster.

Likelihood Analysis

We now apply the likelihood analysis described earlier to the datasets constructed from the three clusters. Before testing out three model redshift distributions we will attempt a cruder test – motivated by the hypotheses used in Chapter 3. We assume that 60% of the galaxies are distributed as the no evolution model and place the remaining 40% at either $z \lesssim 0.2$ or $z \sim 2$. The null hypothesis is that all the galaxies have the no evolution distribution. We perform the likelihood analysis using 10 realisations of each model cluster with a grid of σ_{cl}–r_c values and the three redshift models. Using the combined maximum probabilities from all three clusters we can reject the model with 40% of the population at $z \lesssim 0.2$ at the 99.3% level. The probability ratio between the model with 40% at $z \sim 2$ and the null hypothesis is $\log \Lambda = -0.82$ allowing us to marginally reject the model with a high redshift component at the 85% level.

The two hypotheses tested above are more extreme than our main models and their rejection gives us confidence that we may be able to differentiate between our three model
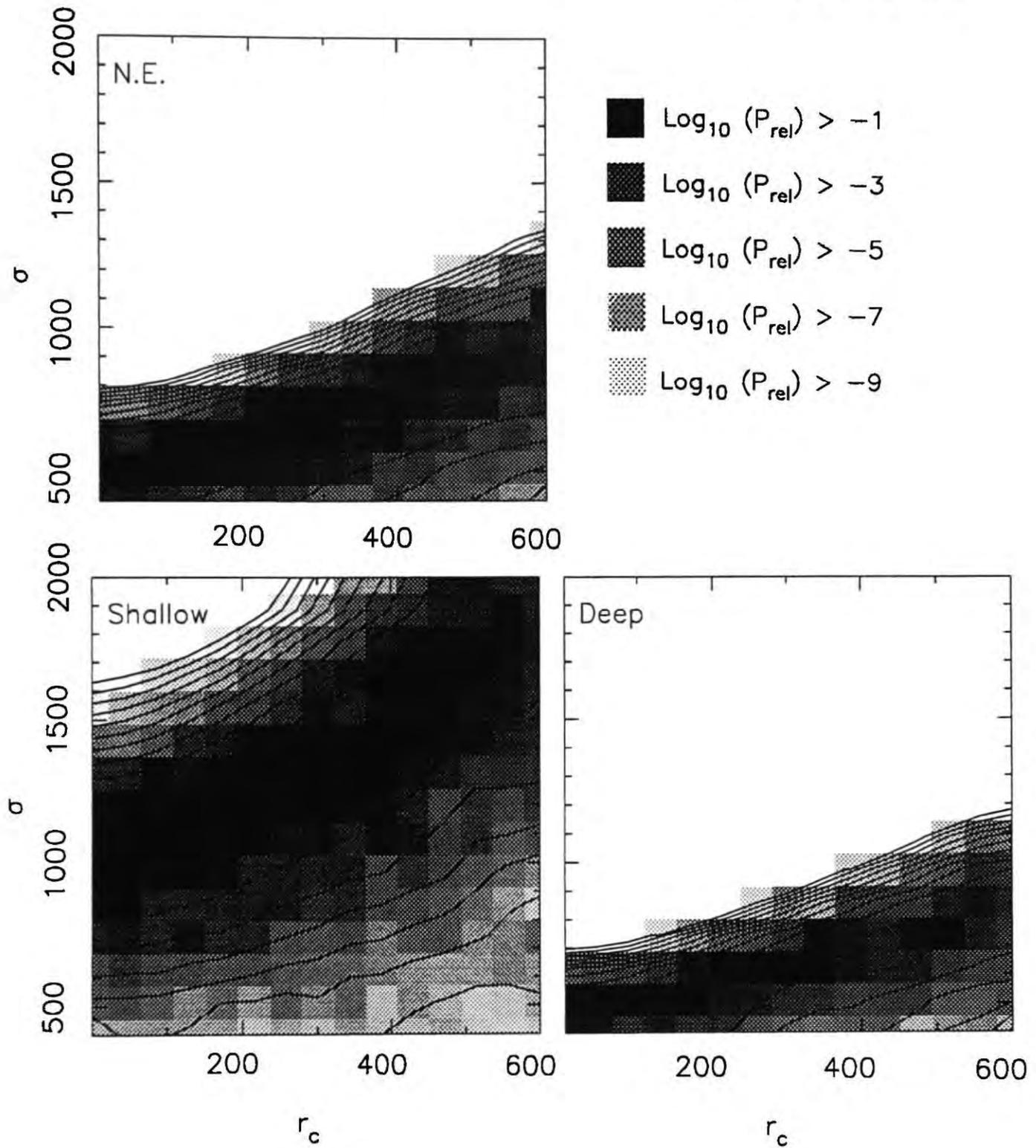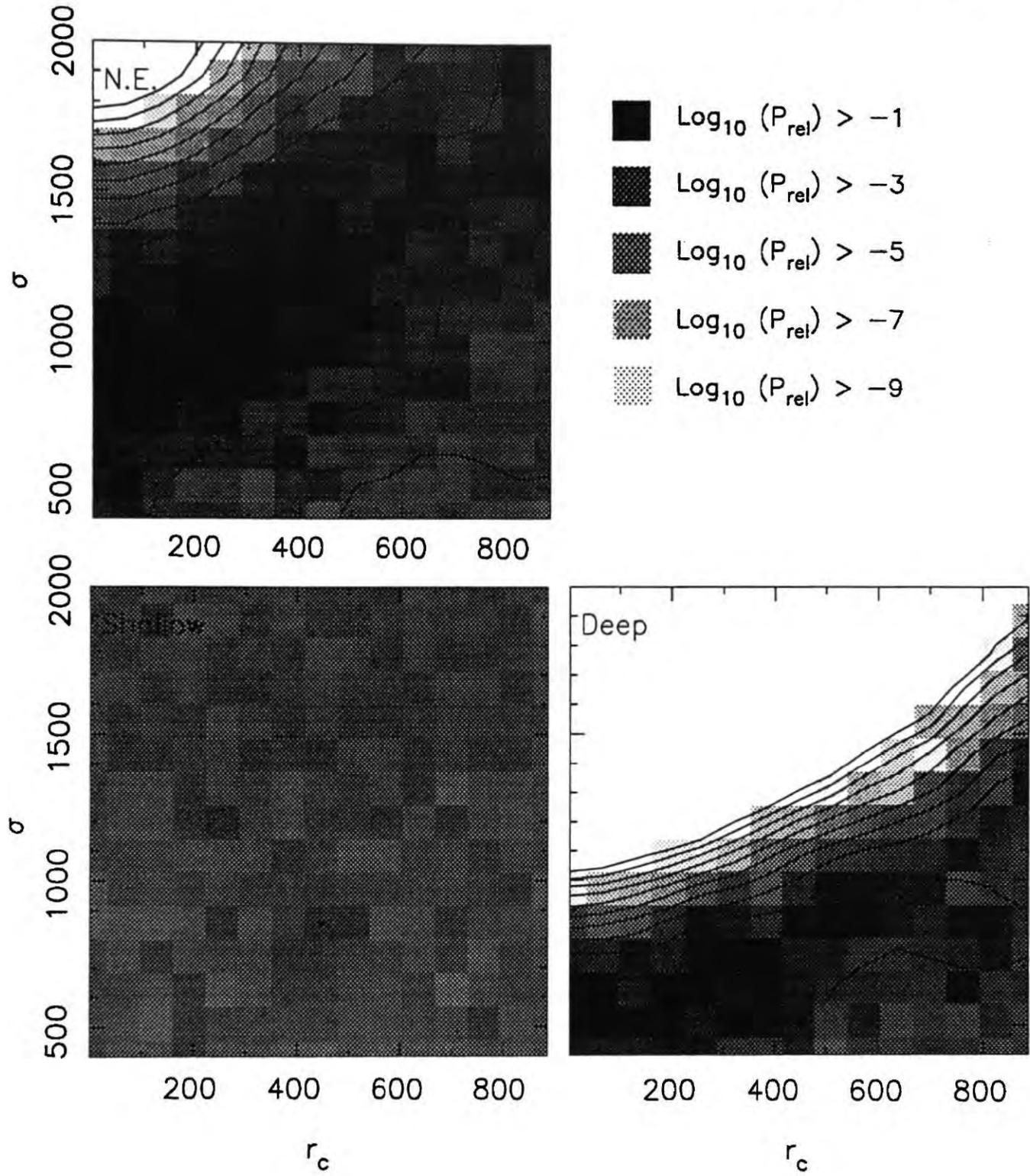
Figure 5.25 The likelihood distributions for the cluster lensing models of Cl1455+22. Each plot is for one of the model redshift distributions. The units for the axes are km/sec and kpc. The contours are for the smoothed probability distributions and are spaced every factor of 10.

$N(z)$'s. For the three clusters we use the complete $I \in [20, 25]$ samples defined above, in conjunction with FOCAS ellipticities cut on $\epsilon \in [0.1, 0.8]$. The likelihood test compares the observed distributions with those from 10 combined realisations of each lens model. This is repeated for each of the three model redshift distributions. The parameter space searched is: $\sigma_{cl} \in [400, 2000]$ km/sec and $r_c \in [0, 2]$ arcmin. The upper limit on the core radius translates into a linear distances at the three clusters of: 0.6, 0.9 and 1.0 Mpc. The rather small lower limit for the cluster velocity dispersion allows for the signal degredation illustrated in Figure 5.14.

For Cl1455+22 the shapes of the likelihood distributions (Figure 5.25) are very similar to those seen in the simulations presented earlier (Figure 5.14). The maximum probabilities for the three redshift distributions are: $\hat{p}_{shall} = -1.1$, $\hat{p}_{NE} = -0.7$ and $\hat{p}_{deep} = -0.8$. Hence, the no evolution $N(z)$ is marginally prefered over the other two models. The lens parameters for this fit are: $\sigma_{cl} = 630 \pm 120$ km/sec and $r_c = 210 \pm 40$ kpc. The quoted errors represent the grid separation searched using the models rather than formal likelihood limits which are much larger and correlated for two parameters (Figure 5.25). The best fit velocity dispersion is a strong lower limit to the actual value due to the systematic effects illustrated in the simulations above.

For Cl0016+16 the likelihood fits also resemble those from the simulations (Figure 5.26). For this cluster the maximum probabilities for the three model $N(z)$ are: $\hat{p}_{shall} = -6.2$, $\hat{p}_{NE} = -2.8$ and $\hat{p}_{deep} = -3.3$. Hence, using just this cluster we can rule out the Shallow model. Again the no evolution $N(z)$ is marginally prefered over the Deep distribution. The lens parameters for the N.E. fit are: $\sigma_{cl} = 860 \pm 120$ km/sec and $r_c = 210 \pm 60$ kpc. Again this velocity dispersion represents a lower limit to the actual value due to the systematic effects from signal degradation in the observations.

Figure 5.26 The likelihood distributions for the cluster lensing models of Cl0016+16. Each plot is for one of the model N(z). The units for the axes are km/sec and kpc. The contours are for the smoothed probability distributions and are spaced every factor of 10.
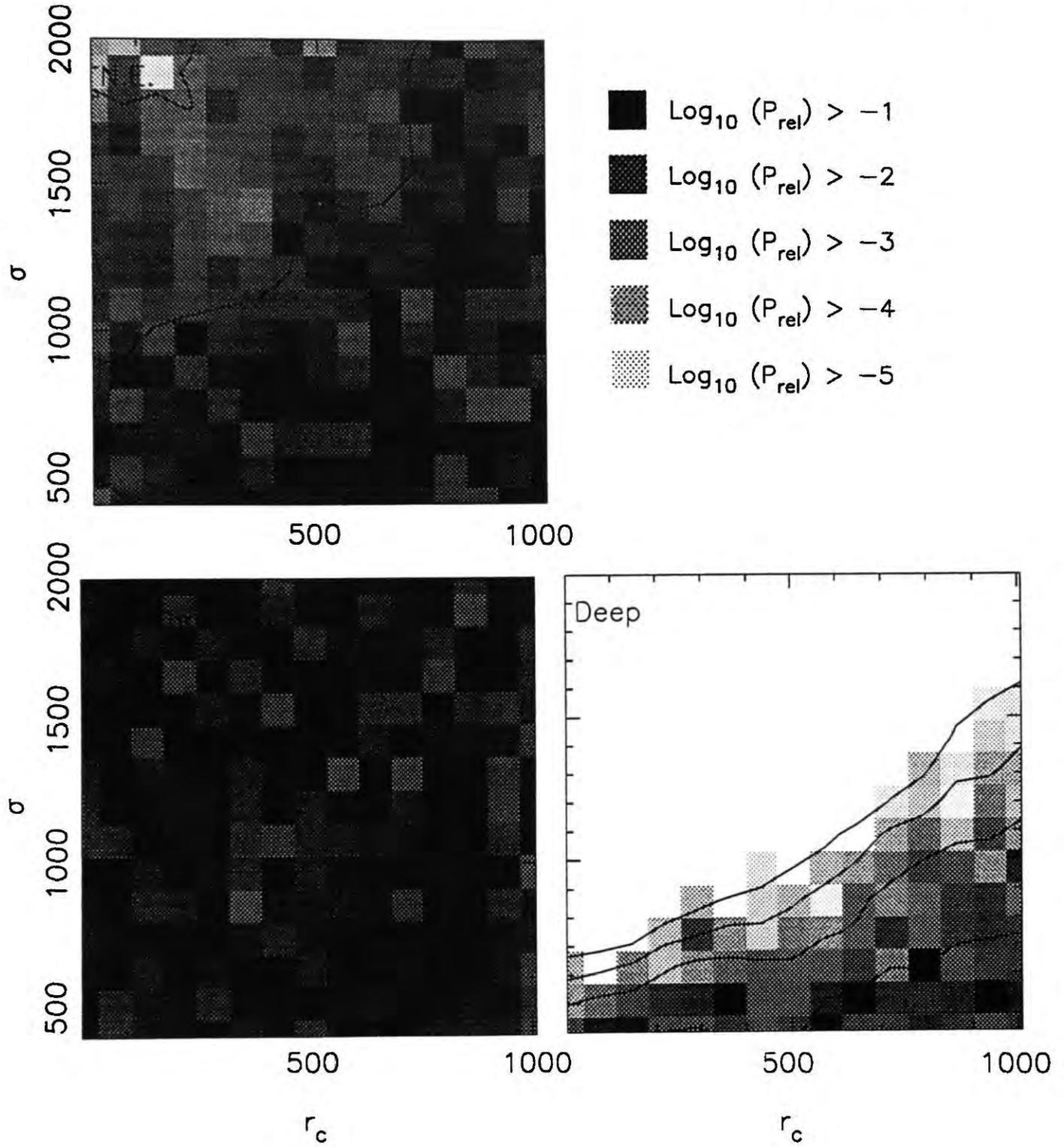
Figure 5.27 The likelihood distributions for the lensing models of the high redshift cluster Cl1603+43. Each plot is for one of the three model redshift distributions. The units for the axes are km/sec and kpc. The contours are for the smoothed probability distributions and are spaced every factor of 10.

Finally, for Cl1603+43 the three models have maximum probabilities of: $\hat{p}_{shall} = -1.2$, $\hat{p}_{NE} = -1.3$ and $\hat{p}_{deep} = -1.4$. Given the uncertain mass of this cluster we are forced to search the very wide parameter space quoted above. The best fitting cluster parameters derived for both the N.E. and Deep models have $\sigma_{cl} \sim 400$ km/sec and $r_c \sim 900$ kpc. However, it is apparent from Figure 5.27 that if a lower limit could be placed on the velocity dispersion of this cluster or an upper limit on its core radius we could strongly reject the Deep redshift distribution.

The combined results from all three clusters signifcantly reject the Shallow redshift distribution at the 99.98% level (3.8 sigma). This reinforces the statement made earlier on the basis of the orientation histograms for the two lower redshift clusters. We can state only a marginal preference for the N.E. model over the Deep distribution at the much lower significance level of: 23% (1.2 sigma). As we have argued above if we take the X-ray detection of the cluster Cl1603+43 as being indicative of a rich compact system ($\sigma \gtrsim 800$ km/sec, $r_c \lesssim 250$ kpc) then we can reject the Deep distribution at greater than the 99% level (Figure 5.27).

Calibration of the cluster parameters is possible from our numerically-simulated images for the two lower redshift clusters. This is because the relatively strong signal in these systems gives a well determined transformation from the observed lens parameters to the instrinsic lens parameters. However, for a null-detection as seen in Cl1603+43 it is impossible to perform this transformation without additional information. From the likelihood fits for the no evolution $N(z)$ we already have rigorous lower bounds to the intrinsic cluster velocity dispersion of $\sigma_{cl} > 600$ km/sec for Cl1455+22 and $\sigma_{cl} > 850$ km/sec for Cl0016+16. We create a set of simulated images for a family of clusters with different lens parameters (σ_{cl}, r_c) at the two cluster redshifts ($z = 0.26$, $z = 0.55$) using the N.E. redshift distribution. The likelihood analysis is run on FOCAS catalogues created from each of these images and the maximum likelihood lens parameters are compared to those derived for Cl1455+22 and

Cl0016+16. The input lens parameters of the simulations which most closely resemble the observations then provide the final corrected estimates of σ_{cl} and r_c for the two clusters.

For Cl1455+22 the simulation with the closest derived lens parameters to the observations had $\sigma_{cl} = 1000$ km/sec and a core radius of: $r_c = 300$ kpc as input parameters. This systematic offset of 300-400 km/sec in the dispersion is similar to that shown in Figure 5.14. However, as in that simulation the best fitting core radius appears to be representative of the intrinsic core size. The grid of core radii searched using the images is relatively coarse (300 kpc steps) so we cannot make a more accurate comparison between the core radius calculated by this method and that derived from the mass maps above. However, singular potentials do not appear to be able to recreate the observed lens parameters for a reasonable choice of input parameters. This fact and the best fitting value are both consistent with the core radius measured off the mass map. The spread in input velocity dispersion for simulations which resemble the observations is ± 200 km/sec and this is correlated with the error in the best fitting core radius (as seen in Figure 5.25). The cluster velocity dispersion is below that inferred from the X-ray derived mass although significantly above the spectroscopic value.

In Cl0016+16 the nearest simulation has an input dispersion of $\sigma_{cl} = 1200$ km/sec and a $r_c = 300$ kpc core. Again, singular models appear unable to reproduce the observed lens parameter values. The systematic dispersion offset is close to the 400 km/sec value with a scatter similar to that seen in Cl1455+22 and the core size is in rough agreement with those previously calculated for both the mass and galaxy distributions. The corrected velocity dispersion provides good independent support for the spectroscopical value measured by Dressler & Gunn (1992).

Our conclusion from the analysis of the strength of the lensing signal in the three clusters is that models predicting redshift distributions significantly shallower than the no evolu-

tion model are ruled out at a high significance. While theoretical redshift distributions deeper than the no evolution predictions are also ruled out if the models allow large mass concentrations at relatively early epochs ($z \sim 1$). We are therefore unable to reject the hierachical model of White & Frenk (1991) as their predictions of both the N(z) of the faint galaxies and the existance of high redshift clusters (from earlier work on CDM) are consistent with the current observations. However, the relatively high inferred masses for our two lower redshift clusters, in particular Cl0016+16, are inconsistent with the predictions of standard CDM with $b = 2$ (Frenk *et al.* 1990). The CDM predictions for the space densities of such systems are 10^{-8}–10^{-10} Mpc^{-3}. The absence of strongly lensed arcs in these two high dispersion clusters can be explained from their relatively large core radii $r_c > 100$ kpc. So, while the selection of clusters on X-ray luminosity does provide massive systems it does not guarantee that the cluster potential will be compact enough to create a giant arc.

5.7   Conclusions

Deep statistical lensing studies such as those presented here are both difficult and time consuming. However, they present one of the cleanest methods of studying the distribution of mass in rich clusters. The mass mapping technique of Kaiser & Squires is a very powerful and model-independent method for probing the morphology of the cluster mass.

These observations also provide us with a statistical probe into the redshift distribution of the faint field population. We can reject galaxy evolution models which have a large fraction of the faint field population ($I \leq 25$, $B_j \lesssim 27$) as dwarf galaxies at moderate and low redshift $z < 0.5$. Our current dataset is too small to provide a definitive solution

to this problem. However, our planned enlargement of this dataset should provide the answer.

• We have successfully reconstructed the mass distributions of two luminous X-ray selected clusters, one at intermediate (Cl1455+22; $z = 0.26$) and one at moderate redshift (Cl0016+16; $z = 0.55$). Both maps show significant substructure in the cluster mass distributions – this would imply significant growth in the cluster mass at relatively recent epochs.

• The morphology of the derived mass distribution shows a remarkable similarity to both the X-ray and galaxy surface density maps of the clusters on large scales. This result directly contradicts the findings of Buote & Cavaliere (1992) who claimed that galaxies did not trace the shape of the cluster potential in low redshift clusters.

• A comparison of the relative distribution of the mass and the galaxies shows that the galaxies are good tracers of the mass outside of the core of the cluster. However, in the core of our intermediate redshift cluster we find a strong decrease in the ratio of mass to galaxy surface density – the galaxies in the central regions of the cluster are more centrally concentrated than the mass. One possible process which would cause this is dynamical segregation (West 1990).

• We find in the mass map of our intermediate redshift cluster (Cl1455+22) a subsiduary peak which is not asssociated with any structure in the galaxy distribution. However, this object does appear as an extended group of faint X-ray sources in the high resolution X-ray image of this cluster. We propose that this may represent an in-falling sub-clump containing several groups which is currently merging with the main cluster. The system must be on its first pass as it would be unlikely to remain bound if it passed through the cluster centre – it would also probably have disrupted the cooling flow seen there.

• The moderate redshift cluster (Cl0016+16) shows a large amount of structure in the mass and galaxy distributions. Both distributions show a strongly bimodal distribution spanning the cluster centre. This bimodality is not visible in the limited spectroscopic dataset. The preponderance of substructure in two of the brightest X-ray clusters in the sky is an indication that such massive structures have undergone significant growth at relatively recent epochs.

• Analysis of the relative strength of the lensing signal in our three clusters allows us to significantly reject models for galaxy evolution which place a large number of dwarf systems at low redshift ($z < 0.5$). Our constraints on models with large fractions of high redshift galaxies are weaker due to the lack of detailed information about the dynamical state of our most distant cluster (Cl1603+43). This cluster is detected in a deep ROSAT exposure and when allowance is made for the strong apparent negative evolution in X-ray luminosity, compared to dynamically estimated cluster masses, at lower redshift it is not unreasonable to claim that Cl1603+43 is at least as massive as Coma. Such a statement would allow us to reject those redshift distributions which are much deeper than the N.E. prediction.

• Our prefered distribution for the faint field population to $I = 25$ ($B_j \lesssim 27$) is the no evolution model. While this model is physically unrealistic there are two models with sound physical motivation which predict redshift distributions in broad agreement with N.E. model. These are the burst model of Broadhurst *et al.* (1988) and the merger model of Broadhurst *et al.* (1992).

• The analysis of the lensing strength of our two lower redshift clusters provides a direct measure of the probable velocity dispersion and core radii for these clusters. However, these estimates are affected by systematic biases – particularly the velocity dispersion. By using simulated images we can correct for this bias to provide an estimate of the intrinsic

cluster velocity dispersions. These estimates are: Cl1455+22 σ_{cl} = 1000±200 km/sec compared to the spectroscopic value: $\sigma_{cl} \sim$ 700 km/sec and for Cl0016+16 σ_{cl} = 1200±200 km/sec compared to the value from spectroscopy σ_{cl} = 1300 km/sec. Both clusters are therefore on the extreme tail of the predicted distribution of cluster dispersions in standard CDM (Frenk *et al.* 1990). The core radii derived by this method are consistent with those measured from the full two dimensional mass distributions. These lie slightly below the canonical value of 250 kpc.

• To improve our understanding of the global properties of our intermediate redshift cluster (Cl1455+22) we plan to undertake a deep spectroscopic survey of the cluster members. This will enable us to determine if the spatial segregation seen in the core of this system is reflected in the velocity dispersion and will provide a better estimate of the cluster velocity dispersion. Identification of cluster members will also provide stronger limits on the global mass to light ratio of the cluster.

• We have demonstrated the use of weak gravitational lensing to map the mass distribution in distant clusters. Enlarging the dataset will allow us to study the prevelance of mass substructure as a function of epoch in the largest bound structures known. Such observations have a direct bearing on the epoch of cluster formation and current models of the growth of structure in the universe.

6 HIGH RESOLUTION IMAGING OF GRAVITATIONALLY LENSED GALAXIES IN THE RICH CLUSTER AC114

6.1 Introduction

We have started a deep imaging programme with Hubble Space Telescope (HST) to reveal the morphological nature of star-forming galaxies in distant clusters. The first target of this programme was the rich cluster AC114 (z=0.31). Despite the well-publicised spherical aberration affecting HST it is still capable of high resolution imaging by virtue of the sharp core of its unique point spread function. The drawback is that because only $\sim$20% of the flux in the PSF is within the core longer integrations have to be undertaken to provide high enough signal to noise in the core to recover the resolution. Here we present observations of a range of gravitational lensing phenomena discovered in the data by virtue of the excellent image quality possible with HST in such long integrations.

The gravitationally lensed objects consist of a number of candidate arcs, including confirmations of arcs in the catalogue constructed in Chapter 3, and a new very wide separation multiply-imaged system. The multiply-imaged object is currently the widest separation system known and we show the results of a multi-frequency campaign to uncover the nature of the lensed source. We also present a preliminary modelling of the potential well of the lensing cluster by application of the unique combination of gravitationally lensed objects in this cluster. We have already seen in Chapter 5 the difficulties in decoupling the effects of the lens models from those from the background N(z). Extensive observations

of the AC114 cluster may provide us with a lens with a sufficient number of constraints to solve this problem.

A plan of the chapter is as follows: in Section 2 we describe the optical dataset and its reduction. In Section 3 we examine the candidate lensed objects, including spectroscopic observations of the multiply-imaged system which confirm that both images arise from a single source beyond the cluster. While in Section 4 we discuss the modelling of the cluster lens using the various lensed objects discovered in the system. Section 5 summarises the main results and gives our conclusions.

6.2   Observations and Reduction

The rich cluster AC114 demonstrates a strong Butcher-Oemler (B-O) effect and was one of three clusters selected by Couch & Sharples (1987) for extensive spectroscopic study to understand the origin of the B-O effect. The rest-frame velocity dispersion they derive from 42 members is high, $\sigma_{cl} = 1649\pm220$ km/sec. The X-ray luminosity of the cluster from the ROSAT all-sky survey in the ROSAT band is surprisingly low at $L_x \sim 4.0\ 10^{44}$ ergs sec^{-1} considering the high mass implied by the velocity dispersion. The spatial distribution of cluster members is relatively compact with a core radius from the red cluster members of $r_c \sim 235\pm85$ h$_{50}^{-1}$ kpc, the cluster centre being dominated by a large cD galaxy. The cluster's lensing ability was first indicated in the survey for giant 'arcs' detailed in Chapter 3, where the cluster had a candidate arc with the largest radial distance in the sample. The foreground extinction from Couch & Sharples is $E(B-V) = 0.05 \pm 0.03$ and we have therefore not applied any extinction corrections to the colours presented in this chapter.

The primary data set consists of two sequences of frames of AC114 taken with the HST Wide Field Camera (WFC) in November 1991 (see Table 6.1). These WFC images were obtained to allow detailed morphological study of selected galaxies from the Couch & Sharples spectroscopic sample. The filters used for the observations were F555W, a key filter closely matched to Johnson V, and F814W, a purported key filter very similar to I. The total exposure times in the two passbands are 20.7 ksec (F555W) and 22.0 ksec (F814W). The problems with the HST mirror are well documented (Burrows *et al.* 1992) and we only note here that for the brighter objects in our frames we have high enough signal-to-noise in the narrow core of the PSF to allow very high resolution imaging using the WFC spatial sampling of $0\rlap{.}''10$/pixel. To further enhance the spatial information for selected objects we have deconvolved suitably processed images using the Lucy-Richardson algorithm (Lucy 1974) implemented by Richard Hook at ST-ECF.

The WFC frames were taken as a series of exposures at three slightly different position angles which conveniently facilitates the removal of cosmic rays and hot spots. The latter are low level single pixel features which do not flatfield out. The original standard pipeline-reduction of the data was far from satisfactory because of problems with the flatfield frames used. We therefore performed a complete re-reduction of all the frames at ST-ECF, Garching using the best matched flatfields yielding much improved frames. These were then combined using a cosmic-ray rejection algorithm to give final frames for each position angle. The frames were then rotated to the dominant orientation and median combined. This removes all the cosmic rays and a substantial fraction of the hot spots. The remaining hot spots were eliminated using the method proposed by Adorf (1991). These combined frames are not amenable to image deconvolution because the rotation applied produces an ill-defined PSF. For deconvolution we use only the deeper of the two single orientation exposures in each filter, these are only marginally shallower than the final frames.

Table 6.1 Observing Logs

HST WFC Observing Log					
Filter	R.A. (1950)	Dec. (1950)	Date	P.A.(V3)	Exposure (s)
F555W	$22^h 58^m 47\!\!\:^s\!0$	$-34°48'13\!\!''5$	19 Nov. 1991	242.464	15300
F555W				243.800	6900
F814W				244.690	13800
F814W				243.800	6900

Telescope: 2.5m HST

Instrument: WF/PC

Detector: WFC 4 TI (800 × 800 pixels)

Pixel size: $0\!\!''10$ /pixel

Danish 1.5m Observing Log					
Filter	R.A. (1950)	Dec. (1950)	Date	Seeing	Exposure (s)
B	$22^h 56^m 12\!\!\:^s\!0$	$-35°04'00\!\!''0$	22/23-23/24 Nov. 1990	$\sim 1\!\!''2$	10800
V			1985-1988	$\lesssim 1\!\!''5$	21600
R			24/25 Nov. 1990	$\sim 1\!\!''2$	2400
I			24/25 Nov. 1990	$\sim 1\!\!''2$	7200

Telescope: Danish 1.5m, La Silla

Instrument: Prime

Detector: RCA (385 × 578 pixels)

Pixel size: $0\!\!''47$ /pixel
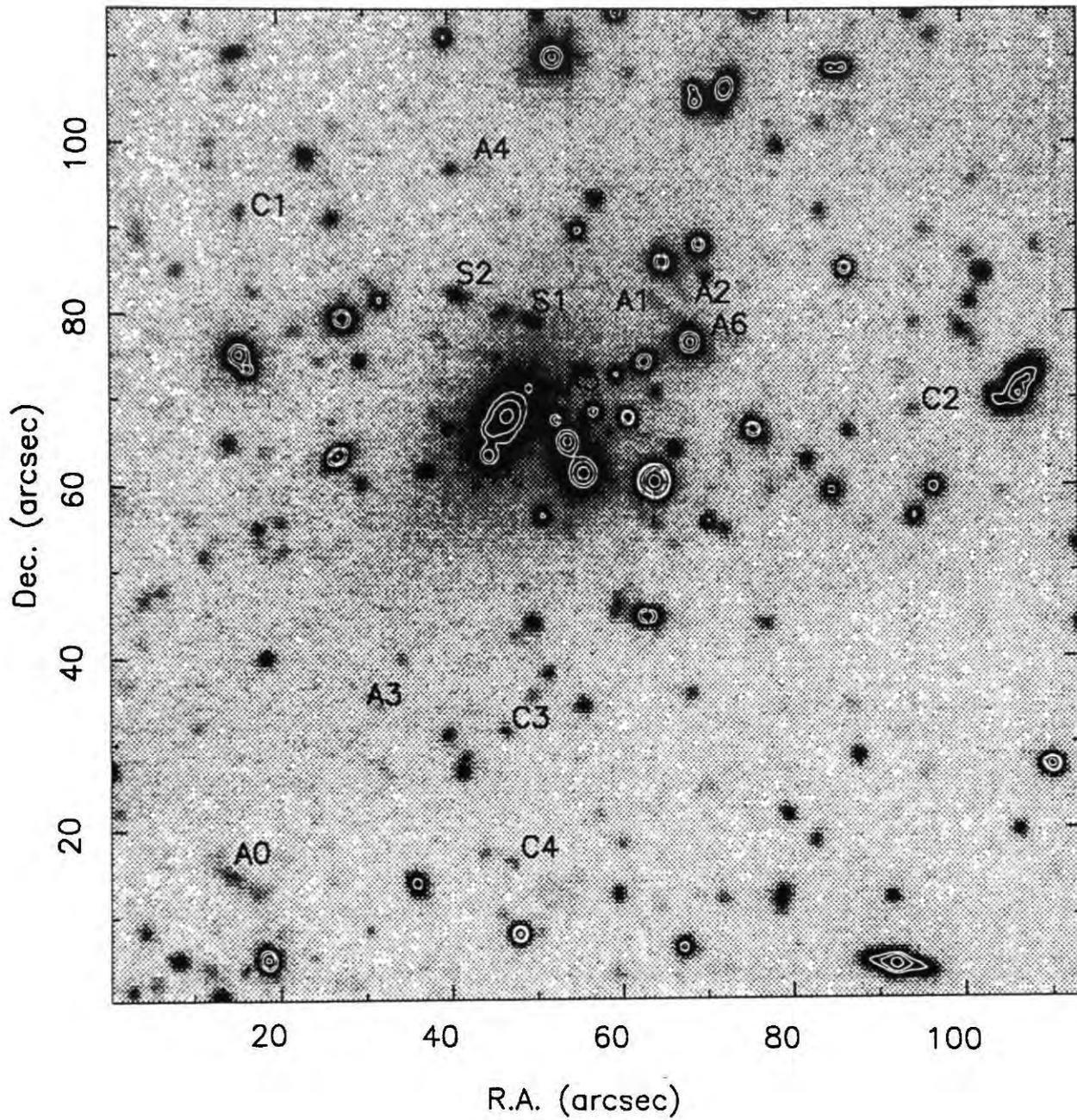
Figure 6.1 A median stacked 6 hour V exposure of the cluster AC114 taken on the Danish 1.5m telescope at La Silla. The scale is in arcseconds and objects referred to in the text are marked, east is to the left and north at the top.

The second part of the data set is a series of multi-colour ground-based frames of the cluster taken with the Danish 1.5m telescope at La Silla. The observing details are given in Table 6.1. The filters used were B, V, R and I. The V exposures (Figure 6.1) were taken over an extended period as part of the distant SNe search programme (Hansen *et al.* 1987) as discussed in Chapter 3. The other frames were taken by Henning Jørgensen as part of a follow-up to the work presented in the same chapter. This data was reduced, along with photometric standards, using standard techniques before registering and combining to give a final set of frames. We conservatively estimate that errors in the absolute zero points of the final frames are less than 0.03 mag in each passband. The R frame has low-level fringing and this results in loss of photometric precision but this is included in the quoted error. The final frames reach 1 sigma surface brightness of limits of: $\mu_B = 26.6$, $\mu_V = 27.2$, $\mu_R = 25.0$ and $\mu_I = 25.1$.

We obtain absolute calibration of the WFC data by measuring zero points relative to the Danish data in the same passband. The colour corrections being those in Harris *et al.* 1991. To perform this the cleaned WFC frame was binned up to the same spatial resolution as the Danish data and the magnitudes of a sizeable number of objects measured on both frames using a large aperture. This results in the absolute zero points of the WFC data having marginally larger errors than the ground based data, however we stress that the relative photometry of objects on the WFC frames is extremely good. Using zero points obtained in this way we estimate 1 sigma surface brightness limits in the final WFC frames of: $\mu_{555} = 27.7$ and $\mu_{814} = 27.0$.

The final ground-based images were converted into surface brightness limited catalogues using FOCAS to facilitate analysis. A similar approach to the WFC data is unilluminating as the data is highly over-sampled leading to confusion by FOCAS during object deblending. In all cases after identification of objects of interest we have gone back to the frames and remeasured photometry interactively. Where ellipticities and orientations

were required for extended objects these were also measured off isophotal contour plots by hand.

6.3 Results and Analysis: Gravitational Arc Candidates

The initial identification of arcs was performed on the F555W WFC data because of its high spatial resolution and blue sensitivity. The first step being to look for those arcs identified in Chapter 3. The frame used in that survey (Figure 6.1) shows a number of extended low surface brightness features in addition to the arcs catalogued in Chapter 3 (A0, A1, A2), these features were interpreted as highly distorted images of background galaxies. However, none of these arcs were above the surface brightness criterion for the survey and so were not included in the final catalogue. These objects are also detected on the WFC frames where the majority appear unresolved (Figure 6.2), the exception being A5 the candidate arc closest to the cluster centre – this arc may lie within the cluster core which would account for its unusual morphology – as such it could also be the counter arc of A0.

The detection of these candidate arcs, which were only marginally detected on ground-based frames, results from the excellent effective seeing provided by the narrow core of the HST PSF. For faint unresolved objects such as the arcs any degradation in the seeing significantly reduces their detectability. We can therefore use the WFC data to confirm the arc's reality and measure accurate ellipticities and orientations. The search of the WFC data produced a final list of 7 candidates whose magnitudes and colours were measured on both the WFC and Danish frames. The majority of these arcs lie perpendicular to an axis passing through the cluster centre at p.a.~45 degrees. The ellipticities and position

Table 6.2 Candidate Arc Catalogue

ID	R.A. (1950)	Dec. (1950)	$[x,y]^1$	ϵ	P.A.[2]
A0	$22^h56^m04\overset{s}{.}6$	$-35°05'07\overset{''}{.}6$	$-32.0,-53.5$	0.50	124
A1	$22^h56^m00\overset{s}{.}7$	$-35°03'59\overset{''}{.}5$	16.9,13.7	>0.9	110
A2	$22^h56^m00\overset{s}{.}3$	$-35°03'58\overset{''}{.}4$	21.1,14.6	$\gtrsim$0.9	126
A3	$22^h56^m03\overset{s}{.}3$	$-35°04'47\overset{''}{.}3$	$-16.0,-33.3$	~0.9	109
A4	$22^h56^m02\overset{s}{.}5$	$-35°03'44\overset{''}{.}8$	$-4.3,28.7$	~0.9	78
A5	$22^h56^m01\overset{s}{.}6$	$-35°04'10\overset{''}{.}1$	6.1,3.3	0.8	113
A6	$22^h56^m00\overset{s}{.}4$	$-35°04'03\overset{''}{.}1$	21.1,9.9	$\gtrsim$0.9	123

ID	M_{555}	$M_{555} - M_{814}$	$B - V$	$V - R$
A0	22.52±0.02	0.44±0.07	0.38±0.08	0.99±0.11
A1	25.19±0.22	<0.6	0.21±0.40	<1.6
A2	25.36±0.20	<1.4	—	—
A3	25.4±0.3	<0.2	0.58±0.29	<0.8
A4	25.6±0.3	<0.5	0.05±0.24	<0.0
A5	24.44±0.12	0.33±0.15	0.75±0.33	<0.9
A6	25.4±0.3	—	—	—

1)   Position in arcseconds west and north from the cD on the Danish frame.

2)   Orientation in degrees, clockwise from north.

Note: There is a 16.36 degree clockwise rotation between the Danish and WFC images.

angles being measured on the WFC data. This final list of candidate arcs is summarised in Table 6.2 and the objects are identified on Figure 6.1 and shown in Figure 6.2.

The brightest and most striking candidate arc is A0 (Figure 6.3) – this is a large image which is spatially resolved showing a high degree of structure but no measurable curvature. The arc has an unusual elliptically shaped surface brightness peak (marked as K in Figure 6.3), this region is not centrally placed and there is also a surface brightness gradient along the arc. The combined colours of A0 fit those of an unevolved late-type spiral (Scd–Sdm) in the redshift range: z~0.6-1.2. We also show colour profiles along the arc in Figure 6.3, from these it is apparent that the surface brightness peak is 0.7 mag bluer in F555W−F814W than the remainder of the arc – possibly a strongly star-forming knot. The orientation and ellipticity of the knot mirrors that of the rest of the arc and points to lensing as the cause. The object (S in Figure 6.3) at the southern end is a galactic K star.

The other candidate arcs, while some are too faint for good photometry, are obviously all blue and the brighter examples have colours towards the blue end of the distribution for the faint field population (Table 6.2, Figure 5.13). Most interestingly of the 7 arcs 5 appear unresolved – a similar conclusion has been reached for ground-based observations of giant arcs (Wu & Hammer 1991). However, our observations push the resolution limit a factor of 5-10 better than the ground-based images. This argues that either the cluster is non-singular and the arc sources are very small (scale lengths $\lesssim 0.1$ arcsec) or that the cluster is at least as compact as a singular potential and the sources have scale lengths consistent with those observed at brighter magnitudes (see Chapter 4 for a discussion). Given the faintness of these arcs no definite conclusion can be drawn from the present dataset, however it does appear that the cluster mass distribution must be fairly compact ($r_c \lesssim 100$ kpc).
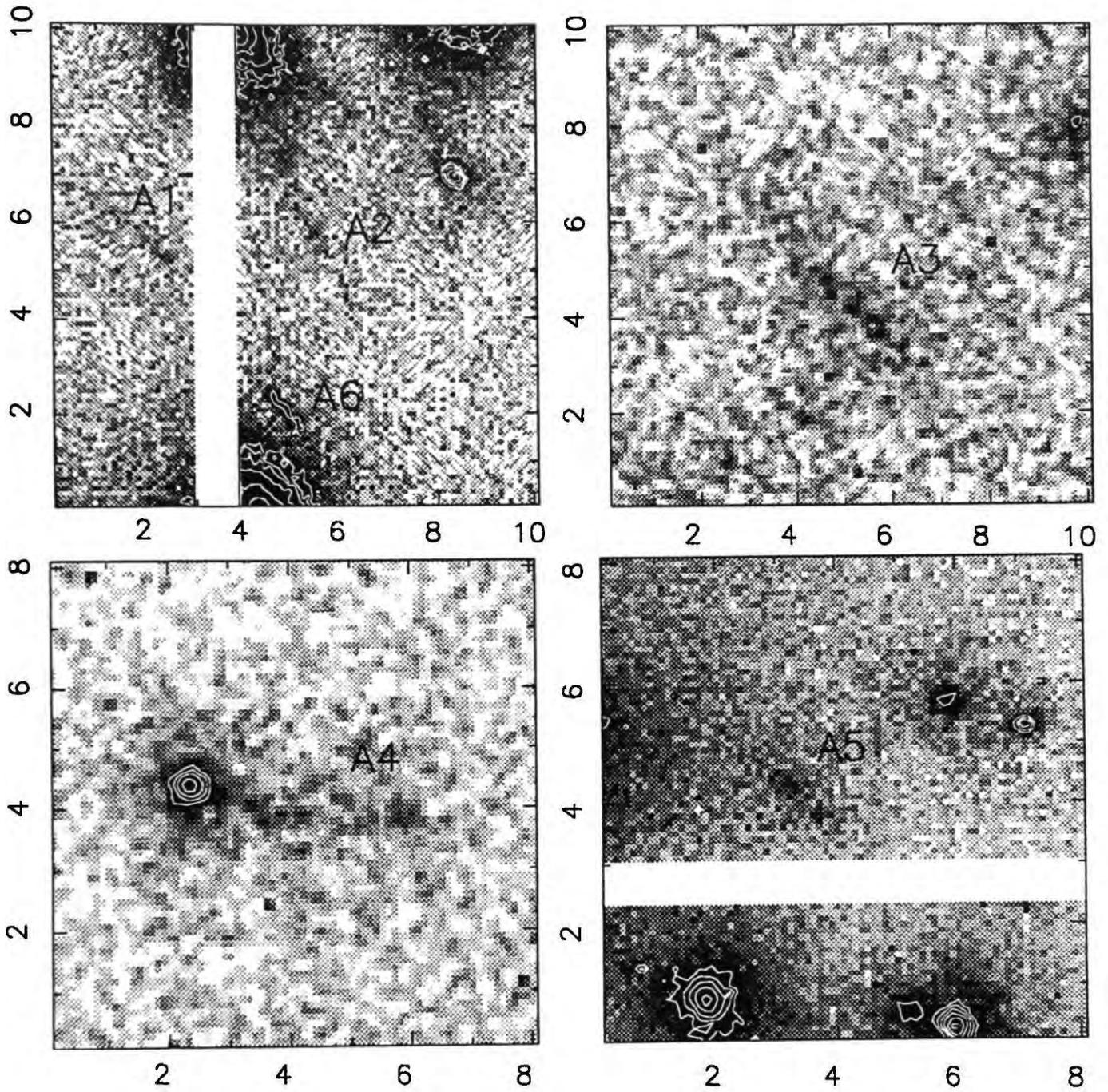
Figure 6.2 Unrestored F555W images of the candidate arcs discovered in AC114. A reconstruction of the giant arc candidate A0 is shown in Figure 6.3. The scale is in arcsec and north is at the top with east to the right.
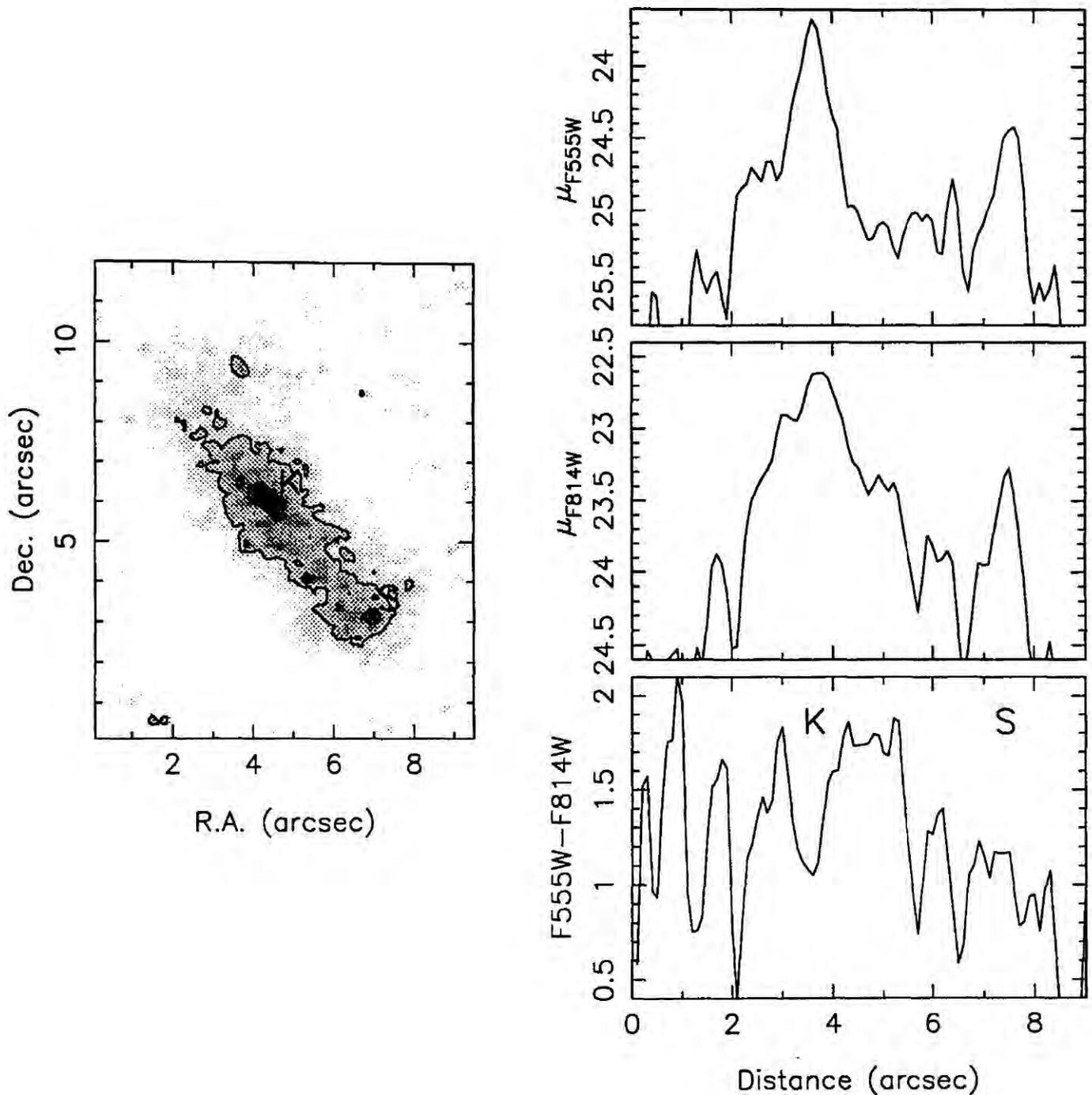
Figure 6.3 (a) A two-channel reconstruction of the WFC F555W and ground-based V image of the arc A0 performed using the Lucy-Richardson algorithm. The scale is in arcsec, features referred to in the text are marked. (b) Surface brightness and colour profiles from the raw WFC data along the major axis of the arc A0 from north to south. The profile has been convolved with a 3 pixel triangular filter to reduce the noise. The bright blue knot (K) the galactic K star (S) are marked.

6.4 Results and Analysis: Multiply-Lensed System

The most interesting candidate lensed system in AC114 is a pair of compact images about 12 arcsec north of the central cD (Figure 6.4 & 6.1). Both objects are very similar in colour (Table 6.3) with a bright compact source (S1/S2) and a fainter L-shaped extension (D1/D2). They are also very blue – the diffuse extension being marginally bluer than the compact source – and both appear unresolved. An even lower surface brightness feature with similar morphology to D1/D2 but of larger extent is apparent just above the sky noise. The separation between S1 and S2 is 10.0 ± 0.16 arcsec. The feature of these two objects which flagged them for special interest is the high degree of symmetry shown by the the combined structures S1+D1 and S2+D2. These structures are nearly perfectly mirror symmetric. This symmetry is observable down to surface brightness levels in the sky noise. We suggest that S1+D1/S2+D2 represent the lensed images of a single compact background source, possibly a faint blue galaxy or very faint AGN, with a companion or jet. We return to possible methods of distinguishing the exact nature of these objects later. The two compact objects in between (E1/E2) are much redder, with colours similar to those of cluster members.

The relative positions of the all objects of interest were measured on the WFC images – this image unfortunately does not contain the nucleus of the cD and so the position of this was measured on the Danish data and transfered to the WFC reference frame using a grid of astrometric objects. This results in a slight increase in the absolute positional errors, although the relative positions of objects on the WFC data are very good. In the modelling of S1/S2 below we retain a coordinate system defined on the WFC chips rather than converting onto the Danish frame. The colours quoted in the table are measured in a 4 arcsec aperture unless otherwise stated. In certain filters S1+D1/S2+D2 are individually too faint to obtain reliable detections and for these frames the flux from both objects has

Table 6.3 Multiply Imaged Object and Candidates

ID	R.A. (1950)	Dec. (1950)	[x,y][1]
S1	$22^h56^m01\overset{s}{.}76$	$-35°04'02\overset{''}{.}2$	6.36,9.89
S2	$22^h56^m02\overset{s}{.}54$	$-35°03'59\overset{''}{.}1$	$-1.73,15.67$
D1	$22^h56^m01\overset{s}{.}83$	$-35°04'02\overset{''}{.}0$	5.71,10.35
D2	$22^h56^m02\overset{s}{.}48$	$-35°03'59\overset{''}{.}5$	$-1.05,15.04$
E1	$22^h56^m02\overset{s}{.}16$	$-35°04'01\overset{''}{.}7$	1.96,11.81
E2	$22^h56^m02\overset{s}{.}07$	$-35°04'01\overset{''}{.}0$	3.23,12.19
C1	$22^h56^h04\overset{s}{.}6$	$-35°03'50\overset{''}{.}4$	$-23.04,31.65$
C2	$22^h55^m58\overset{s}{.}1$	$-35°04'12\overset{''}{.}0$	$45.45,-12.45$
C3	$22^h56^m02\overset{s}{.}0$	$-35°04'50\overset{''}{.}2$	$-10.44,-34.22$
C4	$22^h56^m01\overset{s}{.}9$	$-35°05'05\overset{''}{.}3$	$-14.18,-48.71$

| ID	M_{555}	$M_{555}- M_{814}$	$B - V$	$V - R$	$R - I$
S1+D1	22.65±0.02	0.86±0.06	0.34±0.09	0.72±0.11	-0.38±0.24
S2+D2	22.44±0.01	0.86±0.04	0.39±0.05		
S1[2]	24.86±0.03	0.61±0.09	—	—	—
S2[2]	24.70±0.03	0.46±0.06	—	—	—
D1[2]	25.17±0.07	0.27±0.14	—	—	—
D2[2]	25.03±0.07	0.38±0.08	—	—	—
E1	24.99±0.05	1.84±0.09	1.37±0.12	0.5±0.3	1.2±0.3
E2	24.84±0.05	1.75±0.08			
C1	23.99±0.04	0.74±0.09	0.93±0.12	< 0.4	—
C2	23.92±0.03	0.65±0.09	0.49±0.18	< 0.6	—
C3	23.57±0.08	0.61±0.07	−0.31±0.13	—	—
C4	23.77±0.08	0.71±0.14	−0.30±0.18	—	—

1)   Position in arcseconds north and west from the cD on the WFC data.

2)   Magnitudes measured in a 0.6 arcsec aperture.

been combined to give a joint colour. The combined colours are similar to those of the faint blue galaxy population, but would also be consistent with a $z \lesssim 2$ QSO.

To measure the relative brightness of the two pairs of components S1/S2 and D1/D2 we measured the magnitudes of the objects in 0.6 arcsec apertures on the F555W frame where light contamination from the cluster is minimal (Table 6.3). This gives magnitude differences of $\Delta_{12} = 0.16 \pm 0.04$ for the compact components and $\Delta_{12} = 0.14 \pm 0.10$ for the diffuse objects (S2+D2 being the brighter). These are equivalent to magnification ratios of 0.86±0.03. This result also supports the view that both objects are images of a single source as sub-components of the objects share the same magnification factor. The equivalent values for S1/S2 taken from the deep F814W frame is $\Delta_{12} = 0.32 \pm 0.07$ – roughly consistent with the F555W value given the faintness of the S1/S2 and the increased error due to contributions to the background from the cD envelope in the redder band.

To evaluate possible structure in the components we deconvolved the appropriately processed F555W and F814W frames after sinc-interpolating to a finer sampling. Analytic point-spread functions produced by TINYTIM (Burrows 1991) were used in conjunction with the accelerated version of the Lucy-Richardson algorithm (Figure 6.4). To facilitate comparison in Figure 6.5 we have rotated and reflected S2+D2 to match the orientation of S1+D1. Both objects show a strong L-shaped structure connected to a compact source, the angles of the bends in the L-shaped structures are D1: $\theta =115\pm10$ degrees and for D2: $\theta =80\pm10$ degrees. The ratio of the separations between the compact images and the peaks of the diffuse component is: $d_{12} = 0.92\pm0.04$ – consistent with the magnification derived photometrically and strengthening the case for lensing. The compact sources both show an elongated structure along the east-west direction, this may arise from a mismatch between the actual PSF and the analytic model used. A second fainter L-shaped feature with a much larger extent can be seen extending beyond the brighter structures, D1/D2.
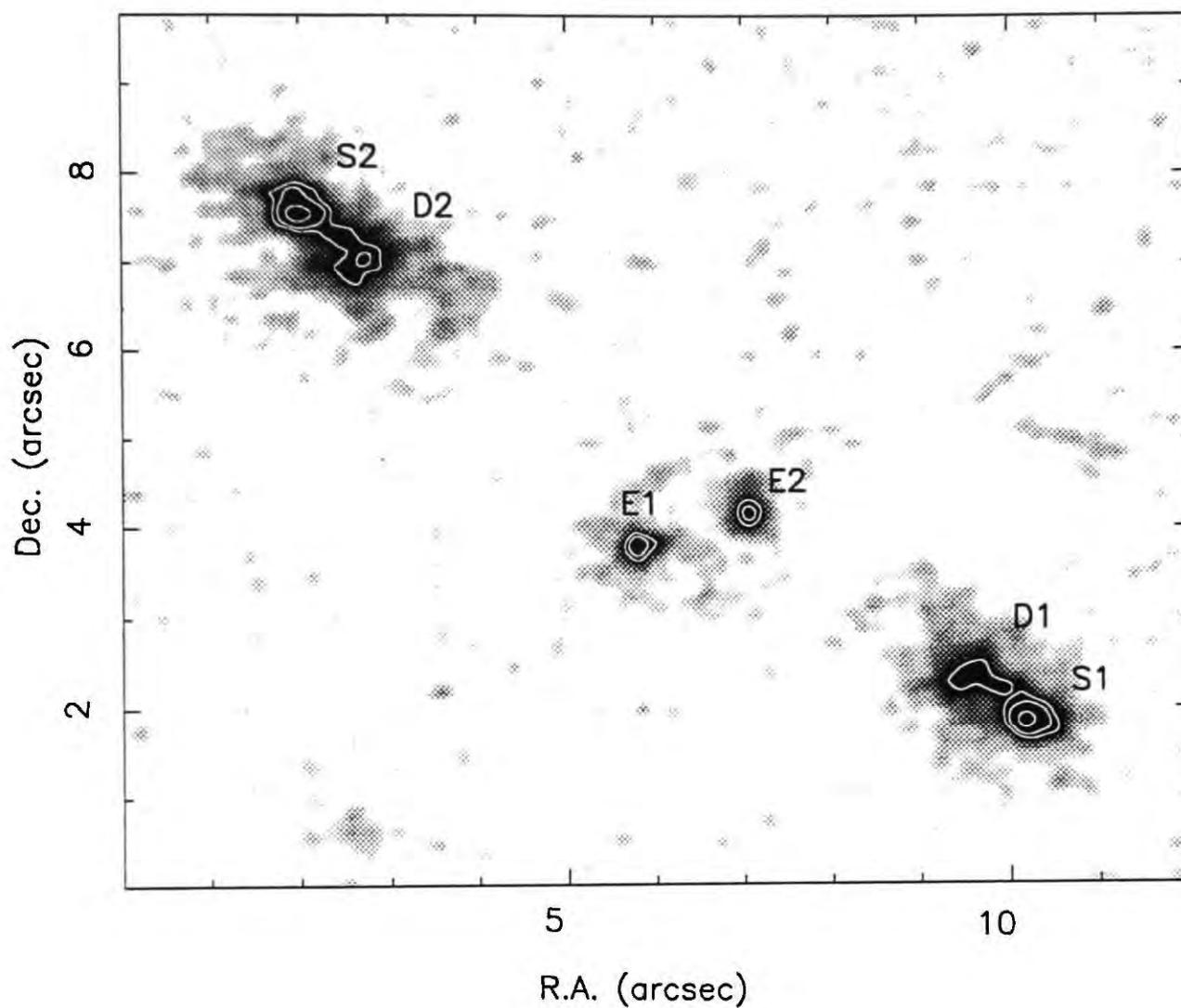
Figure 6.4 A Lucy-Richardson reconstruction of the WFC F555W image in the region around the objects S1 and S2. Objects referred to in the text are marked and the scale is in arcseconds with north at the top and east to the left.
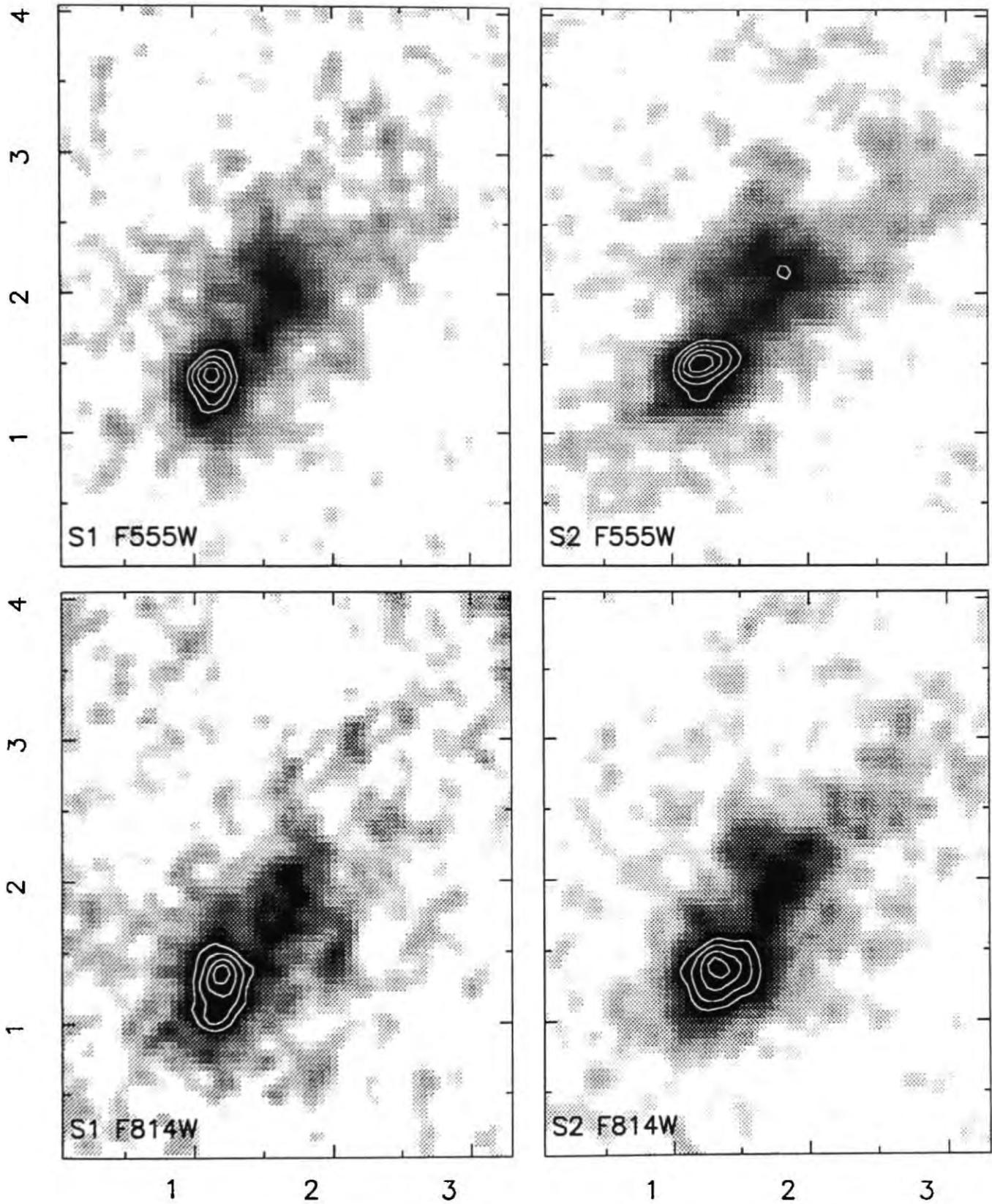
Figure 6.5 Lucy-Richardson deconvolved F555W and F814W images of S1+D1 and S2+D2, The image of S2+D2 has been reflected and rotated to have the same orientation as S1+D1 to facilitate comparison. Both compact components are elongated at the same position angle, although this may be an artifact of the analytic PSF used. The scale is in arcseconds.

To determine the nature of the source which is seen as S1 and S2 we have a number of possible avenues of attack. Spectroscopy to confirm the lensed nature of S1 and S2 by determining the source redshift would also yield line identifications, which could throw light on the mechanism powering the source. If the source is a faint AGN then it may show variability or non-thermal features such as radio emission. In this scenario D1/D2 could be a jet structure emanating from the core.

We can use the original dataset to apply one of these tests. The extended time baseline of the Danish V band data allows us to measure variations in the relative magnitudes of S1+D1 and S2+D2. These would arise from intrinsic variability of the source coupled with the different path lengths for the two images through the lens. The ground-based data spans 37 months between 1985 and 1988 in seven observations and shows no differences for the relative magnitudes above the rather large measurement errors (0.10 mag). The source therefore does not appear to be highly variable on time periods of less than three years, a fact that weighs against it being a variable QSO or AGN.

If lensing is responsible for S1 and S2 it is likely that there are more than two observable images. The blue colours of S1/S2 and their associated structures are distinctive signatures that should enable us to locate any other images if their magnifications are sufficient to make them visible. The long colour baseline of the ground-based data provide us with an easy test. We show in Figure 6.6 a $B - I$ image created by scaling and subtracting the I frame from the B data to remove the cluster galaxies. This image highlights the very blue colours of S1/S2 and allows easy identification of other possible images. There are no unidentified blue objects within a circle centred on the cD and passing through S2. The most interesting objects picked up using this technique are two faint extended structures parallel to S1/S2 and about 5 arcsec to the south east, we return to discuss these below. Complementing this approach we also searched the FOCAS catalogues of the Danish data for objects as blue as S1/S2 in $B - V$ (the deepest images) – this resulted
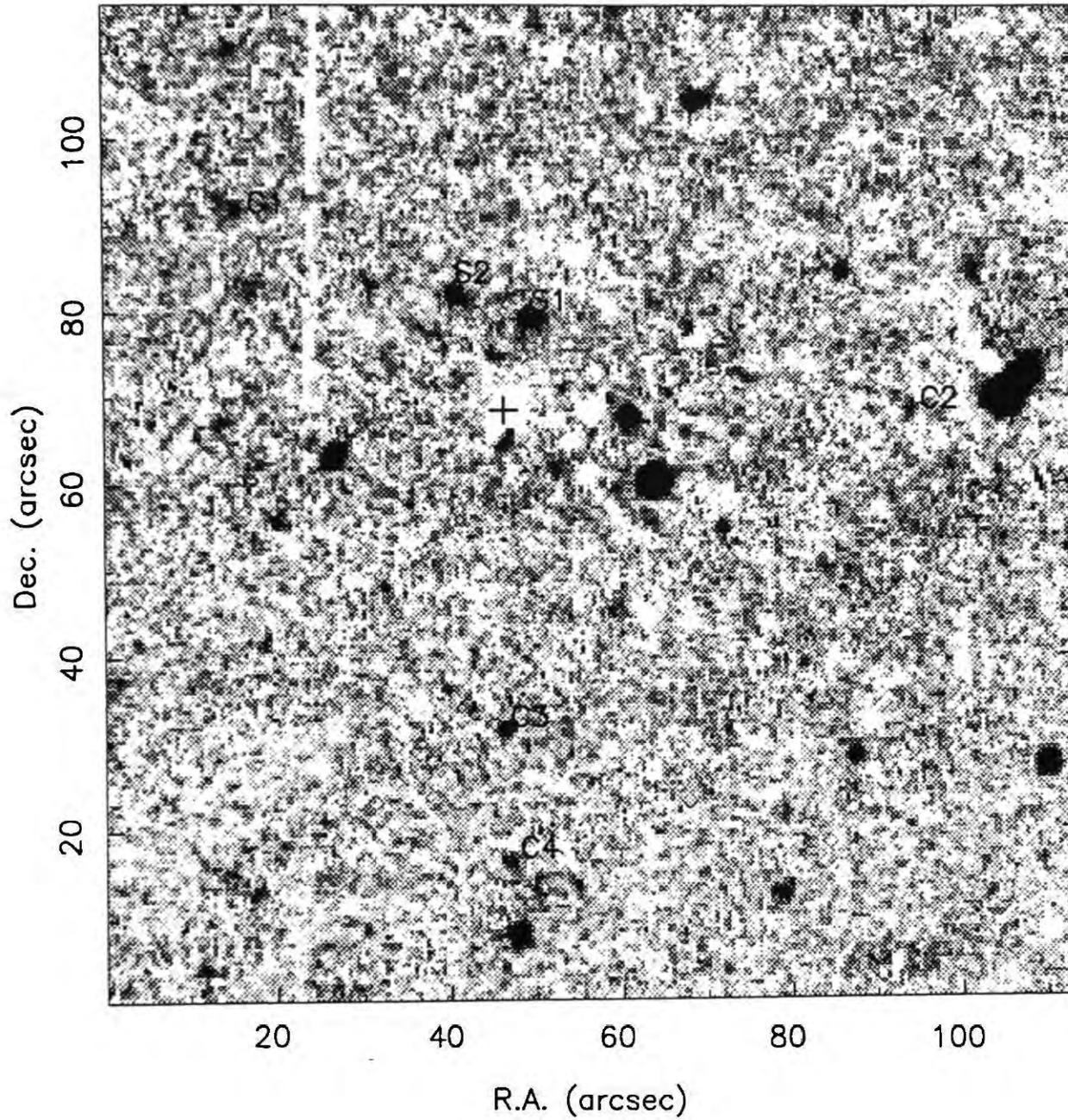
Figure 6.6 A $B - I$ image of AC114 scaled to remove the cluster members. Objects referred to in the text are marked. All objects brighter than S1/S2 are either stars or resolved galaxies. Several of the fainter objects are either tidal tails or faint arcs. The field is the same as Figure 6.1 and the position of the cD is marked (+).

in a list of $\sim$30 objects over the full 6.3 sq. arcmin brighter than $V = 24$ (a factor of 4 fainter than S1/S2). A fainter limit while giving us a larger sample of candidates and remaining within the completeness limit of the V band data would exceed the limit of the shallower B data. These catalogued objects were then located on the WFC data and their morphologies noted. Of the $\sim$30, 3 are brighter than S1/S2 – one of these is a foreground star and the other two are both well-resolved galaxies. The remainder are fainter than S1/S2 and consist of a mixed bag of Butcher-Oemler galaxies associated with the cluster, faint blue galaxies and arcs. The unusual morphology of the arc A5 and its blue colours means that we should retain this as a candidate image. A5 is also a candidate component of a multiply imaged system with A0 if the cluster is sufficiently compact.

With a view to possible slight differences in the colours of other images a visual search of the WFC F555W data was performed looking for objects with similar morphology to S1+D1/S2+D2 (compact+diffuse). It must be borne in mind that any other image may not be magnified enough for the diffuse structure to come above our limiting isophote. This search produced another list of $\sim$20 objects whose colours were then measured - those with highly discrepant colours being rejected. As a final check for faint images in the cluster centre colours were measured from the WFC data for all the objects in a 30 arcsec box centered on the cD, including all objects discernable in the cD's halo. The final list, drawn from all sources, of objects with similar colours and possible morphologies contains only four good candidates C1-4 (Table 6.3, Figures 6.1 & 6.7). One other candidate lies outside the ground based frame, nearly 90 arcsec from the cluster centre – its morphology and size are similar to S1+D1 but its brightness and colours are discrepant ($M_{555} \sim 24.9$, $M_{555} - M_{814} \sim 1.4$) and we will not consider it further.

Given its morphology, orientation and blue colour C3 is probably the best of the four candidates. In addition, the ratio of linear size to magnitude is what would be expected if C3 represented a demagnified copy of S1+D1.

Figure 6.7 also shows the fainter pair of objects to the south-east of S1/S2 – with the better resolution both objects appear to split in two.

We obviously require extra information to both test the lensing hypothesis and determine the nature of the lensed source. To this end we have undertaken spectroscopic observations of S1 and S2 using the Anglo-Australian Telescope (AAT) and radio mapping of the cluster using the Australia Telescope (AT).

Radio observations with the AT: The cluster was imaged in Director's time for 12 hours at both 3cm and 6cm with 2 arcsec resolution by Haida Liang and Warrick Couch. The maps were cleaned at the telescope and show no sources coincident with the positions of S1 or S2 down to a flux limit of $f \sim 65\mu$Jy in either map. This very deep limit effectively rules out any appreciable radio emission from the source. Both S1 and S2 are therefore obviously not radio-loud QSOs and hence are unlikely to be highly variable – in agreement with the variability results from the V band archive.

Spectroscopy with the AAT: Over the nights of 20th and 21st September 1992 a total of six hours integration on S1+D1/S2+D2 was obtained in 1.5-2.5 arcsec seeing using LDSS-1 on the AAT. The combination of the high throughput of LDSS-1 and a blue sensitive Tek chip more than compensated for the average conditions and gave us wavelength coverage from 3800-7000Å. The continum is well detected in both S1+D1 and S2+D2 – in fact the final frame is deep enough to detect E1/E2 at a high enough signal to noise to show that they are most likely cluster members. The S1+D1/S2+D2 spectra were reduced using standard routines before being sky subtracted and then optimally extracted. After fluxing the two spectra have very similar continuim shapes – showing a steep rise towards the blue (Figure 6.8), similar to that seen in extreme-uv observations of nearby star-forming systems (Rosa *et al.* 1984). The similarity of the spectra indicates that they
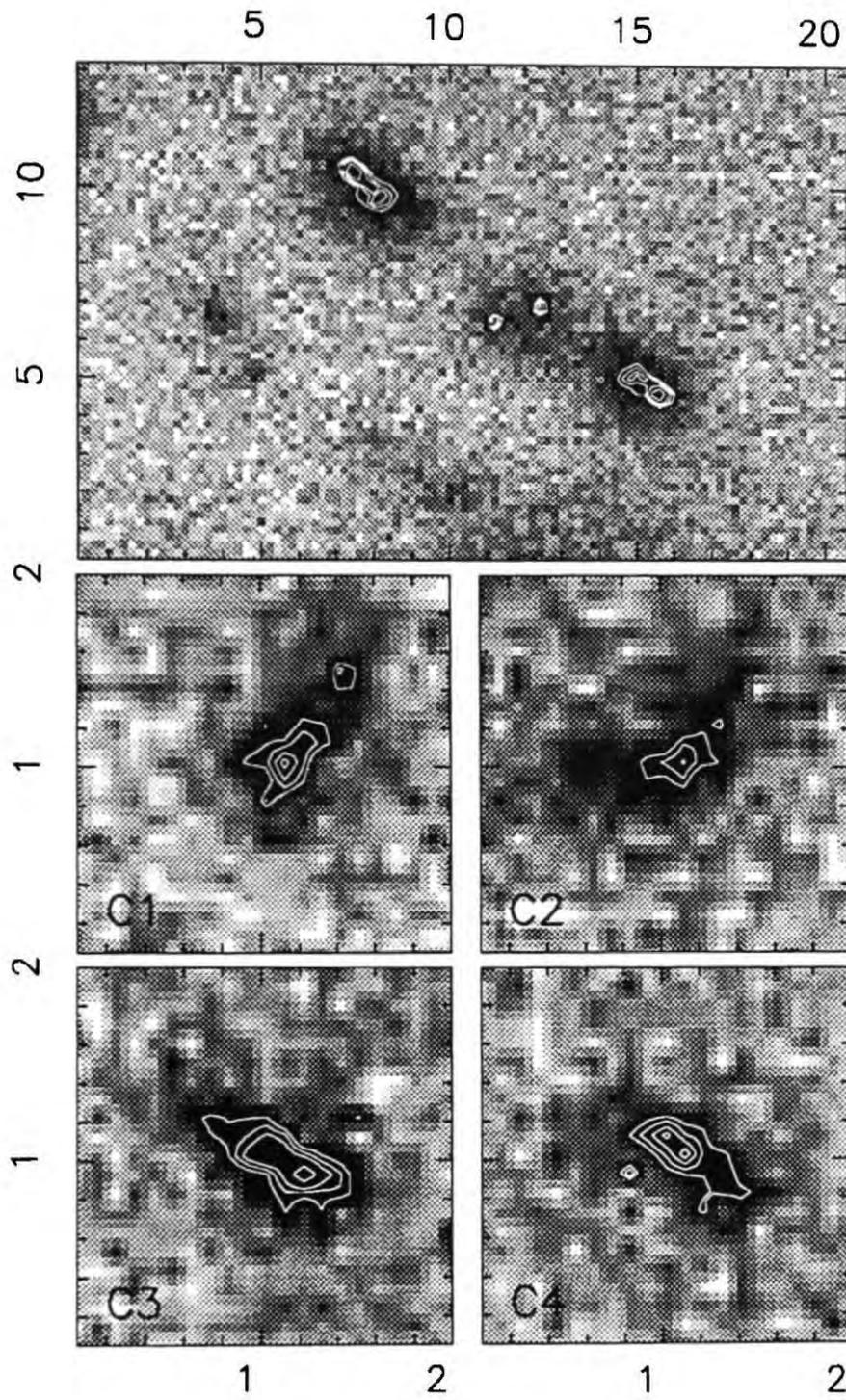
Figure 6.7 The unprocessed WFC F555W images of S1+D1/S2+D2 and C1-4. The scales are in arcseconds and east is to the left with north at the top. Notice the strong similarity between C3 and the primary images. The orientations of C1 and C2 appear perpendicular to that shown by S1+D1/S2+D2 a situation impossible to create using a single simple lens.

are likely to arise from the same source although the lack of strong features makes this statement only tentative.

To check this identification we can turn to a previous shallow observation of S1+D1/S2+D2 taken by Warrick Couch on the AAT on 4th July 1992. Using the dual-arm spectrograph with FORS and RGO camera a two hour exposure was acquired of S1/S2 in 1.5 arcsec seeing. This instrumental setup gives continous spectral coverage from the atmospheric limit to $1\mu m$. After standard reduction and spectral extraction the final combined red and blue arm spectra of both S1 and S2 also show no obvious lines. However, given the strong sky emission longward of 7000Å and our relatively low spectral resolution our detection limit in this spectral range is not particularly stringent. The continuim is again well detected in both spectra and has a similar shape in support of the objects having the same source.

We can use the source's blue colour and the lack of identified emission lines to constrain the source redshift. An absolute upper limit of $z \sim 3.8$ can be derived from the strong B detection, showing that the Lyman-limit has not entered the B band. Our spectral data has continous coverage from 3800Å to $1\mu m$. If the very blue colours of S1+D1/S2+D2 arise from star formation and the source is foreground of the cluster we would expect to see either one or more of Hα6562, Hβ4861 or [OII]3727. Therefore, we can already conclude from the lack of lines that S1+D1/S2+D2 is unlikely to be either foreground of the cluster or a member of it. The nebular emission line [OII]3727 is seen in a large fraction of the faint blue galaxy population and we would expect to easily detect this line if $z \lesssim 1$. Beyond this there is the 'spectroscopic wilderness' of strong emission lines until Lyα1216 comes into the window at $z \sim 2.2$. This limits the source redshift to be in the range $z \in [1.0, 2.1]$ where we would not expect to see any strong emission lines in our window.
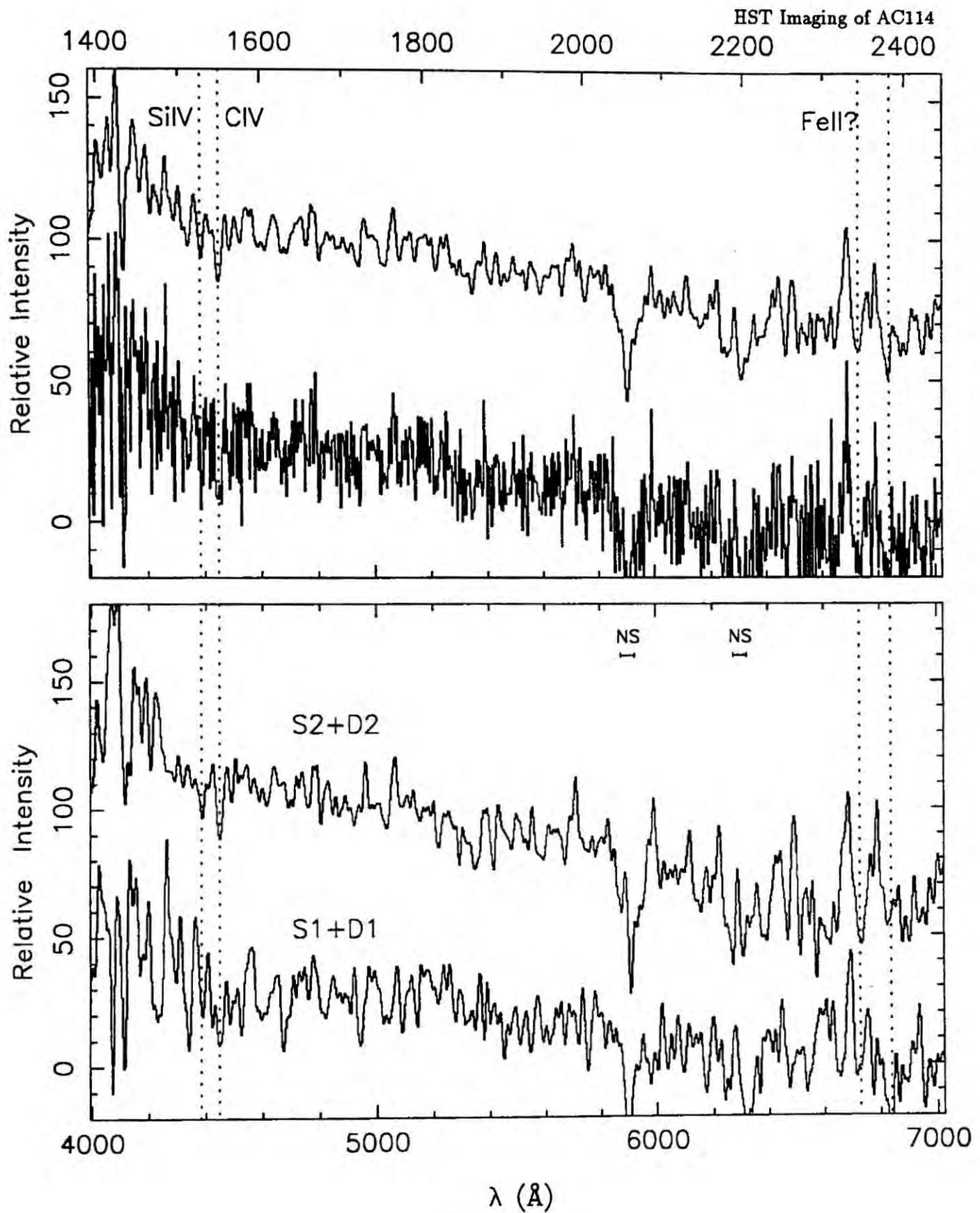
Figure 6.8 The top panel shows the fluxed 6 hour LDSS-1 combined exposure of S1+D1 and S2+D2, the upper spectrum has been smoothed to the instrumental resolution. The top scale shows the rest wavelength assuming $z = 1.87$. The bottom panel shows the smoothed fluxed spectra of each component.

The only significant feature which occurs in both spectra is an absorption feature at 4443Å superimposed on the rising continum. Given the redshift range derived above there are two likely candidates for the strong absorption feature: C IV1550 and SI IV 1405. The stronger of these two features in local star burst galaxies is C IV (Thuan 1986) which would give a redshift of $z = 1.87$. This would put Lyα outside our spectral range, with [OII] appearing at the limit of the FORS spectrum where it would be swamped by the sky emission. However, a comparison of general features of the spectra with IUE spectra of extragalactic HII regions (Rosa *et al.* 1984) supports our identification. In particular the shape of the continum and the break at $\lambda_{rest} \sim 1850$Å point to the source redshift lying in the range $z \in [1.7, 2.1]$.

The conclusions from the spectroscopic data are that the both S1+D1 and S2+D2 show very similar continuim shapes including a single absorption feature which occurs in both spectra. This evidence is convincing enough to conclude that both objects originate from one source. In addition the lack of observed lines in the spectra preclude the source being foreground of the cluster. The identification of the absorption line with C IV gives the redshift of the source as $z = 1.87$. The shape of the spectra and the very blue colours of S1+D1/S2+D2 imply that the system is vigorously forming stars. At the proposed redshift 1 arcsecond corresponds to 8.3 kpc – when the magnification factor is accounted for we are therefore probably observing S1+D1/S2+D2 on sub-kiloparsec scales.

6.5   Modelling and Discussion

Multiply-imaged sources provide strong constraints on the shape and depth of the lensing potential. A multiply-imaged source with spatially extended features is especially useful since, in addition to image separation and relative magnification, the parity shown by

the extended features must also be reproduced. In contrast, for a giant arc, the shape and size of the background source is *a priori* unknown (although for A0 the magnification is somewhat constrained now that the arc is resolved). A multiply-lensed source can, in principle, fully constrain a simple model of the lensing potential and by *inverting* the lensing equations it would then be possible to determine distances to other lensed sources in the system.

Before progressing to the numerical modelling of the system we will attempt to provide a qualitative model of the likely lensing configuration. Depending upon the model used we require information about both the mass distributions in the cluster and the individual galaxies within its core. In the absence of strong spectroscopic evidence to the contrary we assume that the source lies at $z \sim 1.87$ – the results quoted below are not strongly dependent upon this value.

6.5.1 Estimation of Parameters

Under the assumption that light traces mass (*c.f* Chapter 5) we can measure these distributions from the optical images. To perform this we once again turned to the FOCAS catalogues of the ground-based data. Colour-magnitude and colour-colour plots of all the objects on the frame showed a well defined region occupied by galaxies with colours similar to a non-evolved E/S0 at the cluster's redshift. To define the spatial distribution of the cluster we therefore used a joint $B - V$ and $V - I$ colour criterion to preferentially select cluster members. We used the positions and isophotal V magnitudes of all cluster members within a 30 arcsec square box centred on the density peak to compute a luminosity-weighted centre, ellipticity and orientation for the central galaxy distribution. These are: [6.9±2.5,3.1±5.0], $\epsilon_{cl} = 0.48\pm0.12$, $\theta_{cl} = 48\pm9$, where the errors are simulated by the removal of individual galaxies from the dataset. We also smoothed the image
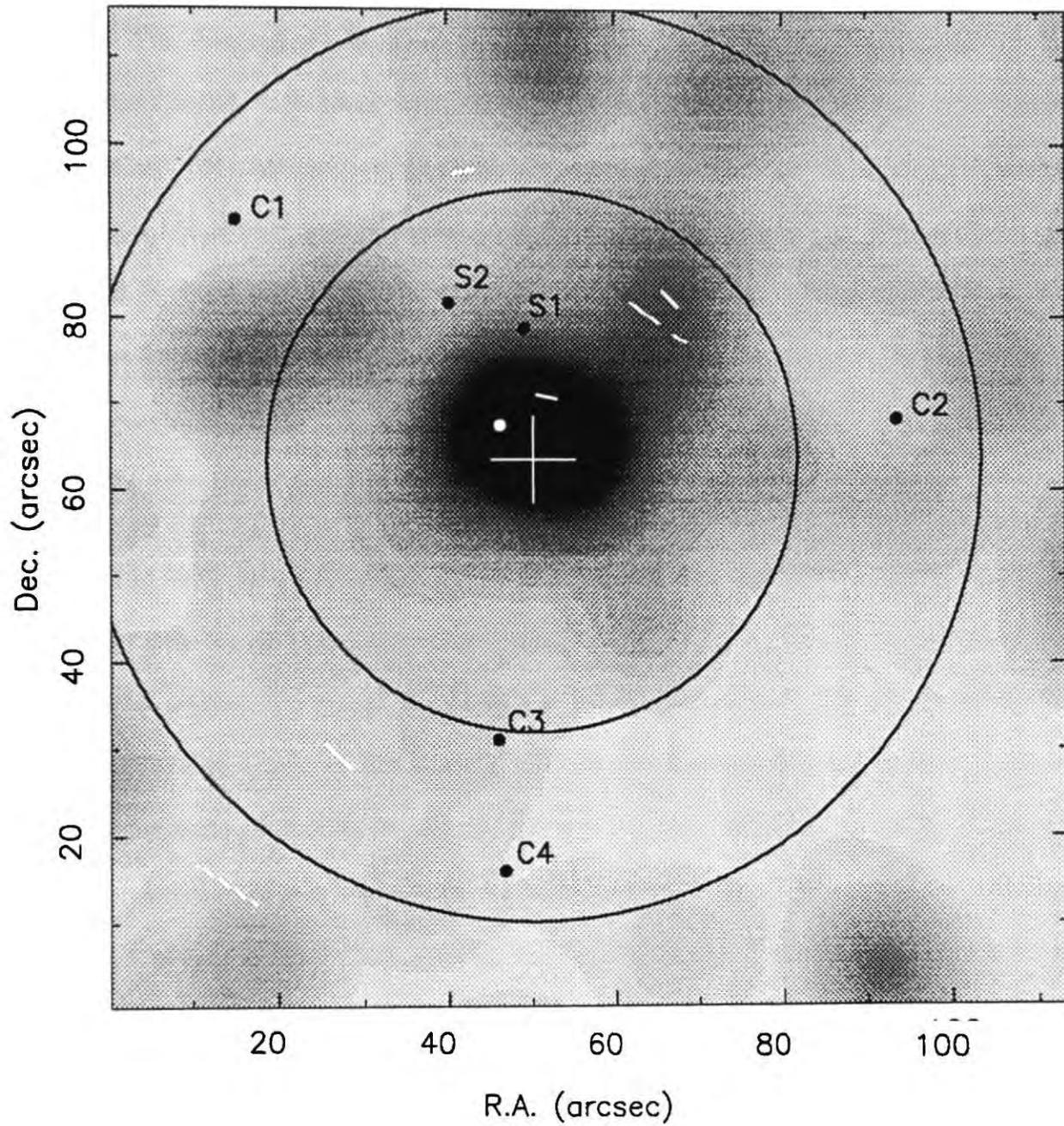
Figure 6.9 A smoothed image of the cluster member's V-band light distribution, the field is the same as that shown in Figure 6.1 and the scale is in arcsec. The two circles shown are the Einstein radii for $z = 1.87$ sources for cluster velocity dispersions of $\sigma_{cl} = 1650$ km/sec (outer) and $\sigma_{cl} = 1270$ km/sec (inner). Also marked are the positions of S1 and S2, candidate third images (C1–C4), the cD (o), the gravitational arcs and the cluster centre as measured using the giant arc candidates (+).

of the cluster galaxies V-band light distribution (Figure 6.9). The position of the centre, ellipticity and orientation from this image are: $[3.0\pm2.5, -2.9\pm1.7]$, $\epsilon_{cl} =0.17\pm0.03$, $\theta_{cl} =121\pm5$. The discrepancy between the orientations from the two distributions is due to a low surface density extension to the core in a north-west direction (Figure 6.9). Both distributions are more strongly peaked than the core radius from Couch & Sharples would imply – in fact the cluster galaxy surface density appears to follow $\Sigma \propto r^{-1}$ on the small scale covered by the CCD data. The positions are relative to the cD on the WFC frame and are given in arcsec north and west, angles are measured clockwise from the WFC Y axis. The equivalent values calculated for the cD are: $\epsilon_{cD} =0.28\pm0.04$, $\theta_{cD} =52\pm10$. The ellipticity and orientation are measured at the $\mu_V = 22.7$ mag/arcsec^2 isophote.

We can use the candidate arcs in the cluster to check some of the values derived above. In particular the most important parameters that we shall use in our discussion below are the position of the cluster centre and the cluster's velocity dispersion. We can estimate the cluster lens centre by applying Kochanek's method (Kochanek 1990) to the entire sample of arcs. The majority of arcs in the sample have very high ellipticities and effectively over constrain the position of the lens centre, we therefore artificially reduce their ellipiticities to obtain a reasonable agreement on the lens centre from all the arcs. The resulting maximum likelihood position is $\sim$7 arcsec south west of the cD (Figure 6.9). To estimate the cluster velocity dispersion we follow the method used in Chapter 3. We perform a maximum likelihood fit to the observed radial distribution, measured from the cD, of the whole sample with a $V =25$ no evolution N(z) and a singular isothermal sphere lens model. This gives a maximum likelihood estimate of $\sigma_{cl} = 1450$ km/sec, which falls to $\sigma_{cl} = 1270$ km/sec if A0 is discarded. While the systematic errors on this value may be large, it is independent of the spectroscopically derived figure and the proximity to that value is at least indicative of a high cluster mass.

An estimate of the velocity dispersion of the central cD can be obtained by comparing its V-band luminosity with those of low redshift cD galaxies in similar enviroments with measured velocity dispersions. We take these from the compilation of Malmuth & Kirshner (1985). The total V magnitude of the cD after the removal of contaminating objects is V = 18.2±0.1 in a 50 kpc radius aperture. This corresponds to an absolute V magnitude of $M_V = -24.2 \pm 0.2$ after k-correcting. The estimated velocity dispersion for the cD is then $\sigma = 380 \pm 40$ km/sec.

6.5.2 Qualitative Modelling

We are now in a position to investigate the various possible lensing configurations and models. The models are primarily determined by the lens parameters while the source position determines the configuration. A wide separation configuration such as that shown by S1/S2 may be produced by one of two general lensing scenarios. These are either lensing by a very compact cluster core, possibly assisted by a cluster member, or lensing by a cluster member assisted by the cluster potential. Currently the most reliable wide separation multiply-imaged system is the two-image system Q0957+561 ($\Delta\theta = 6.1$ arcsec, $z_{QSO} = 1.41$) discovered by Walsh et al. (1979) and repeatedly modelled (see Kochanek 1991 for the most recent and pessimistic attempt). This system is an example of cluster-assisted galaxy lensing, with the initial splitting of the QSO by the brightest member of a foreground moderate redshift poor cluster (recently observed by Garrett et al. 1992 and Bernstein et al. 1993) with the cluster then amplifying the separation. Narayan et al. (1984) state that this type of scenario may be observationally prevalent through a combination of selection effects and biases. A very faint gravitational arc has recently been discovered in this system (Bernstein et al. 1992) and while the original models could easily describe the lensed QSO using a galaxy-cluster scenario they are incapable of simultaneously fitting

the arc. The inclusion of a second lens associated with a background cluster at $z \sim 0.5$ further complicates the models.

The mirror symmetry shown by S1+D1 and S2+D2 cannot be created by a lens between the two images and so both images must be on the same side of the lens centre (allied) – this then rules out E1/E2 as the lens – although they may play a role in one of the models discussed below.

Model 1: Pure Cluster We start with the simpler of the two possibilities, multiple imaging from a cluster potential, this has been discussed in the literature (Narayan *et al.* 1984, Kovner 1987). Such a configuration is easily understood as just a scaled version of the models for galaxy potentials used to describe multiply-lensed QSOs. We can then apply the results of Blandford & Kochanek (1987a) on galaxy potentials to model the system.

Model 2: Perturbed Cluster A variation upon the above model contains a galaxy near a cluster critical line, this case is extensively explored by Kovner (1987) and includes a role for E1/E2 as the perturbing galaxy.

Model 3: Boosted Galaxy These models consist of a galaxy in a marginal cluster (one incapable of multiply-imaging itself) and are also discussed by Kovner (1987). The galaxy-cluster models are far from intuitive, except in rather idealised situations.

The main difference between these classes of models is that in the Models 1 and 2 the cluster is itself capable of multiple-lensing, in Model 2 the galaxy can produce a strong local effect on the separation and amplification of images produced by the cluster. While in Model 3 the cluster is globally sub-critical but is locally super-critical due to the superimposed galaxy mass density. Model 3 is therefore very different and if we wish to understand the S1/S2 system within the framework of such a model we must resort to an

idealised scenario. This idealisation involves a simplification: that the cluster potential is smooth and has a core radius that is large compared to any of the scales involved. We can then approximate the cluster as a thick slab and use the formalism of Turner *et al.* (1984) to predict what the final configuration should be.

In all the three models there are two classes of configuration for S1 and S2, in the terminology of Blandford & Kochanek these are: Allied radially merging images and Allied tangentially merging images. The three models may be capable of producing one or both of these configurations depending upon the choice of centre and ellipticity for the lens components.

Configuration 1: Radially Allied In this scenario S1 and S2 are the brightest pair of three images formed by either a circular or elliptical lens. They are merging across the inner critical curve (r_-) of the lens with the third image outside the outer critical line (the Einstein radius: r_+) on the opposite side of the lens (see Figure 8.3 Appendix A).

Configuration 2: Tangentially Allied With this configuration S1 and S2 are two of five images produced by an elliptical lens. In Model 3 this would be one of the galaxies in the cluster core, with the cluster then magnifying the whole configuration. In Models 1 and 2 the cluster itself produces the images, which in Model 2 are then further magnified by a cluster member (E1/E2). In all models S1 and S2 are merging across the outer critical line of the potential. One of the other three images appears inside the inner critical line in the lens core and is strongly deamplified, while of the remaining two images, one is inside the outer critical line on the same side of the lens as the bright pair and the other outside the line on the opposite side of the lens (Figure 8.4, Appendix A). A variation on this model has three nearly co-linear bright images produced by a source near a naked cusp.

We can now explore the observable results of the various configurations and models. For the radially merging case with a single lens (Model 1) the centre must lie along the line

joining S1 and S2 – which runs roughly east-west. This is not a particularly compelling in the light of the probable centres derived above and the close similarity between light and mass distributions for the clusters studied in Chapter 5. Depending upon the choice of lens centre we could identify either C1 or C2 as the third image – both of these lie close to the line joining S1/S2, although their morphologies are not totally consistent with this hypothesis. The discarded candidate mentioned above also lies in the correct direction to be a third image – although the 1.8 arcmin separation from S1/S2 would require a very large cluster mass. However, an unaligned two lens scenario with the cluster boosting the radially allied images created by a galaxy would be compatable with the observed geometry and the likely cluster centre.

A tangentially merging configuration results in a magnification ratio for the brightest pair of $\sim$0.8 close to that observed. In this case either C3 or C4 could be possible third images, although the separations from the probable lens centre are large compared to S1/S2. The near equality in the observed brightnesses of the two images then requires that the cluster potential is smooth on scales of $\sim$10 arcsec (50 kpc), a point we return to below. In Model 2 the relative brightness of the brightest pair of images compared to the other images may be significantly larger than in Models 1 and 3 (Kovner 1987) due to local amplification associated with the perturbing galaxy.

We take the tangentially-allied case as the more likely on the grounds of both the observed magnification ratio and the probable lens centre:

For Model 1 the critical line for the cluster must pass between the two images S1 and S2. This puts a lower limit of $\sim$ 19 arcsec on the Einstein radius of the lens (from the centre defined by the arcs) – which for a $z = 1.87$ would give a velocity dispersion of $\sigma_{cl} \sim 1000$ km/sec for the central part of the cluster. We can check the approximate value for the Einstein radius by assuming that the arc A1 (which is highly curved) must lie close to the

Einstein radius – it is 23 arcsec from the centre defined above: in reasonable agreement. In this model we would also expect to observe the two other images of the source outside of the core within a similar distance from the lens centre as S1/S2. From Figure 6.6 we can place a fairly strict upper limit on the magnification of these other images – there are no candidates with $V \leq 24.7$ (2 magnitudes fainter than S1+D1) within 30 arcsec of the centre.

Model 2 requires a similar velocity dispersion for the cluster as Model 1, however the inclusion of the effect of the cluster member (E1/E2) on the magnification of S1 and S2 means that the other images could be too faint to be observed. The cluster could also be compact enough ($r_c \lesssim 100$ kpc) to create multiple images of other background objects (A0+A5 are a possible combination).

In Model 3 the outer critical curve corresponds to the Einstein radius of a galaxy in the cluster core. Assuming $z = 1.87$ for the source and the maximum value of σ_g as that calculated for σ_{cD} above, this is $r_+ \sim 2.9 \pm 0.6$ arcsec for an isothermal model. The effect of the cluster is to magnify the whole system (Turner *et al.* 1984) – leaving S1 and S2 12 arcsec from the cD – an increase in the separation of the two images from the lens of a factor of ~4-5. From Turner *et al.* we also have that the increase in the magnification of each image is proportional to the square of the increase in separation. Thus both S1 and S2 are magnified by of order ~15-25 in brightness. We would again expect to find the other reasonably bright images at similar distances from the cD – ruled out by Figure 6.6. However, if we relax the assumption that the cluster potential is flat on the scale of the splitting we can manipulate both the magnification and position of the other images.

In conclusion therefore it appears that the preferred configuration is tangentially merging and that Models 2 & 3 are most likely to be consistent with the observations.

6.5.3 Numerical Modelling

To make quantitative statments about the configuration we must numerically model the system, by using an inversion technique (Kochanek 1991). We use the simplest generic composite model consisting of two superimposed isothermal lenses: a non-singular elliptical potential representing the cluster (orientation θ_{cl}, ellipticity ϵ_{cl}, core radius r_c and scale b_{cl}) and a singular elliptical potential representing a cluster galaxy (orientation θ_g, ellipticity ϵ_g and scale b_g). For simplicity we take this as the cD – although it could reasonably be any other galaxy in the cluster core or a combination of all of them. The effects of changing the identity and therefore the position of the singular potential are discussed below. Elliptical potentials are not only the most general but are also necessary if we wish to model the images as tangentially merging – a geometry which cannot be produced by a circular lens. Our choice of isothermal potentials is due to both their simplicity and their ability to fit data obtained for both cluster and galaxy potentials from a variety of sources (Beers & Tonry 1986, Kochaneck 1991).

The inversion technique used relies on the fact that the equations for the combined potential of the system are linear in the parameters b_{cl} and b_g – which measure a combination of the lens mass and the geometry (Appendix A):

$$\phi(r,\theta) = b_g\left(r + \frac{\epsilon_g r \cos 2(\theta - \theta_g)}{3}\right) + b_{cl}\left(\sqrt{r^2 + r_c^2} + \frac{\epsilon_{cl} r^2 \cos 2(\theta - \theta_{cl})}{3\sqrt{r^2 + r_c^2}}\right) \qquad (1)$$

The position of the images is then given by solving:

$$\vec{r}_{source} = \vec{r}_{image} - \nabla_r \phi(r,\theta) \qquad (2)$$

Using the [x,y] positions of S1 and S2 and a choice of ϵ_{cl}, ϵ_g, θ_{cl}, θ_g and r_c it is possible to invert the above equations and solve for b_g and b_{cl}. These values can then be used to predict the position in the source plane of the bend-point and end of D1/D2 and the relative magnification of S1 and S2 by using:

$$\text{Mag} = \frac{1}{(1 - \delta_{xx}\phi(x,y))(1 - \delta_{yy}\phi(x,y)) - (1 - \delta_{xy}\phi(x,y))^2} \tag{3}$$

The solutions which comply with both the observed magnification ratio and predict the positions of the D1/D2 sources within the observed errors are retained (± 0.05 arcsec for D1/D2 bend points and ± 0.15 arcsec for the end points). The comparison with the measurement errors is performed in the source plane – by taking the image plane errors and demagnifying them by the magnification factor calculated for the model. For each choice of cluster centre the best fitting solution is also output – under the assumption that the errors in the measurements are normally distributed and all three measurements have equal weight. The complete process is therefore to step through the parameter space defined by x_{cl}, y_{cl}, ϵ_{cl}, ϵ_g, θ_{cl}, θ_g and r_c looking for solutions that agree with the constraints. A blind search of the parameter space was selected rather than a minimisation technique because of the unknown topology of the volume. The search of a seven parameter space is computationally intensive, however a search on a reasonably fine grid can be undertaken in an acceptable time using current workstations (a billion points a day). Having constructed a list of solutions from the coarse grid we then iterate by running the code on a finer grid centred on the previous best values to attempt to improve the solutions.

Having produced a final set of parameters and source positions these could then be used by a ray tracing program to predict the positions and magnifications of other images. A comparison would then be made with the positions of objects in the FOCAS catalogues. However, given the shallow depth of the images we prefer a slightly different approach.

We will only recognise a third image in the current if it is relatively bright – we already have a candidate list of objects (Table 6.3) – these can be used along with the positions of S1/S2 in the inversion program to determine lens parameters which are consistent with a given candidate arising from the same source as S1/S2.

6.5.4 Modelling Results

The modelling presented here is preliminary and as such is intended to be only illustrative. Initially we perform a search using just S1+D1/S2+D2 as constraints. If solutions are found the searches are repeated with the constraint from the end points of D1/D2 replaced with S1 and one of the four candidate images C1-4.

The scenarios we wish to test are: 1) a pure cluster lens or cD boosted by the cluster (Models 1 & 3) and 2) cluster lens perturbed by E1/E2 (Model 2). In Case 1 we use a fixed singular potential for the cD and allow the cluster centre to move. However, we have already chosen the cD as the second potential so we constrain its ellipticity and orientation to be close to those of its light distribution. This technique allows us to model both a two component galaxy+cluster lens (Model 3) and a pure cluster lens (Model 1) in one calculation. This is because the method allows a solution with $b_g = 0$ if it is consistent with the data. While in Case 2 the singular potential is fixed on the midpoint of E1/E2. The exact details of the parameter space searched for each model are given in Table 6.4. We will address the final possibility: a cluster lens boosting a galaxy in the cluster core, in the event that no solutions are found using the cD as the singular potential.

We take each case in turn:

Case 1: It is currently possible to fit the two images S1+D1 and S2+D2 using a range of model parameters in Case 1. We sub-divide these into different sets of solutions (orientations/ellipticities are quoted for the mass distributions):

Table 6.4 Model Parameter Space

Parameter	Case 1	Case 2
θ_{gal}	43-61	—
$\delta\theta_{gal}$	3	—
ϵ_{gal}	0.01-0.50	0.01-0.50
$\delta\epsilon_{gal}$	0.10	0.10
$[x,y]_{gal}$	[0.0,0.0]	[2.6,12.0]
$\delta x_{gal}/\delta y_{gal}$	—	—
θ_{cl}	−90-90	−90-90
$\delta\theta_{cl}$	2	5
ϵ_{cl}	0.00-0.50	0.00-0.50
$\delta\epsilon_{cl}$	0.02	0.05
r_{core} (kpc)	0-550	0-550
δr_{core} (kpc)	27.	27.
$[x,y]_{cl}$	[−20,−20]-[20,20]	[−20,−20]-[20,20]
$\delta x_{cl}/\delta y_{cl}$	10,10	5,5

• No cD: We select those solutions which have minimal contribution from the cD ($\sigma_{cD} \lesssim 200$ km/sec) – these correspond to maximum cluster lensing contribution and as such they are all super-critical ($b_{cl} > r_c$). The solutions fall into two types: one set of solutions has a 130 kpc core and a cluster velocity dispersion of $\sigma_{cl} \sim 1450$ km/sec. The cluster is centred due west of the cD [17,3], orientated at $\theta_{cl} \sim 35$ degrees with an ellipticity of $\epsilon_{cl} \sim 0.4$. S1/S2 are magnified by a factor ~ 30. Apart from the position of the cluster centre (which is too far west) these solutions look very attractive – with parameter values very similar to those derived from the light distribution in the cluster. The other set of solutions are marginal lenses producing highly magnified images ($> 10^3$). The cluster is centred close to S1/S2 (radially allied), has a very large core ($r_c \gtrsim 350$ kpc) and consequently a very high dispersion: $\sigma_{cl} \gtrsim 1800$ km/sec.

• Correct cD: These are solutions with a predicted velocity dispersion for the cD lying in the range determined earlier (for a $z = 1.87$ source) and an ellipticity similar to that seen for the light distribution. The vast majority of solutions have $r_c \in [240, 300]$ kpc, $\sigma_{cl} \in [1400, 1580]$ km/sec, $\epsilon_{cl} \in [0.3, 0.5]$ and $\theta_{cl} \sim 45$ degrees. All but one of these models are centred east of the cD and produce magnification factors of ~ 50–80.

• Cluster centre west of cD: These solutions overlap considerably with the first group of 'No cD' solutions.

The full range of acceptable solutions for Case 1 are plotted in Figure 6.10. These solutions comply with the errors on the bend-points of D1/D2, the relative magnifications of S1/S2 and the positions of the ends of D1/D2. The last constraint is not very well defined as it depends upon the differential magnification of the two sources. We therefore plot two groups of solutions – those shown as • are within the quoted errors for the end points of D1/D2, while those shown as o are within twice this error. Its is apparent that the two sets of solutions populate roughly the same region of parameter space. We show two sets

of lines on the (σ_{cl}, r_c) plane the solid line is the approximate locus of the multiple-imaging line: cluster solutions below this line are capable of creating multiple images. The dotted lines shown are the limits for the core radius from the optical data of Couch & Sharples (1987) these should be viewed as upper limits on the likely core radius. The two lines marked on the $(\sigma_{cl}, \sigma_{cD})$ plane are the estimated limits for cD's velocity dispersion. All of the velocity dispersions have been derived assuming $z = 1.87$ for S1/S2.

Case 2: No solutions were found within the errors. There are of course pure cluster models which could be tweaked by inclusion of a potential at E1/E2, but with the current constraints this is not necessary.

The $(\sigma_{cl}, \sigma_{cD})$ plane in Figure 6.10 is probably the most interesting. As the projected mass contained in the cluster core is roughly proportional to: $\sigma_{cD}^2 + \sigma_{cl}^2$, the lowest mass models are those at the bottom left of the plane. These give a lower limit to the velocity dispersion of the cluster of $\sigma_{cl} \gtrsim 1000$ km/sec. This value is on the limit of that expected for moderate redshift clusters in current hierarchical theories with standard biasing (Frenk *et al.* 1990). Since these velocity dispersions are not subject to contamination problems they promise to provide a strong independent constraint on the cold dark matter theory of galaxy formation.

We can attempt to restrict the models by a comparison of the predicted positions of additional images for each of our models with our candidate list. This is done by re-running the Case 1 simulations but replacing the D1/D2 endpoints with S1 and one of the candidate images C1-4. There are no solutions for any of the four images within the measurement errors – if we relax these we eventually get agreement with C3 and then by relaxing them even further C1. If we take C3 to be the third image then the 'best' fitting solution has: $\sigma_{cl}= 1590$ km/s, $\sigma_{cD}= 290$ km/s, $r_c = 195$ kpc, $\epsilon_{cl}= 0.2$ and $\theta_{cl} = 165$ degrees. The cluster centre lies at $[-23.0, -17.0]$ south-east of the cD – along the axis
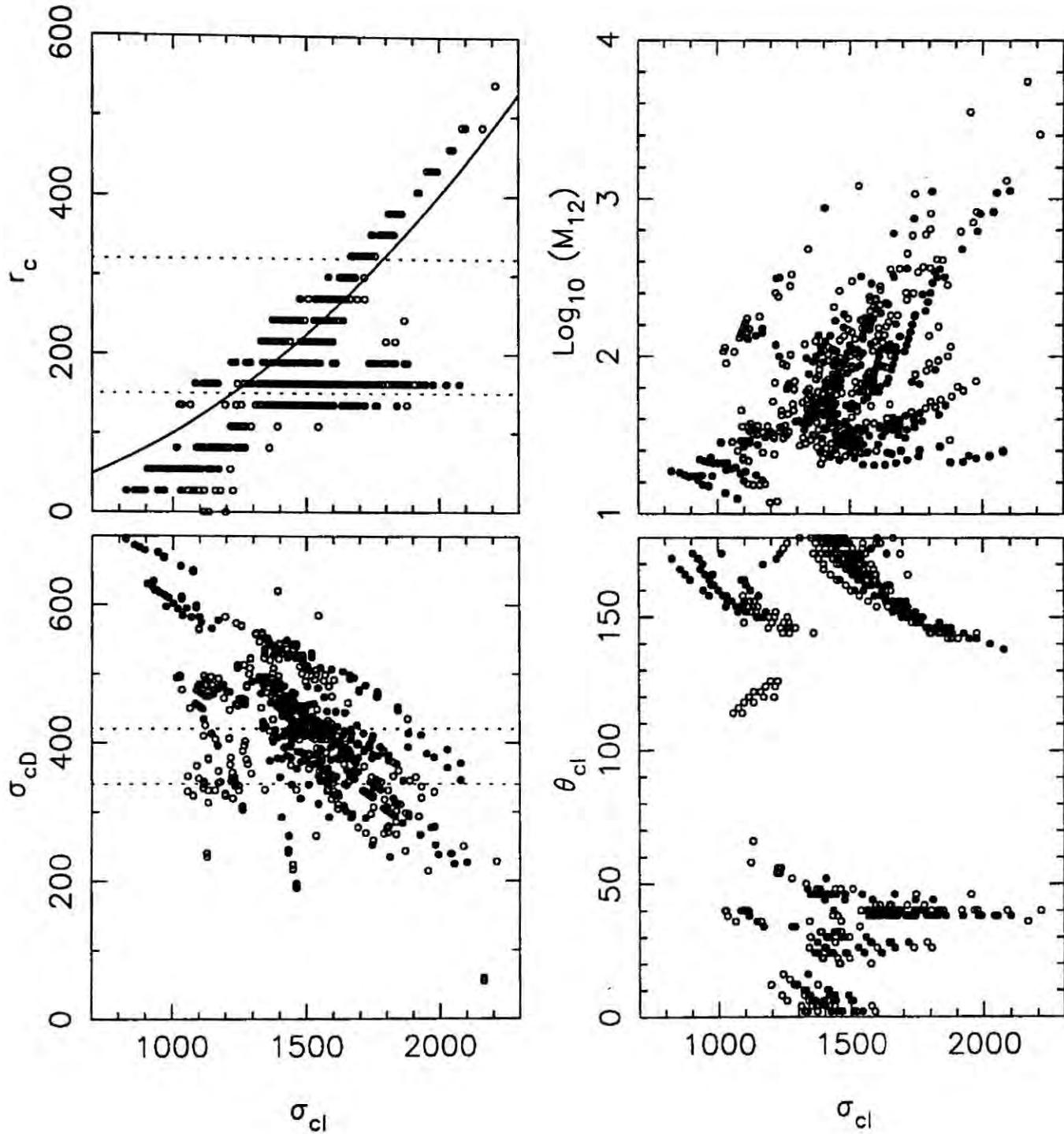
Figure 6.10 Model solutions using only the S1+D1/S2+D2 constraints. The four panels show the cluster core radius (r_c in kpc), the average magnification of S1/S2 ($\log(M_{12})$), the cD's velocity dispersion (σ_{cD}, km/sec) and the cluster orientation (θ_{cl}, degrees) all plotted against the cluster velocity dispersion (σ_{cl}, km/sec). The symbols used are described in the text.

perpendicular to the majority of the arcs. The inferred velocity dispersion is in reasonable agreement with that required to generate the arc A0 given the likely redshift range of that source. Detailed ray tracing of all the available solutions and a comparison of the positions of other images which are predicted to be sufficiently magnified to be visible awaits deeper optical data.

If we leave aside the identification of the third image, the requirement that cluster centre lies either on the cD or to the west allows only pure cluster models. The lens parameters for these models are in good agreement with those derived for the galaxy distribution: $\sigma_{cl} \sim$ 1450 km/sec, $r_c = 130$ kpc, $\theta_{cl} \sim$ 35 degrees and $\epsilon_{cl} \sim 0.4$ from the lens models compared to the values estimated from the galaxy distribution: $\sigma_{cl} = 1649 \pm 220$ km/sec, $r_c = 235 \pm 85$ kpc, $\theta_{cl} = 48 \pm 9$, $\epsilon_{cl} = 0.48 \pm 0.12$. So, even without extra constraints our modelling provides a similar conclusion to that from Chapter 5: galaxies appear to be good tracers of the mass in the centres of rich clusters. In particular the velocity dispersion from the model supports the high spectroscopically derived value: both being well outside the predicted range for standard CDM. A more detailed comparison of the mass and light distributions independent of this model will be possible by applying the techniques used in Chapter 5 to deeper optical images of AC114.

Finally, the success of the modelling supports the lensing hypothesis and shows the detail with which the mass in the inner regions of AC114 may be studied. The ease with which the cluster can be modelled also implies that the forms of the potentials used are fair descriptions of the cluster on the scales of interest: the cluster potential and hence mass distribution is smooth on scales of 50 kpc.

6.6 Conclusions

• The deep high resolution imaging capabaility of HST has provided us with a first view of gravitationally lensed galaxies, without the degrading effect of the atmosphere. Only the brightest arc in our sample is well resolved. The centre of mass of the cluster derived from this system of arcs is is good agreement with the optically determined centre.

• In addition to the arcs we have discovered a new wide separation multiply-imaged system. The separation of the two brightest images is 10.0 arcsec making it the widest system known to date. Such a wide separation between the images implies a very large mass for the lens and we argue that it either comprises a galaxy in the cluster core boosted by the cluster or the cluster itself. The source is not highly variable and does not have any radio emission.

• Spectroscopic observations of the multiple images confirm that they almost certainly arise from the same source. Identification of an absorption feature seen in both spectra with C IV1550, widely seen in extreme-uv observations of local star forming galaxies, gives a redshift of $z = 1.87$. This identification is consistent with the hypothesis that we are seeing a galaxy with a high current star formation rate. Confirmation of the redshift identification will be difficult as unfortunately both [OIII]5007 and Hα fall on strong absorption features in the near-infrared. Therefore, the best approach will be to either obtain higher resolution spectroscopy at $1\mu m$ in an attempt to find [OII]3727 between the sky lines or go after Lyα using the Faint Object Spectrograph on HST.

• We have presented qualitative and semi-quantitative arguments for the most likely configuration for the multiply imaged system. Preliminary modelling of the images using a variety of mass distributions puts a lower limit on the cluster velocity dispersion of $\sigma_{cl} \gtrsim 1000$ km/sec. Additional constraints are available if we are prepared to make assumptions about the position of the cluster centre or the role of the cD in the lensing

system. Requiring the cluster centre to lie close to that determined from the arcs leaves only pure cluster solutions. The cluster parameters for these are close to those derived from the light distribution in the cluster, a similar result to that seen in Chapter 5.

- Even for the lower limit of the range of model magnifications factors from above one WFC pixel corresponds to only 350 pc at the source. The source would have $B \gtrsim 26$ in the absence of the lens and an intrinsic luminosity of: $M_B \sim -21.3$.

- To otherwise constrain the available solutions we have used our list of candidate third images. However, there are no solutions which contain C1-4 as a third image within the errors. The closest match is for C3 – which is also morphologically the best candidate. The cluster velocity dispersion infered is in good agreement with the spectroscopically derived value. This modelling awaits the confirmation of position and magnification of the third image.

- Deeper optical images of the cluster will enable us to both confirm the identity of the third image and provide an ensemble of distorted objects to map the dark matter distribution on larger scales in the cluster (c.f. Chapter 5). AC114 is also the subject of a deep ROSAT pointing to image the hot X-ray gas in the cluster. A well constrained lensing model is immensely useful for cosmological studies since, with a knowledge of the cluster mass distribution, we can 'invert' the lensing equation for any distorted background object viewed through the cluster and estimate its distance.

7 CONCLUSIONS

7.1 Conclusions

• Using a homogeneously selected catalogue of candidate arcs we find that the rate of discovery of arcs with $A > 2$ in moderate redshift rich clusters to be $N_{arcs} \lesssim 1$ per cluster at a surface brightness limit of $\mu_V = 26$ mag/arcsec^2. We have shown that the characteristics of the candidate arc sample are consistent with the lensing hypothesis. We split the clusters into two groups which differ primarily in their mean redshift and apply a number of tests to determine the lensing strength of the two samples. All the tests show that the more distant clusters have a weaker lensing signal compared to the nearer sample. Independent observations imply this may be partly due to evolution in the cluster properties. In addition deep ROSAT X-ray observations of the distant clusters shows that all the clusters are under-luminous in X-rays for their optical richness. We conclude that evolution in the depth and more importantly the shape of cluster's potential wells is affecting both the lensing and X-ray properties of these clusters. Such changes are to be expected if we are observing clusters at an epoch where they are still dynamically young.

• Giant arcs provide us with a unique and easily recognisable probe of the nature of field galaxies at high redshift. Using all the available spectroscopically confirmed arcs we

show that their optical-infrared colours are representative of galaxies found in the deepest field surveys and that their colour distribution shows no evidence of any bias arising from surface brightness or ultraviolet selection effects peculiar to the lensing process. Moreover we conclude that the distribution of intrinsic K luminosities of the arcs indicates that the median luminosity of the sources is less than that of field galaxies at $z \lesssim 0.5$. The optical-infrared colours of the giant arc sample shows strong evidence for enhanced star formation. The blue colours cannot, however, arise from either secondary bursts in pre-existing evolved systems or a dramatic single event associated with galaxy formation. More likely we are witnessing an extended formation phase possibly associated with disk formation at redshifts $z \simeq 1$. The lack of a large fraction of $z \gtrsim 1$ giant arcs provides constraints on the tail of the $B \sim 26$ redshift distribution.

• Using very deep optical images of three rich clusters at redshifts of $z = 0.26$, $z = 0.55$ and $z = 0.89$ we probe the evolution of the gravitational lensing signal with redshift to provide information on the redshift distribution of faint field population at $I \leq 25$ ($B_j \lesssim 27$). Combining the results from the analysis of all three clusters we can reject galaxy evolution models which have a large population of dwarf galaxies at moderate and low redshift $z < 0.5$. Our constraints on models with large fractions of high redshift galaxies are weaker due to the lack of detailed information about the dynamical state of our most distant cluster. However, our prefered distribution for the faint field population to $I = 25$ ($B_j \lesssim 27$) is the no evolution prediction. The burst model of Broadhurst *et al.* (1988) and the merger model of Broadhurst *et al.* (1992) both predict redshift distributions qualitatively similar to the N.E. model's. In addition the latter model also explains the decrease in median K luminosity of high redshift sources probed by the giant arcs.

• We have successfully reconstructed the mass distributions of two luminous X-ray selected clusters at $z = 0.26$ and $z = 0.55$. Both maps show significant substructure in the cluster mass distributions. The preponderance of substructure in two of the brightest X-ray

clusters in the sky is an indication that such massive structures have undergone significant growth at relatively recent epochs. This would imply significant growth in the cluster mass at relatively recent epochs. The morphology of both mass distributions shows a remarkable similarity to the X-ray and galaxy surface density maps of the clusters outside of the core of the cluster. However, in the core of our lowest redshift cluster we find that the galaxies are more centrally concentrated than the mass. One possible process which would cause this is dynamical segregation. The lensing analysis provides estimates of the masses for our two lowest redshift clusters. Both of these have dispersions $\sigma_{cl} \gtrsim 1000$ km/sec and are thus on the extreme tail of the predicted distribution of cluster dispersions in standard CDM.

• We present a new wide separation (10 arcsec) multiply-imaged system in the rich cluster AC114 ($z = 0.31$). Spectroscopic observations of the multiple images confirm that they arise from the same source, which lies behind the cluster probably at $z = 1.87$. Preliminary modelling of the images using a variety of mass distributions puts a lower limit on the cluster velocity dispersion of $\sigma_{cl} \gtrsim 1000$ km/sec. Additional constraints are available if we are prepared to make assumptions about the position of the cluster centre or the role of the cD in the lensing system. Requiring the cluster centre to lie close to that determined from the arcs leaves solutions similar to those derived from the light distribution in the cluster.

7.2 Future Work

We have demonstrated the use of weak gravitational lensing to map the mass distribution in distant clusters. Enlarging the dataset will allow us to study the prevelance of mass

substructure as a function of epoch in the largest bound structures known. Such observations have a direct bearing on the epoch of cluster formation and current models of the growth of structure in the universe.

To improve our understanding of the global properties of our intermediate redshift cluster (Cl1455+22) we plan to undertake a deep spectroscopic survey of the cluster members. This will enable us to determine if the spatial segregation seen in the core of this system is reflected in the velocity dispersion and will provide a better estimate of the cluster velocity dispersion. Identification of cluster members will also provide stronger limits on the global mass to light ratio of the cluster. These new observations will also allow stronger discrimination between various models for the faint galaxy $N(z)$.

Deeper optical images of the cluster AC114 will enable us to both confirm the identity of the third image and provide an ensemble of distorted objects to map the dark matter distribution on larger scales in the cluster (*c.f.* Chapter 5). AC114 is also the subject of a deep ROSAT pointing to image the hot X-ray gas in the cluster. A well constrained lensing model is immensely useful for cosmological studies since, with a knowledge of the cluster mass distribution, we can 'invert' the lensing equation for any distorted background object viewed through the cluster and estimate its distance.

8 APPENDIX

8.1 Glossary and Results

In this appendix we state the main equations used in our lensing calculations. The inten-
tion here is to present the results used in the previous chapters with short explanations of
their derivations to allow the reader to gain insight into some of the main observational
consequences of lensing and the mathematics behind them. The majority of this section
restates results derived by previous workers and in this it relies heavily upon the recently
published textbook on gravitational lensing by Schneider *et al.* (1992). The review by
Blandford & Kochaneck (1987b) also gives a good overview of the field, while Blandford
& Kochanek (1989) and Miralda-Escudé (1991a) cover relevant results and notation. A
number of gravitational lensing theorems, some of which are generally applicable, others
which just apply to the case of multiple-lensing have been derived – what follows in Sec-
tion 1 is a guide and glossary to the main results. While in Section 2 we give details of
the lens mass reconstruction technique used in Chapter 5.

Condition for multiple lensing: For a lens to be capable of focusing two divergent
light paths at the observer its projected mass surface density must exceed a critical value.

Moreover, for the splitting to be observable (see below, Figure 8.2) the lens must be massive. These two conditions are most frequently fulfilled by massive dissipational systems: galaxies and clusters. The critical surface density is defined as:

$$\Sigma_{crit} = \frac{c^2}{4\pi G}\frac{D_{os}}{D_{ol}D_{ls}} \tag{1}$$

$\Sigma_{crit} \sim 0.5$ g/cm^2 for observed lens configurations (1 kpc^2 at 1 g/cm^2 is 4.8 10^9 M$_\odot$). For a non-singular isothermal mass distribution we have:

$$\Sigma \sim 1.4 \left(\frac{\sigma}{1000\mathrm{km/sec}}\right)^2 \left(\frac{100\mathrm{kpc}}{r_c}\right) \mathrm{g/cm}^2 \tag{2}$$

This translates into a condition for multiple-images of:

$$\sigma \gtrsim 1000\sqrt{\left(\frac{r_c}{170\mathrm{kpc}}\right)} \quad \mathrm{km/sec} \tag{3}$$

Deflection Angles and Lens Mapping: The deflection angle is the apparent shift in the position of an object on the sky when a mass is placed close to it in the foreground. The deflection angle for a point mass is given by:

$$\alpha = \frac{4GM}{c^2}\frac{\vec{\theta_i}}{|\vec{\theta_i}|^2} \tag{4}$$

where $\vec{\theta_i}$ is the angular distance in the image plane between the beam and the deflector. Here we have made the implicit assumption that the deflection occurs in a small path length compared to the unperturbed path (the 'thin-screen' approximation). The total deflection due to a distribution of mass can be calculated from the sum over the contributions from

the individual point masses, or for a continous distribution from the integral of the surface density($\Sigma(\theta)$). For a spherical singular isothermal sphere mass distribution this leads to:

$$\alpha = \frac{4\pi\sigma^2}{c^2}\frac{D_{ls}}{D_{os}} \equiv b \qquad \alpha \sim 29 \left(\frac{\sigma}{1000\text{km/sec}}\right)^2 \text{ arcsec} \qquad (5,6)$$

where σ is the one dimensional velocity dispersion, and D_{ls} and D_{os} are the angular diameter distances between the lens and source and the observer and source. The second relation is for an infinitely distant source. Figure 8.1 also shows the main observational effect of a gravitational lens – the distortion of the images of objects seen through the lens. The sources are mapped onto images at larger angular distances from the lens centre. The images have the same angular extent as measured from the lens centre and the same width as the source. They therefore appear tangentially elongated and as surface brightness is conserved in gravitational lensing they will appear brighter.

α is proportional to the gradient of the effective surface potential and is independent of radius for a singular isothermal distribution (see above). b is the angular size of the ring created by placing a source directly behind the lens – the Einstein radius (r_+, Figure 8.1). The geometrical term in the equation is an increasing function of the source redshift for a given lens, so more distant objects create larger Einstein rings and appear more distorted. The deflection angle gives the vector mapping between the source and image plane:

$$\vec{\theta_i} - \vec{\theta_s} = \alpha(\vec{\theta_i}) = \nabla\phi(\vec{\theta_i}) \qquad (7)$$

This is the lens mapping used in all lensing calculations. We illustrate this in Figure 8.2. ϕ is a function of the effective surface potential (ψ) of the lens and the geometry: $\psi = (2D_{ol}D_{ls}\phi)/(D_{os}c^2)$. For a singular isothermal lens $\phi = b\theta_i$. We return to this formulation

when discussing the use of elliptical lens models below. The final relationship to complete the loop is that between the surface potential and the surface density:

$$\nabla^2 \psi(\vec{\theta_i}) = 2\frac{\Sigma(\vec{\theta_i})}{\Sigma_{crit}} \tag{8}$$

A spherically symmetric lens is capable of producing at least one image and at most three images of a single source. For the sub-critical lens curve in Figure 8.2 we have only one intercept for any choice of the source position. In the singular lens case the third central image is unobservable due to strong deamplification by the cusp – leaving only two images. For non-singular lenses the amplificiation of the third image is proportional to the core radius squared. The multiple image configurations of the spherical lens are characterised by whether the brightest pair of images are both on the same side (Allied) or on opposite sides (Opposed) of the lens centre – the images always lie on the a line through the lens centre (Figure 8.3). To produce unaligned images requires a non-spherical potential.

The distortion of an image or a flux bundle – the mapping of the source to image areas – is given by the differential of the deflection mapping:

$$A(\vec{\theta_i}) = \frac{\delta\vec{\theta_s}}{\delta\vec{\theta_i}} \tag{9}$$

$$|A_{ij}| = (1 - \delta_i^2\phi)(1 - \delta_j^2\phi) - (1 - \delta_i\delta_j\phi)^2 = (1 - \kappa^2) - \gamma^2 \tag{10}$$

The inverse of the determinant of the magnification tensor ($|A_{ij}|$) is the amplification, the tensor is symmetric – thus the images can never be rotated by a single lens. The parameters κ and γ are called the convergence and shear of the lens and are evaluated at the image position. κ measures the focusing due to the mass inside the bundle while γ
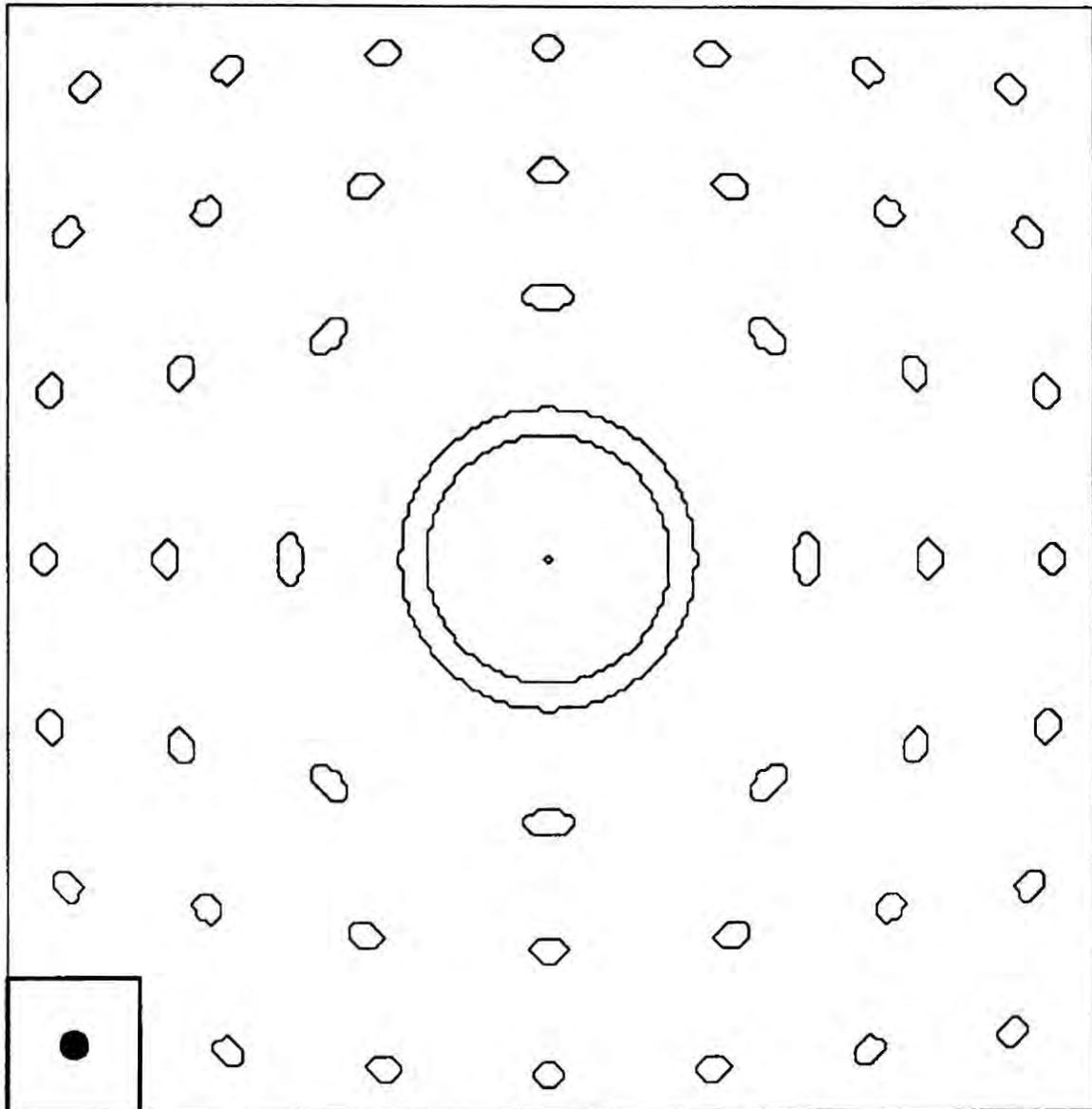
Figure 8.1 The effect of a spherically symmetric singular isothermal lens, in the centre of the field, on a background grid of intrinsically circular sources. While the distortion is obviously strongest near the centre of the lens (the giant arc regime) the large number of slightly distorted objects at larger radii (the arclets) may be used in statistical tests of the lens parameters. The insert shows the original source size.
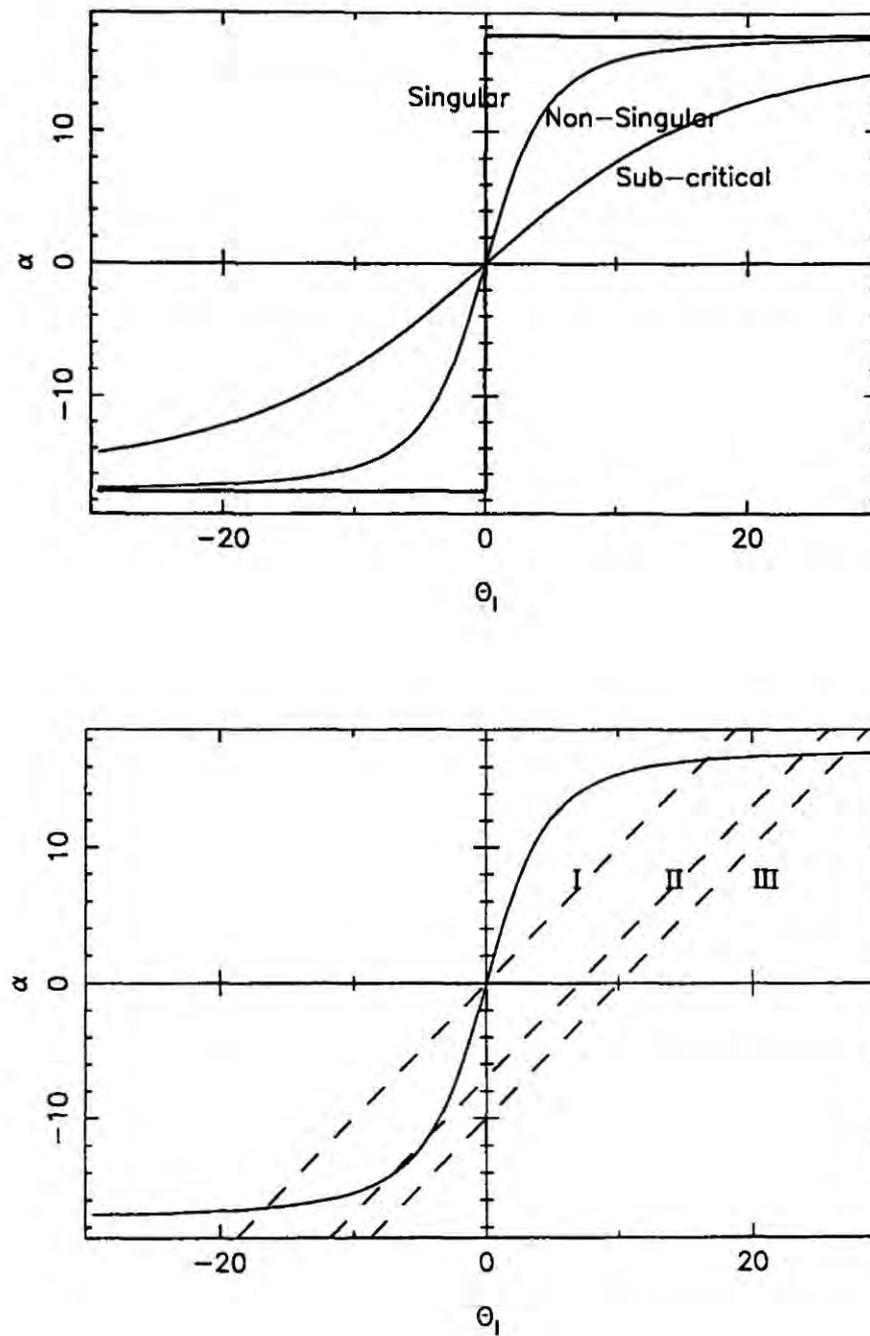
Figure 8.2 (a) A plot of the bending angle (α) as a function of radius for three isothermal sphere lenses, one singular, one non-singular and one sub-critical non-singular. (b) For the non-singular lens we show three positions of the source. Images of a source are located at the intercept of the bending angle curve with dashed line $\alpha = \theta_i - \theta_s$. For a source close to the centre of the lens there are three solutions (I), as the source moves out two of these merge (II) and disappear across a critical line, to leave only one (III).

gives the distortion of the bundle due to mass outside it – this is the term that determines the degree of image distortion.

Transparent Slabs: Uniform transparent slabs are capable of focusing light rays from background sources and so change their observed brightnesses ($\kappa > 0, \gamma = 0$). For multiple images of an object the slab boosts the apparent separation of the images, the deflection is given by:

$$\theta_i - \theta_s = \theta_i \frac{\Sigma}{\Sigma_{crit}} \tag{11}$$

The increase in the separation of two images is just proportional to: $(1 - \frac{\Sigma}{\Sigma_{crit}})^{-1}$. The result of adding a slab to a lens can be illustrated by reference to Figure 8.2. The slab would add an additional term to the deflection angle (α) that is proportional to the distance from the lens centre. This changes the asymptotic behaviour of the curves – pushing out the crossing points and hence the positions of the observed images.

Critical lines and Caustics: For a given lens configuration the regions in the source plane corresponding to different numbers of observed images are separated by closed lines – caustics. As a source crosses one of these lines a pair of images of opposite parity is either created or destroyed (by merging; Figure 8.2 & 8.3). The images appear and disappear at critical lines – these are the mapping of the caustics on the image plane. For a sufficiently dense lens the mass determines the area of the source plane contained within the critical lines. The image amplification diverges near critical lines so the two images have very high magnifications as they merge. Also, the sign of the determinant of the amplification matrix is opposite for images either side of a critical line and so the two images have opposite parity. The parity (handedness) of the images is rarely apparent in optical observations of lensing systems – although both AC114 and Cl2244−02 contain examples.
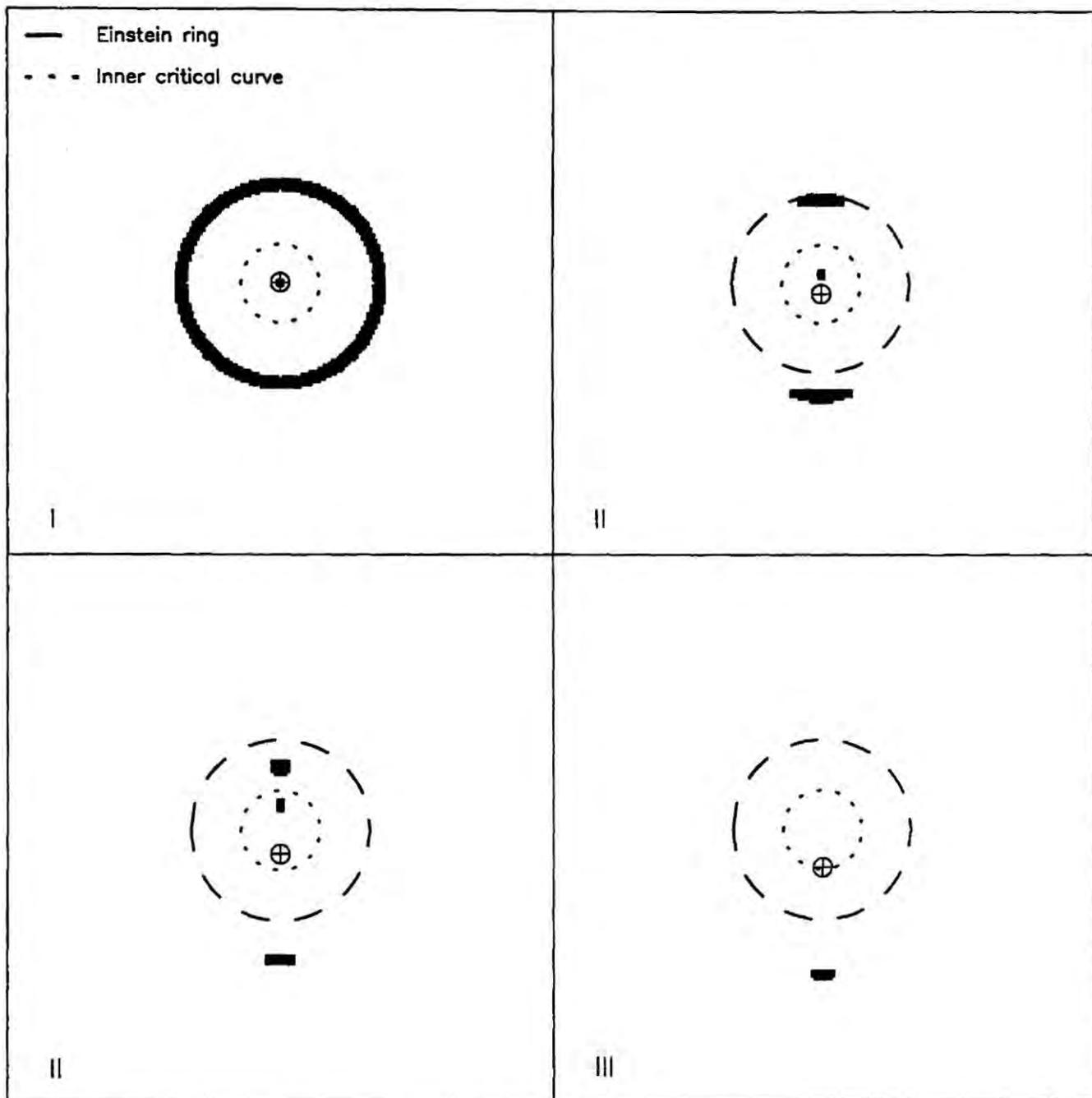
Figure 8.3 Four plots of observations of the lensing configrations shown in Figure 8.2(b) for a spherically symmetric non-singular lens. The images merge (II) across the inner critical line r_- associated with the core. For a singular lens this line shrinks to a point.

Caustics come in a variety of flavours – depending upon the associated singularity in the lens mapping. The simplest is the 'fold', this creates either two additional images or none for a source either side, the singularity is associated with a smooth caustic line. The images are separated along the perpendicular to the associated critical line. The next more complex singularity occurs when the caustic has a cusp in it and this forms either one or three images if the source is either outside or inside of the cusp (Figure 8.4), the images being separated tangentially. The caustics of a spherically symmetric lens are of the fold type, while for an elliptical lens one of these (the tangential caustic) has cusps attached. The relative importance of the two caustics is roughly determined by the ratio of the core size of the lens to its Einstein radius. As the core size is reduced the cusp caustic shrinks to a degenerate point.

Elliptical lenses: Spherically symmetric lenses can produce at most three images of a source – if we introduce an quadrupole perturbation to the potential the lens is capable of forming five images. The potential of an elliptical mass distribution can be approximated by either the addition of a quadrupole term to the deflection angle equation or an elliptical potential. Although the latter does not accurately correspond to the potential of an elliptical surface mass distribution (Blandford & Kochanek 1987a). For a general elliptical surface mass distribution the major axis of the mass distribution is orientated perpendicular to the major axis of the associated caustic and parrallel to the effective surface potential (Figure 8.4). The ellipticity of the potential (ϵ_{pot}) is also not the ellipticity of the mass (ϵ_{mass}) – for an isothermal mass distribution: $\epsilon_{pot} = \epsilon_{mass}/3$. The form of the effective potential used in this work is that of Kochanek (1991) an expansion of a non-singular isothermal potential to quadrupole order:

$$\phi(r,\Phi) = b\sqrt{(r^2 + r_c^2)} + \frac{b\epsilon_{mass}}{3} \frac{r^2}{\sqrt{(r^2 + r_c^2)}} cos(2(\Phi - \Phi_\epsilon)) \qquad (12)$$

Φ_ϵ and ϵ_{mass} are the orientation and ellipticity of the surface mass density of the lens and r_c is the core radius of the mass distribution.

As stated above an elliptical lens has two caustics – one associated with a 1-3 images transition the other with the 3-5 transition (Figure 8.4). For small ratios of core size to Einstein radius the outer of the two curves is always a fold caustic and creates radially merging images as the source approaches it from inside. The inner caustic has cusps at which images are created which are separate roughly tangentially to the lens centre. For large core sizes the cusp caustic can lie outside of the fold in certain regions of the source plane (a 'naked' cusp, Figure 8.4). This configuration can produce either one bright image or three images – if the source is outside or inside the caustic.

Marginal lenses: This class of lenses comprises those systems just on the boundary of being able to create multiple images and has been exhaustively researched by Kovner (1987). The lenses are combinations of sub-critical components which conspire to boost one another to criticality. The important fact about such systems is that they will tend to create images which are just merging and so have very high magnifications – these will therefore tend to dominate any flux limited samples.

Achromatic Gravitational Lenses: Gravitational lenses act as effectively achromatic (or non-dispersive) lenses. This statement covers both individual images and multiple-images – in the former as by definition all photons travel along null-geodesics – so all wavelengths emitted by the source in the same direction travel along the same path. In the case of multiple-images the light arriving at one instant at the observer has traversed different paths but it is only the differences between the path ends – in particular the emission – which is important. We make the reasonable assumption that the expansion factor of the universe does not change on a time scale comparable to the time delay between the paths (the time between the two emission events). Thus the two images must
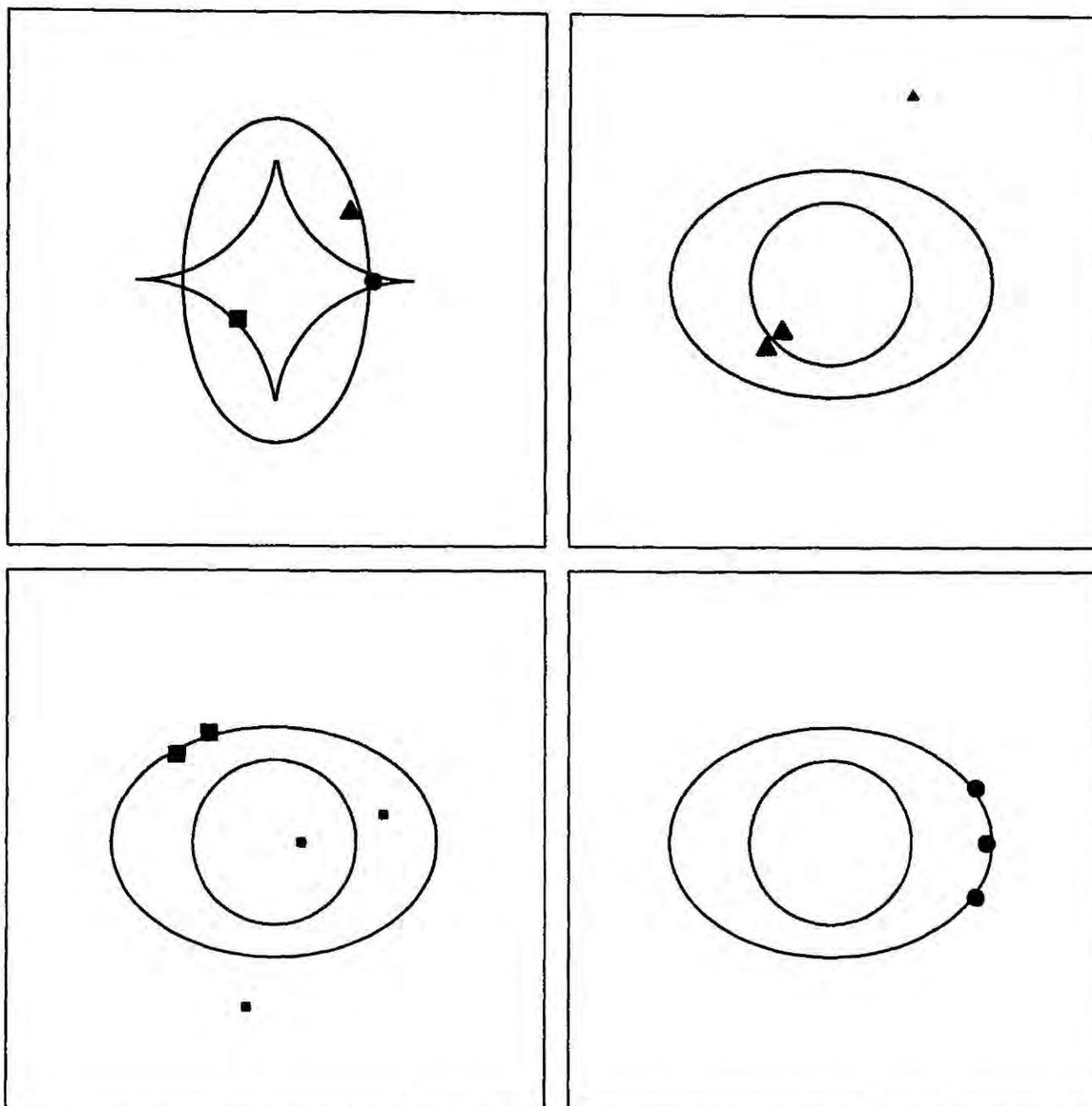
Figure 8.4 A schematic diagram of a variety of lensing configurations produced by an elliptical lens (adapted from Grossman & Narayan (1988)). The major axis of the surface density is horizontal. The illustration at top left shows the structure of the caustics on the source plane as well as the position of the three sources whose images are illustrated in the other panels. The elliptical caustic is a pure fold, while the caustic associated with the core has cusps attached. All the configurations showns are Allied and the lens has a large core.

show the same redshift and hence colour. Therefore in all cases the gravitational lens acts as an achromatic lens. However, it may be possible to observe gravitationally lensed systems with different coloured components – due to differential reddening in the lens or differential magnification of regions of the source with different colours.

Time-delays: The geometrical optics construction of gravitational lensing can be recast into a time-delay model using the arrival time surfaces of spherical wavefronts emitted at the source. The gravitational potential of the lens then behaves as a medium with a variable refractive index – distorting the wavefronts and causing them to self-intersect – appearing as separate images (see Figure 5.1 in Schneider *et al.* (1992)). The points on the associated time-delay surface where its local curvature is zero give the position and parities of the multiple images. This construction is useful for looking at the time-delays between different paths through the lens. For two opposed images the time-delay is given by (Blandford & Kochanek 1987b):

$$\Delta\tau_{12} \propto \frac{1}{H_o} \frac{|\theta_1 - \theta_2|^2}{(A_1 + A_2)} \tag{13}$$

this is a function of the angular separation of the images $(\theta_1 - \theta_2)$ and their average amplification $(A_1 + A_2)$. The dependency upon H_o is the primary motivation for measuring time delays in multiply-imaged systems.

Odd-image Theorem: One of the major theorems of gravitational lensing is the Odd-image theorem. This states that an observer will always see an odd number of images of a source in a gravitational lens system – subject to the lens being transparent and not containing an event horizon (*i.e.* non-singular). To illustrate this we use an argument based on the time-delay model (Schneider *et al.* 1992) – an observer sees an image when they are crossed by the wavefront – for an unperturbed spherical wave they therefore see

only one image. If the wave is sufficiently distorted by the lens it will self-intersect and so the observer will be crossed by several pieces of the same wavefront. However, the wavefront always remains as a single connected surface, the observer is thus passed by two sections of the wave for each intersection – giving two images each time – as well as the original. The total number of images is then always odd.

In reality the differential amplification and position of the images in a lensed system usually results in one image being too faint to observe or superimposed upon a luminous lens leading to an even number of *observed* images.

Micro-lensing: This is a subject which has developed relatively recently – it concerns the effect of the discrete nature of the mass in the lens. The majority of the applications have been to study the effects of stellar mass objects in galaxies on the observed properties of lensed QSOs. In particular the passage of a star across one of the lines of sight to a background QSO causes large short-period fluctuations in its amplification. The subject has little bearing on sources which are significantly extended when compared to the Einstein ring of the micro-lens and so does not effect lensing of galaxies.

8.2 Deriving Mass Maps

The technique we use to construct maps of the projected mass surface density in Chapter 5 was pioneered by Kaiser. The paper detailing the procedure and testing it against simulated datasets is Kaiser & Squires (1992). We refer the reader to the original paper for a rigorous mathematical derivation of the technique.

This method uses the induced distortion in the background galaxy population to derive the mass distribution in the foreground lens. The problem with trying to use the ellipticity

pattern of the background galaxies is that the sources have an inherent distributions of ellipticities and random intrinsic orientations – we are therefore looking for a very weak signal in the presence of strong noise. The method uses two image parameters related to the ellipticity, e_1 and e_2 (Miralda-Escudé 1991):

$$e_1 = \left(\frac{I_{xx} - I_{yy}}{I_{xx} + I_{yy}} \right) \qquad e_2 = \left(\frac{2I_{xy}}{I_{xx} + I_{yy}} \right) \qquad (14, 15)$$

Where I represents the intensity weighted second moments of the image shape. e_1 measures the stretching of the image along the X and Y axes while e_2 measures the stretching in the direction Y=X.

The technique relies upon the fact that in the weak distortion regime the mean induced ellipticities $<e_1>$ and $<e_2>$ are linearly related to the effective surface potential of the lens. To increase the signal to noise in the measurement of the potential we can therefore average over a large number of background images to reduce the noise from the intrinsic ellipticity distribution. The surface potential then gives us the surface density of the lens via Poisson's equation, this can be evaluated on a grid of centres over the image plane. The mass map produced can then be smoothed to reduce shot noise. The final surface mass estimator is:

$$\Sigma(\vec{r}) = \sum W(\vec{r}_g - \vec{r}) \chi_i(\vec{r}_g - \vec{r}) e_i(\vec{r}_g) \qquad (16)$$

$$\chi_1(\vec{r}) = \frac{(r_1^2 - r_2^2)}{r^2} \qquad \chi_2(\vec{r}) = \frac{(r_1 r_2)}{r^2} \qquad (17)$$

W is a weighting function chosen to reduce the divergence encountered when an image at $\vec{r}_g$ lies on one of the evaluation grid points $(\vec{r})$. By varying this we can change the

resolution of the derived mass map – although higher resolution comes at the expense of increased noise. χ is a geometrical operator which gives the two predicted distortion components (e_1 and e_2) of an image at a position $\vec{r}_g$ from a point source lens centred at $\vec{r}$. The estimator thus resembles a weighted scalar product evaluated on a grid of points. The scalar product is of the observed e_1 and e_2 values for each background galaxy with those predicted at that position for a point mass centred on the current grid point.

The absolute scaling of this signal depends upon both the mass in the lens and the distance to the background population. Hence, using this estimator we can derive a relative mass distribution in the lens. If additional information is available – N(z) for the distorted galaxies or a dynamical estimate of the lens mass – then the absolute mass distribution can be constructed. The method is conceptually similar to a deconvolution of the observed induced ellipticity field, using as a point spread function the ellipticity pattern induced by a point mass.

The optimal weighting used in the ellipticity measurement in Chapter 5 tends to circularise images – thus e_1 and e_2 will both be smaller. This would produce a systematic lowering of the estimated Σ – as the induced ellipticities are smaller and so less mass is required in the lens. However, the noise in the individual measurements is reduced by the optimal weighting and this will tend to counter this offset as more images will contribute coherently to the signal. Indeed, this is the case with the optimally weighted reconstructed mass map having a 15-20% higher peak surface density compared to that created using the raw FOCAS moments.

REFERENCES

Abell, G.O., 1958 *Ap. J. Suppl.*, **3**, 211.

Abell, G.O., Corwin H.G. & Olowin, R.P., 1988 *Ap. J. Suppl.*, **70**, 1.

Adorf, H-M. 1992 ST-ECF Newsletter, No 17.

Angonin, M.C. 1992 in *Hamburg International Conference on Gravitational Lensing*, eds. Kayser, R. *et al.*, Springer Verlag, in press.

Angonin, M.C., Hammer, F. & Lavery R.J. 1992 in prep.

Aragón-Salamanca, A. 1991 PhD Thesis, Durham University.

Aragón Salamanca, A. & Ellis, R.S. 1990 in *Gravitational Lenses*, eds. Mellier, Y. *et al.*, Springer Verlag, 288.

Aragón-Salamanca, A., Ellis, R.S. & Sharples, R.M. 1991 *Mon. Not. R. astr. Soc.*, **248**, 128.

Arnaud, K. 1988 in *Cooling Flows in Clusters and Galaxies*, ed. Fabian, A.C., NATO ASI series, 31.

Babul, A. & Rees, M.J. 1992 *Mon. Not. R. astr. Soc.*, in press.

Bahcall, N. 1981 *Ap. J.*, **247**, 787.

Baron, E. & White, S.D.M. 1987 *Ap. J.*, **322**, 585.

Beers, T.C. & Tonry, J.L., 1986 *Ap. J.*, **300**, 557.

Bernstein, G.M., Tyson, J.A. & Kochaneck, C.S. 1993 *Ap. J.*, submitted.

Birkinshaw, M., Gull, S.F., Hardbeck, H.E. & Moffatt, A.T. 1992 *Ap. J.*, submitted.

Blandford, R.D. 1991 *Q. J. R. astr. Soc.*, Vol. 30, No. 3, 305.

Blandford, R.D. & Kochanek, C.S. 1987a *Ap. J.*, **321**, 658.

Blandford, R.D. & Kochanek, C.S. 1987b in *Dark Matter in the Universe*, eds. Bahcall, J. *et al.*, World Scientific, 133.

Blumenthal, G.R., Faber, S.M., Primack, J.R. & Rees, M.J. 1984 *Nature*, **311**, 517.

Boute, D.A. & Canizares, C.C. 1992 *Ap. J.*, **400**, 385.

Bower, R.G., Rose, J., Ellis, R.S. & Sharples, R.M. 1993 in prep.

Broadhurst, T.J., Ellis, R.S. & Shanks, T. 1988 *Mon. Not. R. astr. Soc.*, **235**, 827.

Broadhurst, T.J., Ellis, R.S. & Glazebrook, K., 1992 *Nature*, **355**, 55.

Bruzual A., G. & Charlot, S. 1992 *Ap. J.*, in press.

Burrows, C.J. 1992 ST-ECF Newsletter, No 18.

Burrows, C.J., Holtzman, J.A., Faber, S.M., Bely, P.Y., Hasan, H., Lynds, C.R. & Schroeder, D. 1991 *Ap. J.*, **369**, L21.

Butcher, H. Oemler, A., & Wells, D.C., 1983 *Ap. J. Suppl.*, **52**, 183.

Buzzoni, A. 1989 *Ap. J. Supp.*, **71**, 817.

Castander, F., Ellis, R.S., Couch, W.J., Bohringer, H. & Bower, R.G. 1993 in prep.

Colless, M., Ellis, R.S., Taylor, K. & Hook, R.N., 1990 *Mon. Not. R. astr. Soc.*, **244**, 408.

Colless, M.M., Ellis, R.S., Taylor, K.k, Broadhurst, T.J. & Peterson, B.A. 1992 *Mon. Not. R. astr. Soc.*, submitted.

Couch, W.J. & Sharples, R., 1987 *Mon. Not. R. astr. Soc.*, **229**, 423.

Couch, W.J., Hansen, L., Jørgensen, H., Nørgaard-Nielsen, H.U., Ellis, R.S. & Aragón-Salamanca, A., 1989 in *Particle Astrophysics: Forefront Experimental Issues*, ed. Norman E.B., World Scientific, p192.

Couch, W.J., Ellis, R.S., Malin, D.F. & Maclaren, I., 1990 *Mon. Not. R. astr. Soc.*, **249**, 606.

Couch, W.J., Jurcevic, J.S. & Boyle, B.J. 1993 *Mon. Not. R. astr. Soc.*, in press.

Cowie, L.L. 1991 in *Observational Tests of Cosmological Inflation*, eds. Shanks, T. *et al.*, NATO ASI series, 257.

Cowie, L.L., Lilly, S.J., Gardner, J. & MacLean, I., 1989 *Ap. J.*, **332**, L29.

Cowie, L.L. & Lilly, S.J., 1990 in *The Evolution of the Universe of Galaxies*, ed. Kron, R., ASP Conference Series, 212.

Cowie, L.L., Songaila, A., & Hu, E.M., 1991 *Nature*, **354**, 460.

Danese, L., de Zotti, G. & Tullio, G., 1980. *Astr. Astrophys.*, **82**, 322.

Davis, M., Efstathiou, G., Frenk, C.S. & White, S.D.M. 1985 *Ap. J.*, **292**, 371.

Dressler, A. & Gunn, J.E. 1992 *Ap. J. Supp.*, **75**, 1.

Edge, A., Stewart, S., Fabian, A. & Arnaud K.A. 1990 *Mon. Not. R. astr. Soc.*, **245**, 559.

Efstathiou, G., Ellis, R.S. & Peterson, B.A., 1989 *Mon. Not. R. astr. Soc.*, **232**, 431.

Efstathiou, G., Bernstein, G.M., Katz, N., Tyson, J.A. & Guhathakurta, P. 1991 *Ap. J.*, **380**, L47.

Elias, J.H., Frogel, J.A., Mathews, K., & Neugebauer, G. 1982 *Astron. J.*, **87**, 1029.

Ellis, R.S. 1990 in *Gravitational Lenses*, eds. Mellier, Y. *et al.*, Springer Verlag, 236.

Ellis, R.S., Couch, W.J., MacLaren, I. & Koo, D.C. 1985 *Mon. Not. R. astr. Soc.*, **217**, 239.

Ellis, R.S., Allington-Smith, J.R. & Smail, I., 1991 *Mon. Not. R. astr. Soc.*, **249**, 184.

Evrard, A.E., 1989 *Ap. J.*, **341**, L71.

Fitchett, M.J., 1990 in *Clusters of Galaxies*, eds. Oegerle, W.R. *et al.*, CUP, 111.

Fort, B. 1990 in *Gravitational Lenses*, eds. Mellier, Y. *et al.*, Springer Verlag, 221.

Fort, B., Prieur, J-L., Mathez, G., Mellier, Y., & Soucail, G. 1988 *Astr. Astrophys.*, **200**, L17.

Fort, B. 1992 in *Arcs & Arclets: ESO Key-Project Meeting*, Toulouse.

Frenk, C.S., White, S.D.M., Efstathiou, G. & Davis, M. 1990 *Ap. J.*, **351**, 10.

Fugukita, M., Takahara, F., Yamashita, K. & Yoshii, Y. 1991 *Ap. J.*, **361**, L1.

Gardner, J.P., Cowie, L.L. & Wainscoat, R.J. 1993 *Ap. J.*, submitted.

Garrett, M.A., Walsh, D. & Carswell, R.F. 1992 *Mon. Not. R. astr. Soc.*, **254**, 27.

Gioia, I.M., Henry, J.P., Maccacaro, T., Morris, S.L., Stocke, J.T. & Wolter A. 1990 *Ap. J.*, **356**, L35.

Giraud, E. 1992 *Astr. Astrophys.*, in press.

Glazebrook, K., Broadhurst, T.J., Ellis, R.S., Tanvir, N., Allington-Smith, J. & Taylor, K. 1993 in prep.

Griffiths, R., Elston, R. & Schade, D. 1992 in *Science with HST*, ST-ECF Workshop.

Grossman, S. & Narayan, R. 1988 *Ap. J.*, **324**, L37.

Guhathakurta, P., Tyson, J.A. & Majewski, S.R., 1990. *Ap. J.*, **357**, L9.

Gunn, J.E., Hoessel, J.G. & Oke, J.B. 1986 *Ap. J.*, **306**, 30.

Harris, H.C., Baum, W.A., Hunter, D.A. & Kreidl, T.J. 1991 *Astron. J.*, **101**, 677.

Hammer, F., Le Févre, O., Jones, J., Rigaut, F. & Soucail, G., 1989 *Astr. Astrophys.*, **208**, L7.

Hammer, F. & Rigaut F. 1991 *Astr. Astrophys.*, **226**, 45.

Hansen, L., Nørgaard-Nielsen, H.U. & Jørgensen, H.E., 1987 ESO Messenger, **47**, 46.

Hansen, L., Nørgaard-Nielsen, H.U., Jørgensen, H.E., Ellis, R.S. & Couch, W.J., 1989 *Astr. Astrophys.*, **211**, L9.

Henry, J.P., Gioia, I.M., Maccacaro, T., Morris, S.L., Stocke, J.T. & Wolter A. 1992 *Ap. J.*, **386**, 408.

Hughes, J.P. 1989 *Ap. J.*, **337**, 21.

Jarvis, J.F. & Tyson, J.A. 1981 *Astron. J.*, **86**, 476.

Kaiser, N. 1992 in *Clusters of Galaxies*, ed. Fabian, A.C., Kluwer, 323.

Kaiser, N. & Squires, G. 1992 *Ap. J.*, in press.

Kassiola, A., Kovner, I. & Blandford, R.D. 1992, preprint.

Kellogg, E., Falco, E.E., Forman, W., Jones, C. & Slane, P. in *Gravitational Lenses*, eds. Mellier, Y. *et al.*, Springer Verlag, 141.

King & Ellis, R.S. 1985 *Ap. J.*, **288**, 456.

Kochanek, C.S. 1990 *Mon. Not. R. astr. Soc.*, **247**, 135.

Kochanek, C.S., 1991 *Ap. J.*, **382**, 58.

Koo, D.C., 1981 *Ap. J.*, **251**, L75.

Koo, D.C., 1989 in *Epoch of Galaxy Formation*, eds. Frenk C.S. *et al.*, Kluwer Academic Press, 71.

Koo, D.C. & Kron, R.G. 1992 *Ann. Rev. Astron. & Astrophy.*, Vol. 30, 613.

Kovner, I. 1987 *Ap. J.*, **321**, 686.

Kovner, I. 1989 *Ap. J.*, **337**, 621.

Lavery, R.J. & Henry, J.P. 1988 *Ap. J.*, **329**, L21.

Lilly, S.J. 1992 *Mon. Not. R. astr. Soc.*, in press.

Lilly, S.J., Cowie, L.L. & Gardner, J.P. 1991 *Ap. J.*, **369**, 79.

Lucy, L.B. 1974 *Astron. J.*, **79**, 745.

Lynds, R. & Petrosian, V., 1989 *Ap. J.*, **336**, 1.

McLean, I.S., Chuter, T.C, MacCaughrean, M.J. & Rayner, J.T. 1985 *Proc. S.P.I.E.*, **627**, 430.

Malin, D.F. & Carter, D. 1980 *Nature*, **285**, 643.

Malumuth, E.M. & Kirshner, R.P. 1985 *Ap. J.*, **291**, 8.

Mason, K.O., Spinrad, H., Bowyer, S., Reichery, G. & Stauffer, J. *Astron. J.*, **86**, 803.

Mellier, Y., Soucail, G., Fort, B. & Mathez, G. 1988 *Astr. Astrophys*, **199**, 13.

Mellier, Y., Fort, B., Soucail, G. & Mathez, G. & Cailloux, M. 1991 *Astr. Astrophys*, **380**, 334.

Metcalfe, N., Fong, R.F., Shanks, T.S. & Jones, L.R. 1990 *Mon. Not. R. astr. Soc.*, **249**, 498.

Miralda-Escudé, J. 1991a *Ap. J.*, **370**, 1.

Miralda-Escudé, J. 1991b *Ap. J.*, **380**, 1.

Miralda-Escudé, J. 1992 *Ap. J.*, in press.

Narayan, R., Blandford, R. & Nityananda, R. 1984 *Nature*, **310**, 112.

Nemiroff, R.J. & Dekel, A. 1989 *Ap. J.*, **344**, 51.

Nørgaard-Nielsen, H.U., Hansen, L., Jørgensen, H.E., Aragón-Salamanca, A., Ellis, R.S. & Couch, W.J., 1989 *Nature*, **339**, 523.

Peebles, P.J.E., Daly, R.A. & Juszkiewicz, R., 1990 *Ap. J.*, **347**, 563.

Pelló, R., Le Borgue, J.F., Soucail, G., Mellier, Y. & Sanahuja, B. 1991 *Astr. Astrophys.*, **366**, 405.

Phillipps, S., Disney, M.J. & Davies, J., 1990 *Mon. Not. R. astr. Soc.*, **242**, 235.

Richstone, D.O., Loab, A. & Turner, E.L. 1992 preprint.

Rocca-Volmerange, B. & Guiderdoni, B. 1990 *Mon. Not. R. astr. Soc.*, **247**, 166.

Rosa, M., Joubert, M. & Benvenuti, P. 1984 *Astr. Astrophys. Supp.*, **37**, 361.

Salpeter, E.E. 1955 *Ap. J.*, **121**, 161.

Schild, R., Leach, R., Weekes, T. & Gursky, H. *Astron. J.* **85**, 121.

Schneider, P., Ehlers, J. & Falco, E.E. 1992 *Gravitational Lenses*, Springer Verlag.

Silvey, S.D., 1975 *Statistical Inference*, Chapman & Hall.

Soucail, G. 1992 in *Clusters of Galaxies*, ed. Fabian, A.C., Kluwer, 199.

Soucail, G., Fort, B., Mellier, Y. & Picat, J.P. 1987 *Astr. Astrophys.*, **172**, L14.

Soucail, G., Mellier, Y., Fort, B., Mathez, G. & Cailloux, M. 1988 *Astr. Astrophys.*, **191**, L19.

Soucail, G., Mellier, Y., Fort, B., Mathez, G. & Cailloux, M. 1990 in *Gravitational Lenses*, eds. Mellier, Y. *et al.*, Springer Verlag, 291.

Tresse, L., Hammer, F., Le Fèvre, O. & Proust, D. 1993 *Astr. Astrophys.*, submitted.

Toth & Ostriker 1992 *Ap. J.*, **389**, 5.

Turner, E.L., Ostriker, J.P. & Gott, J.R., 1984 *Ap. J.*, **284**, 1.

Tyson, A.J. 1988 *Astron. J.*, **96**, 1.

Tyson, J.A., Valdes, F. & Wenk, R.A., 1990 *Ap. J.*, **349**, L1.

Walsh, D., Carswell, R.F. & Weymann, R. 1979 *Nature*, **279**, 381.

West, M.J. 1990 in *Clusters of Galaxies*, eds. Oegerle, W.R. *et al.*, CUP, 65.

West, M.J. & Richstone, D.O. 1988 *Ap. J.*, **335**, 532.

White, S.D.M. & Frenk, C.S. 1991 *Ap. J.*, **379**, 52.

White, S.D.M., Silk, J. & Henry, J.P. 1981 *Ap. J.*, **251**, L65.

Wu, X.P. & Hammer, F. 1992 *Mon. Not. R. astr. Soc.*, in press.

ACKNOWLEDGEMENTS